NASA Contractor Report 177454

Rotating Hot-Wire Investigation of the Vortex Responsible for Blade-Vortex Interaction Noise

Richard R. Fontana

(NASA-CR-177454) ROTATING HOT-WIRE INVESTIGATION OF THE VORTEX RESPONSIBLE FOR BLADE-VORTEX INTERACTION NOISE (Massachusetts Inst. of Tech.) 240 p N89-17466
CSCL 20A G3/71 Unclas 0189704

CONTRACT NAG2-182
December 1988

NASA
National Aeronautics and
Space Administration

NASA Contractor Report 177454

Rotating Hot-Wire Investigation of the Vortex Responsible for Blade-Vortex Interaction Noise

Richard R. Fontana
Massachusetts Institute of Technology
Cambridge, Massachusetts

Prepared for
Ames Research Center
CONTRACT NAG2-182
December 1988

National Aeronautics and
Space Administration

Ames Research Center
Moffett Field, California 94035

Rotating Hot-Wire Investigation of the Vortex Responsible for Blade-Vortex Interaction Noise

by

RICHARD REMO FONTANA

Submitted to the Department of Mechanical Engineering
on October, 1986 in partial fulfillment of the
requirements for the Degree of Doctor of Science in
Mechanical Engineering

Abstract

The distribution of the circumferential velocity of the vortex responsible for blade-vortex interaction noise was measured using a rotating hot-wire rake synchronously meshed with a model helicopter rotor at the blade passage frequency. Simultaneous far-field acoustic data and blade differential pressure measurements were obtained. Results show that the shape of the measured far-field acoustic blade-vortex interaction signature depends on the blade-vortex interaction geometry. The experimental results are compared with the Widnall-Wolf model for blade-vortex interaction noise.

The measured far-field acoustic signature due to the blade-vortex interaction is dependent on the blade-vortex interaction geometry. For the model rotor tested, skew of the vortex relative to the plane of the blade causes the vortex to pass closer to the tip of the blade when it passes over the suction side of the blade. When

the vortex passes on the pressure side of the blade near the tip the blade actually cuts the center of the vortex inboard of the blade tip. The steepest velocity gradients occur where the blade passes closest to or cuts the center of the vortex, and the steepest velocity gradients produce the most intense pressure fluctuations on the blade. The flow field near the tip of the blade is complicated by the effect of the flow around the blade tip and the close proximity of several rotor wake vortices other than the one responsible for the blade vortex interaction noise. The flow field away from the blade tip is not as strongly influenced by these effects. This causes the character of the pressure fluctuation produced by the blade-vortex interaction to be different near the blade tip than at inboard sections of the blade. Because of these effects, the character of the far-field acoustic pulse is influenced more by the behavior at the blade tip when the vortex passes closest to the tip and more by the behavior inboard of the blade tip when the blade cuts the vortex. The Widnall-Wolf model does not account for the effect of the flow near the blade tip and does not correlate well with the measured results when the vortex passes closest to the blade tip. When the vortex is cut by the blade then the blade tip effects are less important and the results predicted by the theory are within 2 dB of the measured results. Blade pressure measurements taken at 99% span near the leading edge were used to calculate the fluctuating lift of the blade near the tip. The spectrum of this lift was substituted into the theory to predict the far-field acoustic signature. When the vortex passes closest to the tip of the blade, the far-field acoustic signature is within 1 dB of that predicted from the blade tip pressure measurements and the waveforms have the same characteristic shape.

Variation in the position of the vortex from blade passage to blade passage is on the order of one blade semichord by the time the blade-vortex interaction occurs. This meander of the vortex may be responsible for the fact that averaged measurements by other researchers show a greatly reduced vortex strength or nonexistent vortex at this point. Rotating hot wire rake measurements show that the peak velocities in the vortex are typically reduced on the order of 20% from their initial value by an increase in the viscous core size of the vortex. Vortex circulation before the blade vortex interaction responsible for blade slap is not greatly reduced from its value just after the creation of the vortex. Measurements indicate that using the total circulation of the blade to determine the vortex velocity distribution without accounting for the effect of the vortex rollup process results in an overprediction of the vortex velocity near the center of the vortex by a factor of 2 for these measurements. The Betz vortex model accounts for the variation of the vortex circulation with radial position and is in good agreement with the measured results. This implies that computational models for wake analysis must account for the distributed circulation of the vortex if the velocities near the center of the vortex have a significant effect on the results.

Thesis Committee:

Prof. J. E. Hubbard, Jr., Chairman,
Prof. W. C. Flowers
Prof. J. H. Haritonidis
Dean W. L. Harris, University of Connecticut.

ACKNOWLEDGEMENTS

The author would like to express his appreciation to Professor Jim Hubbard, my committee chairman and advisor who provided excellent guidance, advice, and support while I have been at MIT. He provided me with the freedom to work on my own and insight on the key research requirements. He has also been an excellent advisor and a pleasure work with. Professor Joe Haritonidis is due a special thanks for his generosity with his time, advice, and equipment. He provided helpful discussions and ideas as well as the use of his hot-wire instrumentation equipment. I would like to thank Professor Woody Flowers for his helpful discussions on the design and philosophy of the design for the experiment and Dean Wesley Harris for his foresight and recommendations as to what would be the most significant and rewarding areas of investigation. I would also like to note that Dr. Rudolf Martinez provided a helpful discussion about the theoretical development. I owe Professor Bill Unkel a special thanks. His help was extremely valuable in the task of interfacing the Transiac data acquisition system with the IBM PC-XT computer. He provided the use of his excellent oscilloscope program "Unkel Scope", and wrote the program to interface my data with that program. Without his assistance, advice, and generosity with his equipment, the interfacing task would have taken much more time and would not have been of the same quality and utility. Paul Bauer provided valuable expertise with electronics and instrumentation that is most appreciated. I would like to thank Al Shaw, Don Weiner, and Earl Wassmouth for their help in the wind tunnel and machine shop and Professor Mark Drela for extremely useful and educational discussions on aerodynamics. I would also like to thank Dr. Charles Smith, contract monitor for the NASA Ames Research Center grant which supported this work.

I would like to acknowledge my friends from the office, sailing pavilion, weight room, and other places. They have been helpful and entertaining and have made my experiences at MIT a generally pleasant and interesting one. I value the friends that I have made and the things that I have learned from them as one of the most important benefits of the time that I have spent at MIT.

I thank my family for their support and guidance throughout.

TABLE OF CONTENTS

Chapter 4

List of Figures

LIST OF SYMBOLS

μ = MUE = ADVANCE RATIO

ψ = AZIMUTH ANGLE OF ROTOR BLADE

B0 = ONE BLADE SEMICHORD = (1 INCH)

C_0 = C0 = C = CORE RADIUS OF VISCOUS CORE PARAMETER IN VORTEX MODELS

dB = dB (PEAK) = 20 LOG[($P_{max}-P_{min}$)/.0002 PASCAL]

Γ = GAMMA = CIRCULATION

H/B0 = BLADE VORTEX SEPARATION DISTANCE DIVIDED BY THE SEMICHORD

I.L. = INTERACTION LENGTH

λ = LAMBDA = BLADE-VORTEX INTERACTION ANGLE

Θ = THETA = MICROPHONE COORDINATE SYSTEM (FIGURE 10)

ψ = PSI = MICROPHONE COORDINATE SYSTEM (FIGURE 10)

R = RADIUS OF ROTOR, RADIUS TO MICROPHONE

S_0 = s_0 = S0 = INTERACTION LENGTH/2

V_0 = V0 = VELOCITY OFFSET FOR VORTEX MODELS

CHAPTER 1

INTRODUCTION

Helicopter blade-vortex interaction (BVI) noise, often termed blade slap, is an impulsive noise produced when a rotating blade passes near or through a tip vortex trailed by a previous blade passage. This condition frequently occurs during landing or maneuvers when the rotor descends into its own wake. Pressure fluctuations produced as the blade experiences the vortex velocity field can radiate acoustically as noise spikes that often dominate the other noises produced by the helicopter. Other sources of impulsive noise have been observed, such as the noise generated as the blade tip approaches Mach one on the advancing side of the rotor or the noise generated when a shock is radiated from areas of transonic flow. These noise mechanisms are now relatively well understood [1-7]. Blade-vortex interaction noise is currently the least understood problem in helicopter impulsive noise research [8].

Many people have studied the blade-vortex interaction noise problem and experiments and theoretical developments have been carried out in this area [9-19]. Schmitz, Boxwell, Lewey, and Dahan [20] have done full scale and model rotor tests and have documented helicopter main rotor acoustic behavior under several flight conditions producing blade slap. They have also shown that under conditions where the tip mach number, disk loading, tip path plane, and advance ratio are properly scaled, model helicopter test data agrees well with full scale results. Cox [21] has done full scale flight testing with a rotor blade instrumented with 110 pressure transducers and Nakamura

[22] used this data to predict the far field rotor acoustic signature but did not have good agreement with the measured data and suggested that more blade pressure data points were necessary to predict the acoustic pulse. Hubbard [23] used instrumented model helicopter blades during blade-vortex interaction noise testing and found that stall produced by blade-vortex interaction at very high angles of attack could produce blade slap in the far-field. Widnall and Wolf [24,25] (1978) developed a theoretical model to predict the far field acoustics due to low speed blade-vortex interaction given global flight parameters and the interaction geometry.

Fontana [26,27,28] used miniature tuft and smoke flow visualization to determine that stall did not occur due to blade-vortex interaction at the low angles of attack tested and used smoke flow visualization to determine the interaction geometry for a model helicopter rotor operating at low tip speeds. Measurements showed that the blade-vortex interaction responsible for the impulsive noise under the conditions tested occurs when the blade interacts with a vortex one and one quarter revolutions old on the advancing side of the rotor disk after the vortex has had two previous interactions which did not produce blade slap. The blade azimuth angle during the interaction was 40-50 degrees (depending on the advance ratio). The angle between the blade and the vortex as well as the blade vortex separation distance were determined from smoke flow visualization measurements. This information was used to test the theory of Widnall and Wolf, and the predicted acoustics were compared with the measured acoustics. The theory was generally found to agree well with the data when the blade-vortex separation was large and poorly when the blade vortex separation was small. This work also highlighted some of the limitations of the theory and indicated that the variation in the blade vortex separation was probably a significant source of error when the blade-vortex separation was small. The vortex velocity distribution predicted by the theory was also suspected as a source of error since many effects are not accounted for by the vortex model. Chan [29,30] used blades instrumented with pressure transducers to determine the accuracy of the blade loading information and surface mounted hot-film gauges to verify that the flow remained attached during the interaction. He combined the new information on the blade loading from pressure measurements with the geometric data of Fontana, then used the Widnall-Wolf model to obtain similar results to those found by Fontana.

Martinez [31,32] has formulated a theory for blade slap at high tip speeds including the effect of compressibility, and Amiet [33] has formulated a theory that accounts for skew of the vortex relative to the plane of the blade and a theory that can be used for tail rotor noise as well [34]. At high speeds additional compressibility effects appear to become important; for example, Tangler [3] has shown that the interaction of the blade with the vortex at high speeds can cause shocks that radiate to the far field. These complexities can be avoided and the important features of the behavior of blade slap noise due to fluctuating pressure produced as the blade interacts with the vortex can be isolated if the tests are done at low tip speeds (less than mach 0.3).

Hardin and Lamkin [35] did a Navier-Stokes solution for a two dimensional blade-vortex interaction at very low Reynolds number (Reynolds number = 200). This technique does not account for the angle of the vortex relative to the blade and requires a large amount of computational effort; however, it does yield interesting results on the basic flow behavior during blade-vortex interaction. Extension of the technique to higher Reynolds numbers could provide useful information on the behavior of the blade-vortex interaction and the effects of the vortex rotation and viscosity. It is not likely that a three-dimensional Navier-Stokes solution of this type will be useful as a design tool for analyzing the effect of design changes on the rotor's far-field acoustics since the computational burden is high; however, the results of such detailed investigations could be very useful for developing a simplified model or as generalized input to a simpler model. For design purposes a relatively simple model which gives quick results and indicates trends in the behavior of the far-field rotor acoustics for different parameters is desireable.

Fontana's investigation indicated that the predicted vortex structure was a probable source of error in the Widnall-Wolf model for the close blade-vortex interaction case. Although the vortex structure of a hovering rotor has been measured [36,37], there is very little known about the tip vortex structure of helicopters in forward or descending flight because the vortices pass close to the blades making measurement with physical devices difficult [38]. Biggers and Orloff [39] used a laser velocimeter to measure the tip vortex velocity profile of a model helicopter rotor in forward flight by strobing the data acquisition with the rotor position and found that the vortex appeared to be relatively unaffected by blade-vortex interactions at large blade-vortex interaction angles with separation distances on the order of 0.4 blade chords. They also measured large distortion or dissipation of the vortex for a very close encounter, but this was near the tip of the interacting blade so the effect of the newly generated tip vortex dominated the flow field and obscured the older vortex. A serious problem with their measurement technique is that it does not account for variations in the vortex position from measurement to measurement. Steep velocity gradients near the vortex core mean that variations in the position of the vortex result in an averaged velocity that bears little relationship to the actual vortex velocity distribution.

One purpose of this research is to measure the vortex velocity distribution just before the interaction that produces the blade slap far-field acoustic pulse. In order to do this, the measuring device must be able to measure the vortex velocity distribution for each vortex and, if averaging is required, the variation in the position of the vortex must be accounted for so that the velocity profile is not smeared. Since the blade passes through the vortex, the measuring device must be moved out of the way when blades pass through the measurement area. These criteria were met by rotating a rake of hot-wire probes through the vortex just before the passage of the blade through the vortex. This allows the simultaneous measurement of the velocity and position for each vortex so that changes in the vortex position from measurement to measurement can be accounted for. Rotating hot-wire probes have recently been used to study the flow fields around stationary objects [40,41,42,43], but this technique has not previously been used in conjunction with rotating blades.

Simultaneous pressure measurements were taken to obtain the interaction angle and an estimation of the measured fluctuating lift. Combining this information with the measurements of blade-vortex spacing determined in reference [26 or 27] allows a detailed investigation of the low speed blade-vortex interaction phenomenon and its correlation with the Widnall-Wolf theory.

The Widnall-Wolf model for the blade-vortex interaction noise is used for correlation with this experiment because it is a general theory which combines several distinct models. Because the vortex velocity distribution, fluctuating lift, and radiated acoustics are calculated in distinctly separate steps, any one part which is inaccurate can be modified without major redevelopment of the theory. As formulated it uses an incompressible model for the fluctuating lift which is necessary for comparison with data from this thesis since the flow is well below the velocities at which compressibility effects become important. Since the model relies primarily on global input parameters and the calculations are not demanding computationally, potential exist for the use of the model as a design tool rather than just a research tool. The ability to improve the parts of the theory separately without affecting other parts is very useful for development and modification for different conditions.

Chapter 2 is a brief description of the blade-vortex interaction phenomena. Chapter 3 describes the theoretical model of Widnall and Wolf. Discussion of the model is useful at this point because it clarifies the terminology and geometry of the blade-vortex interaction (BVI) phenomena. Chapter 4 is a description of the rotating hot-wire measurement technique and an analysis of the performance requirements of the system. Chapter 5 is a description of the experimental apparatus. Data acquisition and reduction are described in Chapter 6. The results and discussion of the experiment are presented in Chapter 7. Comparison of theory and experiment are made in Chapter 8. Conclusions and recommendations follow in Chapters 9 and 10.

CHAPTER 2

DESCRIPTION OF THE BLADE VORTEX INTERACTION PHENOMENA

A brief review of the blade-vortex interaction as produced in this experiment is presented in this section. A rigid wake plot, shown in Figure 1, is very useful for visualizing the flow patterns of the rotor wake. Tip vortices are represented by the spiral pattern trailed from the blade tips and swept down stream by the wind tunnel flow. The ratio of the tunnel speed to the tip speed determines the basic shape of this spiral pattern and is called the advance ratio. This pattern becomes distorted by self-induced vortex motion so the exact angle and curvature of the vortex are not accurately modeled, but this plot is adequate for visualization purposes since it shows the general position of the vortices relative to the blades and each other. In Figure 1 the blades are rotating counter clockwise and the flow is from the right to the left; the lower blade is rotating into the wind and is therefore called the advancing blade. This blade is in the position at which the blade-vortex interaction responsible for blade slap occurs.

For the conditions tested the rotor is in descent so it is effectively flying down through its own wake and the vortices are passing close to the blades. It is apparent from the Figure that the advancing blade is interacting with a vortex that lies essentially parallel to the span of the blade. Smoke flow visualization of this interaction is shown in Figure 2. The nearly parallel blade-vortex orientation means that pressure fluctuations produced by angle of attack changes induced by the vortex propagate rapidly along the blade. Measured acoustic pressure for this case is shown in Figure 3. The large pulses are produced by the blade-vortex interaction and dominate the acoustic signature of the rotor. If the angle between the blade and the vortex is large, the pressure disturbance from the early part of the interaction is radiated through the fluid at the speed of sound while the pressure fluctuations generated by the blade-vortex interaction as it moves down the blade follow later. These pressure fluctuations are therefore somewhat self cancelling in the far-field. When the angle is small, the pressure disturbance generated by the vortex can propagate at Mach one or greater through the fluid, and the pressure waves are added efficiently. This effect can be visualized by noting that for small angles the pressure fluctuations are being radiated at the speed of sound but are also being generated by the interaction as it moves along the span of the blade as rapidly as the previously radiated acoustic waves are traveling. A diagram of this effect is shown in Figure 4. This results in efficient addition of the wave fronts and strong radiation to the acoustic far-field in the directions which the generated wavefronts are steepest. The term "trace Mach number" is often used to refer to the speed of the interaction. This small angle interaction results in a high trace Mach number and is responsible for blade slap in these experiments.

Closer inspection of Figure 1 indicates that the blade will interact with another vortex as it continues to rotate. Figure 5 shows this interaction more clearly. For the conditions tested this interaction does not produce a large acoustic pulse because the trace Mach number is too low for efficient radiation to the far-field; however, evidence that this interaction can produce a small far-field acoustic pulse is shown in Figure 6 where the circled small pulse is due to this interaction at a large angle. Although this interaction does not result in large amplitude acoustic spikes at tested tip speeds, it is expected that the interaction will have some effect on the behavior of the vortex since the lift fluctuations generated on the blade will introduce new vorticity to the flow and may significantly change the structure of the vortex. As the blade rotates further there is another interaction at a very large angle as shown in Figure 7. Figure 8 shows smoke flow visualization for these vortices. Further flow visualization data is available in reference [26].

Under the tested conditions blade-vortex interaction produces a dominant acoustic pulse for the geometry shown in Figure 1. Previous interactions at large angles do not result in large amplitude peaks compared with the dominant pulse because of the low trace Mach number but are likely to change the vortex structure. Examination of Figures 5,7, and 8 shows that two large angle interactions (large compared to the angle for a critical trace Mach number) occur before the interaction responsible for blade slap occurs. It has been suggested that such interactions result in rapid dissipation of the vortex [11,18,35,39,44]; however, in these tests it is apparent that the vortices are not completely dissipated after these interactions because blade-vortex interaction noise is generated. The vortex position and structure reflect the effect of these interactions as well as the effects of viscosity. For these reasons the measurement of the vortex must be made just before the blade-vortex interaction to determine the structure of the vortex responsible for the blade slap acoustic pulse.

CHAPTER 3

DESCRIPTION OF THE THEORY

Data from the model rotor experiment is used to evaluate the theoretical model of Widnall and Wolf for several reasons. A very important feature of the model is that it does not require detailed knowledge of the blade surface pressure. Calculating the detailed blade surface pressures is in itself a difficult problem under the conditions which generate blade slap due to blade-vortex interaction. Measuring the detailed blade surface pressures on a full scale blade is very expensive and does not allow rapid design development. Model tests reduce the cost associated with such measurements, but the small size of the model blades makes detailed measurements over the blade difficult, so the independence of the model from detailed pressure measurements results in a significant potential savings in the evaluation of blade-vortex interaction noise. Another useful feature of the Widnall-Wolf model is that the model requires primarily global input parameters. For these reasons the model can be used as a design tool since the effect of basic changes in the design, such as blade load distribution or tip speed, on the acoustic blade slap signature can be quickly ascertained. The model is developed as a combination of separate parts that are relatively independent. This allows modification and improvement of areas for which the models are inaccurate without modification of the other parts. As originally developed, the model uses an incompressible flow theory which is necessary since the experiments are for a low speed flow. Several aeroacoustic models exist for the case of blade vortex interaction in compressible flow [17,31,33] and Harden [35] has developed a two dimensional fully viscous calculation for the low Reynolds number of 200; however, it is computationally demanding. The Widnall-Wolf model treats each step primarily analytically and is not computationally demanding. The primary numerical calculation is the evaluation of (Fast) Fourier Transforms.

Widnall and Wolf have modeled the blade-vortex interaction and associated acoustics. A basic description of the theoretical model follows; further details are available in references [24,25,26,28]. First the tip vortex velocity distribution is determined, given a circulation distribution for the blade tip, using the Betz model [45,46]. This model assumes that the vortex rolls up into a symmetric circular vortex distribution but does not account for viscosity, vortex aging, axial flow (visible in Figures 2 and 6), or the effects of the two large angle blade-vortex interactions that precede the interaction responsible for blade slap discussed in Chapter 2.

Figure 9 illustrates the geometry of the interaction. Note that the vortex is assumed to be straight and lie in a plane parallel to the plane of the blade path with a constant spacing, h, and a constant angle, λ, to the span of the blade. The model does not account for rotation of the blade or blade sweep, and the blade is assumed to be in uniform motion at a velocity U. All values are nondimensionalized by the blade semichord and velocity in the analysis.

Given this geometry, the upwash of the vortex in the plane of the path of the blade is determined. This upwash is then transformed into its Fourier components. The fluctuating lift is determined using the Filotas theory [47] for linearized incompressible inviscid flow on a thin airfoil. This fluctuating lift is modeled acoustically as a line of acoustic dipoles (a compact source) as shown in Figure 10. Again there is no rotation or sweep in the model as originally formulated. It is apparent from Figure 10 that some blade-vortex interaction length ($2^* s_0$) must be used as the active length of the acoustic dipole line, but Figure 2 shows that the entire span of the blade interacts with the vortex. Modeling the entire blade as the interaction length is not sensible since the actual blade is rotating and the inboard sections are not moving fast enough to generate lift or sound as effectively as the tip. Corrections for this effect have been implemented and their development is given in Appendix A.

Finally, the far-field acoustics are calculated using the method of stationary phase and the problem is transformed back into the time domain. Implementation of the theory in the form of a Fortran computer code is very similar to that of reference [25] with the exception of a few corrections which are noted in Appendix B. The theory is basically a linear model and the predicted acoustic pressure is linearly dependant on the amplitude of the upwash induced by the vortex.

CHAPTER 4

THE ROTATING HOT WIRE MEASUREMENT TECHNIQUE

4.1 Vortex Velocity Measurement Using a Rotating Hot-Wire Rake

Measurement of the vortex velocity distribution is difficult because passage of the blade near or through the vortex core prevents the use of a stationary probe. Vortex meander from blade passage to blade passage causes error when the measurements are averaged without knowledge of the vortex core position because the large velocity gradients near the core cause large differences in the measured velocity at a point for only small changes in the core position relative to that point. Ideally the measurement of the vortex velocity profile will determine the velocity distribution and position of each vortex without interfering with the rotor wake or vortex position and behavior.

A rotating hot-wire rake, as shown in Figure 11, has several useful characteristics. The rake can be synchronized with the blades to prevent contact, and the additional bias velocity of the hot-wire simplifies the measurement. Vortex measurement using a rake is limited by flow reversal as shown in Figure 12. Once the measured relative velocity becomes small, the direction of the flow becomes ambiguous and probe interference and vortex self-induced motion become significant. Moving the probe through the vortex at a velocity greater than the maximum vortex velocity eliminates this problem; however, increasing the probe velocity decreases the time allowed for the velocity measurement over the area occupied by the vortex and thus increases the frequency response requirements of the measurement system.

A high probe velocity greatly reduces the difficulty of data reduction for the hot-wire rake. Velocity components <u>parallel to the wire</u> have a negligible effect on the hot-wire response, so only velocities <u>perpendicular to the wire</u> will be considered further. Figure 13a shows the effect of a flow velocity vector in a plane perpendicular to a stationary wire. The effective cooling velocity is $(u^2 + v^2)^{1/2}$ and the direction of the flow cannot be determined from the single wire measurement; however, if the probe is moved through the velocity field at a velocity U as shown in Figure 13b, then the effective cooling velocity is $q = ((U+u)^2 + v^2)^{1/2}$. This leads to the result

$$q^2 = U^2 + 2Uu + u^2 + v^2 \qquad (4.1)$$

thus if $U \gg v$ then the effect of the second order term for v is small. Dropping the v^2 term leads to the result

$$q = U + u \qquad (4.2)$$

Thus if U is very large compared with v then the velocity measurement is dominated by the velocity component in the direction of the probe velocity U. A way to visualize the effect is to note that the error from ignoring the v component is equal to the difference between the magnitudes of the vectors of q and U+u in Figure 13b.

Estimates of the error for the rotor experiment can be made by assuming a vortex velocity distribution given the other parameters of the experiment, but at this point some restrictions imposed by the experiment become important. First the probe must be rotated at an even multiple of the rotor RPM to maintain synchronization, and second, the radius of the probe is limited by the wind tunnel floor and components to less than 1.5 ft. Probe rotational velocity is limited by the fact that at some probe rotation rate the probe's own wake will not be adequately cleared by the tunnel air flow before another passage of the probe occurs. Considering the operating conditions of a helicopter rotor during blade slap (rotor advance ratios in the range of 0.15 to 0.21) leads to the conclusion that a probe mounted on a single rotating arm of 1.25 ft radius with a counterweight, spinning at twice the rotational speed of the model helicopter rotor is a good choice given the constraints of the wind tunnel. Since the model helicopter rotor radius used in the experiments presented here is 2.18 ft, this results in a probe tip speed slightly greater than the rotor tip speed. For a two bladed rotor the probe passage frequency is then equal to the blade passage frequency, and selection of these values leads to a separation distance between the probe and the wake due to the previous probe passage typically on the order of 0.5 to 0.75 ft.

An irrotational vortex velocity distribution

$$v(r)= \Gamma/(2\cdot\pi\cdot r) \qquad (4.3)$$

is useful for estimating hot-wire performance since the velocity gradient may be made arbitrarily steep as the center of the vortex is approached. The actual vortex is known to have a finite core radius which is likely to be greater than 1/8 inch according to flow visualization experiments (see Figure 8). Using this model and the given rake geometry, the errors due to ignoring the velocity component perpendicular to the probe velocity may be estimated. Figure 14 shows a possible hot-wire rake/vortex orientation and the resulting hot wire anemometer output. The maximum velocity variation of the wire which passes through the center of the vortex is representative of the error due to neglect of the v component. Note that there is no v component when the probe is cutting the center of the vortex, and at that point the error due to v is zero.

The vortex velocity distribution can be determined by sampling the value of the velocities measured when the probe cuts the vortex center. Subtracting the known probe and tunnel velocities from the measured velocity for each hot-wire gives the velocity due to the vortex and wake at each hot-wire position. Plotting the resulting measurements at their corresponding position on the probe as shown in Figure 15 gives a direct measurement of the vortex velocity profile. This provides a "snap shot" of a single vortex. Comparing many of these "snapshots" allows the meander of the vortex to be determined. Vortex to vortex deviations may be determined by comparing a single "snapshot" with one obtained by averaging many measurements after shifting the data so that the vortex centers are aligned for each average.

The required frequency response of the system can be determined for any assumed core radius using the irrotational vortex model. The velocity component u varies as the probe passes through the vortex as described by the following equation

$$u(t) = + \frac{\Gamma}{2\cdot\pi} \frac{d}{(R\cdot\Omega\cdot t)^2 + d^2} \qquad (4.4)$$

where Γ is the vortex circulation, d is the separation distance between the plane of the path of the hot-wire and the center of the vortex, R is the radius of the hot-wire rotation, and Ω is the angular frequency of the probe (rad/sec). The Fourier transform of equation (4.4) is

$$H(f) = \frac{\Gamma}{2\cdot\pi\cdot d}\cdot\frac{1}{2}\cdot\frac{2\cdot\pi\cdot d}{R\cdot\Omega} \cdot \exp\left[-\frac{2\cdot\pi\cdot d}{R\cdot\Omega}|f|\right] \qquad (4.5)$$

where f is the frequency in terms of the inverse of the period (cycles/sec). The time signal and the corresponding spectrum are shown in Figure 16.

Previous experiments using smoke flow visualization [26] indicate that the typical values of the critical vortex parameters under the conditions that will be tested are: $\Gamma=10$ ft²/sec, $R= 1.25$ ft, $\Omega= 167$ radians/sec. This leads to the result that for a 0.25 inch core radius 99% of the energy content is at frequencies below 3.7 kHz and for a 0.125 inch core radius 99% of the energy content is at frequencies below 7.4 kHz. In terms of the amplitude relative to H(0) instead of the energy content, the amplitude of the theoretical signal produced by the vortex velocity measurement is 1% of H(0) at 7.5 kHz for a 0.25 inch core radius, and 1% of H(0) at 14 kHz for 0.125 inch core radius. This frequency response, required to accurately measure the vortex velocity distribution, is within the range available using hot wire anemometry circuitry and hot-wire probes.

The dynamic range of the measurement also depends on the core radius. Under the same operating conditions as the previous calculation the measured velocity is

$$q = V_{net} + \Gamma/(2\cdot\pi\cdot d) \, . \qquad (4.6)$$

Given the operating conditions to be tested and assuming a 0.25 inch core radius for the vortex, the maximum velocity fluctuation experienced by the hot-wire due to the vortex is 32% (240ft/sec probe velocity with a fluctuation of 76 ft/sec because of the vortex velocity). Assuming a 0.125 inch core radius, which is a minimum expected core size estimated from the smoke flow visualization, the maximum measured velocity fluctuation due to the vortex is 63%. At one inch from the vortex core the measured velocity fluctuation due to the vortex is 8% and at 2 inches it is 4%. Hot-wire anemometers can measure such a range but are non-linear and must be calibrated over the range for which measurements are made. For this experiment the probe is calibrated in-situ by rotating it in the freestream. This also allows frequent corrections to be made for drift and wire aging.

There are many other factors which affect the flow measurements. The effect of turbulence and its intensity in the vortex is not known. Angular variation in the probe velocity will directly affect the measurements; however, radial variation due to vibration will have little effect since it is not in the primary flow direction. A more practical problem is that of wire breakage due to vibration and dust in the flow; however, the use of in-situ calibration simplifies recalibration of wires replaced after wire breakage.

4.2 Mechanical Requirements of the Experiment

The probe must pass close to the blade to determine the velocity distribution just before the blade-vortex interaction. This requires accurate synchronization of the probe with the rotor. The position of the vortex varies for different test conditions so the position and angle of the probe must be adjustable. The rotor blades are hinged for flapping and flap wildly during start-up and shut-down. Some arrangement must be made for extra clearance between the blade and the probe during these periods. The power required to drive the probe to adequate speeds for self calibration is estimated to be 0.8 hp at 3000 rpm with an average torque of 1.4 ft·lbs and an estimated fluctuation of 7 ft·lbs. For actual test conditions the power required is much less because the power required varies as the cube of the velocity; for example, the power required for the highest anticipated rotor test speed of 1000 rpm (2000 rpm probe speed) is estimated to be 0.24 hp.

4.3 Chapter Summary

Initial calculations show measurement of the vortex velocity is possible using the rotating hot-wire rake. Data will be produced in a unique "snapshot" format which provides a more detailed insight into the vortex behavior than is presently available. The unique capabilities of the rotating hot-wire with self calibration allows errors to be reduced because wire aging and drift can be corrected as the experiment proceeds. Wire breakage due to high speed, high g forces, and dust in the wind tunnel is a potential problem. Another potential problem is the interference of the probe and related structure on the flow field. An estimate of this effect can be determined by observing changes in the acoustic signal. Because of this possibility, a design goal is minimum flow disturbance by the measurement device.

CHAPTER 5

EXPERIMENT AND INSTRUMENTATION

5.1 Experimental Apparatus

All test were done in the M.I.T. 5 X 7.5 ft open jet anechoic wind tunnel. The tunnel was acoustically treated with cremer blocks and acoustic foam which provided free field conditions down to 160 Hz [48]. Details of the tunnel and rotor test rig are given in references [49,50]. Changes made since the work of references [26-30] include repair of the return section fairing and replacement of some of the fiber glass treatment with foam wedges. Damaged areas of fiberglass acoustic treatment were replaced with six inch deep "Super Sonex" acoustic foam wedges. These repairs have resulted in little change in the acoustic properties of the tunnel.

Blade surface pressures were measured using the apparatus and parameters described in reference [30]. A layout of the instrumented blade is shown in Figure 17a and b. The pressure gauges themselves have a frequency response of over 50 kHz and the Helmholtz resonance frequency of the cavities above the pressure transducers, shown in Figure 17 b, is on the order of 50 kHz. The Vishay strain gauge amplifiers used begin to roll off in frequency response above 5 kHz, so the amplitude and phase of measurements at frequencies above 5 kHz are not precisely correlated to the actual pressure disturbance at that frequency. Details of the rotor are given in Table I.

5.2 Description of Hot-Wire Rake

The primary purpose of the experiment is to measure the vortex velocity distribution just before the interaction responsible for blade slap. The idea is to rotate a hot-wire probe synchronously with the rotating blades so that the vortex velocity distribution can be measured just before the interaction with a blade. A rake of hot-wire probes was constructed for this purpose. The rake is shown in Figure 18. The wires are spaced at 0.25 inches and mounted perpendicular to the plane of rotation with a wire length of .062 to .094 inches and diameter of 0.00012 to 0.0002 inches. The characteristics of the wire used are discussed in more detail in the section on instrumentation (section 5.4). Although there are 9 pairs of support prongs, only the 8 nearest to the tip were used in this experiment; the extra prongs were to serve as a backup in case of a prong failure. Centrifugal loading near the tip of the probe reaches 1,700 g's during calibration at 2,000 RPM and 3,800 g's at 3,000 RPM, so the design of the apparatus was critical to prevent the vibration and deflections from disturbing or destroying the hot-wires. The wire support prongs are made from jewelers broaches with all but the last 0.25 inches of the tapered tips cut off. The diameter of the base is 0.0315 inches tapering to 0.0145 inches in diameter in the last 0.25 inches. This stiff support by the broach is critical to reduce deflections under the high g loads. The base of the broach is attached to a piece of fiberglass composite 0.0685 inches thick, tapered from 0.25 inches wide at the base to 0.125 inches wide at the tip. The tips of these broaches extend 0.5 inches in front of the leading edge of the fiberglass supporting structure to reduce the effect of the probe itself on the measurement. Kevlar strands were used to reinforce the areas of highest stress. Cyanoacrylate and epoxy adhesives were used to attach the prongs and the kevlar reinforcing.

This glass fiber reinforced plastic, with broaches mounted, is glued into a piece of 1/4 inch outside diameter, 0.035 nominal wall thickness, type 304 annealed stainless steel tubing 17 inches long. The joint is reinforced with kevlar. Teflon insulated 36 gauge, 7/44 strand, wires are run inside the tube and out to the broaches where they are soldered and glued for support. The wire inside of the tube is braided to reduce the crosstalk between hot-wires. Miniature connectors from Micro Dot Inc. are used to connect the wires where they exit the tube inside the hub to the wires leading to the slip ring to allow easy removal for hot-wire repair. The other end of the probe tube is threaded and the probe is counter balanced by nuts and washers attached to that end. The probe is 19.625 inches long and the distance from the center of rotation to the tip prongs is 15.0 inches. Hot-wires are soldered across the .064 to .068 inch gap between the broach tips as final preparation before the experiment.

5.3 Description of Probe Drive Mechanism

Probe drive mechanism design requirements were:

1) Minimum flow disturbance to reduce interference with the rotor wake.
2) Low vibration operation to insure accurate measurements and prevent hot-wire fatigue.
3) Remote position control to keep the blade from hitting the probe and to position the probe such that the vortex is near the center of the rake.
4) Adequate power rating to prevent breakdowns and keep the

slip ring environment cool.

5) Synchronous operation at twice the rotor rpm to match the tip speeds and prevent blade probe contact.

6) Low noise generation to reduce interference with the measured rotor acoustics.

The design is shown in Figure 19 and can be described as follows:

Power is taken directly from the vertical shaft of the hydraulic motor, which also drives the model helicopter rotor, using a gear belt pulley arrangement with a two to one speed step up. The vertical axle of the driven pulley drives another gear belt arrangement which drives the vertical shaft of a ninety degree, one to one spiral bevel gear box. This gear belt passes over two idler pulleys. The idler on the non-tension side of the drive belt is mounted on a swinging arm that is tensioned by an elastic chord to take up the slack in the belt. The belt driven gear box is mounted on a plate with the cross shaft in the horizontal plane and the input shaft vertical. The plate on which the gear box is attached is mounted on a pair of ball bearing dovetail slides so that the mechanism can be moved fore and aft in the direction of the flow (relative to the rotor). The gearbox cross shaft drives a 5 mm pitch, 15 mm wide, high torque drive type gear belt with an 18 tooth steel drive pulley. The gear belt is enclosed by the 1-5/8 inch outside diameter, .095 inch wall steel probe support tube. At the top of this tube the 18 tooth driven pulley is mounted on a hollow shaft which drives the probe and contains the slip ring assembly. The probe is mounted to the hub/axle assembly by a clamp plate. Details of the hub assembly are shown in Figure 20.

The probe/support/gearbox assembly is mounted on slides and the position of the slide is controlled by a motor driven screw. The position of the sliding probe drive structure is limited to a range over which the probe will not contact the blades by limit switches so that when the probe support is moved during operation there will be no contact with the blades. The positioning motor is controlled from outside the wind tunnel. Slide position was determined using a visual scale and pointer arrangement which was observed through a video monitor. Motion of the probe assembly on the slides causes the distance between the gear belt driven pulleys to change, and this change is accounted for by the swing arm mounted, elastically tensioned, idler pulley. The length of the section of belt between the driving and driven pulley changes as the assembly slides, so the probe angular position relative to the rotor angular position varies as the screw drive slides the assembly upstream or downstream in the wind tunnel relative to the rotor test stand. The magnitude of this phase angle adjusting effect is varied by adjusting the position of the stationary idler pulley.

Gear belt backlash and stretch were insignificant. Backlash was primarily due to the spiral bevel gears in the gear box and was on the order of 5 degrees or less. It was not important during operation since the drag of the probe always kept the gears meshed in one direction. Back lash was properly accounted for during the initial set up procedures and the probe position is measured at the probe hub, so the effect of backlash was negligible. The tunnel floor and walls are isolated from the structural walls in the building for acoustic isolation purposes, so all probe support structures were attached to the rotor motor support stand which is cantilevered to a concrete wall just outside of the wind tunnel.

The net result is a mechanism which drives the probe synchronously with the rotor at twice the rotor rpm. The angular position can be adjusted manually before operation and motion along the dovetail slide allows the position of the probe relative to the blade to be varied during operation to prevent contact with the blades due to flapping during startup and shutdown, while allowing the probe to be positioned very close to the blade under test conditions. This minimum probe/blade separation position is set by a limit switch located to prevent probe-blade contact.

The design goals were met by the apparatus. Testing was done up to 4000 RPM (2000 RPM model rotor speed) to insure safety during possible overspeed conditions. Measured acoustic pulse shapes and amplitudes were not affected by the probe, and the noise generated by probe rotation was well below the noise generated by the rotor at the location of the microphone.

5.4 Instrumentation

Hot-wire data was taken through slip rings. Two slip ring circuits were used per hot-wire circuit lead to reduce the effects of the rotational variation in the slip ring resistance. The miniature slip rings contain 32 circuit connections which allows the use of 8 hot-wires with four slip ring circuits required per hot-wire. No special slip ring noise reduction circuitry was required. The most important parameters for slip ring performance were to use the proper lubricant and a high resistance hot-wire. The higher the hot wire resistance the less the resistance fluctuation of the slip rings affect the resistance measured by the hot-wire anemometer circuit.

Slip rings were Poly-Scientific P/N 1444 (32 circuits) or the equivalent version manufactured by KDI Electro Tech. Contacts were gold on gold. Slip ring noise level increased as the test proceeded due to wear and contamination of the contacting surfaces. Slip rings were cleaned with freon and lubricated with the equivalent of ESSO Univisk P38 which was labeled MES 210 lot no. 81-2-0401 part no. 3272894-1 manufactured February 1981. Liberal slip ring lubrication is required to minimize the slip ring noise.

Probe position was determined by an optical pickup mounted at the top of the probe support tube. This optical pickup and associated circuit changed output state when the probe was above the horizontal plane of the hub. This signal was used to switch the clock rate of the digital data acquisition system as well as to locate the angular position of the probe. The optical sensing arrangement and associated circuitry has a significant delay from the time the probe is horizontal to the time that the circuit output responds. This delay was accounted for in the data processing procedures. A one per rotor revolution signal was generated by an optical sensor mounted on the rotor test stand and driven by a small gear belt at the rotor rotational speed. These two signals allow the relative position of the probe and rotor to be determined as the phase angle of the probe is adjusted by moving the probe along the screw driven dovetail slide. The strobe control circuit described in reference [26] was used to observe and verify the status of the system during operation.

The hot-wires were operated at constant temperature and several hot-wire materials were tried. The best were platinum plated tungsten 0.00012 inches in diameter and 10% rhodium-platinum 0.0002 inches in diameter. Both were manufactured by Sigmund Cohn Corp.

The tungsten wire provided higher frequency response than the 10% rhodium-platinum wire and appeared to have the same strength while requiring less operating current, thus reducing the effect of slip ring noise; however, this wire is not easily obtainable and the 10% rhodium-platinum was used when the supply of tungsten wire was depleted. Frequency response of the tungsten wire was initially adjusted to 17 kHz when the probe was not rotating and increased to over 20 kHz under operating conditions due to the increased velocity. (Increasing the velocity thins the boundary layer of the hot-wire and increases the heat transfer coefficient, which decreases the time constant of the hot-wire). The 10% rhodium-platinum wire had a 12.5 kHz non-rotating frequency response which also increased to 20 kHz or more when rotating in the flow. The hot-wire anemometry circuitry had to be modified to accommodate the different over heat ratios and current requirements of the two wire types. A schematic of the basic hot-wire circuits is given in Figure 21 and details of the circuit are given in reference [51]. Typical cold wire resistance was 16 to 20 ohms including the leads. The ratio of hot to cold resistance was typically set between 1.2 and 1.8 for all measurements. Damping was adjusted to near critical with the probe rotating in the tunnel flow at the speed corresponding to the operating conditions which were to be tested. This results in maximum frequency response and minimum phase shift in the measured voltage output corresponding to fluctuating velocities. For more information on hot-wires see reference [52]. Hot-wire breakage due to the high concentration of dust, primarily fiberglass from the acoustic treatment, was the major problem with this experiment.

The hot-wire circuits were initially located outside of the wind tunnel; however, degradation in performance due to the long cable lengths required (approximately 50 ft) was eventually solved by locating the hot-wire circuits inside the tunnel with a total lead length of approximately 15 ft.

5.5 Data Acquisition

The tunnel flow velocity was measured with a pitot-static tube as in reference [26]. Outputs from the various instrumentation was monitored on a Nicolet Explorer digital oscilloscope, a B&K four channel oscilloscope and a Nicolet 660 B spectrum analyzer. Acoustic data was taken with B&K 1/2 inch condenser microphones and amplifiers as in reference [26]; however, the acoustic signal was not B-weighted to avoid changes in the pulse shape.

A significant improvement in data acquisition was the implementation of a CAMAC "crate" type analog-to-digital conversion data acquisition system. The A-to-D converters were two Transiac model 2812 8 channel 12-bit signal converters linked to two Transiac model 5000 memory modules. The crate controller was a Kinetic Systems model 3989RZ1A, S/N 113, RS232 serial interface device. This system was interfaced with an IBM PC/XT computer. The CAMAC "crate" itself was an Optima-850 CAMAC Powered Crate. This system allowed up to 100 kHz per channel simultaneous sampling for 16 channels.

Data is stored in blocks consisting of up to 16 channels with 1024 points per channel in each block. Up to 32 blocks of 16 channels of data can be stored at the full data rate. This allows 32 blocks of continuous data for each channel. This data must then be transferred to the computer for permanent storage. The sampling rate is switchable by an external signal and the state of this switch is transmitted as part of each data set. The sampling rate switch was controlled by the hot-wire probe optical hub position sensor so that the data rate could be increased during the passage of the probe through the rotor wake and decreased at other times to conserve memory space. Interface software was written to allow the important parameters such as clock rates, number of data channels, and number of data blocks to be transferred to the computer to be selected by the user, and to control the data transfer, data type conversion, and data storage. A major problem with this arrangement was the basic constraint of the serial interface. Although the serial controller had a maximum baud rate of 19200 baud, the IBM PC had a maximum baud rate of 9600 baud. The system was operated at the highest available data rate of 9600 baud in hexadecimal format with no parity or check sum; data transmission of a full 16 channel 32 block (1024 data points per block) data set from the "crate's" Transiac model 5000 memory modules, through the Kinetic Systems crate controller, and to the IBM PC computer took approximately 2 hours during which time the system could not be used to take data. Over half of this time was required for the actual data transmission over the serial port interface and the rest was dominated by the time required to write the data to the 10 megabyte hard disk. Very little time was required to convert the data from the transmitted hex code to the internal IBM format for integer*2 used for data storage. A major improvement in the transfer time could be obtained with direct memory access type interfacing which requires a different "crate" controller module (to replace the Kinetic Systems 3989 controller). The data on the hard disk was later stored on 5 1/4 inch 360 kilobyte format floppy disks requiring three disks for a 16 channel 30 block data set leaving two blocks to be stored on an additional floppy disk.

The data acquisition software was written primarily in Microsoft Fortran linked with an assembly language subroutine. The data could be converted to a format compatible with the "Unkel Scope" IBM PC program which allowed the results to be viewed and preliminary analysis to be performed. Final data reduction software is discussed in the section on data reduction. All data reduction was done with the IBM PC/XT or an IBM PC/AT compatible computer.

The data acquisition system was set for bipolar operation and the output of the CAMAC crate was converted into an integer count from 0 to 4095 representing the full 12 bit range of -5 to +5 volts. Hot-wire data was stored on the first 8 A/D channels. Channel 9 was used to record the acoustic signal, and channel 10 was used for the one per rotor revolution signal. Pressure transducer data was stored in data channels 11 through 15. Channel 16 was not used because of a failure of the Transiac circuitry which caused it to drop a high bit which in turn caused jumps in the record of the digitized data. Data transfer is done for 16 bit words so the upper 4 bits are available for additional data. The probe position signal was used to switch the clock rates and is recorded as information in these upper bits transmitted with the 12 bits of data. The data on the state of the clock is separated from the 12 bit digitized data by the computer and the state of the clock switch is also stored along with the data. This clock switch encoding is essentially an extra data channel that implicitly contains the angular position of the probe as well as the A/D sampling rate. The simultaneous data acquisition allows a one to one correspondence of events to be made.

CHAPTER 6

DATA REDUCTION

6.1 Description of the data

A top view of the experiment is diagrammed in Figure 22. In this position the probe cuts through several vortices in the rotor wake. A typical data set taken simultaneously from each of the eight hot-wires is shown in Figures 23a-h with a through h representing hot-wire measurements from hot-wires 1 through 8 where hot-wire 1 is at the tip of the probe and hot-wire 8 is closest to the hub. The wires are spaced 0.25 inches apart. The vertical axis is the digital count representing the A-to-D converter output corresponding to the voltage produced by the constant temperature anemometer circuit. The digital count is converted directly into the velocity using the calibration data only for the values of interest to save computation time. The spikes in the data correspond to the vortices as indicated in Figure 22. The relationship between the hot-wire measurements and the vortex velocity profile is shown in Figure 14 and 15. Each hot-wire senses a relative increase or decrease in velocity due to the vortex resulting in the peaks visible in Figures 23a-h. The hot-wire outputs shown for each wire in Figures 23a-h essentially consist of a sinusoidal shape due to the probes rotation in the free stream combined with some voltage fluctuations near the top of the sinusoid due primarily to the velocity fluctuations produced by tip vortices of the rotor blades, and a voltage fluctuation near the bottom of the sinusoid due to flow around the probe's support post. Other sources of fluctuations in the hot-wire output are due to features of the helicopter rotor wake, such as downwash and turbulence, and to slip ring noise.

6.2 Calibration of the Hot-Wires

Calibration is obtained by rotating the hot-wire probe in the wind tunnel without the model helicopter rotor blades so that the wind tunnel flow is not disturbed and comparing the measured voltage with the calculated velocity of the probe as it rotates in the freestream. Since the probe rotation rate and position are known along with the wind tunnel velocity, the velocity experienced by the hot-wires at each data point can be calculated. These calculated velocities correspond directly with the voltage signal from the hot-wire measured at the position at which the velocities are calculated. A polynomial curve-fit is used to fit these data points and the resulting coefficients are used later to determine the velocity from the measured voltages. Too get an adequate range of velocities the calibration is done for two rotational speeds and each of these runs are done at different wind tunnel speeds so that there is always actual data from a calibration run in the velocity range that will be measured later in the actual experiment. This is important because the hot-wires are nonlinear and calibration cannot be reliably extrapolated outside the range of the actual calibration data. Calibration of the hot-wires is corrected for drift due to the increase in the tunnel temperature during operation by adding the correction to adjust the hot-wire data from one of the runs so that data that represents the same velocity overlaps. The direction of the drift is consistent with the wind tunnel temperature fluctuation. The data from the calibration runs is curve-fitted with a polynomial using a least squares fit. Figure 24 shows a typical set of calibration data and Figure 25 shows the calibration curve used for each of the hot-wires. The two steeper curves are for the 10% rhodium platinum wires and the others curves are for the plated tungsten wires.

6.3 Extraction of the Vortex Velocities from the Data

The peaks and valleys in the voltage output of the hot-wire anemometer data corresponding to vortex induced velocity fluctuations were converted to velocities using the calibration data. Subtracting the known wind tunnel freestream and probe velocities at that probe position results in a vortex velocity distribution as shown by the small circles in Figure 26. The data around each chosen peak velocity value is also shown in Figure 26 to verify the location of the peaks and valleys. This illustrates the relative sharpness of the velocity gradients. The calibration was corrected for drift for each wire based on the known wind tunnel and probe velocity at a probe position approximately 90 degrees from vertical when the probe is furthest upstream in the wind tunnel. At this position the effect of the rotor wake is minimal and the velocity is used to calculate the constant offset applied to the calibration data to correct it for thermal drift. This correction was typically small and consistent from wire to wire. This also indicates that no serious changes in the wire and corresponding calibration have occurred.

Error in the measurement can be estimated by comparing the measured velocity with a known velocity at some location in the flow that is not near the location where the calibration is corrected for drift. Figure 27 shows the difference between the measured velocity data and the known velocity of the probe and free stream when the probe is approximately 180 degrees from the location at which the drift correction is made. Perfect accuracy would have all of the points equal to zero. The maximum velocity error is on the order of 5 ft/second. This location in the wind tunnel is near the trailing edge of the rotor disk so the flow is being thrust away from the probe slightly and is not as steady as it is further upstream where drift correction is made, so the error shown is an upper bound on the actual error expected to occur in the data as long as the calibration characteristics of the wires remain constant.

A program was written to automatically find the local maxima (peaks) and minima (valleys) for a selected hot-wire from the data set as shown in Figure 23 a-h and find the corresponding peaks and valleys in the other hot-wire measurements. The voltage at these values is then converted to velocity corrected for drift as previously described. The velocity of the probe and the tunnel free stream at the calculated angular position of the probe and radius of the hot-wire are then subtracted so only the vortex and rotor wake velocities remain. This is how the data shown in Figure 27 was produced. Once the positions of the probe vortex interactions are known they are used in a program that loops through large data sets searching for the vortices by finding the peaks and valleys, determining their velocities, and sorting them into the proper angular positions so that the vortex velocities for several vortices at the same rotor azimuth and probe position are sorted out of the rest of the data. Variations in the vortex positions are taken into account by using the zero crossing point of the measured vortex velocities as the center of the vortex then shifting the vortex samples so that the centers are aligned. This results in the vortex velocity distribution for many measurements as shown in Figure 28. (In Figure 28 the data points for each sample are connected by lines for clarity).

Superimposing several vortex measurements without shifting the data to correct for the variations in the vortex position produces the image shown in Figure 29a. From this figure it is apparent that the variation in the vortex position can be on the order of one semichord. A typical laser measurement technique essentially (although not exactly) averages this image at each position along the x-axis. A more accurate representation of the measurement that would be obtained from a typical single point sampling measurement system, such as a Laser Doppler Anemometer, is shown in Figure 29b. For this type of data there is no information on which data points are associated with each other; therefore, this does not produce an accurate measurement of the actual velocity distribution of the vortex when the position of the vortex varies significantly from measurement to measurement. The variation in the vortex position becomes more pronounced as the vortex moves downstream and interacts with the blades. The vortex shown in Figures 30 a and b was measured at the position shown in Figure 31. (This data is at a different advance ratio because the probe does not cut the center of the vortex at this point for the advance ratio in Figure 29). This vortex has had no interaction with a blade since its creation but it lies near the vortex trailed by the previous blade (Figure 31). Variation in the vortex position can be seen in Figure 30b. The vortex shown in Figures 28 and 29 was measured at the position shown in Figure 24. This vortex has had two interactions with a blade and variation in vortex position is significant as can be seen in Figure 29. The measurements taken by Biggers and Orloff are shown in Figure 32 for comparison and it is important to note that the apparent reduction in vortex intensity in Figure 32 may correspond to a similar variation in the vortex position rather than a large dissipation of the vortex.

6.4 Determining the Vortex Characteristics

Measured vortex velocities are fitted with a vortex model using a least squared error curve fit to determine the circulation, core radius, offset velocity, and position of the center of the vortex. Four parameters are required for the curve fit. For all of the models used here the most significant vortex parameters relate to the circulation and the core radius of the vortex since these parameters determine the character of the velocity field. These parameters must be obtained from the measured data points which have other effects which must be accounted for in the curve fit in order to get accurate results for the circulation and core radius parameters. One of these effects is that the measured data also includes the velocity difference between the calculated effect of the tunnel flow velocity and the actual flow velocity which is affected by the rotor wake. The rotor wake therefore causes an offset in the data. Assuming that this offset can be modeled as being essentially uniform over the probe measurement area, this effect is modeled as a constant offset velocity. The second effect is that the position of the center of the vortex relative to the probe varies from measurement to measurement, so the plot representing the vortex model must be shifted relative to the data measured by the probe so that the position of the vortex center for the model corresponds with the position of the center of the measured vortex. Accounting for these two effects as well as determining the circulation and core radius of the vortex requires the use of a four parameter optimization procedure to reduce the squared error between the data and the vortex model to a minimum. This was accomplished by an iterative optimization between the measured vortex and the curve fit values at the point of the measurement. The program is written to allow the use of various vortex models and allows each set of vortex velocities to be fit individually or as a shifted average. Three vortex models were used for this curve fit. One of the models is a simple model which is that of an irrotational vortex with a core. One of the models includes the effect of the vortex roll up and resulting distribution of vorticity due to the distributed vortex sheet trailed from the blade as well as accounting for a core. The other model is a commonly used model which includes the effect of a core. These were chosen to illustrate that the way in which the vortex is modeled can have a significant effect on the values determined for the circulation. A brief summary of the models follows.

The first model used is that of an irrotational vortex with a core described by the equation

$$v(r)=\Gamma\cdot r/(2\cdot\pi((r)^2+c_o^2)) - v_o \qquad (6.1)$$

which is often used because of its simplicity [11]. The r in equation (6.1) includes the vortex position factor r=(radius−position offset) and v_o represents the offset velocity used for the curve fits, Γ = the circulation of the vortex, and c_o is the core radius parameter. The offset terms for the position offset and v_o are not important for the discussion of the model since they are only needed when the model is compared with the measurements. Equation (6.1) can be interpreted in several ways. One interpretation is that of an irrotational vortex model with a core. The maximum velocity for this model occurs when

$r=c_o$. Another interpretation is that of the upwash induced perpendicular to a plane by an irrotational vortex at a distance c_o from that plane where r is the distance from the point on the plane closest to the vortex to the point on the plane where the upwash is calculated (not the distance from a point on the plane to the irrotational vortex itself).

The other vortex model is essentially an adaptation of the first model to include the rotational core region predicted by the Betz vortex model. This model will be referred to as the modified Betz model. Equation (6.1) is used but Γ becomes $\Gamma(r)$ which is a decreasing function of the radius inside a rotational region as described by the Betz vortex model; the resulting equation is

$$v(r)=\Gamma(r)\cdot r/(2\cdot\pi(r^2+c_o^2)) \; - v_o \; . \qquad (6.2)$$

Betz's theory predicts a rotational region with an extent and circulation distribution which is a function of the circulation distribution of the vortex generating blade. Inside of this region Γ is a function of the radial position. Outside of this region Γ is constant at the value of the total circulation, and equation (6.2) becomes equivalent to eq.(6.1). Details of the Betz model are available in references [25], [45], and [46].

The third model is a commonly used model with an exponential form (reference [33]),

$$v(r)=(1+1/2\alpha)(c_o/r)G_o[1-\exp(-\alpha(r/c_o)^2)] \; -v_o \qquad (6.3)$$

where $\alpha=1.25643$ so that the maximum velocity occurs at $r=c_o$, c_o is a core size parameter, and G_o is an amplitude that plays a role similar to Γ in the previous equations. The total circulation from this model is

$$\Gamma=2\cdot\pi\cdot(1+0.5/\alpha)c_o\cdot G_o \; . \qquad (6.4)$$

Determining the position of the vortex model corresponding to the measured velocities can be done in several ways. Individual vortex measurements can be fit as in Figure 33, or the vortices can be corrected for changes in position and a curve fit to find the parameters can be applied to a group of vortices to get an average value as shown in Figure 34. For comparison the vortex parameters determined without shifting the data to account for the variations in vortex position is shown in Figure 35; this figure is representative of the results that would be obtained by a measurement technique that averages data points without accounting for variations in the position of the vortex from measurement to measurement. Note that the core radius is 36% greater for the unshifted data. Determining the vortex model parameters for individual vortices is the most useful technique since it takes full advantage of the fact that the measurement can be directly correlated with the corresponding blade pressure and acoustic data.

6.5 Analysis of the Pressure Data

The blade surface pressure measurements are used to determine the interaction angle between the blade and the vortex and estimate the fluctuating lift being developed by the blade. Measured differential pressure for the transducers nearest the leading edge at 99% and 76% span are shown in Figures 36 and 37. The pressure fluctuation responsible for the blade slap is circled. This pressure fluctuation corresponds to the acoustic pulse shown in Figure 38 when the 4 ms propagation delay due to the distance from the microphone to the blade and the speed of sound in the fluid is accounted for. Measurements are plotted as the difference between the pressure on the pressure (bottom) side of the airfoil, and the pressure on the suction (upper) side of the airfoil, so that the plots also reflect the lift trend. The burst of high frequency fluctuations on the retreating side are interesting. The frequency content of the bursts correspond to the frequency of unstable disturbances in a shear layer calculated to range from 8 to 14 kHz for the conditions tested. These frequencies are above the roll off frequency of the equipment used so the phase and amplitude values are not accurate for this data; however, the measurements do reflect the presence of these frequencies. The spectrum (Figure 39) of the pressure data at the location of the burst shows that the frequencies between 8 and 14 kHz dominate the signal when this burst occurs. Spectra of the acoustic measurement show little acoustic radiation above 9 kHz so this boundary layer noise is not radiated effectively to the far field. The acoustic frequency for pressure waves travelling back and forth from the leading and trailing edges is approximately 6.7 kHz. It is possible that the strong and regular character of this noise burst is partially due to feedback between the boundary layer instability and the pressure fluctuations produced as the boundary layer waves or vortices leave the trailing edge of the blade. Highly separated flow observed on the retreating side in reference [26-28] using tuft flow visualization appears to show stall or separation over a large part of the retreating side which is further evidence that the behavior described is actually present. Further details on this behavior are available in references [55,56,57]. Differences between this data and that of reference [29,30] are primarily due to the limited frequency response of the recording instrumentation used in that work.

A diagram of the interaction is given in Figure 40. The blade has just returned to the advancing side and, in the absence of the wake effects, the blade would show a steady increase in lift as the velocity increases. Figures 41, 42, and 43 are expansions of the region of interest in Figures 36, 37 and 38 with the x-axis changed to a time scale. First the vortex induces a downwash on the blade which reduces the lift, this results in the steadily steepening decrease in the pressure which is similar in character to the velocity distribution of the downwash. Since the change in the downwash velocity occurs over a large distance relative to the chord of the airfoil, the airfoil response is fast enough to accommodate the change in the angle of attack. When the leading edge of the blade reaches the center of the vortex, the angle of attack induced by the vortex is suddenly changed as the vortex induces an upwash on the blade. This causes the very steep increase in the pressure as the airfoil changes lift to correspond to the new angle of attack. The upwash velocity induced by the vortex then decreases as the blade moves away from the vortex and this causes the decrease in pressure. Measured blade pressure for a blade-vortex interaction on the advancing side is then characterized by a gradual decrease in the lift as the blade approaches the center of the vortex, then a very steep increase in the lift as the blade passes over the center of the vortex; this is followed by a decrease in pressure as the blade moves away from the vortex and the induced upwash is reduced.

The next fluctuation in the pressure data is due to the interaction of the type shown in Figure 5 and shows a behavior similar to that just described except that the blade vortex spacing and interaction angle are different. The angle is larger so the effective frequency of the induced upwash distribution is reduced.

As described previously in Chapter 2, the key to efficient radiation of the acoustic pulse to the far-field is the high trace Mach number of the pressure disturbance through the fluid. The pressure fluctuations responsible for the blade slap occur very closely in time although one measurement is for 99% span and the other is for 76% span. This indicates that the fluctuation occurs almost simultaneously over the span and thus has a high trace Mach number. In contrast, the fluctuation produced by the vortex immediately following that interaction occurs much sooner at the tip than at 76% span and the fluctuations are not as efficiently radiated to the far field because the trace Mach number is low and radiated pressures are not added in a steep wave front.

The microphone is located 57 inches from the blade tip region so the acoustic wave takes approximately 4 ms to reach the microphone. The acoustic measurement is shown in Figure 43. Note that the blade slap pulse follows the measured blade pressure fluctuation due to the interaction at the center of the vortex by 4 ms.

The blade-vortex interaction angle is determined from the pressure measurements by determining the time difference between pressure fluctuations measured at 99% span and 76% span. Measured blade pressure shows a steep increase in the slope as the blade cuts the center of the upwash distribution. The angle is determined by the speed of the blade and the time delay between the measured pressures by assuming that the vortex is straight. The vortex is actually curved; however, flow visualization from reference [26] shows that the curvature is smaller than that predicted by the rigid wake plots so the assumption of a straight vortex is reasonable. The blade is also rotating throughout the interaction so the angle is continuously changing during the interaction. Using the point on the measured pressure fluctuations at which the slope is steepest to determine the interaction angle is the most representative angle to use for the trace Mach number because it is directly related to the trace Mach number near the tip of the blade.

CHAPTER 7

RESULTS OF THE VORTEX MEASUREMENT

This chapter is primarily devoted to the behavior of the tip vortex responsible for blade-vortex interaction noise. Vortex velocity measurements were taken to determine the character of this vortex. This vortex is influenced by interactions with the blades and aging effects between the time it is generated and the time it interacts with the blade to produce blade slap. In order to determine the change in the character of the vortex, the vortex velocity distribution was measured just after it was generated by the blade as well as just before the interaction responsible for blade slap. The vortex measured just after it is generated by the blade is discussed in section 7.1. The vortex measured just before the interaction is discussed in section 7.2.

7.1 Vortex Velocity Distribution Just After the Generation of the Tip Vortex

Vortex velocity distributions are presented for four test cases. The first is the velocity of the vortex just after the vortex is created and before any interactions with the blades. The vortex ultimately responsible for the blade-vortex interaction is created as the blade passes through the second quadrant on the advancing side. The hot-wire probe was positioned so that it passed behind the trailing edge of the blade as shown in Figure 44. The results of several measurements are shown in Figure 45. The data has not been shifted to account for variations in position and it is apparent that the vortex is located at a consistent position from measurement to measurement just after it is generated by the blades.

Three curve fits of the vortex were used. (See Chapter 6 for details). The results for each type of curve fit are shown in Figures 46, 47, and 48 for one of the vortices shown in Figure 45. Since the difference between the each of these vortices is small, any one of them is an adequate representation of the measured vortex. The models appear to give essentially similar results; however, closer inspection reveals that the Betz vortex model with core has higher velocities in the region outside of the vortex core. This is because the circulation increases from zero at the center to the total value at radius of 4.7 semichords. This results in a much greater circulation for the vortex than using the simple constant circulation model because the distributed rolled up vorticity of the Betz model increases the total circulation required to achieve the velocities measured near the center of the vortex.

The two data points furthest from the center of the vortex are each approximately one semichord from the center of the vortex. The circulation at this radius in the vortex is between 5.5 and 7.5 ft^2/second as determined from these measurements. Smoke flow visualization of the vortex with the smoke at a radius of approximately 4 semichords from the vortex center indicates that further from the center of the vortex the circulation is on the order of 10 ft^2/second. Therefore there must be additional circulation outside of that measured at a radius of one semichord. The Betz model predicts this distribution of vorticity given the circulation distribution of the lifting airfoil.

The routine developed to determine the values of the parameters for the vortex models which produce the best fit to the data does not constrain the values of those parameters. Since there is no data available far from the center of the vortex where the circulation is essentially constant, the value determined for the circulation cannot be considered as a valid representation of the actual circulation of the blade. (The extent of the rotational region obtained from the Betz model for the assumed blade circulation distribution has a radius of 4.7 semichords). The Betz model converges to a total circulation of 11.4 ft^2/sec; whereas, the simple model and exponential model converge to a circulation of 5.9 and 5.25 ft^2/sec respectively for the same data. All three vortex models produce curves that fit the data reasonably well, but the actual circulation trailed by the blade as computed from the Betz model is much closer to the circulation required to generate the measured lift and the circulation estimated from smoke flow visualization photographs [28]. It is apparent from Figure 46 that the Betz vortex model (with core) over estimates the velocity near the edges of the vortex in order to reduce the error in the data near the center of the vortex. Using the Betz model to fit only these outside points results in a predicted total circulation of 10.1 ft^2/second which is in good agreement with the flow visualization.

The amount of circulation calculated using the Betz model with a core is dependent upon the spanwise position of maximum circulation assumed for the blade since this determines the radius of the rotational region predicted by the Betz model. If the point of maximum circulation is moved towards the tip of the blade then the effective span of the Betz model is reduced, the size of the rotational region is reduced, and the total circulation calculated to fit the data points is reduced since the circulation is not reduced until the radius decreases to within the outer core radius which depends on the distance from the point of maximum circulation of the blade to the blade tip. Unfortunately the point of maximum circulation is not known because there are not enough pressure transducers along the span to accurately determine this point. For this work the 76% location is assumed to be the maximum circulation point and an elliptical circulation distribution is assumed. For an elliptical circulation distribution the Betz model predicts a rotational region with a radial extent of 78.5% of the length of the span from the point of maximum circulation to the tip. Figures 49 and 50 show the effect of assuming the position of maximum spanwise loading is 3 and 1 semichords from the tip respectively. This reduces the extent of the rotational region proportionately and results in a lower total circulation required to fit the measured velocities in the center of the vortex. Since the actual circulation is not important for calculating the acoustics as long as the measured velocities are accurately determined in the region through which the blade passes, this is not a serious problem, especially since the measured values are in reasonable agreement with the predictions using the Betz model.

The closeness of the fit of the vortex models used to the measured data points should not be assumed to be an accurate reflection of the accuracy or validity of the vortex model. For example, the exponential model for the vortex appears to match the data well, but the predicted circulation is half of the actual circulation determined from the smoke flow visualization. This effect is not important here since the measured velocities are known; however, it would be very important if the measured or predicted blade circulation were used to predict the vortex velocity distribution since using either the exponential model or the simple core model would predict much higher velocities in the core region than are actually present. This is demonstrated in Figure 51 where the velocities predicted by the three models given the same total circulation of 11.4 ft^2/sec are superimposed. From this Figure it is apparent that the Betz model or some model that accounts for the distribution of circulation due to the variation in the circulation over the span of the blade is required to prevent extreme overprediction of the velocities near the center of the vortex when the blade circulation is used to determine the vortex velocity.

7.2 Vortex Velocity Distribution Just Before the Interaction Responsible for Blade Slap

Vortex measurements taken just before the interaction by locating the probe so that it passes just in front of the blade before the interaction (approximately 3 semichords or less) as shown in Figure 22 indicate that the character of the vortex has changed since the initial rollup. Figures 52,53, and 54 show the vortex measurement and curve fits for the same operating condition as shown in Figures 46, 47, and 48, but measured just before the blade-vortex interaction responsible for blade slap. Note that the vortex is more spread out but the circulation is close to that found initially for the vortex just after rollup. Another data point using the Betz curve fit model is presented in Figure 55. Note that there is a large variation in the character of the data and that, even though the vortex has a consistent character just after its creation (Figure 45), there is a wide variation in the shape of the vortex after the two large angle blade-vortex interactions which precede the interaction responsible for blade slap and the action of viscosity for 1.25 revolutions. The data shows that the vortex is not necessarily circularly symmetric, varies in position from measurement to measurement, and does not always match the velocity distribution of the model well; however, the basic rotationality and steep velocity gradient of the core region is still present and these factors are the basic cause of the blade-vortex interaction noise phenomena. Even though the vortex is not consistent in character, the primary change that accounts for the new velocity distribution is the increase in the core radius which indicates the effects of viscosity and the two blade-vortex interactions which precede the measurement.

Figure 56 shows a different condition at which more data points are available (advance ratio of 0.19). Figure 57 is the same data shown in Figure 56 except that the data has not been shifted to account for variations in the vortex position. Note the variation in the vortex position and the increase in the scatter of the data points. Aging, turbulence, and the two interactions with blades at large blade-vortex interaction angles which precede the interaction responsible for blade slap have caused the vortices to fluctuate in position, increase in core radius, and vary in shape. This causes the blade-vortex interaction acoustic pulse to vary slightly in shape, amplitude, and azimuthal position.

Variation of the measured values for the vortices shown in Figures 56 and 57 around the values determined for the vortex model parameters can be quantified in several ways. Points of interest are the variation of the data points from the vortex model and the variation of the parameters for each individual vortex. The modified

Betz vortex model is used to determine the variation in the vortex parameters for the advance ratio of 0.19. Figure 34 is the shifted data and corresponding vortex model determined using all of the data points to determine the vortex parameters. The standard deviation of each set of data points from a given hot-wire to the velocity values determined at corresponding radial positions using the parameters of the vortex model are typically between 0.8 and 1.4 ft/sec at any radial position with no basic dependency on the position. The standard deviation divided by the magnitude of the velocity at that point is a useful indication of the amplitude of the scatter of the data points relative to the vortex velocity. This ratio ranges from 0.042 to 0.08 within 0.7 semichords of the center of the vortex to up to 0.24 for points outside of that region where the velocity is low. This means that the scatter is dominated by the effects of turbulence since the standard of deviation around the vortex model is relatively constant and is not related to the velocity of the vortex. Another consideration is the variation of the vortex parameters determined using the individual vortex measurements separately compared both with each other and the parameters determined using all of the data points after shifting the data. Determining the average value of the vortex parameters from the individually calculated vortex parameters (calculated for each individual vortex) results in an average circulation of 13.75 ft^2/sec with a standard of deviation of 2.78 ft^2/sec, an average core radius of 0.20 semichords with a standard of deviation of 0.07 semichords, a vortex position of 0.6 semichords from the tip of the probe with a standard of deviation around that point of 0.17 semichords, and an average offset velocity (v_o) of 4.6 ft/sec with a standard of deviation of 2.7 ft/sec. For comparison the circulation determined using all of the data, after shifting to account for variation in the vortex position, is 13.4 ft²/sec and the core radius using that technique is 0.185 semichords. These values indicate the variation of the vortex measurements from the vortex model and the variation of the measured vortices from each other.

It is apparent that the vortices vary slightly in shape, amplitude, and azimuthal position. For this reason the simultaneously obtained experimentally measured results for each vortex measurement, with corresponding blade surface differential pressure measurements and far-field acoustic measurements, are used individually so that the events of a single interaction are correlated on a one to one basis. The measured vortex for a given blade slap pulse is used to predict the acoustic pulse using the theory without averaging any of the measurements so that there is a maximum correspondence between the measured and predicted acoustics. No attempt was made to include the effects of the variation in the position of the vortex since the variation in the blade-vortex spacing over the span is greater than these variations and this effect cannot be accounted for with the Widnall-Wolf theory. Using the fact that an individual blade-vortex interaction is typical of any other one under the same test conditions combined with the fact that the data is simultaneously obtained for the vortex velocity distribution, blade pressures, and far-field acoustics, allows the important characteristics of the blade-vortex interaction to be determined from individual blade-vortex encounters without any averaging.

CHAPTER 8

COMPARISON OF MEASURED AND PREDICTED ACOUSTICS

8.1 DESCRIPTION OF THE INPUT PARAMETERS

Theoretical prediction of the acoustic pulse using the Widnall-Wolf theory requires several input parameters. The source of each of these parameters and the error associated with each is summarized in this section. The rotor is inverted in the wind tunnel so that it thrusts downward; however, all references to the rotor in this work account for this and the rotor and coordinate system referred to in the text is as it would be for a helicopter in normal flight. The only parts of this thesis where the rotor is not presented as a normal rotor are the flow visualization photographs which show the rotor as it operates in the wind tunnel.

The rotor blades used in the experimental aspects of this research are NACA 0012 section 2 inch chord with -8 degrees of linear twist (wash out) from the root of the blade to the tip. The rotor diameter is 50.25 inches, with two blades on flapping hinges and no cyclic pitch. Blade pitch was set to 5 degrees positive angle of attack at the tip. The effective (airfoil shaped) part of the blade is the outer 20 inches; the inner part consist of hub attachment hardware and the rotor hub. The blade semichord of one inch is used to nondimensionalize the length scales in the theoretical development of Widnall and Wolf.

The microphone was located directly above the hub of the model helicopter rotor which operates inverted in the wind tunnel; this corresponds to the microphone being directly below the helicopter. The theory requires an input for the microphone location which is referenced to the center of the dipole source of the blade. Microphone location as given in Table I corresponds to the coordinate system of Figure 10 including the angle of the interaction of the blade with the vortex and the direction of the circulation of the vortex.

Interaction length is accounted for by the modification of the theory described in Appendix A. Interaction angle is determined as previously described in section 6.5 using pressure transducer measurements which indicate the propagation time associated with the angle of the vortex relative to the blade more accurately than the angle determined from the smoke flow visualization measurements of reference [28]. The actual interaction angle between the blade and the vortex is continuously changing as the blade rotates, but this effect is partially accounted for by using the measured pressure to determine the interaction angle because the angle determined in this way is directly related to the propagation delay of the disturbance as the blade sweeps through the vortex.

The velocity used as input to the theory is the tip velocity including the component of the tunnel flow in the chordwise direction at the azimuth angle of the interaction. This azimuth angle is determined from the tip pressure transducer measurement. The variation of the velocity due to the blade rotation is accounted for by the modification of the theory as described in Appendix A. The blade-vortex separation distance varies on the order of one semichord over the span of the blade. The theory does not account for this variation, so the separation measured near the tip of the blade in reference [28] using smoke flow visualization is used as input for the theory. All parameters are measured near the blade tip because the outer part of the span dominates the far field acoustic behavior (see Appendix A). The velocity distribution of the measured vortex is used to construct the upwash distribution acting on the blade instead of the vortex calculated from the blade circulation using the Betz model.

8.2 Comparison of the Measured Vortex Velocity Distribution and the Vortex Predicted by the Widnall-Wolf Model

The vortex velocity distributions of the three vortex models (equations 6.1, 6.2, and 6.3) were found to correlate well with the measured data when the parameters were unconstrained; however, each produces different values for circulation and core radius. When the blade-vortex separation is within the range of data points used to determine the parameters for the corresponding vortex model and these models are used to predict the upwash and corresponding acoustics in the Widnall-Wolf theory, there is generally little difference in the predicted shape or amplitude as long as the parameters determined are used in the corresponding model of the vortex in the theory. The vortex velocity distributions for all of the vortex models are very similar in the range of the experimentally measured data points, even though the parameters such as circulation and core radius are significantly different, because they are constrained by the measured data. Examples of the acoustic pulses predicted from each vortex model when the blade-vortex separation is in the range of the data points are shown in Figure 58. The modified Betz vortex (with core) produces a slightly wider predicted acoustic pulse than the other vortex models because the velocity gradients on either side of the core are not as steep as for the other models. The pulse amplitudes are similar because the amplitude is determined by the velocity gradient as the upwash changes sign. This velocity gradient is determined by the peak amplitudes of the upwash in the plane of the blade and the distance between those peaks. Near the vortex core, when the blade-vortex separation is on the order of the core radius, the upwash is primarily determined by the velocity at a slightly greater radius than the blade-vortex spacing. (Slightly greater because the upwash is the component of the vortex velocity that is perpendicular to the plane of the path of the blade). Since the measured vortex velocities determine the velocity near the core, the vortex model chosen does not have a large effect on the velocities in that region.

If the blade-vortex spacing is larger than the core region, then the behavior of the upwash is dominated by the vortex velocity far from the core of the vortex. The Betz vortex model produces a much higher circulation and therefore has much higher velocities far from the core than the other models which determine a circulation on the order of half of that produced by the Betz vortex model. For this reason the predicted acoustic amplitude for a large vortex spacing is highly dependent upon the total circulation of the vortex and therefore on the choice of the vortex model used, as can be seen in Figure 59. The acoustic pressure is linearly dependant on the vortex circulation for the Widnall-Wolf model because the upwash velocity appears linearly in the equations. Because it is a better physical model according to the measured total vortex circulation, the modified Betz model, as described in section 6.4 and equation (6.2), is used for all of the following calculations.

The first part of the original Widnall-Wolf model is the calculation of the velocity distribution of the vortex given the spanwise circulation of the vortex generating blade. This is done using the Betz vortex model (without the core parameter). Essentially the only difference between the Betz model as originally used in the Widnall-Wolf model and the modified Betz model is the inclusion of the core parameter as described in equation 6.2. Therefore, the most significant difference is the behavior of the vortex in the core region. For these comparisons the circulation used is held constant at the value determined from the measured vortex velocity distribution since this is very close to the value predicted from the thrust or determined from smoke flow visualization. Figure 60 shows the predicted Betz vortex velocity distribution without the core compared to the modified Betz model for the measured vortex. The original Betz model does not account for the effects of viscosity. The elliptical circulation distribution assumed for the blade results a finite circulation at the origin for the Betz vortex model which results in an infinite velocity at the origin. For computation using the Widnall-Wolf model as originally formulated the computational step size limits the peak amplitude and the circulation at the origin is set to zero. This results in a significant overprediction of the noise amplitude when the blade-vortex separation is small. For comparison, the peak amplitude of the predicted acoustic pulses for the vortices shown in Figure 60 with a separation distance and interaction angle equal to zero are 109 dB for the model without the core and 101 dB for the modified Betz model with the measured core size. Increasing the blade-vortex separation reduces the difference between the upwash induced in the plane of the blade by the two vortices shown in Figure 60 because only the component of the velocity perpendicular to the plane of the blade path appears as an upwash to the blade. The upwash induced by the two vortices of Figure 60 on a plane 0.25 semichords from the centers of the vortices is shown in Figure 61. For 0.25 semichord separation distance the peak sound pressure is 99 dB for the vortex without the core and 98 dB for the vortex with the core.

Figure 62 shows a comparison of the predicted vortex and the vortex measured just after its creation (as in Figure 46). It is apparent from this figure that the Betz model predicts the vortex velocity reasonably well outside of the region where the effects of viscosity create a viscous core. Using the same technique as in reference [28], where the advancing blade was assumed to be generating 90% of the measured mean thrust, results in a total circulation within 10% of the value obtained with the modified Betz model and the measured vortex data for most cases; the greatest deviation is 30% for the advance ratio of 0.15. This results in predicted acoustic pulses using the blade thrust and the Betz vortex model within 1 dB (peak) for most cases and within 2 dB for the advance ratio of 0.15 when compared with the calculated results using the measured vortex data. Apparently, within the assumptions of the model, the Betz model is good for predicting the initial vortex velocity distribution except for the viscous core. For the test cases in this research the blade-vortex spacing used is always on the order of the core radius or larger so the difference between the Betz vortex model and the modified Betz model is less important. If the blade-vortex spacing is less than the core radius, then the difference between the predicted acoustics using the Betz vortex model and the modified Betz model which includes the core is important.

8.3 COMPARISON OF FAR-FIELD ACOUSTICS FROM THEORY AND EXPERIMENT

Three conditions generating blade-vortex interaction noise were tested. The simplest case occurs when the blade vortex separation is large and the vortex passes on the suction side of the blade. The large separation distance reduces the influence of the core region of the vortex. For this case many of the assumptions of the model are more accurate since the velocity fluctuations produced by the vortex in the plane of the blade are smaller relative to the mean flow than when the vortex passes close to the blade. The next case covered is similar to the first but with a reduced blade-vortex separation. This condition generates a larger acoustic pulse due to the reduced blade vortex separation distance and resulting increased upwash amplitudes and depends more heavily on the velocity field near the center of the vortex. Finally, the case when the vortex passes on the pressure side of the blade near the tip is covered. This results in a significant change in the shape of the measured acoustic pulse.

8.3.1 Large Blade-Vortex Separation with the Vortex on the Suction Side of the Blade Near the Tip

When the rotor is operated at the conditions shown in Table I at an advance ratio of 0.19, the blade-vortex separation near the tip is 1.7 semichords (ref [28]) and the interaction angle, determined from the pressure transducers, is 0 degrees. The vortex passes on the suction side of the blade and has a circulation with the same sign as the blade so the blade experiences a downwash followed by an upwash. The actual blade-vortex spacing varies over the span of the blade (ref [28]), but this is not accounted for in the Widnall-Wolf theory so the spacing near the blade tip is used for these calculations since the tip is a more efficient acoustic source. Using the measured vortex with the modified Betz vortex velocity distribution (which includes a core) shown in Figure 33 and the input parameters summarized in Table I, the calculated acoustic pulse is 83 dB compared with a measured value of 87 dB. Corresponding plots of the acoustic waveforms are given in Figures 63 and 64. Comparison of the wave forms shows that the theory predicts a small negative pressure followed by a large positive pulse that returns to zero with a very slight undershoot while the measured wave form shows very little initial negative pressure then a large positive pulse that is followed by a negative pulse. The pulse widths, however, are very similar for the measured and predicted acoustics. A significant amount of insight can be gained by looking for the source of this difference in the acoustic pulse shapes.

The predicted lift on the blade (as calculated using the Filotas theory) is shown in Figure 65. The lift exhibits an asymmetric behavior because the response is a function of the frequency content of the upwash. As the blade cuts through the core of the vortex the frequencies of the spectrum representing the steep velocity gradient of the vortex become very high. The lift response at high frequencies is reduced and phase shifted. The result of this is that the lift does not respond to the upwash variation with the same characteristic shape to match the upwash as it did during the gradual approach of the vortex where the velocity gradient is small and the content of the upwash spectrum is primarily concentrated at low frequencies. This results in a reduction of the amplitude of the positive excursion compared to the initial negative one. Since the value of the pressure of the acoustic waveform is roughly proportional to the derivative of the fluctuating lift, the acoustic pulse has a small negative excursion followed by a large positive pulse that is caused by the very steep positive slope of the lift as the blade cuts the vortex core. The lift then has a small negative slope and gradually returns to zero which results in a very small, almost insignificant, negative pressure in the acoustic waveform. This behavior is consistent with the linearized aerodynamic theory of Filotas used for this calculation.

The measured differential pressure at the tip of the blade at 99% span 18.75% chord, Figure 41, shows that the slope of the measured pressure is similar to the predicted lift before the blade interacts with the central region of the upwash, but the steep positive slope produced as the blade passes over the core of the vortex is followed by a steep negative slope, not the gradual slope predicted by the theory. Observing the pressure measurement located at 76% span of Figure 42 shows that at this location the leading edge pressure experiences a small dip before the steep positive slope produced as the upwash changes sign and a more gradual following negative slope than the pressure at the blade tip. The small size of the initial decrease in pressure may be caused by the fact that the net lift of the blade is increasing as the blade moves onto the advancing side. Corresponding pressure measurements at midchord at the 99% span and 76% span indicate that there is a very small correlated pressure fluctuation at midchord that is essentially in phase with the pressure measured at the 18.75% chord location. This indicates that the fluctuating lift of the blade follows the same trend as the leading edge pressure measurements. Thus, the steep negative slope in the pressure measured near the tip of the blade following the passage of the blade under the center of the vortex results in the large negative peak in the measured acoustic signal.

The lift is calculated from the measured pressure by assuming that the chordwise pressure distribution has a constant shape that is scaled by the pressure at any given chordwise location (a similarity solution). McCroskey's [55] experiments on a NACA 0012 airfoil in pitch show that in the absence of stall this may be a valid assumption. Although McCroskey's results cannot be assumed to apply directly to the case of a vortex interacting with a rotating blade, the measured pressures at the midchord position in this research indicate that the assumption of a similarity solution may be valid. The exact form of the similarity curve is not accurately known and cannot be determined with only the three pressure transducer locations along the chord of the blade. (There is a pressure transducer near the trailing edge of the blade but there is very little discernable response to the blade-vortex interaction there). McCroskey's data suggest that the chordwise differential pressure distribution predicted by linear theory is a good approximation to the actual differential pressure distribution. This pressure distribution has a large amplitude near the leading edge which rapidly falls to a very small value which is in agreement with the behavior measured by the pressure transducers on the model helicopter blade. Details of the pressure to lift conversion using the chordwise pressure distribution determined from linear theory as a similarity pressure distribution profile are given in Appendix C.

The pressure data is converted to a lift trend as outlined in

Appendix C by multiplying the measured pressure by a constant which relates the pressure at that point on the chord to the total lift per unit span over that section of the chord. This "measured lift" is then substituted into the theory of Widnall and Wolf in place of the calculated lift. In order to actually perform this substitution the measured pressure data must be redigitized to match the time step of the Widnall-Wolf model and multiplied by a raised cosine window to allow the application of the Fast Fourier Transform (FFT) algorithm. This is then used to determine the measured spectrum of the lift at the spanwise location of the pressure measurement which is used instead of the predicted lift in the Widnall-Wolf theory. The resulting acoustic pressure, calculated from the measured differential surface pressure at 99% span and 18.75% chord of Figure 41, is shown in Figure 66. The predicted peak pressure using this technique is 91 dB. The measured pressure is 87 dB. The acoustic pulse width predicted by using the leading edge tip pressure transducer data in the theory is slightly narrower than the measured pulse. This could also cause the overprediction of the peak pressure level since the acoustic pressure depends on the slope of the lift fluctuations, but the agreement in the shape of the pulses is good. The blade pressure signal from the 76% span 18.75% chord location shown in Figure 42 has some large noise spikes that have a very large derivative so the predicted acoustic signal (Figure 67) from this measurement is dominated by this noise. Low pass filtering this data with a zero phase shift FFT filtering technique removes most of this noise and results in the pressure plot shown in Figure 68. Using this filtered data to predict the acoustics produces the pulse shown in Figure 69 which still over predicts the peak to peak amplitude by 2.5 dB but agrees well with the measured acoustic pulse shape.

For the acoustic signatures predicted from the measured leading edge pressure, only the acoustic pulse produced by the fluctuating pressure due to the blade-vortex interaction is representative of the actual phenomena. The higher frequency noise and the noise away from the region of the blade vortex interaction are not accurately described by this technique because the measured pressure is assumed to act over the chord of the blade to produce lift as described in Appendix C, and this lift is assumed to be correlated over the span of the blade as determined by the blade-vortex interaction angle. Clearly this is not the case for the "broadband" noise which appears in the predicted acoustic signature since the fluctuating pressures due to turbulence are not correlated in that manner.

Some other effects have been investigated to determine the reason for the discrepancy between the measured pressure and predicted lift. Figure 1 shows that there is another vortex that will interact with the blade after the interaction responsible for blade slap. Since the second vortex is not far from the first, the velocity induced by this vortex increases the steepness of the velocity gradient between the vortices; this could produce the large negative slope in the measured pressure. This effect was tested by adding the velocities of two vortices spaced according to the measured time between the fluctuating pressures due to the interaction with each vortex. The predicted acoustic signal is shown in Figure 70. The second peak is much bigger than it should be because the model uses the same interaction angle for both vortices, while the second vortex actually has a large angle with respect to the blade. Ignoring this second peak because it is not actually radiated effectively and looking at the effect on the first peak, note that there is a larger negative peak following the large positive peak. This can be viewed in two ways. The first is the described increase in the upwash velocity gradient due to the second vortex. The second interpretation is that superimposing the small negative peak at the beginning of the second pulse, which essentially matches the first peak, causes the effect shown in the Figure. Since the equations are all linear, the second interpretation of superposition is valid. This means that the fluctuating lift and acoustics due to the interaction of the blade with the upwash velocity field of two closely spaced vortices produces the same result as the superposition of the waveform produced from a single vortex interaction time shifted by an amount corresponding to the spacing between the vortices and added to the original pulse. This superposition principle is valid for both the predicted lift and acoustic pulse wave forms.

The problem with the second positive peak in Figure 70 is that the second vortex interaction occurs at a much greater blade-vortex interaction angle and generally at a different blade-vortex spacing. The dominant factor in this case is the large angle which results in lower frequency content of the upwash and lower slopes in the lift fluctuations as well as a greatly reduced trace Mach number. The interaction angle is determined in a manner similar to that used for the first interaction by determining the time delay from the pressure data. Because the large blade-vortex interaction angle is the dominant effect that changes the amplitude and shape of the acoustic pulse produced by the second vortex, the predicted acoustic pulse due to the second vortex is determined by using the same vortex velocity distribution and blade-vortex spacing as used for the first vortex but using the measured blade-vortex interaction angle. The pulse calculated for this interaction is then added to the pulse calculated for the first vortex interaction with the proper time shift to account for the spacing between the vortices. This yields the net effect of both interactions by superposition. The result of this process is shown in Figure 71. The results do not closely match the measured results in that the negative pulse which follows the large positive pulse is not of the same magnitude or shape as the measured acoustic waveform; however, the pulse width and double peak shape does match the measured acoustic pulse fairly well. The actual situation of the blade interacting with the vortices in the wake is a continuous process where the interaction angle, blade-vortex spacing, and vortex velocity distribution are all changing continuously as the blade rotates; however, the analysis of the effect of the two vortices using the two techniques of superposition described in the previous paragraphs indicate that the effects of the second vortex and its associated velocity field do not adequately account for the difference in the predicted and measured acoustic pulse shapes when the Filotas model is used to calculate the fluctuating lift.

Other causes of the observed differences between the measured data and the theoretical predictions could be:

1) Other noise is superimposed on the signal and causes the whole pulse to be skewed by the low frequency noise; however, removing the low frequency component actually accentuates the size of the negative peak since the low frequency waveform is rising at this point.

2) Measured pressure shows that the lift model does not accurately describe the lift measured near the tip of the blade. This could be

because the model assumes inviscid flow while the Reynolds number (175,000) is probably not high enough for this to be an accurate assumption, or it could be due to tip effects which are not considered in the Filotas model. Another possibility is that the close positioning of several tip vortices at the edge of the rotor wake (Figure 1) produces a significantly different flow field near the tip of the blade than that produced by one or two vortices as modeled.

3) Tip effects may cause the lift to respond differently than the models predict since the models do not account for the highly three dimensional flow around the tip. Flow visualization using miniature tufts [28] show that the tip has a vortex that is formed on the suction side. It is possible that tip effects decrease the lift response time constant so the response of the airfoil near the tip may be more rapid than predicted.

Since the measured pressure indicates that the lift is not accurately reflected by the Filotas model, another model for the lift might produce a more accurate prediction of the acoustics given the velocity distribution of the vortex. Fluctuations in the pressure appear to reflect the characteristics of the vortex induced upwash, so a simple model that relates the lift directly to the angle of attack induced by the upwash was substituted for the Filotas model and used to predict an acoustic pulse shape. This was done using the simple model for the lift of a thin airfoil in steady flow

$$C_L = 2\cdot\pi\cdot\text{(the angle of attack in radians)} \qquad (8.1)$$

instead of the Filotas model. The resulting predicted acoustic pressure is shown in Figure 72. The pulse shape is nearly symmetric (the directivity of the acoustics also has an effect the pulse shape) because the lift response is symmetric and the agreement with the measured shape is reasonable; however, the peak to peak amplitude is over predicted. As the wave number of the upwash frequency increases, the lift response of the blade is reduced, but this is not accounted for by the simple theory of equation 8.1. Theodorsen's solution [58] indicates that the lift can be reduced on the order of half of the value determined from equation (8.1) and Filotas's model indicates an even greater reduction in amplitude. Theodorsen's theory is not for an upwash velocity field and both it and the Filotas model predict phase shifts associated with the wave number, but the trend of reduced airfoil lift response with increasing wave number is consistent. For the reduced frequencies in the upwash due to the blade-vortex interaction for this case the reduction in the peak dB level of the radiated acoustic pulse due to this effect is typically on the order of 4 to 6 dB.

Large blade-vortex separation reduces the significance of the details of the vortex. At a large blade vortex separation distance the circulation of the vortex dominates the upwash induced on the blade and the details of the inner vortex core are not important when predicting the far field acoustics due to the upwash induced by the vortex. The use of the upwash model itself is also more valid since the flow is less rotational at large distances from the vortex. Comparison of the predicted lift with the measured pressure shows a large discrepancy of the behavior of the lift after the blade passes over the center of the vortex. This discrepancy is responsible for the difference between the predicted and measured pulse shapes. Using the measured blade leading edge (18.75% chord) pressure difference at 99% span and 76% span to determine the fluctuating lift at a point on the blade span and then substituting this fluctuating lift into the theory to predict the acoustics results in excellent agreement with the measured acoustic pulse shape. Use of the pressure transducer at 76% span results in the best agreement in the predicted peak pressure, for this case over predicting the peak pressure level by 2.5 dB. The technique which gives the best results for the pulse shape without the measured pressure data as input uses a simple (quasi-steady) model of the lift being proportional to the angle of attack which over predicts the peak acoustic pressure by 3.5 dB. The Widnall-Wolf model, using the Filotas model for the fluctuating lift, under predicts the peak acoustic pulse by 3 dB.

8.3.2 Small Separation Distance

Reducing the advance ratio from the case described in section 8.3.1 changes the geometry of the blade-vortex interaction. The interaction angle changes as does the azimuthal position at which the interaction occurs. Changes in the rotor thrust, tip path plane, and rotor wake spacing also occur. The rotor is operating in a descent mode with the tip path plane tilted so that the free stream tends to convect the vortices over the suction side of the blades and the rotor downwash convects the vortices towards the pressure side of the blades. When the advance ratio is reduced, by reducing the tunnel speed, the rotor convection pulls the vortices closer to the suction side of the blades because the relative convection of the freestream is reduced. For the advance ratio of .17 the blade-vortex spacing near the tip is reduced from the previous case to 1/4 semichord and the interaction angle is 7 degrees with the interaction starting at the tip and progressing inward along the span of the blade. A rigid wake plot for this case is shown in Figure 1. The measured vortex velocity distribution is shown in Figure 52. Using the parameters for the vortex shown in Figure 52, a circulation of 10.6 ft^2/sec and a core radius of 0.14 semichords, along with the parameters for the blade-vortex interaction geometry, gives the acoustic pulse calculated from the Widnall-Wolf theory shown in Figure 73 which has an amplitude of 96 dB. The measured acoustic pulse ,shown in Figure 74, has an amplitude of 90.4 dB. The predicted acoustic pulse is narrower than the measured pulse which is also partially responsible for the high predicted peak amplitude since the amplitude of the pulse is related to the time derivative of the fluctuating lift. The difference in the pulse shapes follows the same trend as the previous case with 1.7 semichord spacing.

The fluctuating lift calculated by the Filotas theory, shown in Figure 75, exhibits the same characteristics as for the previous case (section 8.3.1). Measured differential blade pressure is shown for the tip transducer in Figure 76. Using the same technique of calculating the lift from the measured leading edge pressure data and using this for the fluctuating lift in the acoustic calculation as described in section 8.3.1 results in a predicted acoustic pulse of 91 dB as shown in Figure 77. Agreement with the measured acoustic pulse shape and amplitude is very good. The blade pressure at 76% span, shown in Figure 78, has noise spikes which again dominate the predicted acoustic signal when this is used to predict the acoustics as shown in Figure 79. These high frequency noise spikes may be due to the pressure fluctuations generated by a boundary layer instability or a similar phenomena; this noise occurs consistently at this position in the data so random noise sources are not likely to be the cause of this behavior. It was previously noted that on the retreating side, where flow visualization using minitufts shows a large separation over the span of the blade (reference [28]), that the pressure transducers also show a burst of high frequency noise. The frequency content of this noise indicates that this may be a similar phenomenon. The low Reynolds number of the blade (175,000) is a probable reason for this behavior. Full scale helicopters operate well above the Reynolds number where a boundary layer effect such as a shear layer instability could occur over a significant part of the blade. The frequency is so high that the pressure fluctuations are self canceling over the chord and in the far field. Filtering this noise out of the pressure signal then calculating the acoustic pressure gives the pulse shown in Figure 80.

The Widnall-Wolf model with the velocity field of two vortices instead of one gives the result shown in Figure 81. The superposition of predicted acoustic pulses from two vortices accounting for the different interaction angles is show in Figure 82. Both show a similar trend in the predicted acoustic pulse shape as for the large blade-vortex separation covered in section 8.3.1.

The acoustic pulse predicted using the simple lift model of equation (8.1) is shown in Figure 83. For this case the predicted acoustic pulse amplitude is over predicted by 18 dB, much more than that for the advance ratio of 0.19 (section 8.3.1). This is because the spectrum of the upwash contains much higher frequencies due to the close blade-vortex separation. This simple model for the lift does not account for the reduction in the lift response to an increase in the gust frequency and is therefore not an accurate model; however, the behavior of the pulse shape which is generated by this model is of interest because there is no phase shift associated with the lift model.

Variation in the predicted acoustic pulse shape from a symmetric shape using this model is due to the effects of the interaction geometry and the acoustic directivity.

For this advance ratio all of the cases where the predicted acoustics are calculated from the measured vortex velocity distribution result in over prediction of the amplitude and a pulse width that is too narrow. The vortex passes on the suction side of the blade and has the same circulation as the blade. The effect of the vortex self induced motion due to the close proximity to the blade was approximately modeled by using the analogy of a vortex and its image vortex on the other side of a wall. This is not an accurate or rigorous description of the behavior of a vortex as it passes over an airfoil; however, it does provide a tool for evaluating the possible effects of the vortex self induced motion. Using the image vortex analogy leads to the conclusion that the passage of the vortex over the blade is slowed by the induced velocity and pressure field of the vortex acting on the blade. This could account for the wider pulse width of the measured acoustic waveform. To test this effect the bulk velocity of the flow in the Widnall-Wolf model was reduced by an amount equivalent to that induced by an image of the vortex. This increases the pulse width slightly and reduces the predicted dB level by 2dB for both the Filotas and simple lift models but does not have a large enough effect on either the peak amplitude or the pulse width to bring the results into agreement with the measured results.

In both test cases in section 8.3 considered to this point, the basic form of the pulse shape is modeled more accurately by the measured leading edge pressure based prediction than by the fluctuating lift model of Filotas. The source of this discrepancy is probably a combination of the velocity fields of the multiple vortices near the tip of the blade and the effects of the three-dimensional flow near the blade tip. The next section covers the case of the vortex passing on the other side of the blade (the pressure side) and the shape of the measured acoustic waveform changes character significantly.

8.3.3 Close Blade Vortex Interaction with Vortex on the Pressure Side of the Blade Near the Tip

Reducing the advance ratio from .17 to .15 allows the rotor flow to move the vortices onto the pressure side of the blades near the tip. The tip path plane of the blades and blade-vortex interaction angle also change. The result is a blade-vortex interaction with a measured blade-vortex spacing at the tip of 1/4 semichord, but the vortex now passes over the pressure side of the blade near the tip. Smoke flow visualization shows that the vortex passes on the suction side of the blade on the inner span so the blade actually cuts the vortex for this case (reference [28]). The interaction angle determined from the pressure measurements is 15 degrees. The trace Mach number is one for an interaction angle of 10 degrees and 0.7 for an interaction angle of 15 degrees, so previous cases covered in section 8.3.1 and 8.3.2 have a trace Mach number that is greater than one, while this case has a trace Mach number that is less than one. The cut off in the efficiency of the acoustic radiation is not abrupt at a trace Mach number of one, however, because the wave fronts are still close together and are reinforcing if the wave length of the sound is large compared to the wave length difference between the propagation of the disturbance through the fluid and the propagation of the acoustic wave ahead of this disturbance which depends on the interaction length. The difference between the wave form when the trace Mach number is greater than one and when it is less than one is that when the trace Mach number is greater than one the positive pulse has a steep positive slope leading edge and a less steep negative slope trailing edge because the wave fronts are adding directly into a very steep wave front, or Mach cone, for the advancing acoustic wave. When the trace Mach number is less than one the wave form has a less steep positive slope because the wave fronts are spread since the pressure fluctuation is being produced slightly behind the advancing acoustic wave. The other side of the pulse now has a steep negative slope.

Using the measured vortex shown in Figure 84 results in a predicted acoustic pulse, shown in Figure 85, which is similar in characteristics with the other predicted pulses since there is no difference in the model to account for the side of the blade over which the vortex passes. The only difference is the change in the pulse shape due to the subcritical trace Mach number. The amplitude of 92 dB. and pulse shape and width are very close to the measured acoustic pulse produced by this vortex, shown in Figure 86, which has an amplitude of 91 dB. The measured pulse is now characterized by a small negative excursion followed by a large positive peak and the negative peak which follows is very small and does not extend below the initial negative peak. Low frequency noise in the measurement, primarily at the blade passage frequency (see Figure 87), distorts the pulse and raises the negative pulse because the low frequency wave form is rising at this point. In order to determine the extent of this effect, the signal was high-pass filtered with a zero phase shift FFT filtering technique and the resulting pulse, without the low frequency noise, is shown in Figure 88. This increases the size of the negative peak slightly; however, it is still apparent from this measured pulse that the pulse shape has changed significantly from the previously discussed cases where the vortex passed over the suction side of the blade.

The predicted lift, Figure 89, is basically the same as for the previous cases. As described previously the large positive slope is followed by a gradual return to zero lift which is responsible for the shape of the predicted acoustic pulse. Comparing the predicted lift with the measured leading edge pressure at the tip, shown in Figure 90, indicates that the same characteristic steeper negative slope in the measured pressure relative to the predicted lift occurs, so the measured pressure at the tip still shows the same shape as for the previous cases. Using the measured leading edge tip pressure of Figure 90 to calculate the fluctuating lift gives the acoustic pulse shown in Figure 91. The pulse width is similar to the measured pulse but the shape is similar to those calculated previously using the same technique in sections 8.3.1 and 8.3.2. This shape no longer agrees with the measured pulse shape.

Using the 76% span pressure transducer data shown in Figure 92 to calculate the predicted acoustic pulse gives the pulse shown in Figure 93. The amplitude and pulse shapes agree well for this case and the noise spikes in the pressure data are lower in amplitude and do not distort the predicted pulse as much as for the previous cases where the 76% span pressure measurement was used. Figure 94 is the predicted acoustic pulse using the low pass filtered pressure data from the 76% span position to eliminate the effects of this noise entirely. The final negative pulse is lower in amplitude when this inboard transducer is used to predict the acoustic pulse. This difference between the inboard and outboard transducers is relatively consistent for all of the close blade-vortex interaction conditions tested, but for this case the predicted peak to peak acoustic pulse from the 76% pressure data is greater than that predicted from the 99% span location. For previous cases the 76% location produced a smaller pulse. This indicates that a steeper lift gradient occurs at this location than at the tip. This occurs because the blade cuts the center of the vortex in this region when the vortex is on the pressure side of the blade near the tip.

Figure 95 represents the results of using the velocity distribution of two vortices and the only significant difference is the previously described pulse shape change due to the subcritical trace Mach number. The superposition method using the two different blade-vortex interaction angles predicts an acoustic pulse as shown in Figure 96. Results of the superposition method provide good agreement with the measured acoustic pulse shape and agree within 2 dB in peak amplitude. The simple lift model predicted pulse shape (Figure 97) produces a pulse shape which is in good agreement with the previous cases where the vortex passes on the suction side of the blade near the tip (sections 8.3.1 and 8.3.2) but is in poor agreement with the measured results for this case. The asymmetry in the shape is now dominated by the effect of the interaction angle and resulting subcritical trace Mach number.

The case of the vortex passing over the pressure side of the blade causes a significant change in the character of the measured pulse shape compared with the cases when the vortex passes on the suction side of the blade. Likely sources of this behavior are the passage of the vortex over the pressure side of the blade, the trace Mach number of 0.7, and the fact that smoke flow visualization shows that the vortex passes over the suction side of the blade near the tip but the pressure side near the root, so the blade actually cuts through the vortex at some point on the span. The pressure measurements combined with the acoustic pulse shapes predicted from these measurements indicate that the most important factor appears to be the fact that the blade cuts through the center of the vortex.

8.3.4 Summary and Discussion of the Results of the Comparison of Experiment with the Widnall-Wolf Theory

Significant changes in the behavior of the measured acoustic pulse occur when the vortex passes on the pressure side of the blade instead of the suction side of the blade. Several potential sources of the change in the behavior exist:

1) The vortex passes on the other side of the blade so the effects of vortex induced velocities not accurately modeled as upwash, which are not accounted for by the theory, are different.

2) The trace Mach number is below one for the case where the blade passes on the pressure side of the blade. This changes the pulse shape for the predicted pulses. It may be that tip effects become a dominate factor when the trace Mach number is below one as suggested in references [24 and 25].

3) The blade actually cuts the vortex at some point along the span so the inboard sections contribute more to the acoustic pulse than for the previous cases.

Any combination of the above effects could be responsible for the difference in the measured behavior between the cases when the vortex passes over the suction side of the blade and the pressure side of the blade, but the measured blade pressure indicates that the third effect is the dominant one.

The measured pressure at the tip does not correlate well with the predicted lift. The pressure measurements from the 76% span leading edge location are more in agreement with the lift predicted by the Filotas model. From this information it is apparent that the behavior at the tip is not modeled by the Filotas model. The Widnall-Wolf model accounts for the tip by the boundary condition on the radiating dipole, but the lift at the tip is modeled as though the blade extends to infinity using the Filotas model, so aerodynamic tip effects are not accurately modeled. The measured pressure data shows that at the tip the lift fluctuation responds more directly to the upwash distribution than predicted by the Filotas model. Flow around the tip may have a similar effect to reducing the effective chord of the blade. A smaller effective chord decreases the relative frequency of the upwash (decreases the relative wave number) and decreases the response time of the airfoil to the upwash.

Smoke flow visualization shows that when the vortex passes on the suction side of the blade, the tip passes the closest to the center of the vortex and the blade-vortex separation increases moving from the tip to the root. The lift at the tip is not accurately predicted by the Filotas model and actually responds more quickly to the upwash than predicted. This is reflected in the measured acoustic data as well as the measured blade tip pressure.

When the vortex passes on the pressure side near the tip it is actually cut by the blade further inboard; therefore, the inboard

C-2

part of the blade becomes more important to the far field acoustics than it was previously, and the pulse shape reflects this trend. Since the lift at this point (76% span) correlates well with the Filotas model, the predicted acoustic pulse shape is in agreement with the measured pulse shape.

Modeling the lift with the simple quasi-steady model (equation (8.1)) results in better correlation of the predicted acoustic pulse shape but in an over prediction of the peak amplitude when the vortex passes nearest to the blade on the suction side of the blade near the tip. Reduction in the lift with an increase in the frequency of the upwash is expected. Using the correction for this effect associated with reduced frequency of the vortex induced gust frequencies would reduce the amplitude of the predicted acoustic pulse for the simple model for the lift.

The Reynolds number at the blade tip of 175,000 is much lower than that of a full scale blade which is typically at least 1,000,000. This results in a much different boundary layer behavior than would be expected for a full scale helicopter. At such a low Reynolds number the size of the transition region from laminar to turbulent flow can be on the same order as the blade chord which can result in flow behavior that is much different than the behavior at high Reynolds numbers where the boundary layer flow quickly becomes turbulent. High frequency noise measured with the pressure transducers is at a frequency which corresponds to the most unstable frequency of a free shear layer using an approximate analysis and the equations presented in references [55] and [56]. It is therefore possible that the flow is basically different than for a full scale Reynolds number flow. The effect of the blade rotation also plays a significant roll in the behavior of the boundary layer, so direct comparison with non-rotating flow behavior may not be valid. The low Reynolds number may also affect the character of the vortex since the vortex contains the fluid from the boundary layer. The low Reynolds number of the experimental data in this thesis may produce differences in the behavior of the flow compared to full scale helicopters which operate at much higher Reynolds numbers, so the details of the flow behavior may not correspond exactly; however, the basic phenomena of vortex induced pressure fluctuations is similar and useful results have been obtained.

8.4 Directivity of Blade-Vortex Interaction Noise as Predicted by the Widnall-Wolf Theory

The directivity of the blade-vortex interaction noise as described by the Widnall-Wolf model is basically a dipole directivity as described in reference [25] and shown in Figure 98. If the microphone position is mirrored onto the other side of the plane of the path of the blade, then the pulse shape is also mirrored, so for a microphone located above the rotor the acoustic pulse is the same as that measured below the rotor but inverted. The directivity is also affected by the Mach number of the blade and the blade-vortex interaction angle. For the results presented in this thesis the tip Mach number is typically 0.15. For such a small Mach number the peak directivity is essentially directly below the plane of the rotor as has been found by previous researchers using the same rotor facilities. At higher Mach numbers the directivity pattern is beamed forward and this accounts for the difference between the directivity pattern for full scale blade vortex interaction test results in reference [19] and

[20] and those measured at lower tip speeds.

The effect of the interaction angle on the directivity pattern evident in Figure 98 can be visualized using Figure 4. Figure 4 shows that changing the interaction angle results in a change in the direction in which propagating wave fronts are steepest. The significance of this effect is evident in Figure 98. Figure 98 shows that at a blade Mach number of 0.5 the effect of the interaction angle on the directivity can be extreme. Measured acoustic data from references [19] and [20] are for Mach numbers at which several of the possible interactions on the advancing side have blade-vortex interaction angles that result in trace Mach numbers that are greater than one. Depending on the corresponding blade-vortex separation distances, several blade vortex encounters may then result in blade slap. Evidence of multiple interactions exist in the data from both reference [19] and [20]. Each interaction has its own directivity pattern which can produce different results for measurements at different microphone positions. Particularly for four bladed rotors, as in reference [19], the number of possible interactions and resulting different directivities result in a complex relationship between the microphone position and the acoustic signature of the rotor. For this reason the conditions which generate the maximum peak blade slap amplitude can also be observer position dependent. The position of the observer must also be related to the azimuth of the blade during the interaction when comparisons with theories are made. The microphone location used in this research is directly above the hub of the rotor so the angle of the microphone relative to the blade is constant at all azimuth angles.

CHAPTER 9

CONCLUSIONS

Important characteristics of the vortex responsible for the blade-vortex interaction noise were measured using a rotating hot-wire rake. Blade differential pressure measurements and far-field acoustic measurements were also obtained using a simultaneously sampling, high speed, digital data acquisition system. Smoke flow visualization results of reference [28] combined with the measured data were used to evaluate the theoretical model of Widnall and Wolf. This model was chosen because the inputs required are global in character: the model may be useful for determining the acoustic signature during blade slap from basic design information which may allow the effect of design changes on the blade-vortex interaction noise to be determined. The model is actually a combination of several separate models so modifications and evaluations can be made on each part individually. Each part of the model was compared with the measured results.

The Betz vortex model [45, 46] is not accurately evaluated because there are not enough pressure transducers along the span of the blade to determine the circulation distribution of the blade; however, using a reasonable assumption for the circulation distribution results in a vortex which correlates well with measured vortex velocities outside the viscous core region of the vortex. The viscous core was accounted for using the measured data and equation 6.2. The simple irrotational vortex with core (equation 6.1) and the commonly used exponential vortex model (equation 6.3) greatly over predict the peak velocities near the center of the vortex when the bound blade circulation is used to determine the velocity distribution of the vortex. The reduction in the circulation near the center of the vortex due to the rollup of the trailed vorticity sheet, determined by the Betz model and often termed the outer core region, is therefore important if the velocities in this region must be accurately determined. The Betz model does not accurately predict the velocity in the inner viscous core region since it does not include viscous effects. The high velocities predicted inside of this region result in a significant overprediction of the acoustic pulse due to the blade-vortex interaction if the blade cuts the vortex center; however, if the blade-vortex interaction takes place outside of the this viscous core region then the error in the calculated far-field acoustics due to ignoring the viscous core altogether is small when the Betz vortex model is used (on the order of 1 dB at a blade-vortex separation of two viscous core radii). The Betz vortex model appears to accurately represent the vortex velocity distribution outside of the viscous core region while the other two models used do not.

Pressure measurements show that the fluctuating lift is dominated by the blade leading edge pressure. Measurements near the blade tip (99% span) show that the lift predicted using the Filotas theory is not accurate at the tip of the blade. The tip of the blade is also close to the other vortices at the outside edge of the rotor wake. These vortices alter the velocity gradient experienced by the blade during the blade-vortex interaction. Results indicate that three dimensional flow near the tip of the blade (not modelled by the Filotas theory) combined with the velocity field of the other vortices appears to be primarily responsible for the difference between the measured and predicted results. Inboard pressure measurements at 76% span are in better agreement with the Filotas theory. At this point the velocity field has less distortion due to other vortices, but an important factor is that away from the tip the infinite span assumption of the Filotas model is more accurate.

All data in this thesis is for a low Reynolds number (175,000 based on the tip velocity and airfoil chord). The flow is affected by viscous boundary layer effects much differently than for full scale helicopter Reynolds numbers. The low Reynolds number also makes the inviscid flow assumptions of the Filotas theory less accurate. All of the assumptions of the Filotas model should be more accurate at the higher Reynolds numbers of full scale helicopters until the speed becomes so high that compressibility effects become important. The Filotas theory is for incompressible flow. For higher speeds the compact source assumption may not be adequate and a superposition of sources may be required along the chord of the blade, but, for all of the conditions tested in this thesis, the compact source assumption is valid.

Work by other researchers done at higher Reynolds numbers shows a pulse shape more consistent with the predicted pulse shapes (references [19],[20]); however, the information on the interaction geometry is inadequate or nonexistent, so comparison with theory is not possible. Under the conditions tested in this research the vortex is not rapidly dissipated by the blade-vortex interactions which occur before the interaction responsible for blade slap. Just after the vortex rollup the vortex remains in a consistent position. This means that for this condition the vortex can be measured accurately by taking single point measurements at a consistent point and time in the flow and the results after combining the data over a measured area will provide an accurate description of the vortex velocity profile. Variation in the vortex position becomes large as the vortex moves down stream and passes close to the blades: however, the vortex is not necessarily dissipated and a large dissipation was not observed prior to the blade-vortex interaction responsible for blade slap. This variation in position means that single point measurement techniques, which depend on the consistency of the vortex position, will not be able to resolve the velocity distribution of the vortex and the results from such data can be misleading. The presence of a strong vortex which is not in a consistent position can be sensed with a single measurement by the fact that the variations in the measured velocity will be high. If this is the case then the results of the averaged data do not provide an accurate measurement of the vortex velocity profile. Since a single point measurement is often the simplest or only practical way to make some measurements, the standard deviation or some other measure of the variation of the data at a given point must be considered to be sure that the averaged data accurately reflects the true flow field. The rotating hot wire rake technique measures the vortex velocity in one pass and provides an accurate measurement of individual vortices. This provides information on the variation in the vortex position and velocity distribution of individual vortices.

The Widnall-Wolf model predicts the acoustic pulse shape well when the vortex passes over the pressure side of the blade. When the vortex passes on the suction side of the bade the pulse shape and amplitude are not accurately predicted. A primary problem with the model appears to be the behavior of the fluctuating lift near the tip of the blade. This is because effects of the flow near the blade tip are not accounted for by the model. The variation in the blade-vortex spacing, which is not accounted for by the theory, also appears to be a source of error. The Betz vortex model in the theory is in good agreement with the measured vortex except for the viscous core region. The acoustic model and stationary phase technique appear to work well and provide a technique for calculating a predicted acoustic pulse from the measured blade leading edge pressure. Since the pressures may be self similar over a significant extent of the blade. detailed blade surface pressure measurements may not be necessary to predict the acoustics from measured pressures as long as some method of accounting for the phase relationship over the span is used as was done in this research. The basic framework of the Widnall-Wolf theory shows promise as a tool for predicting the acoustic signature of blade-vortex interaction if some of the mentioned inconsistencies with the measured data can be corrected.

CHAPTER 10

RECOMMENDATIONS

Future experimental investigations of blade-vortex interaction noise need to include measurements of the interaction geometry so that the results can be compared with theory. Results of this research indicate that a comparison of the Widnall-Wolf theory with experiment at higher Reynolds numbers is warranted since the pulse shape for data from references [19] and [20] appears to be in good agreement with those predicted by the theory in this research. The Filotas model is not applicable at the higher speeds of full scale helicopters if compressible flow effects become important. If this is the case then a compressible lift model can be substituted for high speeds or the blade-vortex interaction models of Martinez or Amiet can be used for these cases.[31,33]

The varying circulation due to the rollup phenomena results in much lower velocities near the vortex core than that predicted by the simpler models which do not account for this effect when the circulation of the blade is used to determine the vortex velocity distribution. According to the Betz model the rotational region of the vortex has a large extent which depends on the length of the span from the point of maximum circulation to the tip. Simple vortex models such as the irrotational vortex and the exponential vortex (equations 6.1 and 6.3) are often used for computational investigations of rotor wakes and blade loads. The Betz model with an elliptical blade tip circulation distribution predicts a rotational region of the vortex with a radial extent of 78.5% of the distance from the point of maximum spanwise circulation to the tip of the blade. The circulation trailed from the blade is distributed in this region and the velocity near the center of the vortex is much less than the velocity predicted from the models which do not account for this effect. Measured vortex velocity distributions in this research indicate that this effect is important. This may be why some researchers have found better correlation between measured and computed blade loads when the vortex strength is reduced before the velocity field of the vortex is calculated. The observed effect may actually be the reduction in the circulation of the vortex as the center of the vortex is approached, as predicted by the Betz model, which is not accounted for by the simple vortex models often used for such calculations. The Betz vortex model does not account for the effects of viscosity which dominate the behavior of the flow very near the center of the vortex. Some analytical technique to account for the effect of viscosity on the viscous core region of the Betz vortex would be useful.

The Betz vortex velocity distribution is much more computationally intensive than the simpler models; however, the Betz vortex velocity distribution can be tabulated for a few different blade circulation distributions and only the scale needs to be varied to account for the location of the maximum spanwise circulation (this was done for all of the calculations presented in this thesis since it saves a significant amount of computation time). For final iterations the Betz vortex velocity distribution for the exact tip loading can be calculated if necessary. This technique would require little additional computer time over the simpler models if properly implemented.

Variation in the blade-vortex separation over the span of the blade is significant and the theory of Amiet which accounts for this variation or a modification to the Widnall-Wolf theory to account for this variation would result in a significant improvement. Variation in the blade-vortex interaction angle occurs continuously during the interaction, but the variation in the blade-vortex spacing appears to be a more important effect. Some accounting for blade rotation, even a simple one such as that used in this work (see Appendix A) is necessary if the theories are compared with measured data. The effect of three dimensional flow near the tip of the blade on the behavior of the lift fluctuation due to the blade vortex interaction should be investigated since the tip region is efficient at radiating acoustics to the far-field [59]; however, data from full scale test is in agreement with the shape predicted by the Widnall-Wolf theory so the tip effect may not be as important as for the low speed model test of this research.

The rotating hot-wire rake is an excellent tool for determining the velocity field of rotor vortices and other phenomena. The applicability of the technique to further rotor testing should be considered. Difficulties with wire breakage, primarily due to the high concentration of fiberglass "dust" from the acoustic treatment in the wind tunnel, was the primary problem with the technique. The technique is certainly useful for investigating a variety of flows, not just rotor wake characteristics. Application of the technique to full scale tip speeds may be difficult due to the wire breakage problem, however, and the technique is not inherently safe since a failure could easily cause severe damage to the test apparatus if the probe hits the blade.

Measurements taken with laser anemometers provide a way to investigate the flow field of the rotor without intruding on the flow or risking damage to the rotor. When using the laser velocimeter technique the amount of scatter in the data points must be considered to determine whether the variation in the vortex position is significant. If this variation is large then the use of two or more closely spaced simultaneous measurement positions might be used to determine the vortex position as well as the velocities so that the variation in vortex position can be accounted for. Laser velocimeter measurements, such as those of Biggers, Lee, and Orloff [39], could also be used to determine the blade-vortex interaction geometry.

References

1. Schmitz F.H. and Boxwell D.A.: "In-Flight Far Field Measurement of Helicopter Impulsive Noise". Journal of the American Helicopter Society, Vol. 21, No. 4, October 1976.

2. Schmitz F.H. and Y.H. Yu: "Theoretical Modeling of High Speed Helicopter Impulsive noise". Presented at the Third European Rotorcraft and Powered Lift Aircraft Forum, Aix-en-Provence, France, Sept. 7-9, 1977 (Paper No. 54).

3. Tangler J.L.: "Schlieren and Noise Studies of Rotors in Forward Flight". Presented at the Thirty-third Annual National Forum of the American Helicopter Society, Washington, D.C., May 1977.

4. Farassat, F.: "Theory of Noise Generation from Moving Bodies with an Application to Helicopter Rotors". NASA Technical Report, TR R-451, Langley Research Center, December 1975.

5. Vause. C.R., Schmitz F.H., and Boxwell, D.A.: "High Speed Helicopter Impulsive Noise". Preprint No. 1004, Presented at the Thirty-second Annual National Forum of the American Helicopter Society, May 1976.

6. Baush, W.E., Munch, C.L., and Schlegel: "An Experimental Study of Helicopter Impulsive Noise. USAAVLABS Technical Report 70-72, June 1971.

7. George, A.R. and Chang, S.-B.: "Flow Field and Acoustics of Two-Dimensional Transonic Blade Vortex Interactions". AIAA/NASA 9th Aeroacoustics Conference, Williamsburg, VA, October 15-17,1984.

8. Krothapalli, A. and Smith C.A. (Editors): "Recent Advances in Aeroacoustics". Proceedings of an International Symposium held at Stanford University, August 22-26, 1983. c 1986, Springer-Verlag, New York, New York.

9. Chu, S.: "Helicopter Noise Due to Blade/Vortex Interaction". Master's Thesis, MIT, Department of Aeronautics & Astronautics, June 1971.

10. Widnall, S.E., Chu, S., and Lee A.: "Theoretical and Experimental Studies of Helicopter Noise due to Blade- Vortex Interaction:. Presented at the Helicopter Noise Symposium, Durham, North Carolina, September 1971.

11. Widnall, S.E.: "Helicopter Noise Due to Blade-Vortex Interaction". Journal of the Acoustical Society of America, Vol. 50, No. 1, Part 2, 1971.

12. Hubbard, J.E. Jr. and Leighton K.P.: "A Comparison of Model Helicopter Rotor Primary and Secondary Blade/Vortex Interaction Blade Slap". Presented at the 8th AIAA Aeroacoustics Conference, Atlanta, Georgia, April 11-13, 1983.

13. Hubbard. J.E. Jr. and Leighton. K.P.: "Some Results of a Preliminary Investigation of Model Helicopter Rotor Secondary Blade Slap". Presented at the National Technical Association Region II Student Symposium. Hampton, Virginia, March 1980.

14. Hubbard, J.E. Jr., Humbad, N.G., Bauer, P.,and Harris, W.L.: "Parametric Studies of Model Helicopter Blade Slap and Rotational Noise". MIT Fluid Dynamics Research Laboratory Report No. 79-1, Cambridge, MA, February 1979.

15. Hubbard, J.E. Jr. and Harris W.L.: "An Investigation of Model Helicopter Rotor Blade Slap at Low Tip Speeds". Presented at the AIAA Fifth Aeroacoustics Conference, Seattle, WA, March 1979.

16. Hubbard J.E. Jr.: "A Parametric Study of Model Helicopter Blade Slap". Master's Thesis, MIT, Department of Mechanical Engineering, 1978.

17. Fujita, H. and Kovasznay, L.S.G.: "Unsteady Lift and Radiated Sound from a Wake Cutting Airfoil". AIAA Journal, p. 1216, September 1974.

18. Booth, E.R. Jr. and Yu, J.C.: "Two Dimensional Blade-Vortex Interaction Flow Visualization Investigation". AIAA/NASA 9th Aeroacoustics Conference, Williamsburg, VA, October 15-17, 1984.

19. Martin, R.M., Elliot, J.W., and Hoad, D.R.: "Comparison of Experimental and Analytical Predictions of Rotor Blade-Vortex Interactions Using Model Scale Acoustic Data". AIAA/NASA 9th Aeroacoustics Conference, Williamsburg, VA, October 15-17, 1984.

20. Schmitz, F.H., Boxwell, D.A., Lewey, S., and Dahan, C.: "Model-to Full-Scale Comparisons of Helicopter Blade-Vortex Interaction Noise". Presented at the 38th Annual National Forum of the American Helicopter Society, Anaheim, CA, May 1982

21. Cox, C.R.: "Helicopter Aerodynamics and Aeroacoustic Environments". Presented at the AIAA Fourth Aeroacoustics Conference, Atlanta, Georgia, October 1977.

22. Nakamura, Y.: "Prediction of Blade-Vortex Interaction Noise From Blade Pressure". Presented at the Seventh European Rotorcraft and Rotor Powered Lift Forum, Garmisch-Partenkirchen, Federal Republic of Germany, September 1981 (Paper No. 32).

23. Hubbard, J.E. Jr. and Harris, W.L.: "Measured Surface Pressure and Velocity Trends on a Highly Loaded Model Helicopter Rotor Experiencing Blade Slap". Fluid Dynamics Research Lab Report 81-6, MIT, Cambridge, Massachusetts, October 1981.

24. Widnall, S.E. and Wolf T.L.: "Effect of Tip Vortex Structure on Helicopter Noise due to Blade-Vortex Interaction". Journal of Aircraft, Vol. 17, No. 10, p. 705, October 1980.

25. Wolf, T.L.: "The Effect of Tip Vortex Structure on Helicopter Noise Due to Blade/Vortex Interaction". Master's Thesis. MIT, Department of Aeronautics & Astronautics, June 1978.

26. Fontana, R.R.: "A Determination of Flow Field Characteristics Responsible for Model Helicopter Rotor Blade Vortex Interaction Noise and a Comparison with Theory". Master's Thesis, MIT, Department of Mechanical Engineering, September 1983.

27. Fontana, R.R. and Hubbard, J.E. Jr.: "A Comparison with Theory of Peak to Peak Sound Level for a Model Helicopter Generating Blade Slap at Low Tip Speeds". Ninth European Rotorcraft and Powered Lift Aircraft Forum, Stresa, Italy, September 1983.

28. Fontana, R.R. and Hubbard, J.E. Jr.: "A Comparison with Theory of Peak-to-Peak Sound Level for a Model Helicopter Rotor Generating Blade Slap at Low Tip Speeds". Vertica, The International Journal of Rotorcraft and Powered Lift Aircraft, Vol. 9, No. 2, 1985.

29. Chan, D.C-l. and Hubbard, J.E. Jr: "Model Helicopter Blade Slap at Low Tip Speeds: Theoretical and Experimental Correlations, Presented at the 41st AHS Forum, May 15-17,1985, Fort Worth, TX.

30. Chan, D.C-1: "A Correlation with Theory and experiments using Measured Blade Loads on a Model Helicopter Rotor Generating Blade Slap at Low Tip Speeds". Master's Thesis, MIT, Department of Aeronautics and Astronautics, September 1984.

31. Martinez, R. and Widnall, S.E.: "An Aeroacoustic Model for High-Speed, Unsteady Blade-Vortex Interaction". AIAA Journal, Vol. 21,No. 9, p. 1225, September 1983.

32. Martinez, R. and Widnall, S.E.: "Unified Aerodynamic-Acoustic Theory for a Thin Rectangular Wing Encountering a Gust". AIAA Journal, Vol. 18,No. 6, p. 636, [Article No. 80-4055].

33. Amiet, R.K.: "Airfoil Gust Response and the Sound Produced by Airfoil-Vortex Interaction". AIAA/NASA 9th Aeroacoustics Conference, Williamsburg, VA, October 15-17, 1984.

34. Schlinker, R.H. and Amiet, R.K.: "Tail Rotor Blade-Vortex Interaction Noise". Presented at the 8th AIAA Aeroacoustics Conference, Palo Alto, California, October 1981 (Preprint No. 18-2002).

35. Hardin, J.C. and Lamkin, S.L.: "Aeroacoustic Interaction of a Distributed Vortex with a Lifting Joukowski Airfoil". AIAA/NASA 9th Aeroacoustics Conference, Williamsburg, VA, October 15-17, 1984.

36. Tung, C., Pucci, S.L., Caradonna, F.X., and Morse, H.A.: "The Structure of Trailing Vortices Generated by Model Rotor Blades". Vertica, Vol. 7, No. 1, pp. 33-43, 1983.

37. Chigier, N.A. and Corsiglia, V.R.: "Tip Vortices - Velocity Distributions". Presented at the 27th Annual National V/STOL Forum of the American Helicopter Society, Washington, D.C., May 1971.

38. Tangler, J.L.: "Experimental Investigation of the Subwing Tip and Its Vortex Structure". NASA Contractor Report 3058, 1978.

39. Biggers, James C., Lee, Albert, Orloff, Kenneth L., Lemmer, Opal J., "Measurements of Helicopter Rotor Tip Vortices", Preprint No. 77.33-06, Presented at the 33rd Annual National Forum of the American Helicopter Society, Washington, D.C., May 1977

40. Coles, D. and Wadcock, A.J.: "Flying-Hot-Wire Study of Flow Past an NACA 4412 Airfoil at Maximum Lift". AIAA Journal, Vol. 17, No. 4, April 1979.

41. Wadcock, A.J.: "Two-Dimensional Stalled Airfoil". AFOSR-HTTM-Stanford Conference on Complex Turbulent Flows, Vol. 1, p. 234, 1980-81.

42. Coles, D., Cantwell, B., Wadcock, A.: "The Flying Hot Wire and Related Instrumentation". NASA CR Report 3066, 1978.

43. Corsiglia. V.R., Schwind. R.G., and Chigier. N.A.: "Rapid Scanning. Three-dimensional Hot-Wire Anemometer Surveys of Wing-tip Vortices". Journal of Aircraft. Vol. 10. No. 12. pp. 752-757, December, 1973.

44. Miller, R.H.: "The Aerodynamics and Dynamics of Rotors - Problems and Perspectives". International Symposium on Recent Advances in Aerodynamics and Aeroacoustics, Stanford, CA, August 22-26, 1983.

45. Betz, A.: "Behavior of Vortex Systems". NACA TM 713, 1932.

46. Rossow, V.: "On the Inviscid Rolled-up Structure of Lift Generated Vortices". Journal of Aircraft, November 1973.

47. Filotas L.T.: "Theory of Airfoil Response in a Gusty Atmosphere - Part I, Aerodynamic Transfer Function". UTIAS Report No. 139, University of Toronto, October 1961.

48. Leighton, K.P.: "A Parametric Study of Model Helicopter Rotor Blade Slap at Moderate Tip Speeds". Master's Thesis, MIT, Department of Aeronautics and Astronautics, February 1981.

49. Widnall. S.E., Harris. W.L., Lee, A., and Drees, H.M.: "The Development of Experimental Techniques for the Study of Helicopter Rotor Noise". NASA CR-137684, 1974.

50. Harris, W.L. and Lee, A.: "The Development of Experimental Techniques for the Study of Helicopter Rotor Noise". Presented at the AIAA Second Aeroacoustics Conference, March 1975.

51. Breuer, K.S.: "An Experimental Investigation into Transitional Pipe Flow". MIT Fluid Dynamics Research Report, No. 85, January 1985.

52. Blackwelder, R.F.: "Hot-Wire and Hot-Film Anemometers". Methods of Experimental Physics: Fluid Dynamics, Vol. 18, part A, Academic Press, Inc, N.Y., 1981.

53. Perry, A.E.: "Hot Wire Anemometry". Oxford Science Publications, 1982.

54. McCroskey, W.J. and Pucci, S.L.: "Viscous-Inviscid Interaction on Oscillating Airfoils". AIAA 19th Aerospace Sciences Meeting, St. Louis, Missouri, Paper No. 81-0051, January 12-15, 1981.

55. Blackwelder, R.F.: "Boundary Layer Transition". Research Note, pp.583, Physics of Fluids, vol. 22, March 1979.

56. Ho, C-M, and Huerre, P.: "Perturbed Free Shear Layers". Annual Reviews of Fluid Mechanics, 16:365-424, #0066-4189/84/0115-0365, 1984.

57. Goldstien, R.J.: "Fluid Mechanics Measurements". pp. 371, Copyright 1983, Hemisphere Publishing Co.

58. Bisplinghoff, R. L., Ashley, H., Halfman, R. L.: "Aeroelasticity". PP. 272, Copyright 1955, Addison-Wesley Publishing Co.

59. Humbad, N. G., Harris, W. L.: "On the Acoustic Power Emitted by Helicopter Rotor Blades at Low Tip Speeds." Journal of Sound and Vibration, Vol. 66, No. 2, p. 290, 1979.

APPENDIX A

An Approximate Method to Account for the Effect of Blade Rotation on the Interaction Length and Efficiency of Acoustic Radiation

The interaction length is not accurately defined without accounting for the blade rotation since essentially the entire span interacts with the vortex. The effect of the variation in the blade Mach number over the blade span on the efficiency of the far-field acoustic radiation is not accounted for in the original formulation of the Widnall-Wolf model. The velocity over the inboard section of the blade is much less than that at the tip. This reduces the effective lift fluctuation and the acoustic efficiency of this part of the blade. The following derivation is basically similar to the derivation in Appendix 2 of reference [26] except it is extended to account for the efficiency of the acoustic radiation as well as the effect of blade rotation on the fluctuating lift. It is not intended to be a rigorous technique that accounts for the details of the blade rotation, but is an approximate technique that is usable as a first order solution to the problem of blade rotation. In reference [26] there is an error in the equations. The sine term in the imaginary part should be divided by the denominator of the cosine term and the cosine term is not divided by that term. The equations presented here are correct and supersede the original formulation.

The vortex interacts with essentially the entire span of the blade; however, the inner span is not moving through the fluid as quickly as the tip. The upwash velocity induced by the blade is assumed to be essentially the same over the span of the blade, but the blade velocity varies over the span. For a vertical upwash velocity w the angle of attack changed induced by w depends on the velocity U of the airfoil through the upwash as shown below:

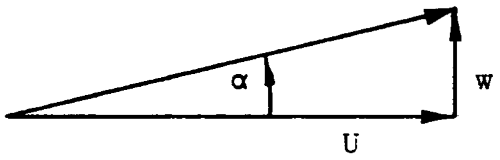

$$\alpha = \arctan(w/U)$$

Figure A1. Angle of Attack Due to Vertical Upwash w.

The lift coefficient C_L is related to the angle of attack, α, to the first order by the relation $C_L = k \cdot \alpha$ where k is constant. Then the lift is approximately described by the relation $L = K \cdot U^2 \cdot C_L$ where K is constant. For small angles

$$\tan(\alpha) \approx \alpha \text{ and } \tan(\alpha) \approx w/U$$

therefore $L \approx K \cdot U \cdot w$. (A1)

To the first order the fluctuating lift produced by the upwash is then linearly dependant on the velocity.

For a rotating rotor blade in a freestream the primary streamwise velocity fluctuations are dominated by the rotor rotation since $U = R \cdot \Omega + V_{free\ stream}$. Where R is the position along the span of the blade.

The Widnall-Wolf model applies the calculated fluctuating lift to an acoustic dipole with a length equal to the interaction length. From reference [25] this dipole and boundary conditions are described as

$$\text{for } x < s_0;\quad p^-(x,y,0)-p^+(x,y,0)=L(t-x/U_c)\ \delta\{b_0(y-t)\}$$

$$\text{for } x > s_0;\quad p^-(x,y,0)-p^+(x,y,0)=0 \qquad \text{(A2)}$$

where x is the position along the line of acoustic dipoles, the interaction length is $2s_0$, $L(t-x/U_c)$ is the lift function, U_c is the nondimensionalized convection velocity of the vortex along the blade span, and δ is the delta function. It is apparent from equation (A1) that the effect of the variation in the velocity over the span of the blade is to reduce the lift linearly from the tip of the blade to the root of the blade. This can be done by multiplying the lift function by the tapering function T(x). The new boundary conditions become

$$\text{for } x < s_0;\quad p^-(x,y,0)-p^+(x,y,0)=T(x)\cdot L(t-x/U_c)\ \delta\{b_0(y-t)\}$$

$$\text{for } x > s_0;\quad p^-(x,y,0)-p^+(x,y,0)=0 \qquad \text{(A3)}$$

where the convection velocity U_c is constant and the variation in the velocity over the span of the blade is accounted for by the tapering function T(x) on the acoustic dipole. Given a function T(x) the boundary conditions can be applied and the integrals of reference [25] can be reevaluated. Before this is actually done another effect is considered.

The velocity U_c is related to the Mach number of the flow and the Mach number has a strong effect on the efficiency of the radiation to the far-field. Equation (3.26) of reference [25] shows that the Mach number is involved in many of the terms and allowing it to vary increases the complexity of the mathematics significantly; however, the Mach number also multiplies the entire equation linearly. Reducing the Mach number therefore reduces the amplitude of the radiated acoustics. The effect of the variation in the speed of the blade due to rotation is to reduce the effective acoustic radiation from the inboard sections as well as reduce the fluctuating lift as previously described. This effect can be accounted for to the first order by holding the Mach number constant in the more complex part of the equations and applying a correction to the strength of the acoustic dipole to account for the variation in the Mach number in a manner similar to that previously done for the fluctuating lift.

Applying a linear correction to account for the variation in the Mach number and a linear correction to account for the fluctuating lift results in a net tapering function T(x) which is parabolic.

The Fourier Transform of the boundary conditions is taken as given in reference [25] equation (3.5).

$$\Delta P(k_x, k_y, S) = \int_{-\infty}^{\infty}\int_{-\infty}^{\infty}\int_{-s_0}^{s_0} T(x)\cdot L(t-x/U_c)\cdot\delta(b_0(y-t))$$

$$\cdot\exp[-ik_x x-ik_y y+iSt]\ dx\ dy\ dt \qquad (A4)$$

Integration over y and t is not effected by the addition of T(x) and the result is

$$\Delta P(k_x, k_y, S) = \frac{2\pi}{b_0} \cdot L_0(\tilde{s}) \int_{-s_0}^{s_0} T(x) \cdot \exp[i(\tilde{s}/U_c - k_x)x]\ dx$$

where L_0 is the lift transform

$$L_0(\tilde{s}) = \frac{1}{2\pi} \int_{-\infty}^{\infty} L(t')\ \exp[i\tilde{s}t']\ dt' \qquad \text{(A5)}$$

The final integration requires the function T(x) to evaluate the integral. The function $T(x) = \delta x^2 + \alpha x + \beta$ is chosen to represent the effects of the blade rotation on the amplitude of the fluctuating lift and amplitude of the radiated acoustics and the equation becomes

$$\Delta P(k_x, k_y, S) = \frac{2\pi}{b_0} \cdot L_0(\tilde{s}) \int_{-s_0}^{s_0} (\delta x^2 + \alpha x + \beta) \cdot \exp[i(\tilde{s}/U_c - k_x)x]\ dx\ .$$

Substituting $\Theta = (\tilde{s}/U_c - k_x)$ produces

$$\Delta P(k_x, k_y, S) = \frac{2\pi}{b_0} \cdot L_0(\tilde{s}) \left[\int_{-s_0}^{s_0} \delta x^2\ \exp[i\Theta x]\ dx + \int_{-s_0}^{s_0} \alpha x\ \exp[i\Theta x]\ dx \right.$$

$$\left. + \int_{-s_0}^{s_0} \beta\ \exp[i\Theta x]\ dx \right] . \qquad \text{(A6)}$$

Equation (A6b) is equivalent to the original formulation of Widnall and Wolf if δ and α are set equal to zero and β is set equal to 1. The integrals are evaluated by successive integration by parts which leads to the result

$$\Delta P(k_x, k_y, S) = \frac{-1}{(2\pi)^2 b_0} \int_{-\infty}^{\infty}\int_{-\infty}^{\infty}\int_{-\infty}^{\infty} L_0(\tilde{s}) \cdot \Big[(2\beta/\Theta)\sin(\Theta s_0)$$

$$+ (2\alpha i/\Theta) \cdot \{\sin(\Theta s_0)/\Theta - s_0\cos(\Theta s_0)\}$$

$$+ (2\delta/\Theta) \cdot [(s_0{}^2 \sin(\Theta s_0) + (2s_0/\Theta) \cdot \cos(\Theta s_0) - (2/\Theta^2) \cdot \sin(\Theta s_0)]\Big]$$

$$\cdot \exp[iz \cdot (k^2 - k_x{}^2 - k_y{}^2)^{1/2}]$$

$$\cdot \exp(i(k_x x + ik_y y - iSt)\ dk_x\ dk_y\ dS \quad . \qquad (A7)$$

The method of stationary phase is applied as in reference [25] by substituting the new version of $F(k_x, k_y, S)$ which is

$$F(k_x, k_y, \tilde{s}) = \frac{-2}{(2\pi)^2 b_0} \frac{L_0(\tilde{s})}{\Theta} \Big[\beta\sin(\Theta s_0)$$

$$+ i\alpha \cdot \{\sin(\Theta s_0)/\Theta - s_0\cos(\Theta s_0)\}$$

$$+ \delta \cdot \{s_0{}^2 \sin(\Theta s_0) + (2s_0/\Theta) \cdot \cos(\Theta s_0) - (2/\Theta^2) \cdot \sin(\Theta s_0)\}\Big]$$

where $\Theta = (\tilde{s}/U_c - k_x)$.

The result is easily extended to a polynomial tapering function T(x) of any order by successive integration by parts. Some other function T(x) could be used for tapering if desired. For the parabolic profile the coefficients used are:

$$\delta = 1/(4s_0^2)$$

$$\alpha = 1/(2s_0)$$

$$\beta = 1/4 \quad .$$

This produces the weighted acoustic dipole as diagrammed below.

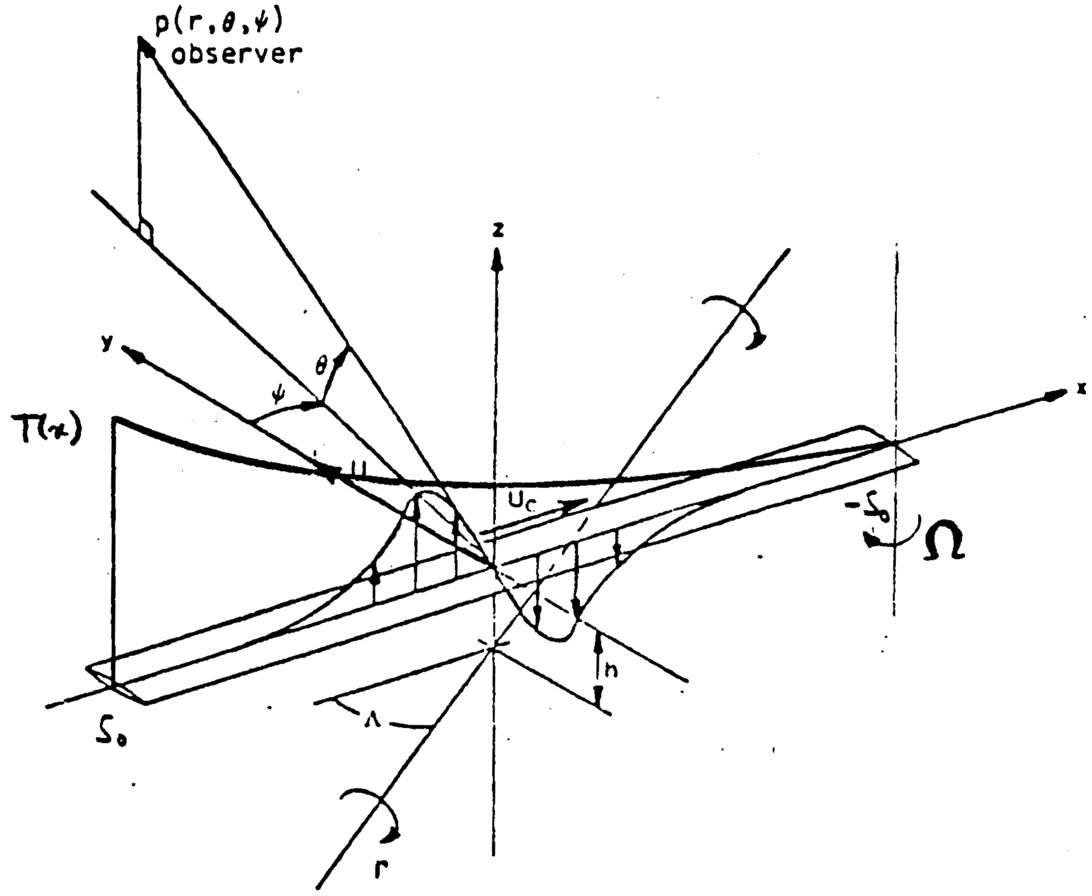

APPENDIX B

Corrections to the Widnall-Wolf Theory as Presented in Reference [25]

Errors found in reference [25] during this research are summarized below. All equation numbers refer to the equations in reference [25]. In order to match the coordinate system, equation 2.7 should be:

$$t' = -\xi'\cos(\lambda) \qquad (2.7)$$

which means equation 2.8 should be

$$W(S) = W_0^*(\sigma)/\cos(\lambda) \qquad (2.8)$$

(where * represents the complex conjugate)

which then appears indirectly in the form of equation (2.10).

In equation (3.6) the "y" should be a "t" since the "y" integration has been done at this point.

Equation (3.9) should be multiplied by $1/b_0$.

Equation (3.24) should be multiplied by negative one.

The most significant effect is produced by the implementation of equation (2.8) and the sign in equation (3.24). If these corrections are not made then the errors cancel each other and the final answer is correct, but the intermediate results are affected , and modifications such as substituting the spectrum of the measured lift without taking these corrections into account will result in erroneous results. All results were checked for the modified codes used in this work. Since all of the input values, such as the vortex induced upwash, are real in the time domain, all of the final results must also be real in the time domain. This serves as a useful quick check when making modifications to the Widnall-Wolf theory.

APPENDIX C

Determination of the Fluctuating Lift from the Measured Pressure

The measured pressure at the leading edge is used to determine the fluctuating lift at that spanwise location which is then substituted for the calculated lift in the Widnall-Wolf theory to predict the acoustics from the measured blade pressure. In order to do this the total lift must be calculated from the measured pressure difference at the location of the leading edge pressure transducer (18.75% chord). This was done assuming that the chordwise lift distribution is self similar with a distribution as described by linear theory. The pressure difference at any chordwise location from the leading edge is

$$\Delta p(x) = 4q_{\infty}\alpha((c-x)/x)^{1/2} \, . \qquad \text{(C1)}$$

The total lift L' is defined by $L' = q_{\infty}\, C\, 2\pi\alpha$.
Substituting to get L' in terms of Δp gives the result

$$L' = \pi\, \Delta p(x) \cdot c/(2((c-x)/x)^{1/2}) \, . \qquad \text{(C2)}$$

This equation is used with x= 18.75% of c and c = 2 inches to determine an estimate for the lift L' given the measured leading edge differential pressure.

TABLE I

BLADE CHARACTERISTICS

SECTION	CHORD	TWIST	EFFECTIVE LIFTING SPAN
NACA 0012	2 INCHES	-8 DEGREES	20 INCHES

B0 = ONE BLADE SEMICHORD = 1 INCH

ROTOR CHARACTERISTICS FOR TESTED CONDITIONS

ROTOR DIAMETER	BLADE TIP PITCH	ROTOR RPM
52.25 INCHES	+5 DEGREES	800 RPM

MICROPHONE POSITION: 52.5 INCHES ABOVE THE ROTOR HUB

CORRESPONDING MICROPHONE POSITION IN WIDNALL-WOLF THEORY
(SEE FIGURE 10)

RADIUS	THETA	PSI	INTERACTION LENGTH	(S_0)
56 INCHES	-74 DEGREES	90 DEGREES	20 INCHES	(10 INCHES)

ALL MEASURED VORTEX PARAMETERS USE MODIFIED BETZ VORTEX MODEL

ADVANCE RATIO = .19; AZIMUTH OF BVI = 40 DEGREES
BLADE-VORTEX SPACING = 1.7 SEMICHORDS NEAR THE TIP
INTERACTION ANGLE= 0 DEGREES
VORTEX PARAMETERS: GAMMA = 9.9 FT^2/SEC; C_0 = .100 SEMICHORDS

PEAK SOUND LEVEL	(dB =20 LOG[(DELTAP/2)/.0002 PASCAL])
MEASURED	**86.8**
PREDICTED USING FILOTAS MODEL	82.9
PREDICTED FROM TIP LEADING EDGE PRESSURE	91.4
PREDICTED FROM 76% SPAN LEADING EDGE PRESSURE	89.6
PREDICTED FROM SIMPLE LIFT MODEL	90.2

ADVANCE RATIO = .17; AZIMUTH OF BVI = 45 DEGREES
BLADE-VORTEX SPACING = 0.25 SEMICHORDS NEAR THE TIP
INTERACTION ANGLE= 7 DEGREES
VORTEX PARAMETERS: GAMMA = 10.6 FT^2/SEC; C_0 = .140 SEMICHORDS

MEASURED	**90.4**
PREDICTED USING FILOTAS MODEL	95.8
PREDICTED FROM TIP LEADING EDGE PRESSURE	91.2
PREDICTED FROM 76% SPAN LEADING EDGE PRESSURE	88.2
PREDICTED FROM SIMPLE LIFT MODEL	108.3

ADVANCE RATIO = .15; AZIMUTH OF BVI = 47 DEGREES
BLADE-VORTEX SPACING = 0.25 B0's NEAR THE TIP ON PRESSURE SIDE
INTERACTION ANGLE= 15 DEGREES
VORTEX PARAMETERS: GAMMA = 13.5 FT^2/SEC; C_0 = .137 SEMICHORDS

MEASURED	**90.4**
PREDICTED USING FILOTAS MODEL	94.8
PREDICTED FROM TIP LEADING EDGE PRESSURE	86.7
PREDICTED FROM 76% SPAN LEADING EDGE PRESSURE	88.2
PREDICTED FROM SIMPLE LIFT MODEL	102.9

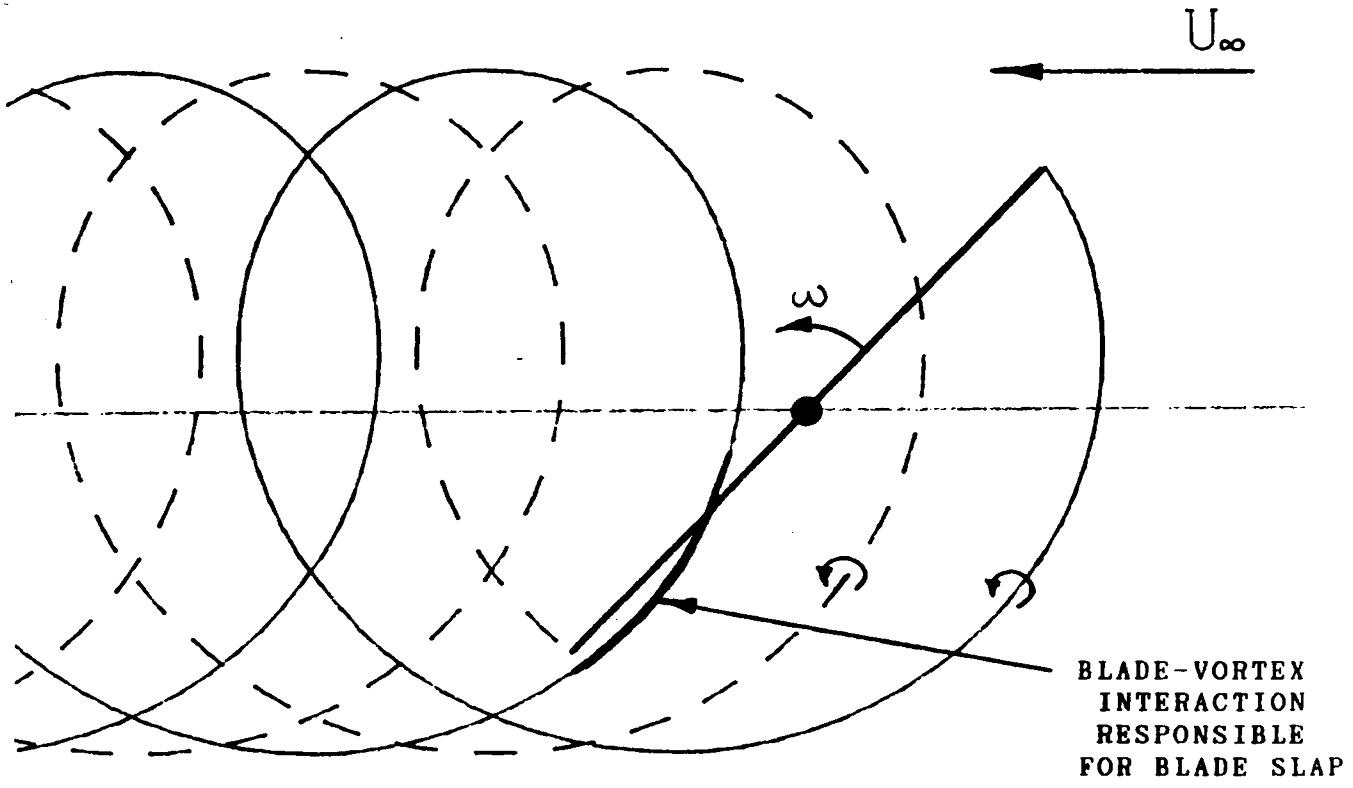

FIGURE 1. RIGID WAKE PLOT FOR ADVANCE RATIO OF 0.17 AT AN AZIMUTH ANGLE OF 45 DEGREES SHOWING BLADE-VORTEX INTERACTION.

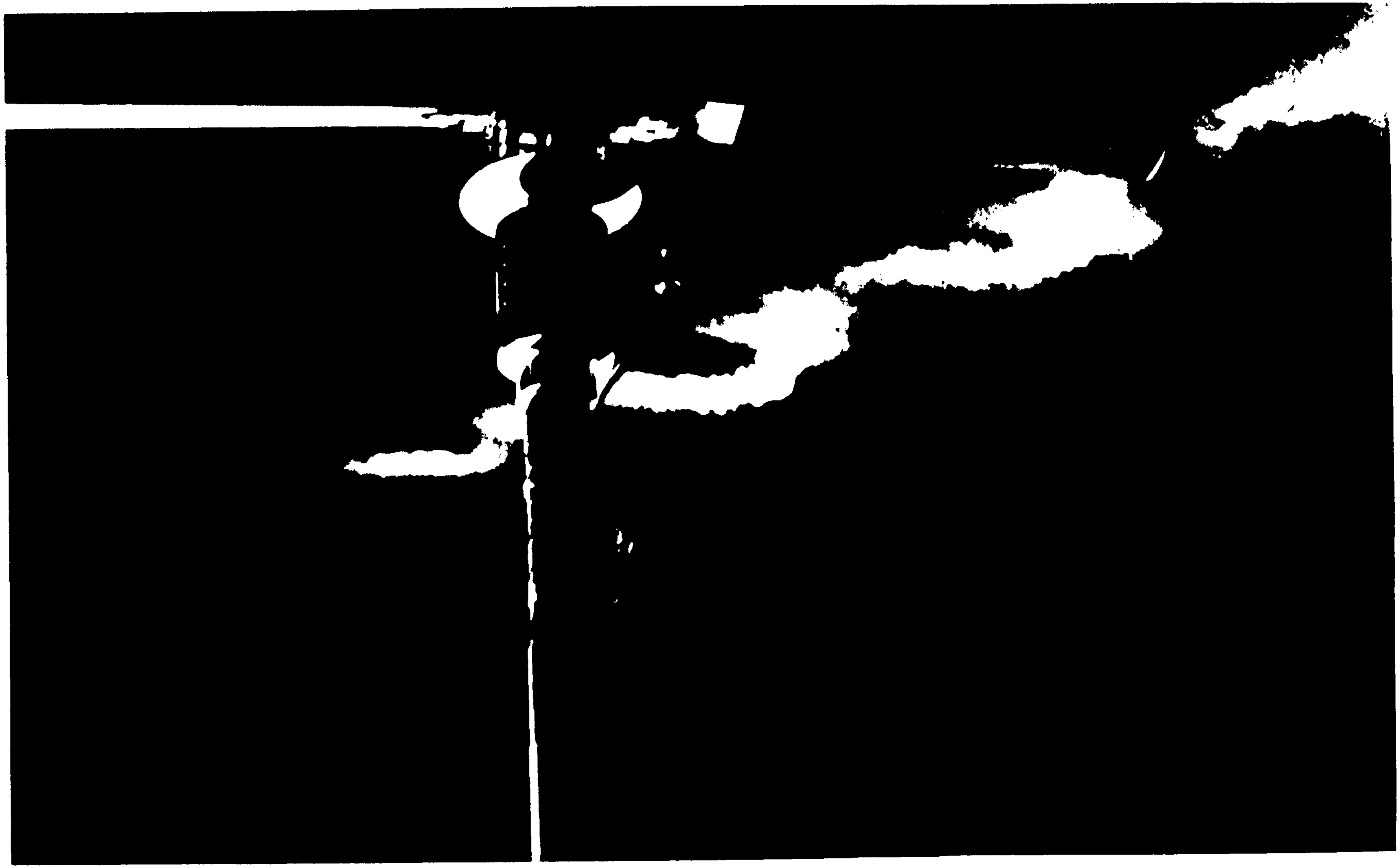

Figure 2. Photograph of the smoke flow visualization taken just before the blade-vortex interaction responsible for blade slap $\mu = .17$ $\Omega = 800\,\text{RPM}$ $\psi_{B.V.I.} = 45°$ $\Theta_T = 5°$

ORIGINAL PAGE IS
OF POOR QUALITY

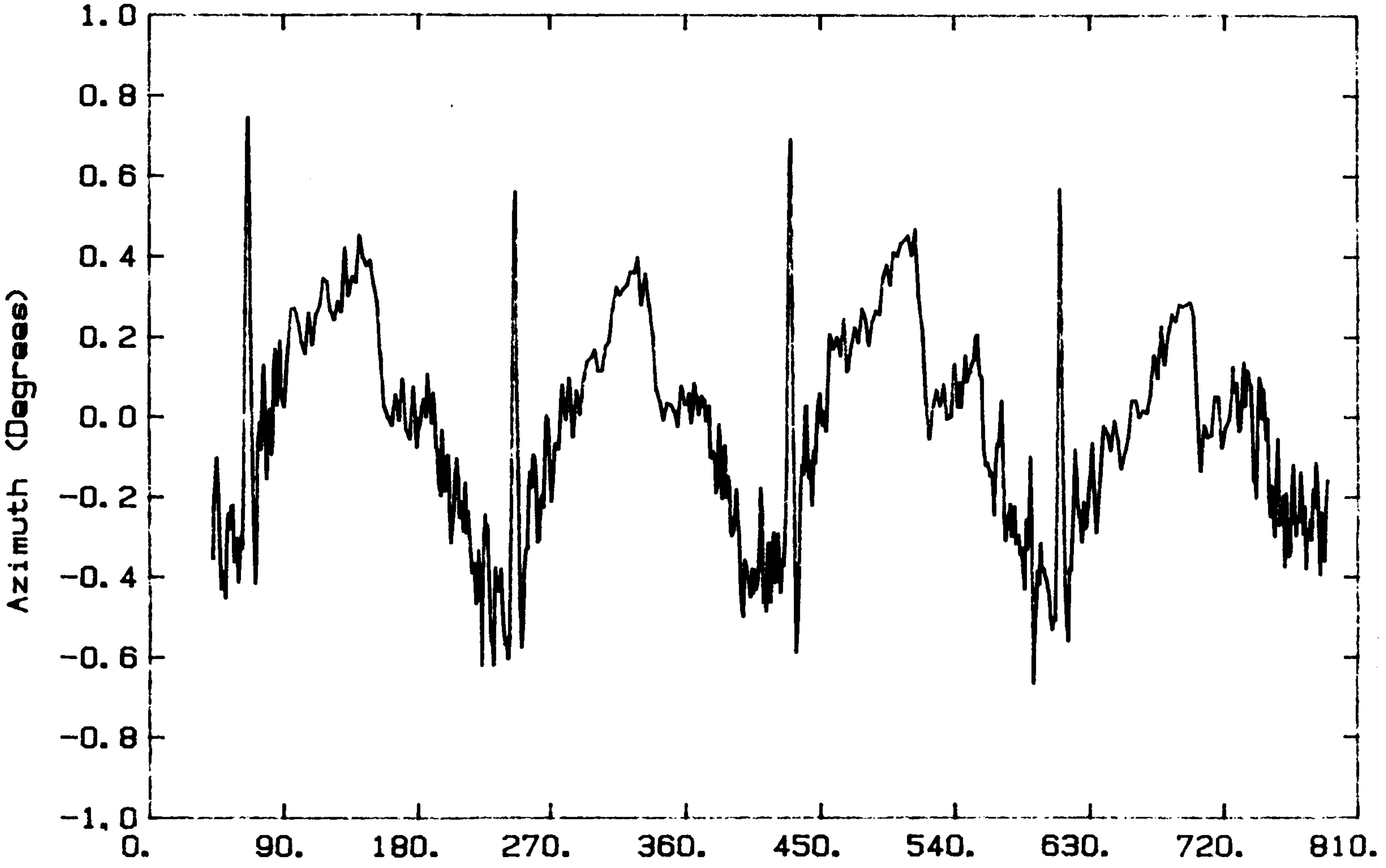

FIGURE 3. MEASURED ACOUSTIC SIGNATURE OF BLADE SLAP AT AN ADVANCE RATIO OF 0.17

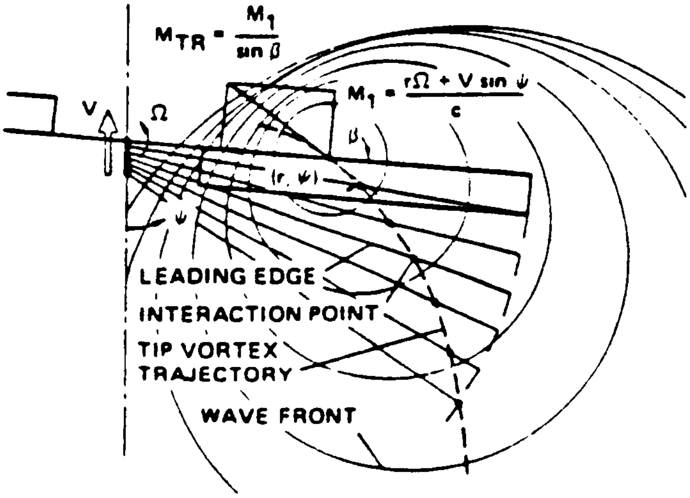

FIGURE 4. TRACE MACH NUMBER IN THE AMBIENT FLUID
[FROM REFERENCE 22]

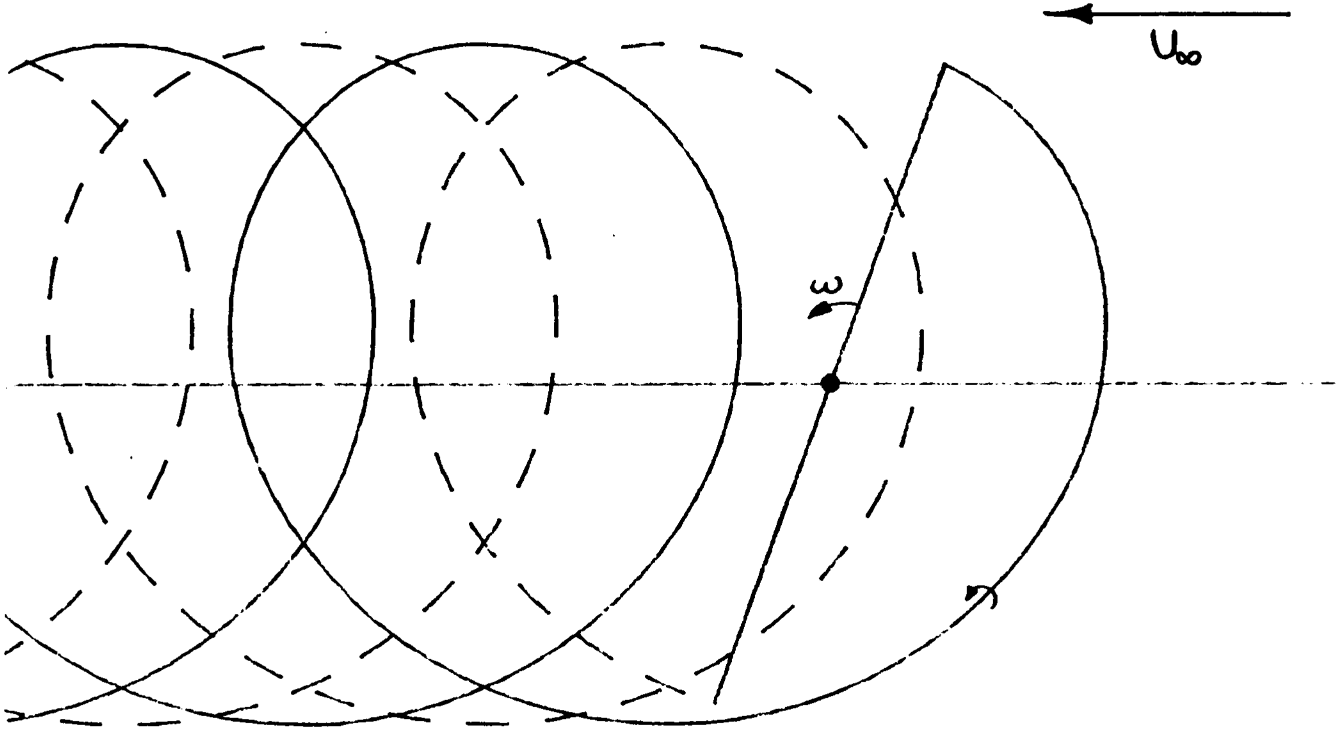

FIGURE 5. RIGID WAKE PLOT FOR ADVANCE RATIO OF 0.17 AT AN AZIMUTH ANGLE OF 70 DEGREES

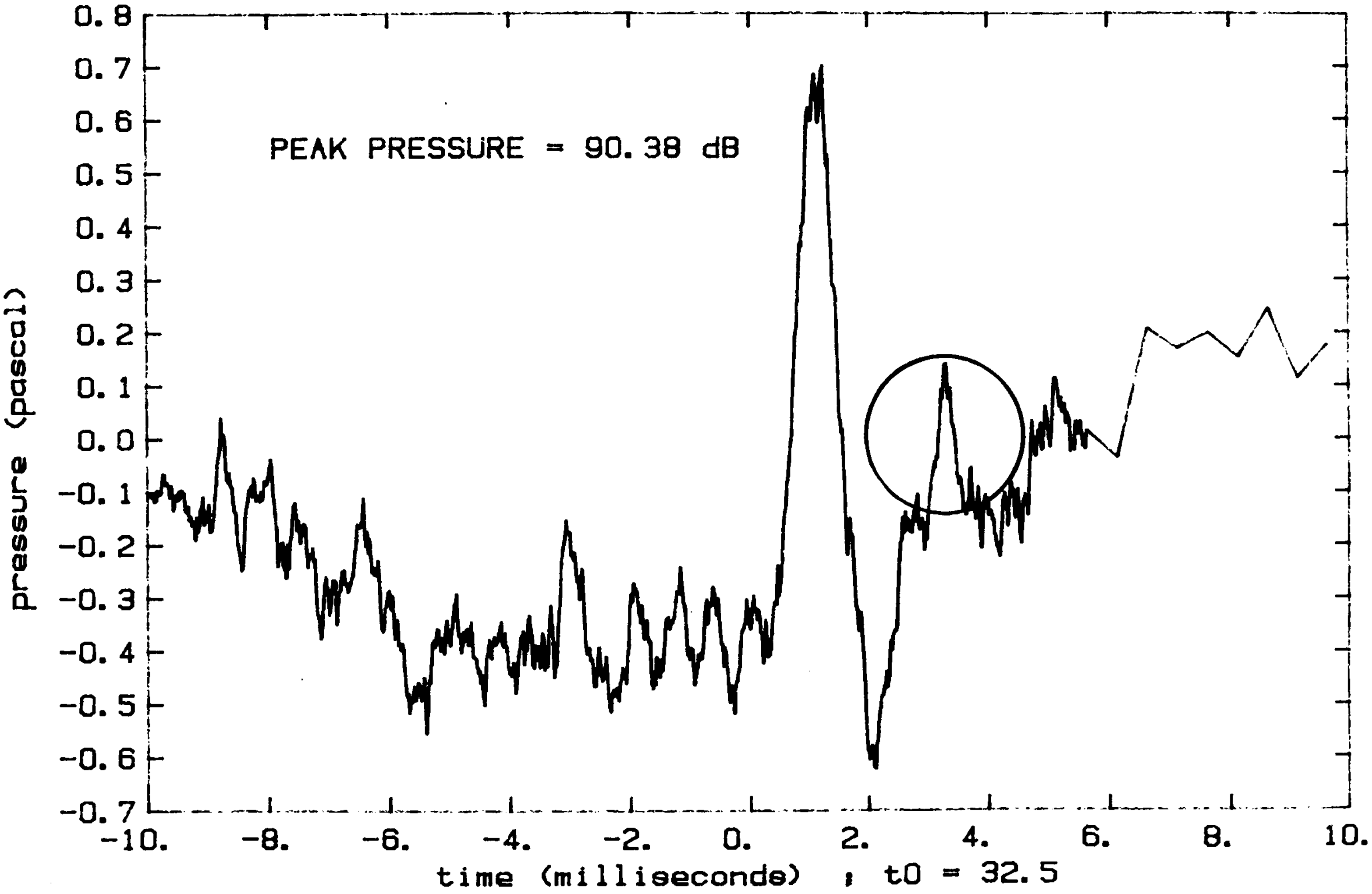

FIGURE 6. MEASURED ACOUSTIC SIGNATURE OF BLADE SLAP PULSE. CIRCLED SMALL PULSE IS ASSOCIATIED WITH THE LARGE ANGLE BLADE-VORTEX INTERACTION

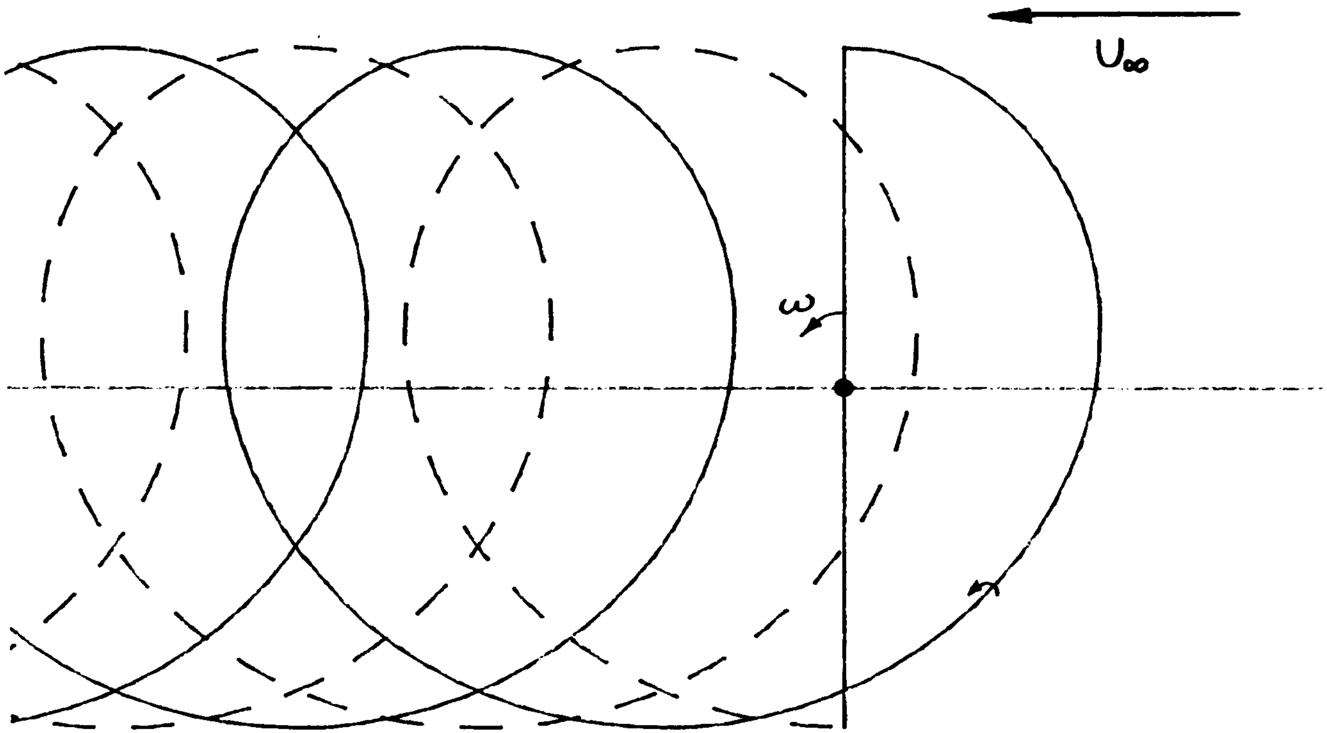

FIGURE 7. RIGID WAKE PLOT FOR ADVANCE RATIO OF 0.17 AT A ROTOR AZIMUTH OF 90 DEGREES.

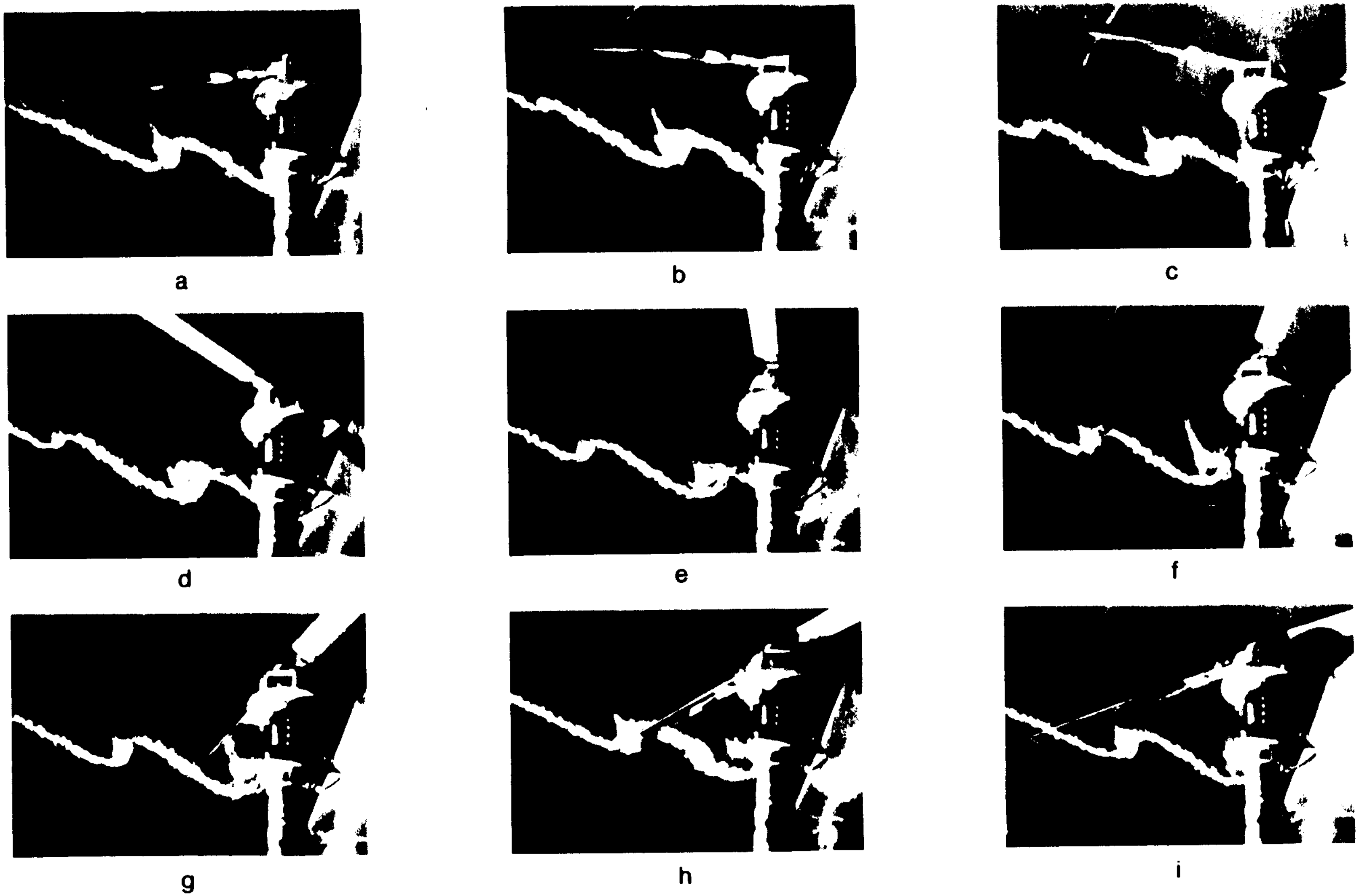

Figure 8. Development of the smoke pattern due to the action of the tip vortices

ORIGINAL PAGE IS
OF POOR QUALITY

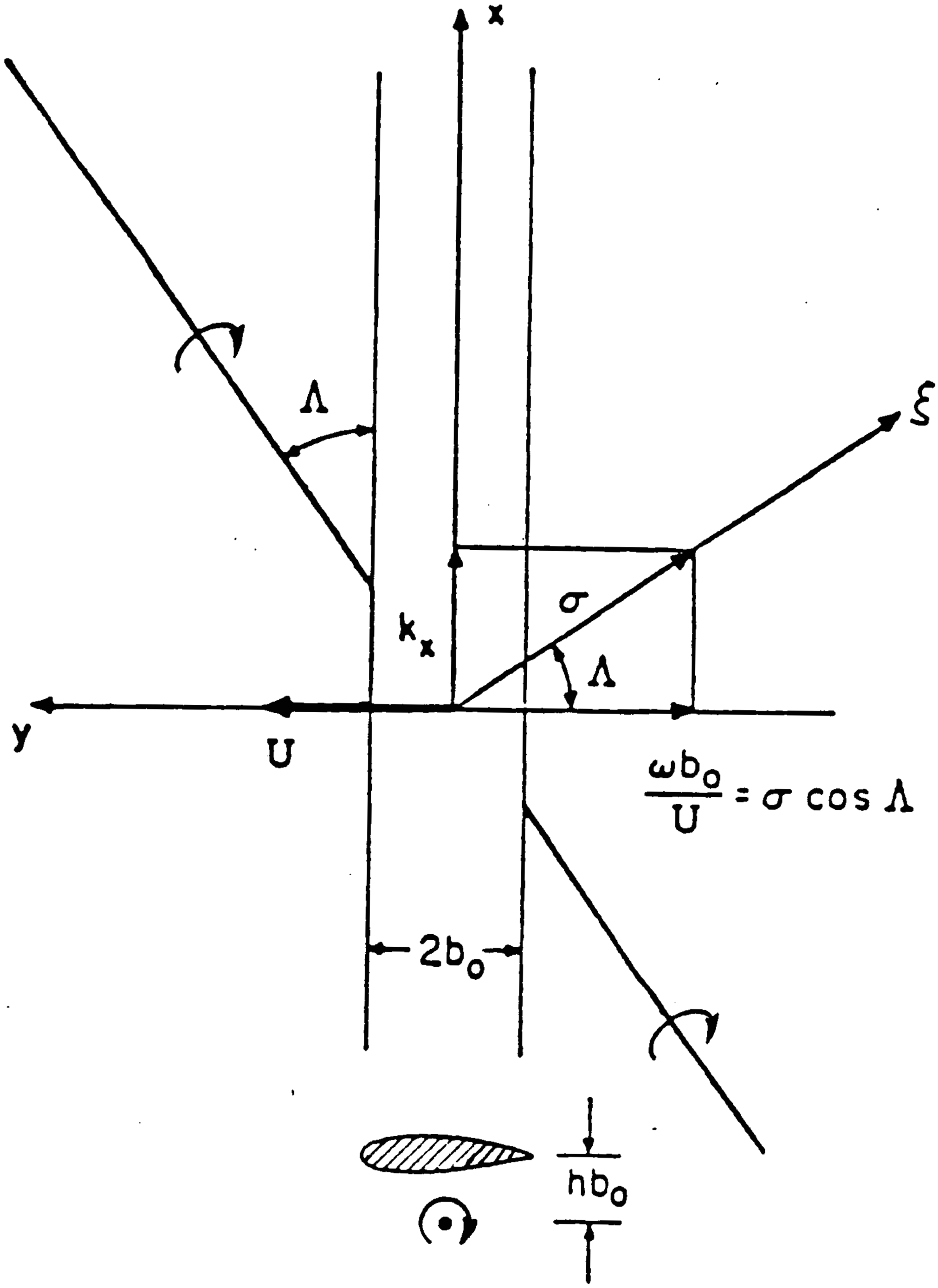

FIGURE 9. GEOMETRY OF BLADE-VORTEX INTERACTION [REFERENCE 25]

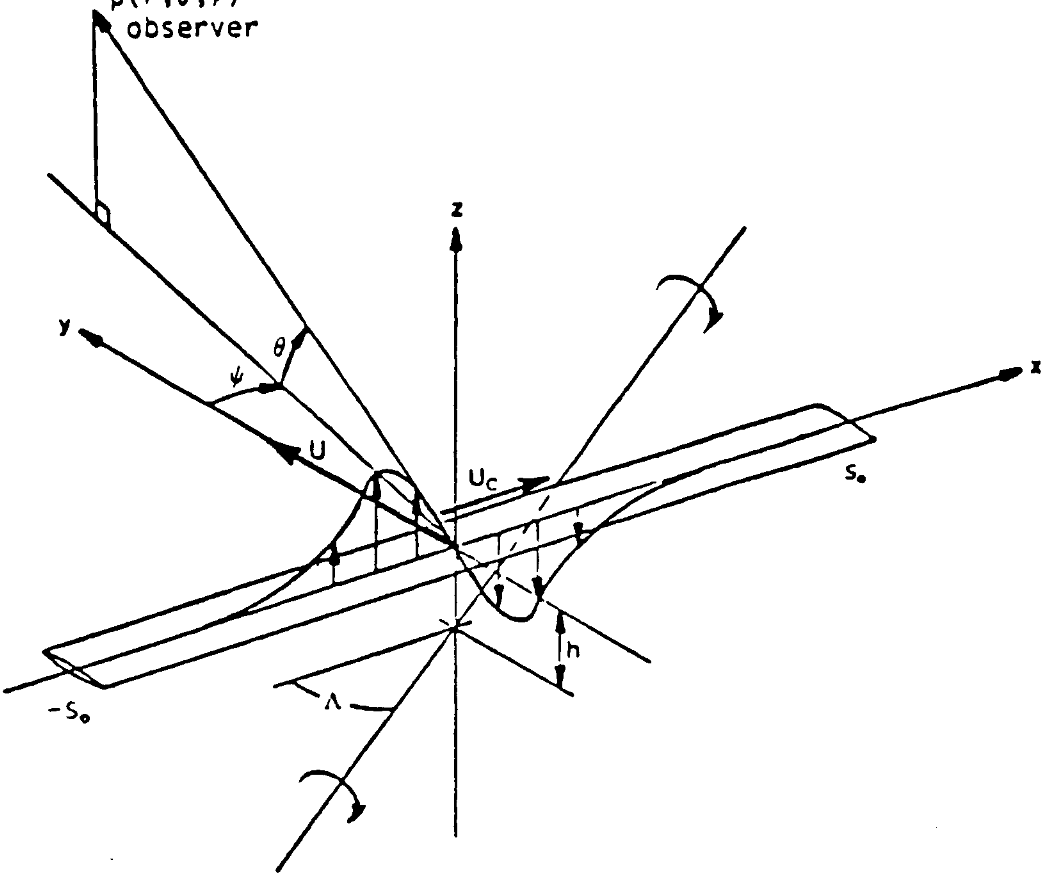

FIGURE 10. GEOMETRY OF ACOUSTIC MODEL [REFERENCE 25]

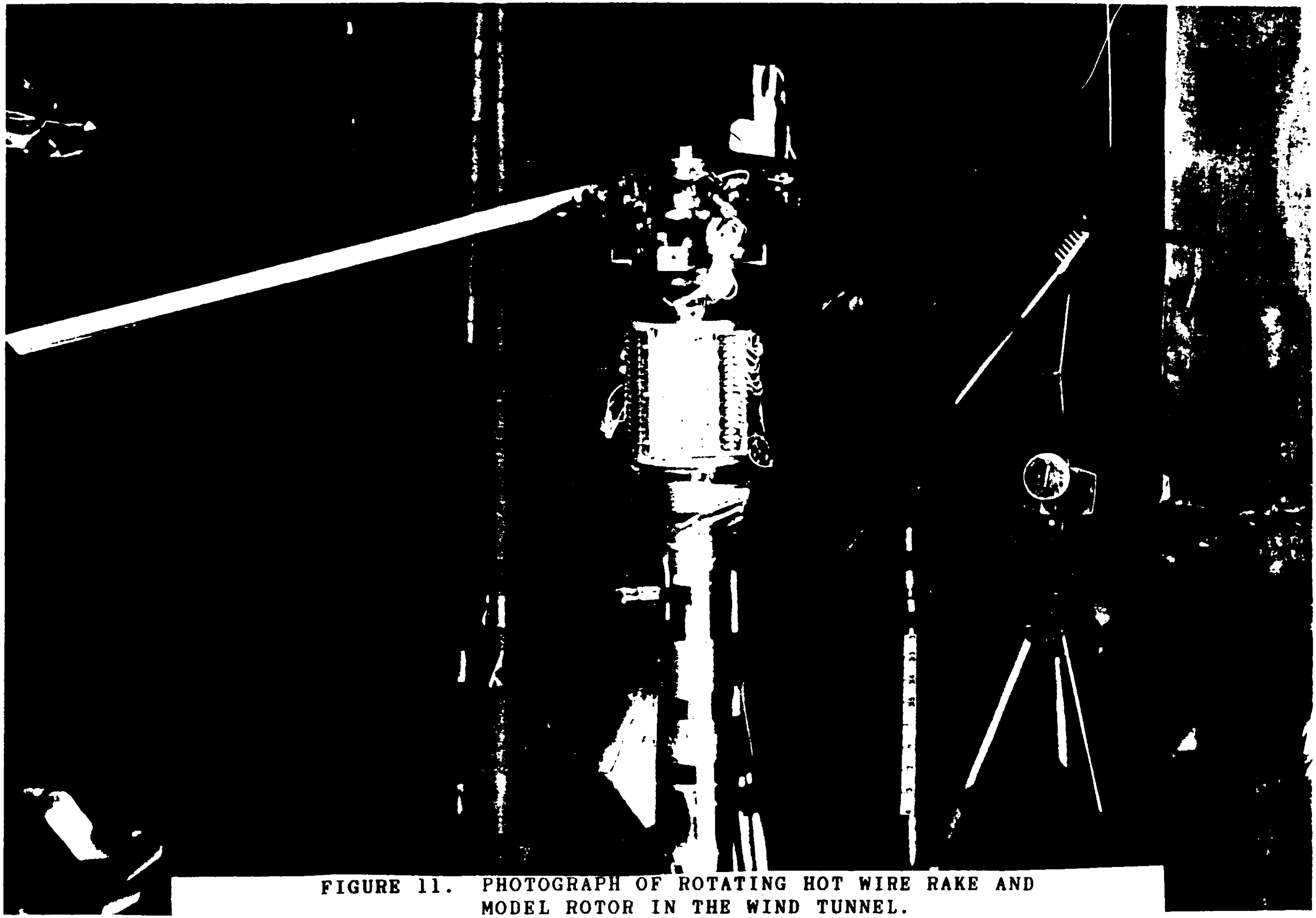

FIGURE 11. PHOTOGRAPH OF ROTATING HOT WIRE RAKE AND MODEL ROTOR IN THE WIND TUNNEL.

ORIGINAL PAGE IS
OF POOR QUALITY

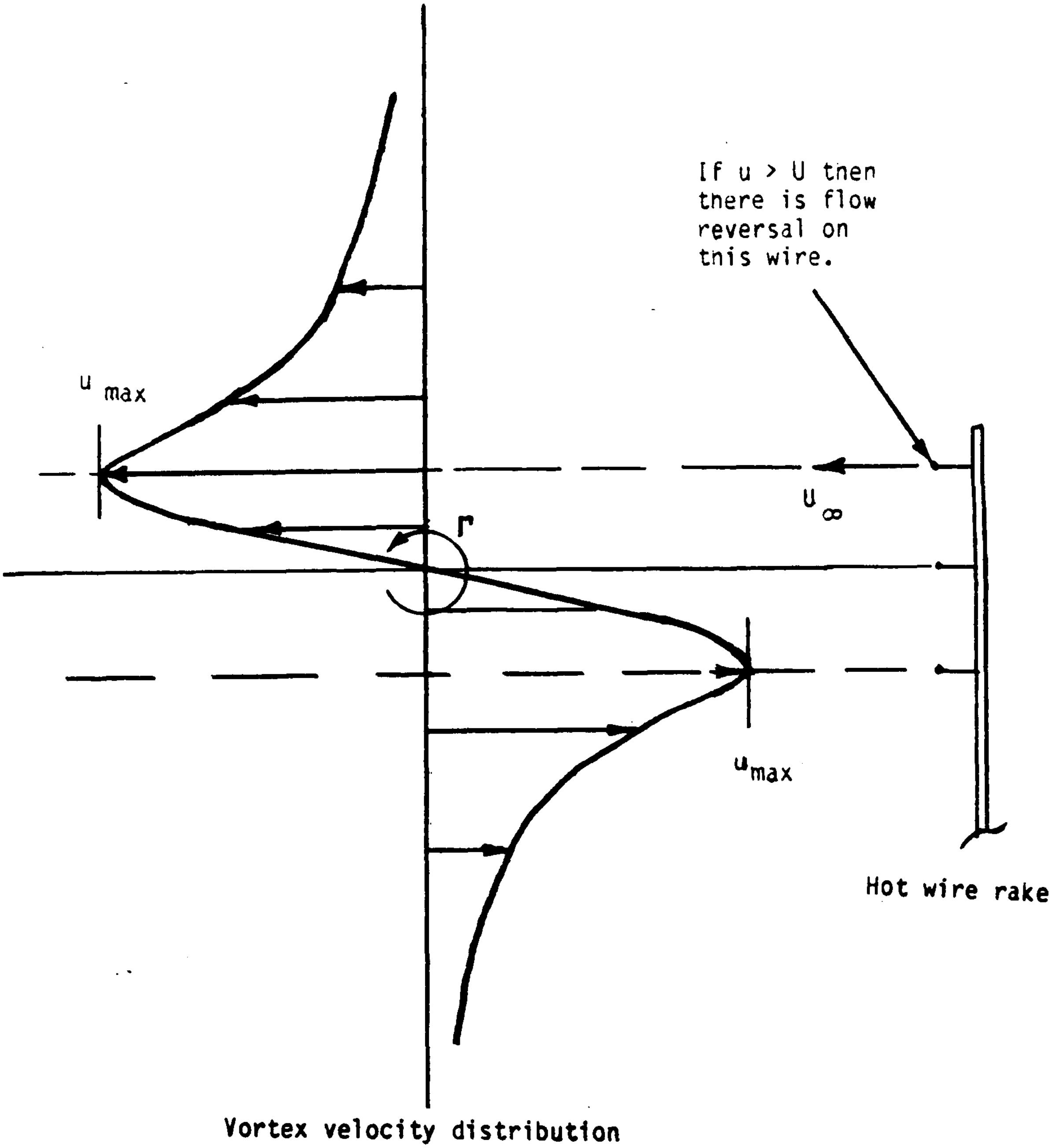

FIGURE 12. VORTEX MEASUREMENT USING A HOT WIRE RAKE.

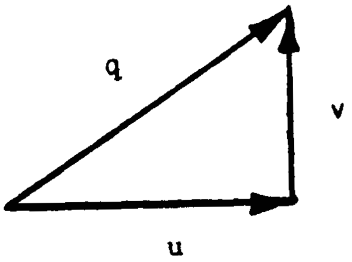

$$q^2 = u^2 + v^2$$

FIGURE 13a. MEASURED FLOW VELOCITY FOR A STATIONARY HOT WIRE.

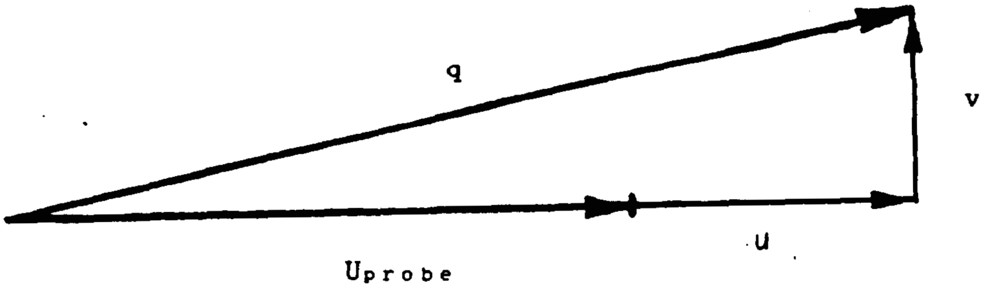

$$q^2 = (U + u)^2 + v^2$$

FIGURE 13b. MEASURED FLOW VELOCITY FOR A PROBE MOVING AT VELOCITY U.

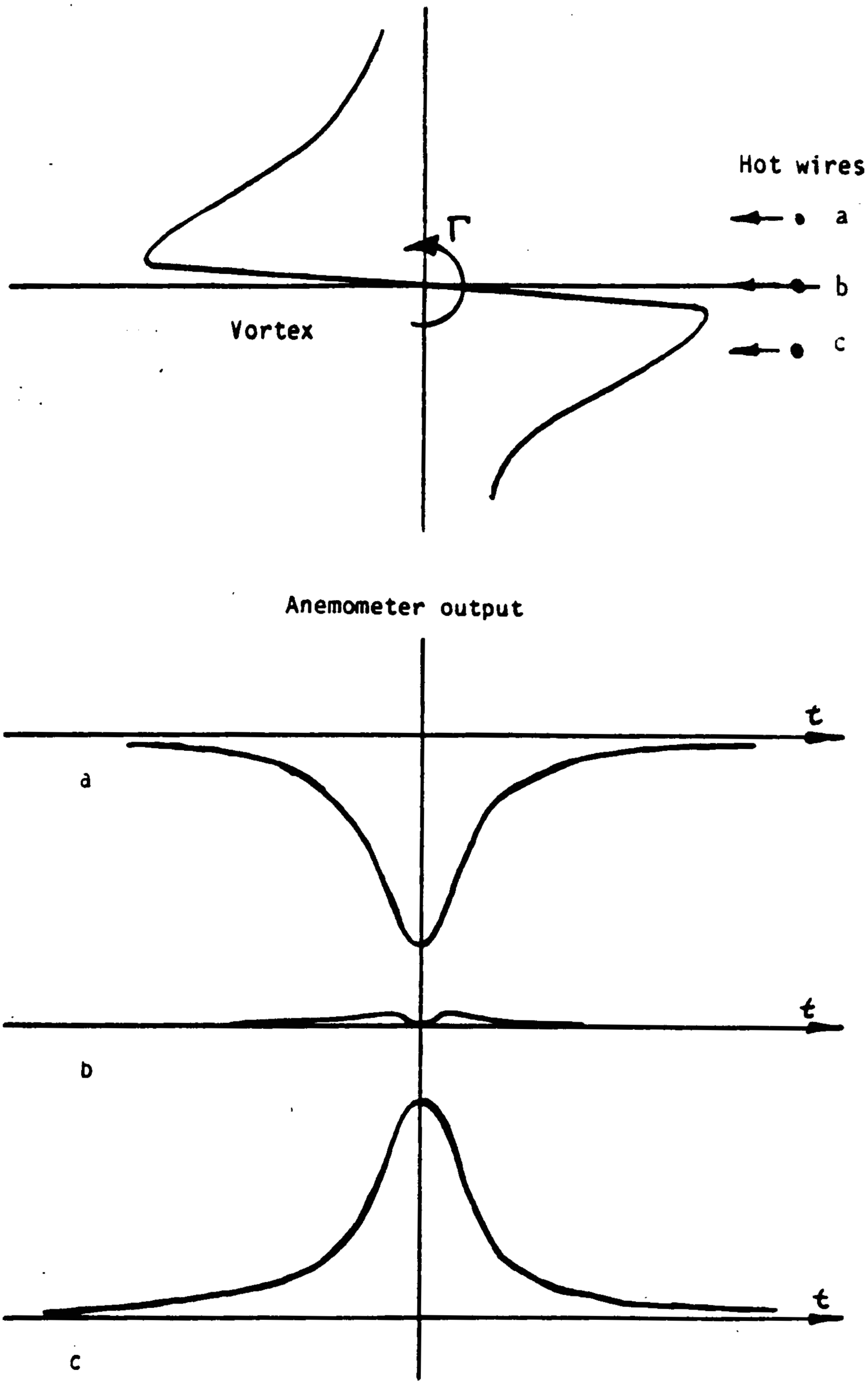

FIGURE 14. HOT WIRE RAKE ANEMOMETER OUTPUT FOR A VORTEX MEASUREMENT.

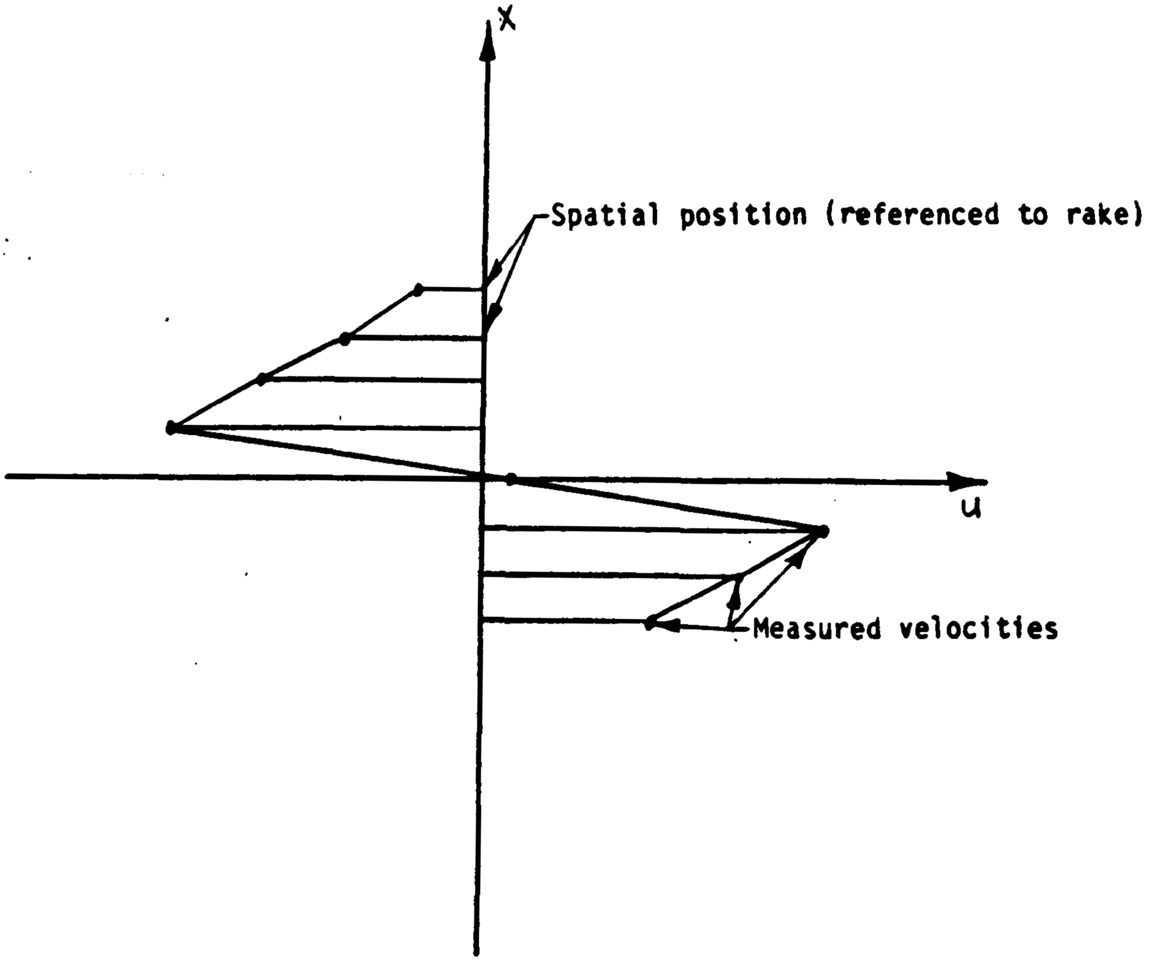

Measured vortex velocity distribution

FIGURE 15. VORTEX VELOCITY DISTRIBUTION OBTAINED FROM HOT WIRE RAKE.

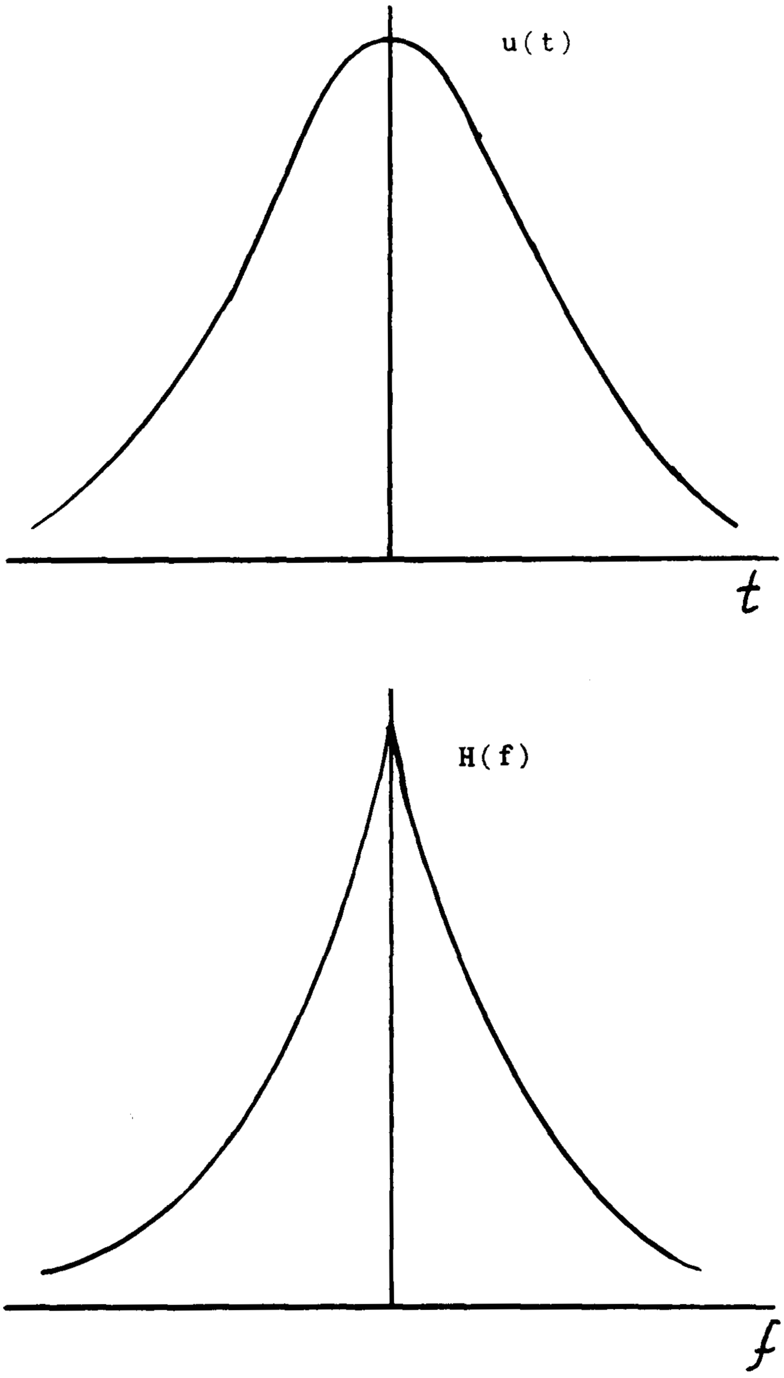

FIGURE 16. APPROXIMATE TIME HISTORY OF THE HOT WIRE OUTPUT AND ASSOCIATED FOURIER TRANSFORM.

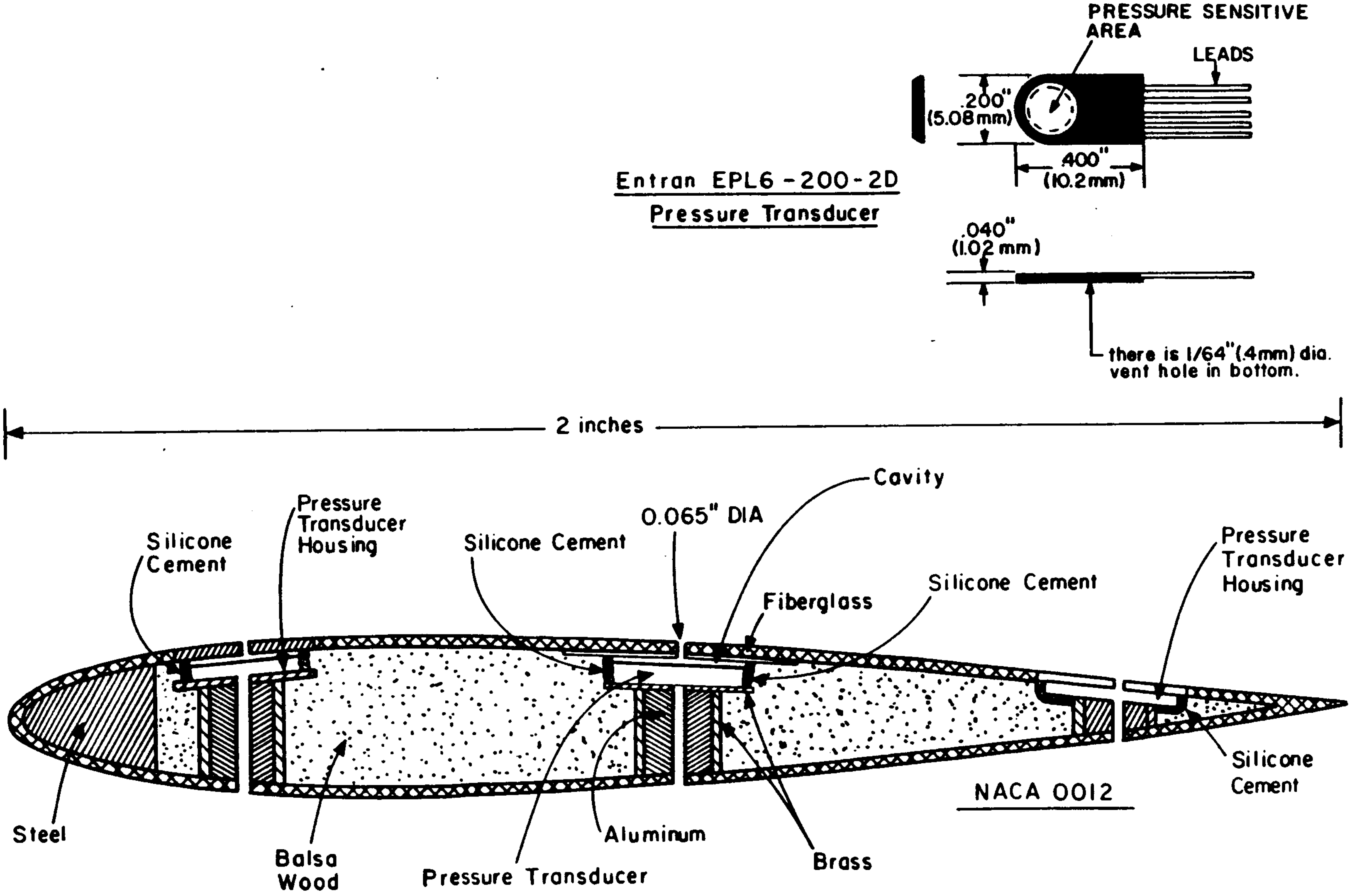

FIGURE 17a. DIAGRAM OF THE LOCATION OF THE PRESSURE TRANSDUCERS.

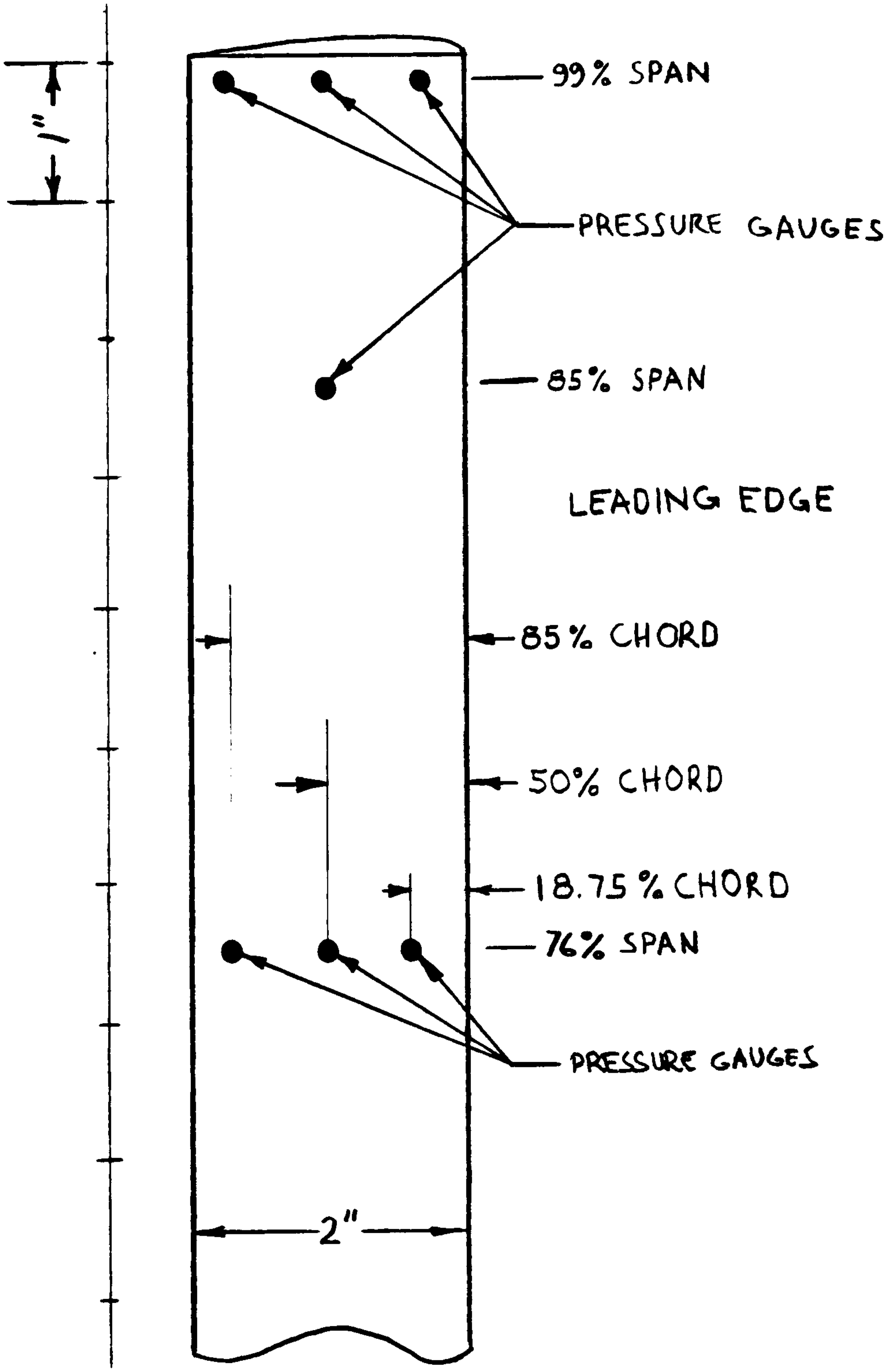

FIGURE 17b. SECTION OF BLADE SHOWING INSTALLATION OF THE PRESSURE TRANSDUCERS. [REFERENCE 30]

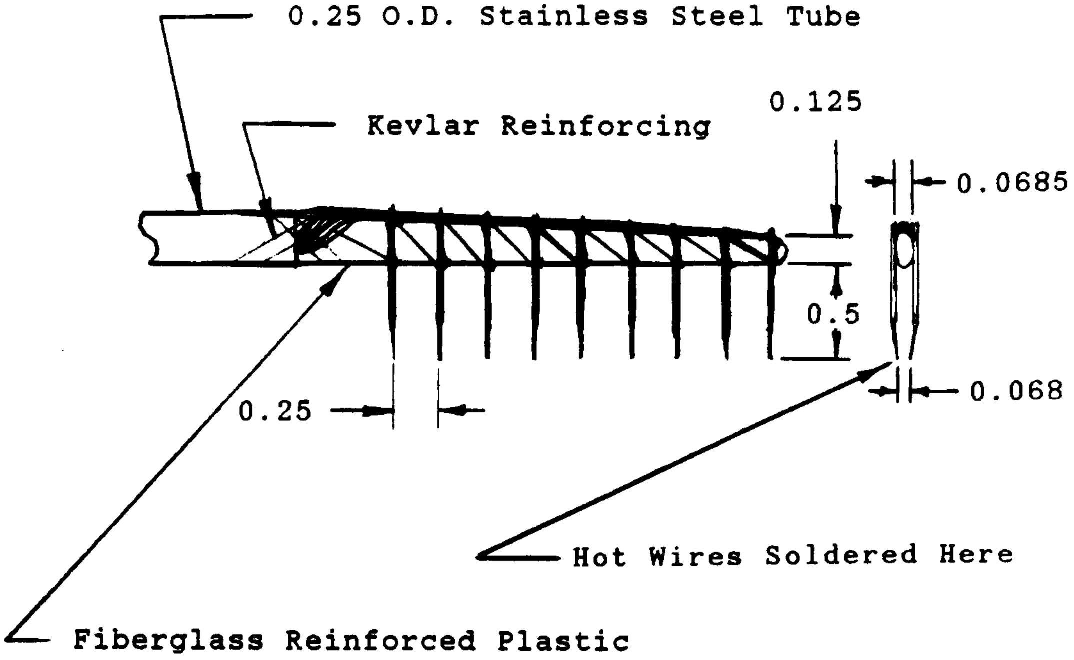

All Dimensions in Inches

FIGURE 18. DETAIL OF THE HOT WIRE RAKE.

ORIGINAL PAGE IS
OF POOR QUALITY

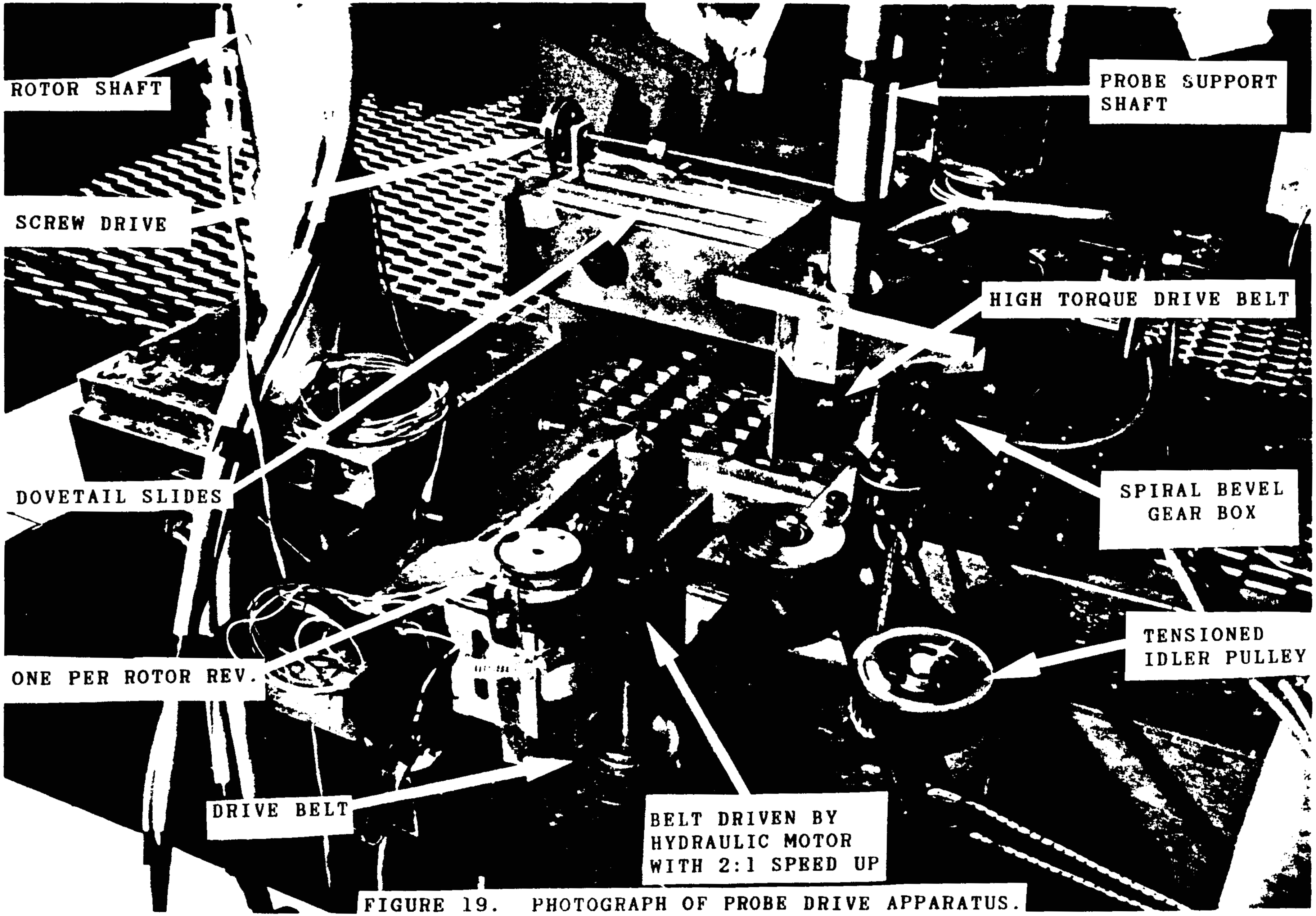

FIGURE 19. PHOTOGRAPH OF PROBE DRIVE APPARATUS.

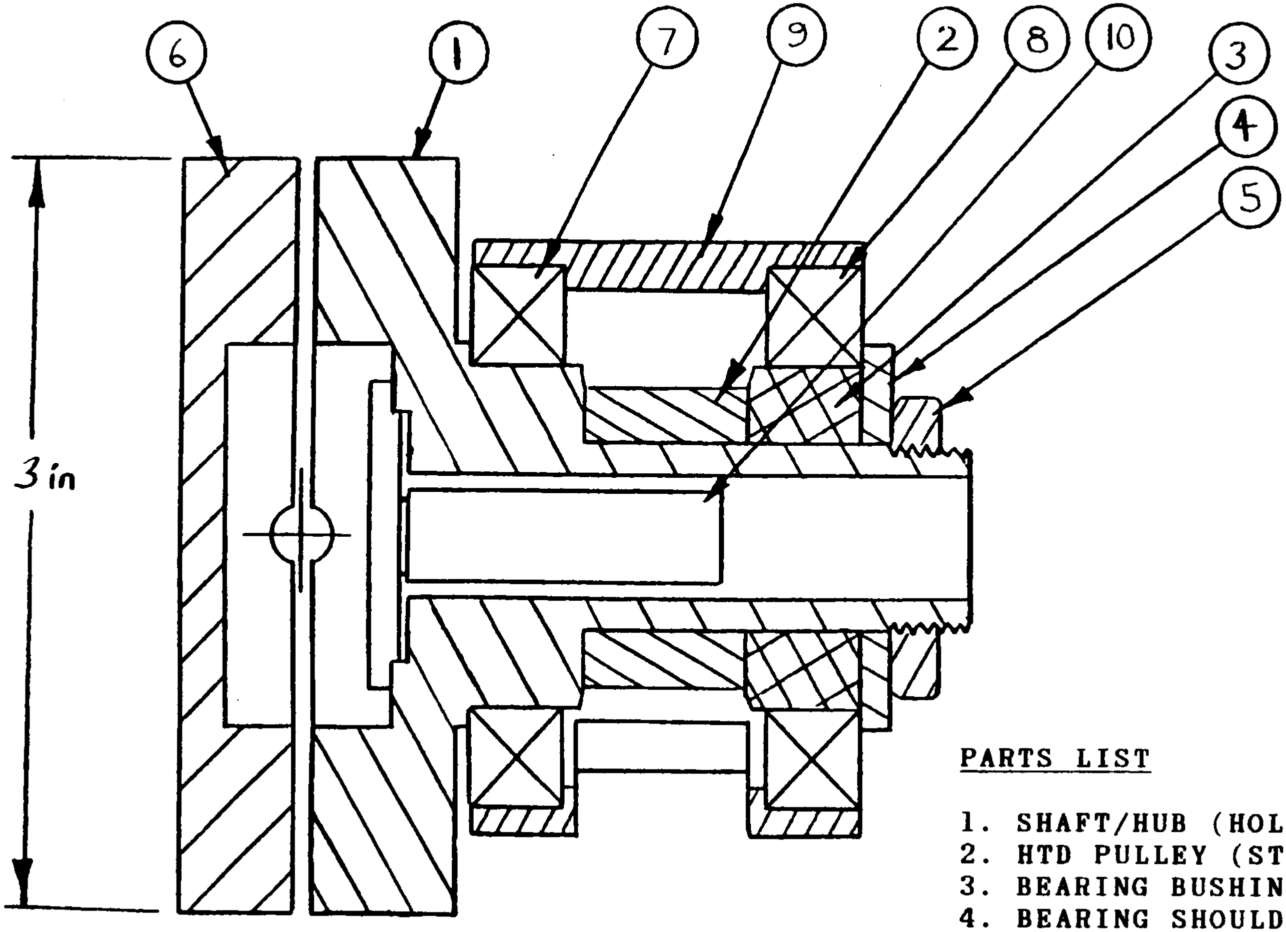

FIGURE 20. ASSEMBLY DRAWING OF THE HUB.

PARTS LIST

1. SHAFT/HUB (HOLLOW)
2. HTD PULLEY (STAKED TO SHAFT)
3. BEARING BUSHING
4. BEARING SHOULDER WASHER
5. 3/4 INCH UNF NUT
6. CLAMP PLATE
7. 35X55X10 mm SHIELDED BEARING
8. " " BEARING
9. HOUSING (WELDED TO PROBE SUPPORT TUBE)
10. 32 CHANNEL MINIATURE SLIP RING

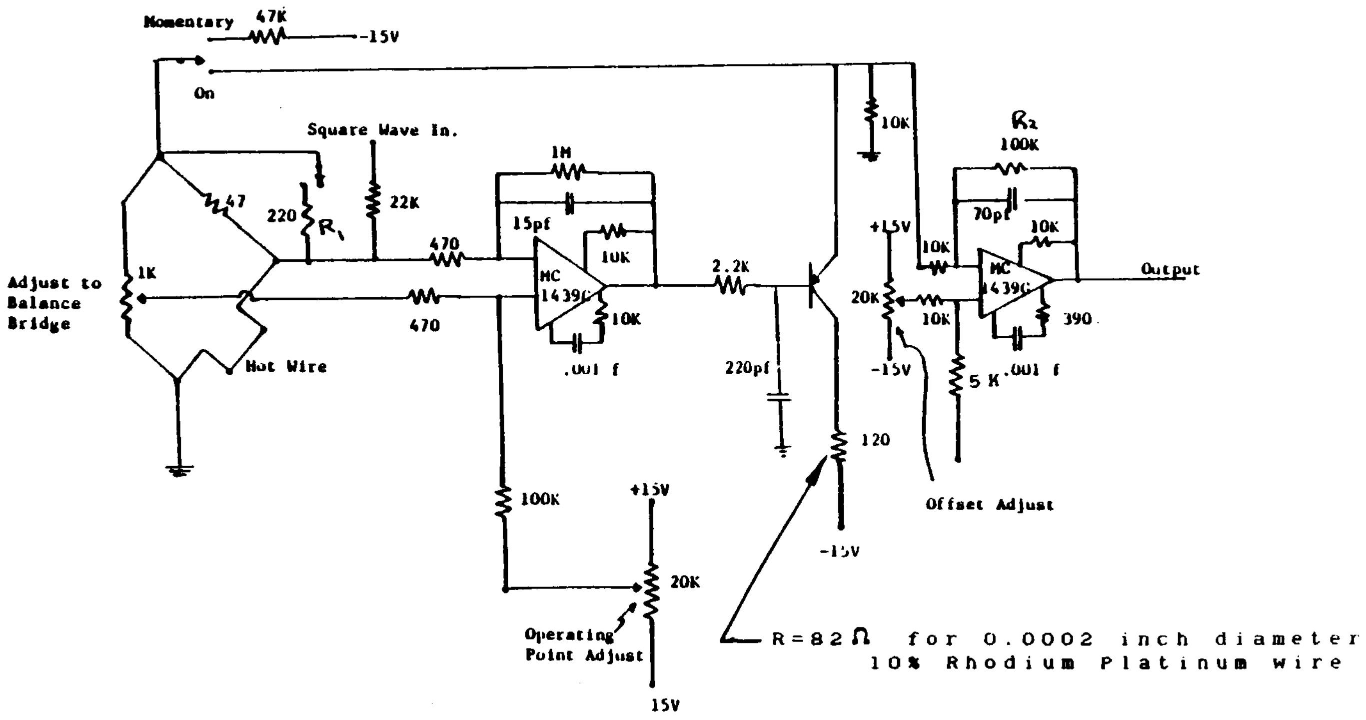

R = 82 Ω for 0.0002 inch diameter 10% Rhodium Platinum wire

FIGURE 21. HOT WIRE ANEMOMETER CIRCUIT DIAGRAM. [REFERENCE 51]

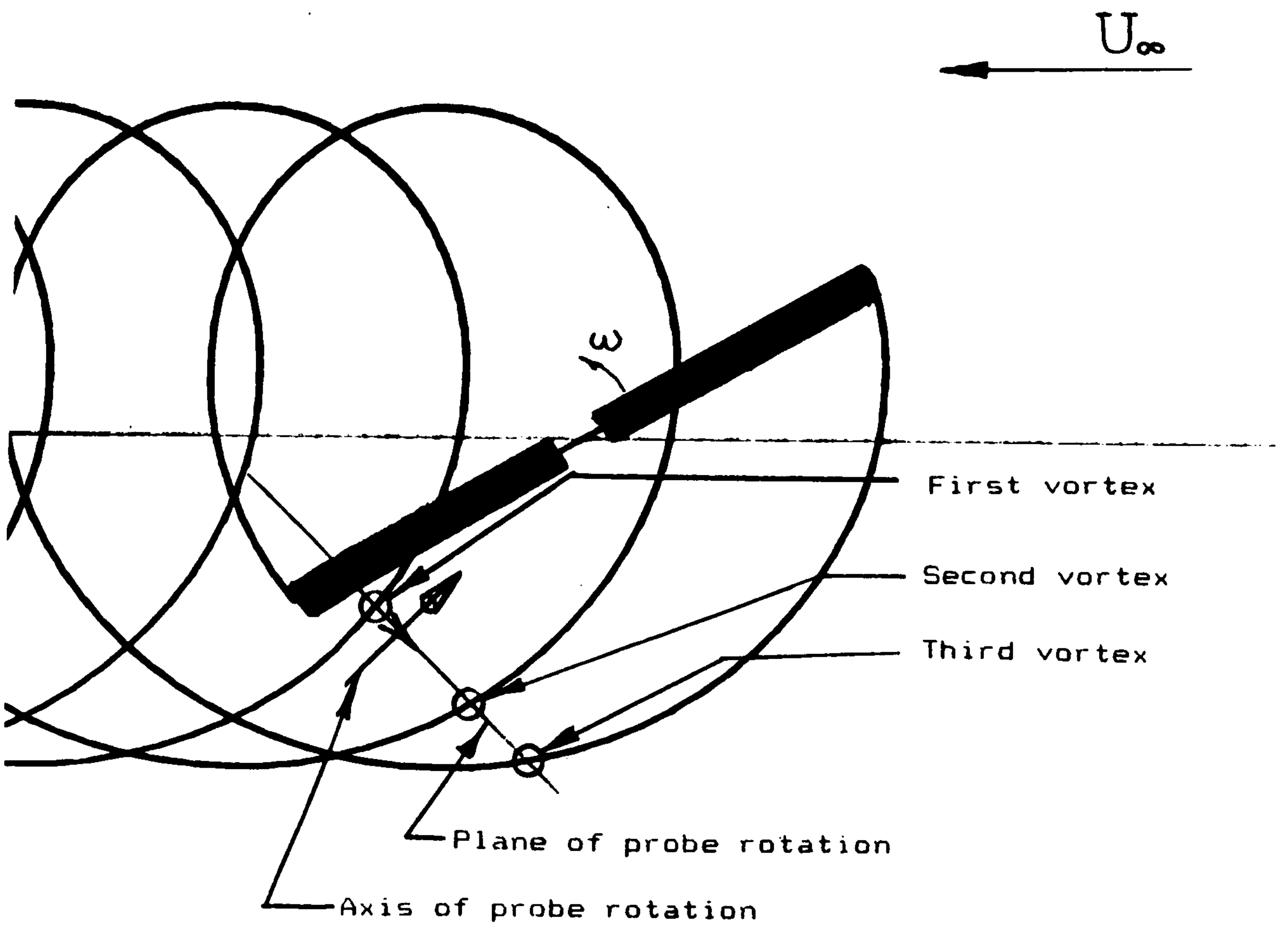

FIGURE 22. TOP VIEW OF EXPERIMENT WITH RIGID WAKE PLOT.

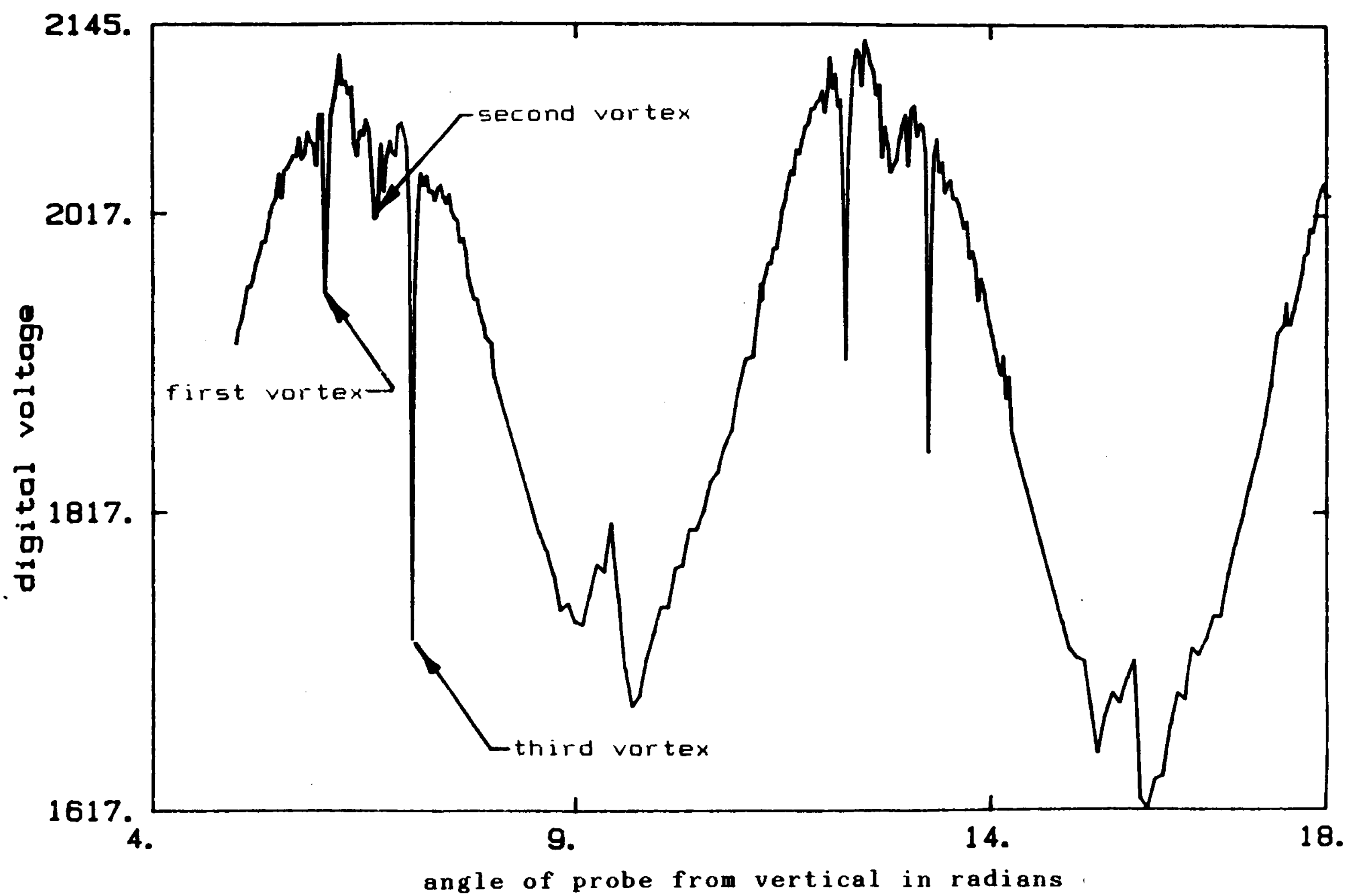

FIGURE 23a. HOT WIRE ANEMOMETER OUTPUT FOR BLADE VORTEX INTERACTION CONDITION AT ADVANCE RATIO OF 0.19 FOR HOT WIRE NUMBER 1.

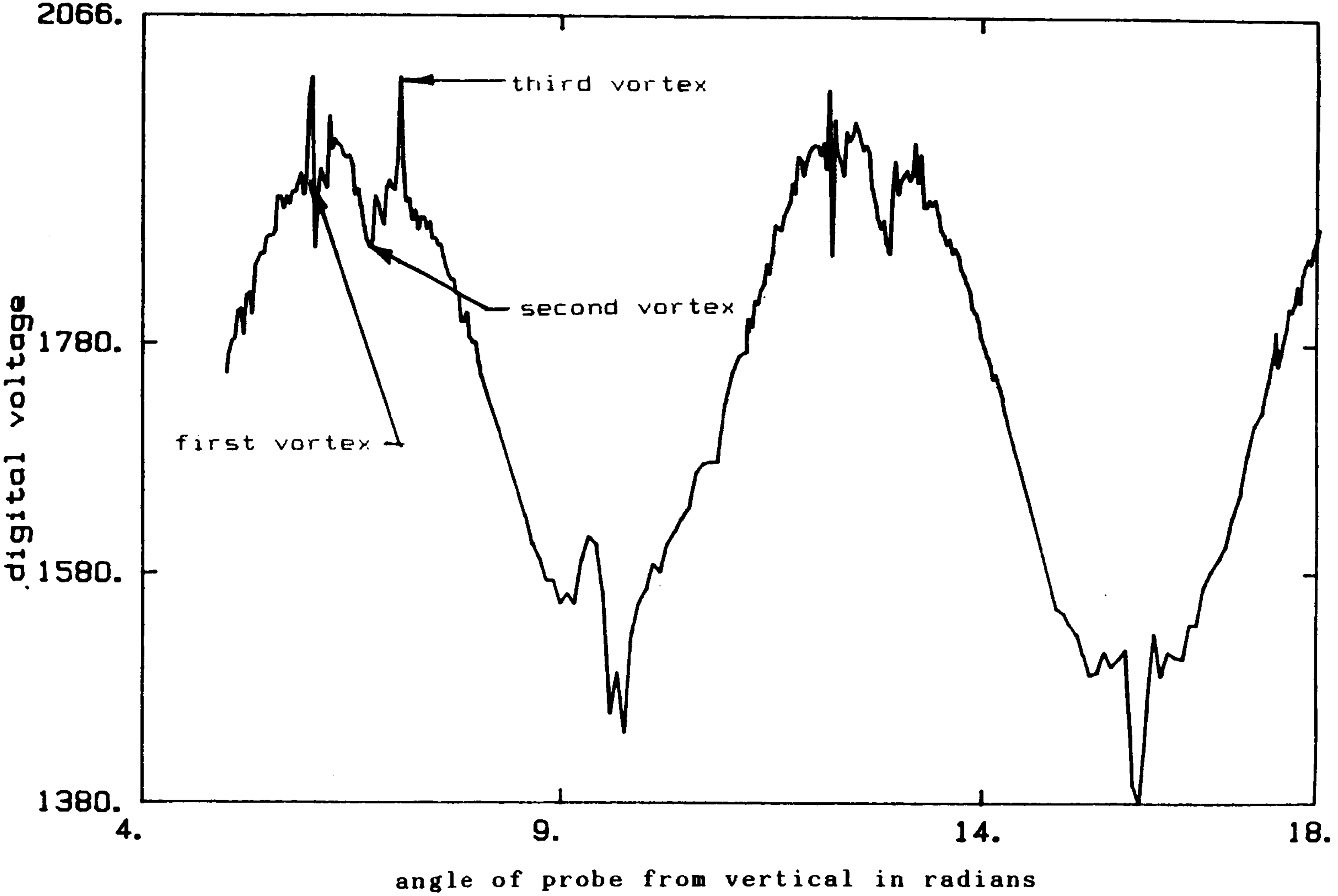

FIGURE 23b. HOT WIRE ANEMOMETER OUTPUT FOR BLADE VORTEX INTERACTION CONDITION AT ADVANCE RATIO OF 0.19 FOR HOT WIRE NUMBER 2.

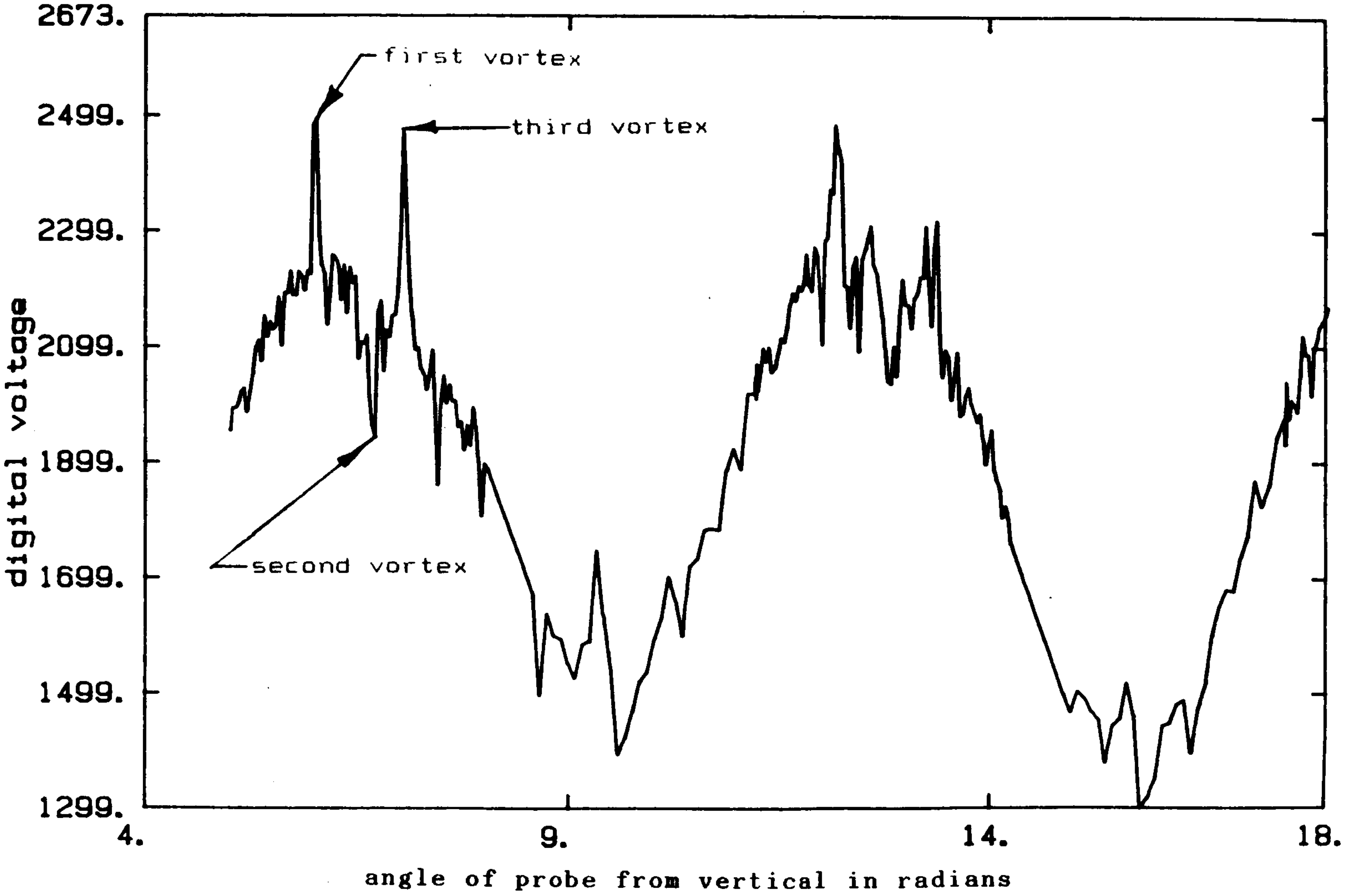

FIGURE 23c. HOT WIRE ANEMOMETER OUTPUT FOR BLADE VORTEX INTERACTION CONDITION AT ADVANCE RATIO OF 0.19 FOR HOT WIRE NUMBER 3.

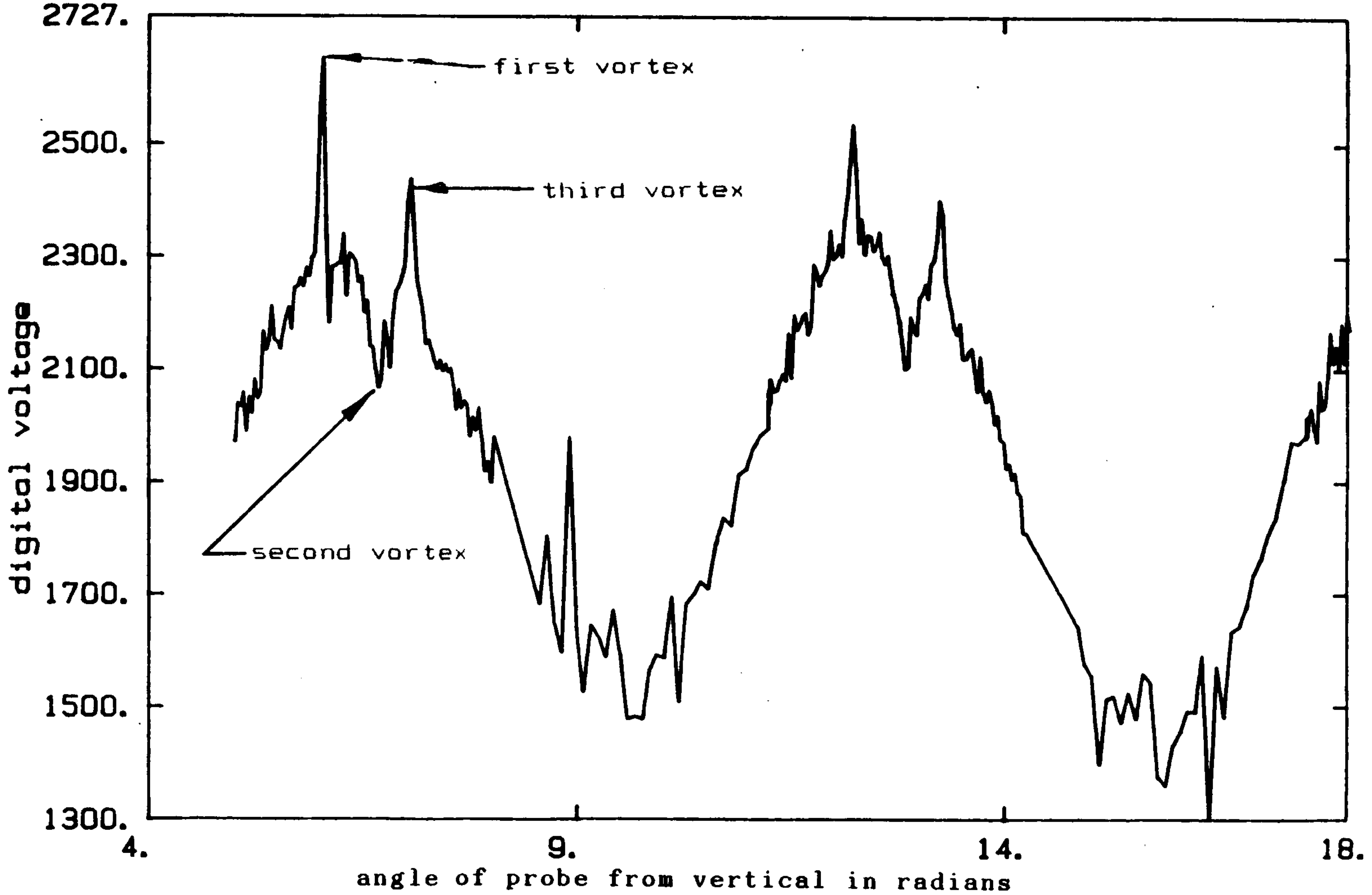

FIGURE 23d. HOT WIRE ANEMOMETER OUTPUT FOR BLADE VORTEX INTERACTION CONDITION AT ADVANCE RATIO OF 0.19 FOR HOT WIRE NUMBER 4.

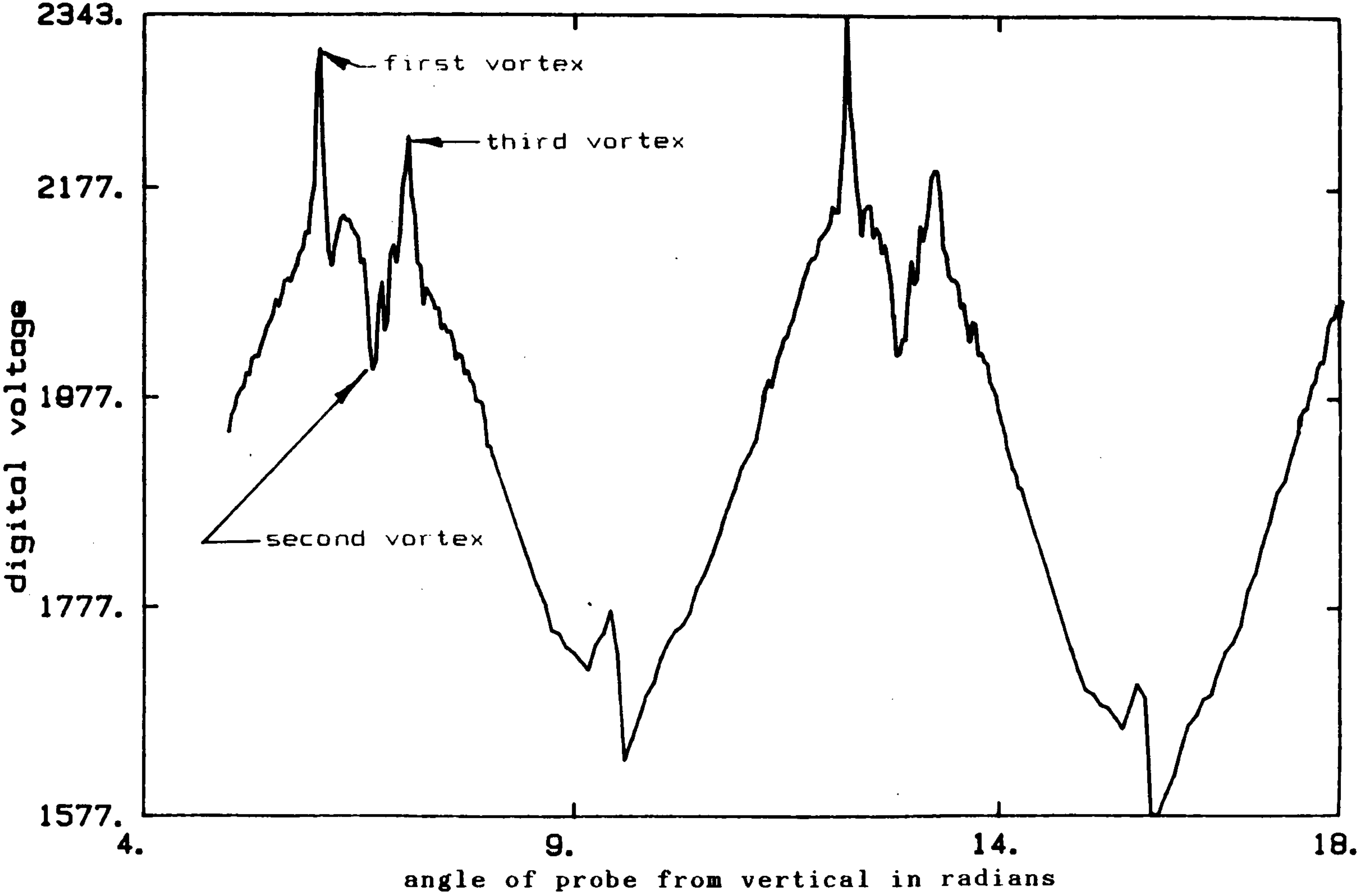

FIGURE 23e. HOT WIRE ANEMOMETER OUTPUT FOR BLADE VORTEX INTERACTION CONDITION AT ADVANCE RATIO OF 0.19 FOR HOT WIRE NUMBER 5.

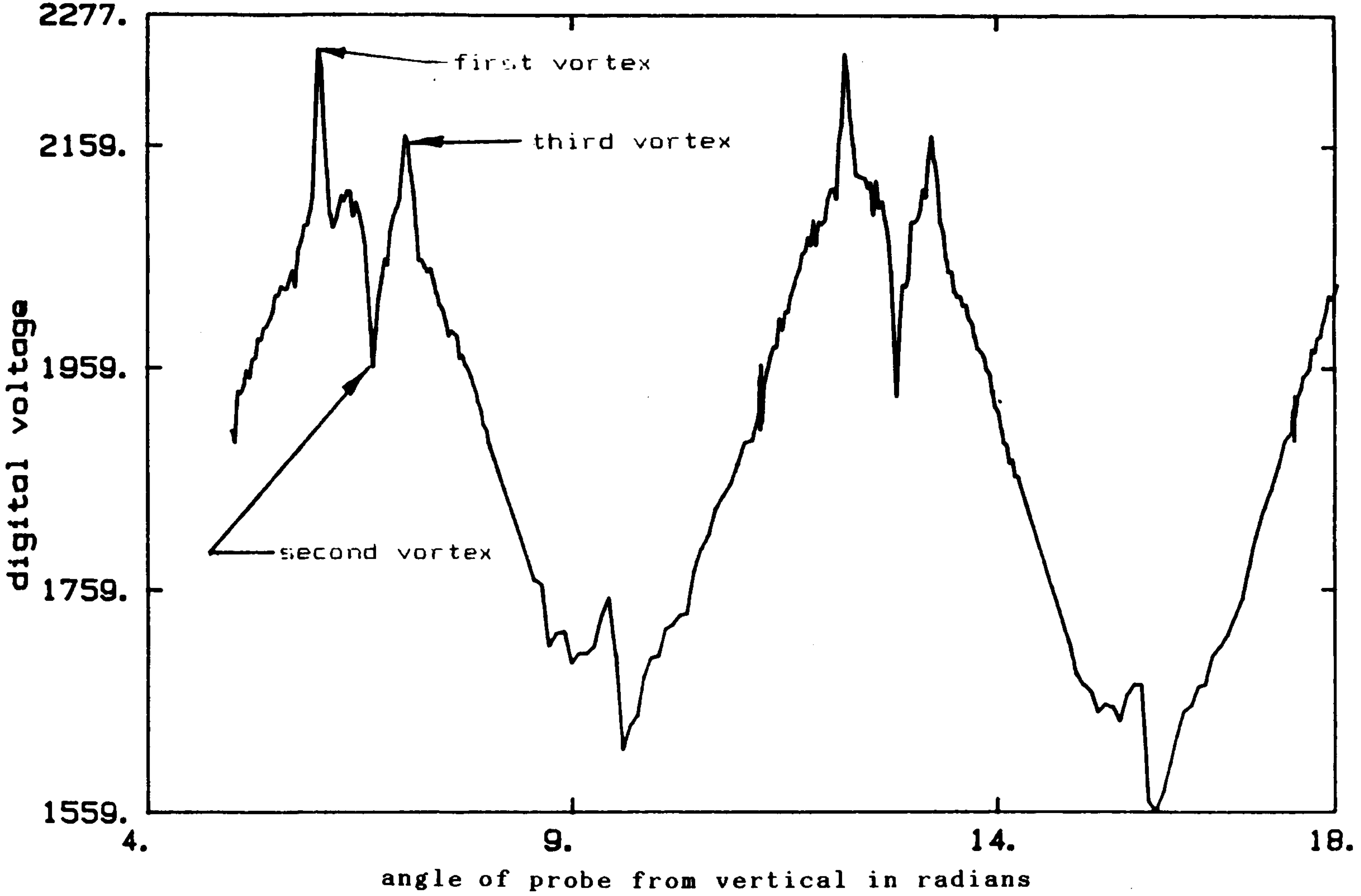

FIGURE 23f. HOT WIRE ANEMOMETER OUTPUT FOR BLADE VORTEX INTERACTION CONDITION AT ADVANCE RATIO OF 0.19 FOR HOT WIRE NUMBER 6.

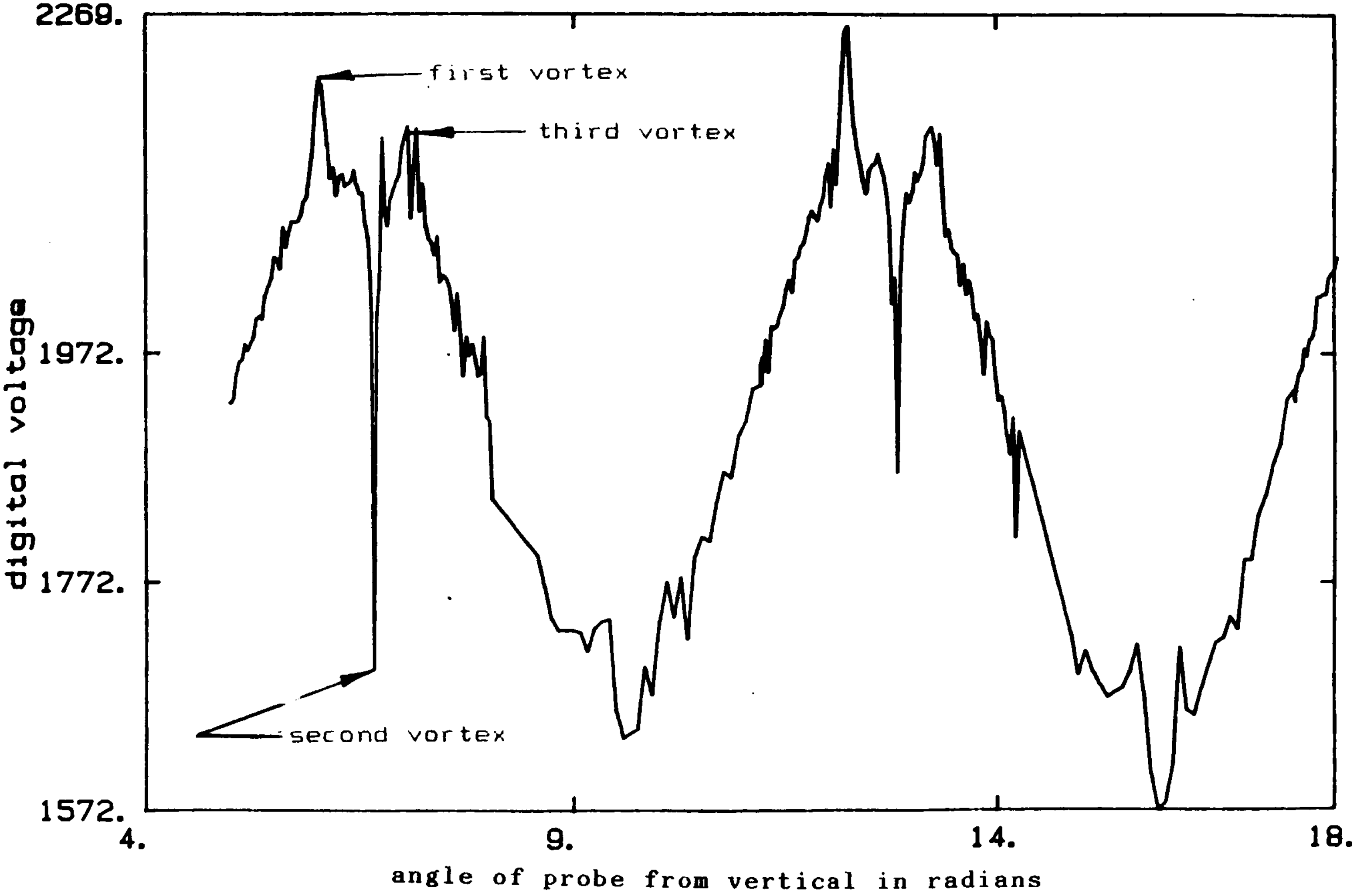

FIGURE 23g. HOT WIRE ANEMOMETER OUTPUT FOR BLADE VORTEX INTERACTION CONDITION AT ADVANCE RATIO OF 0.19 FOR HOT WIRE NUMBER 7.

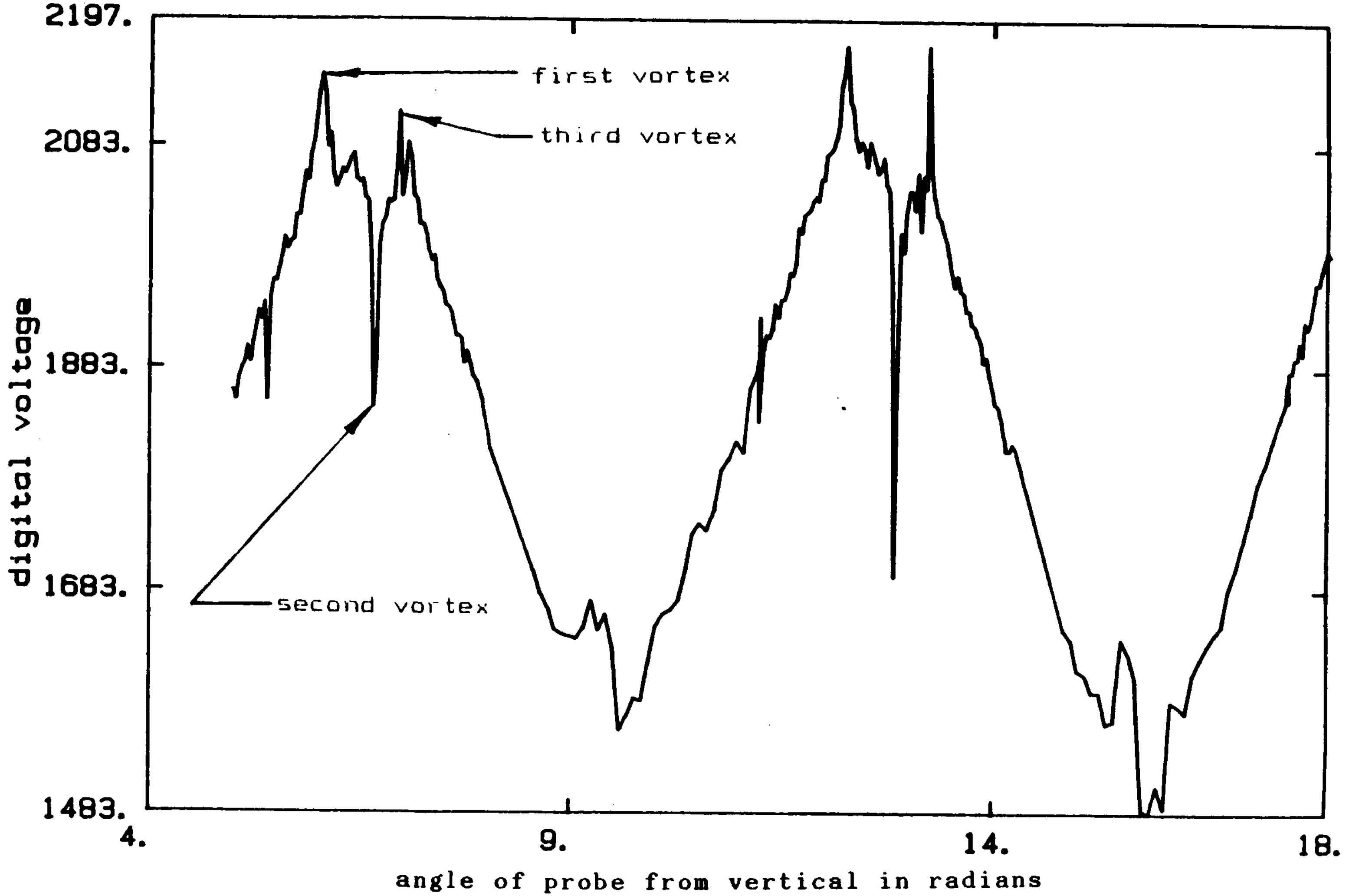

FIGURE 23h. HOT WIRE ANEMOMETER OUTPUT FOR BLADE VORTEX INTERACTION CONDITION AT ADVANCE RATIO OF 0.19 FOR HOT WIRE NUMBER 8.

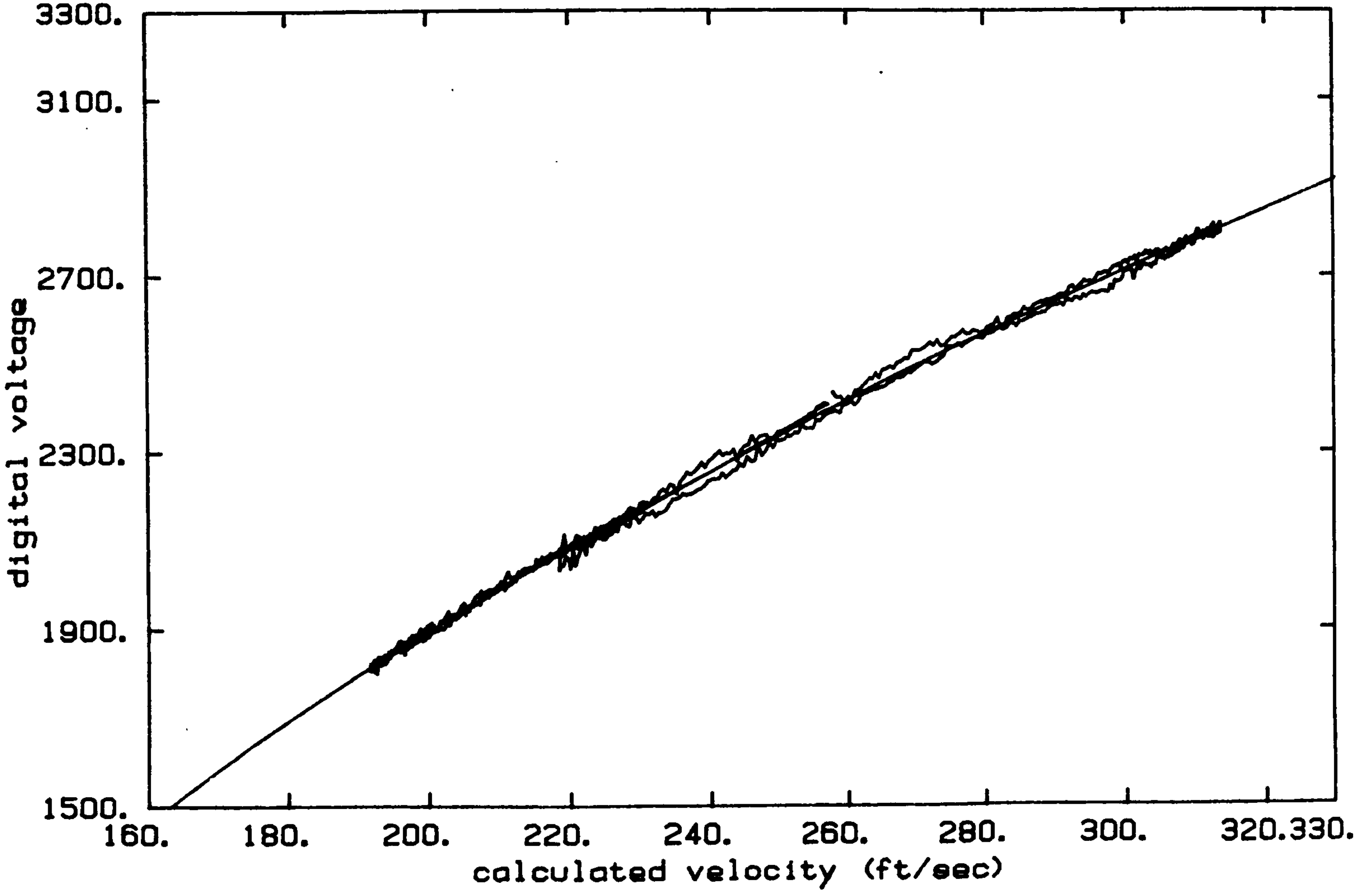

FIGURE 24. CALIBRATION DATA FOR HOT WIRE NUMBER 1.

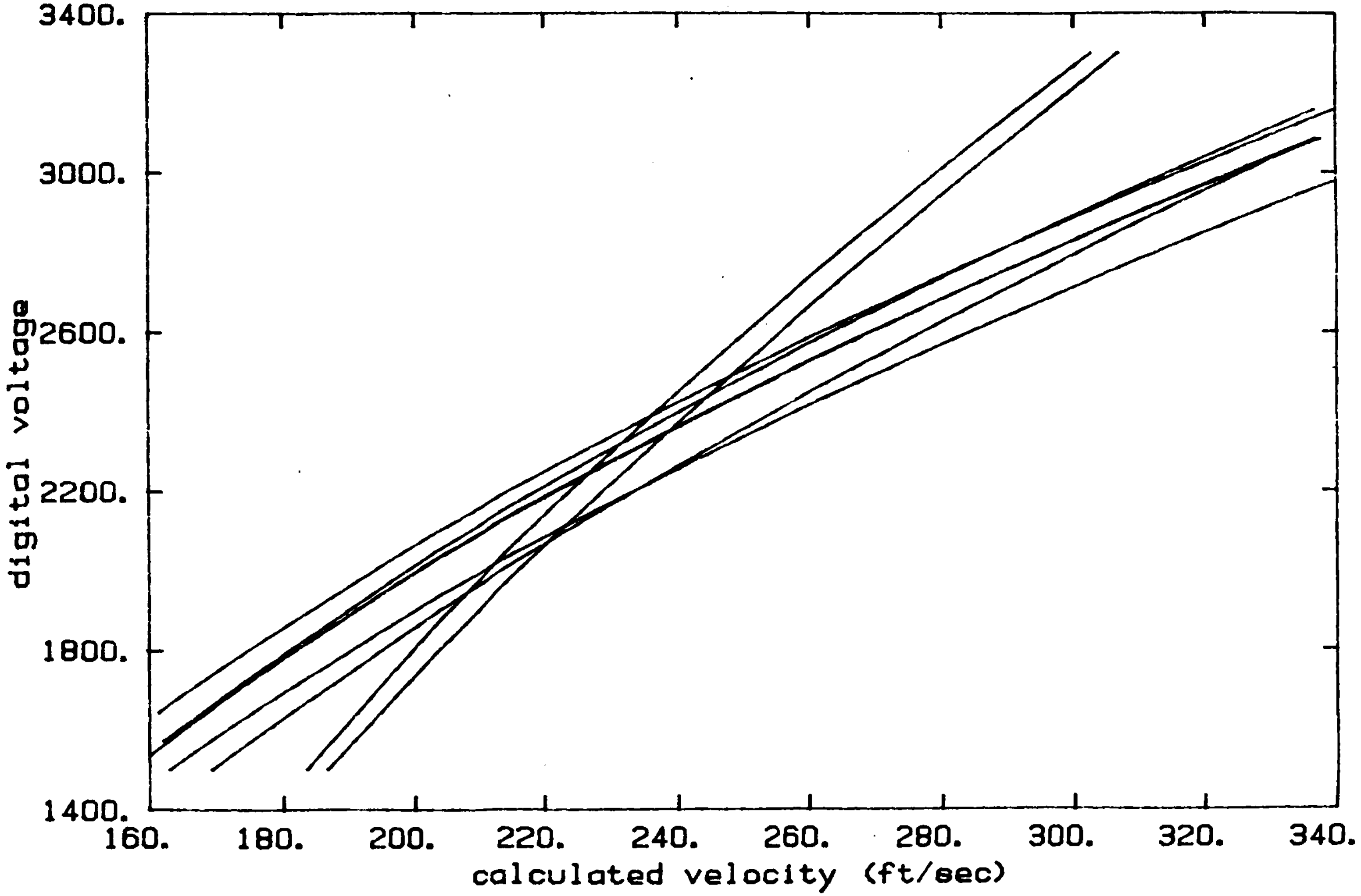

Figure 25. Calibration curves for the hot wires.
The two steepest curves are for 10% Rhodium Platinum wires. The others are for the Platinum plated Tungsten wire.

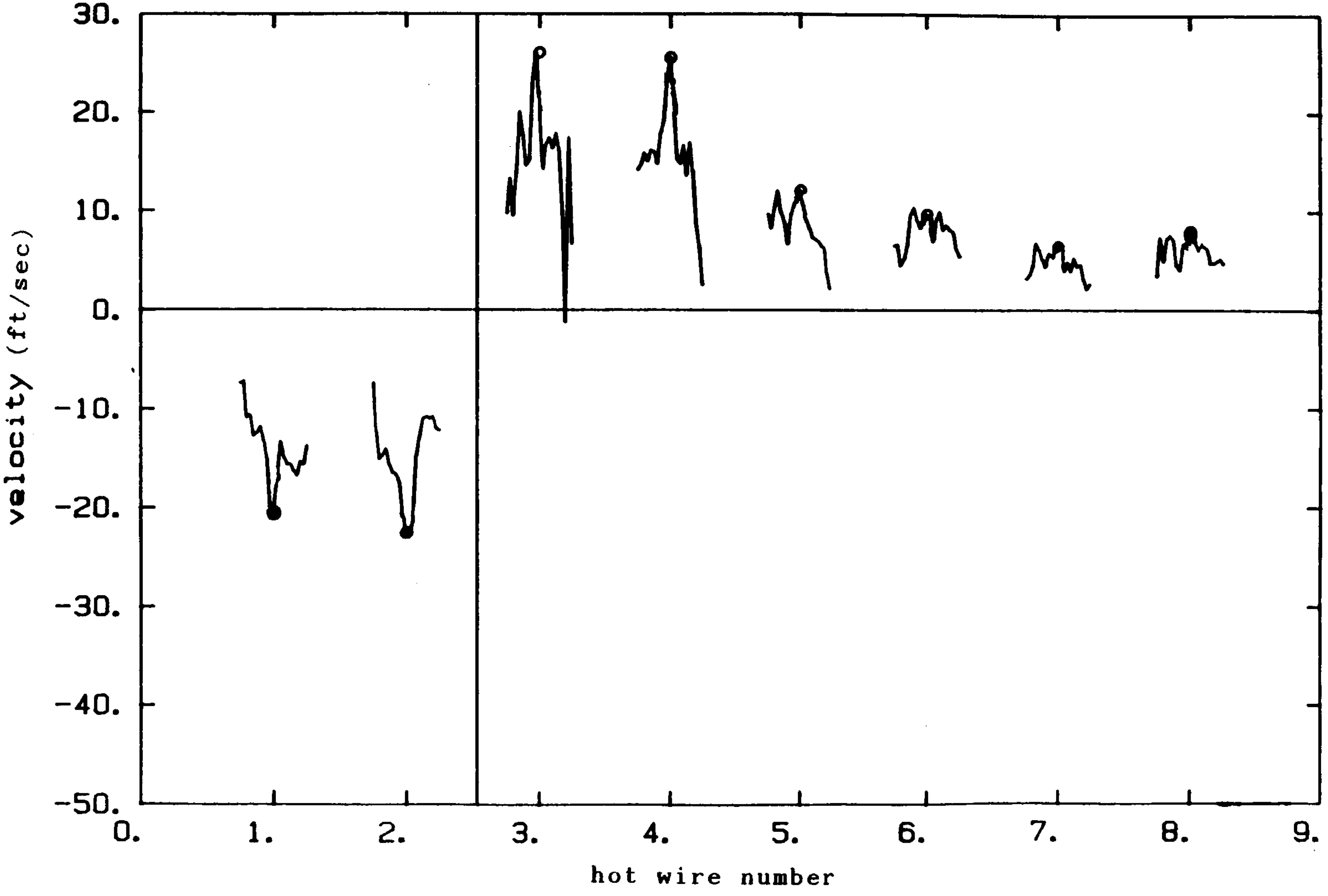

Figure 26. Vortex velocity distribution (circled) and the velocities around the peak value (solid line segments).

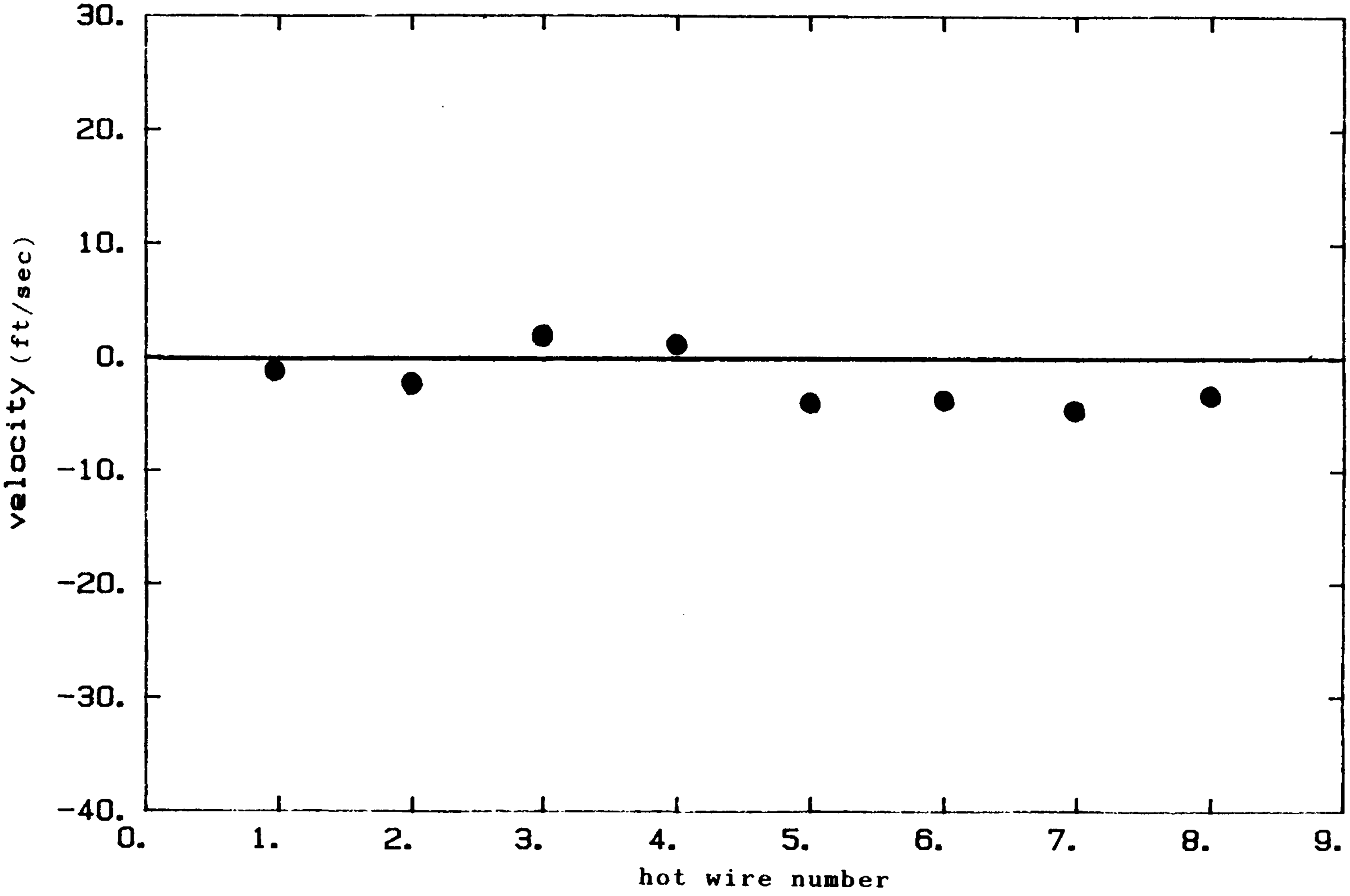

Figure 27. Error associated with the hot wire measurement.

Each wire should be at zero ft/sec for zero error.

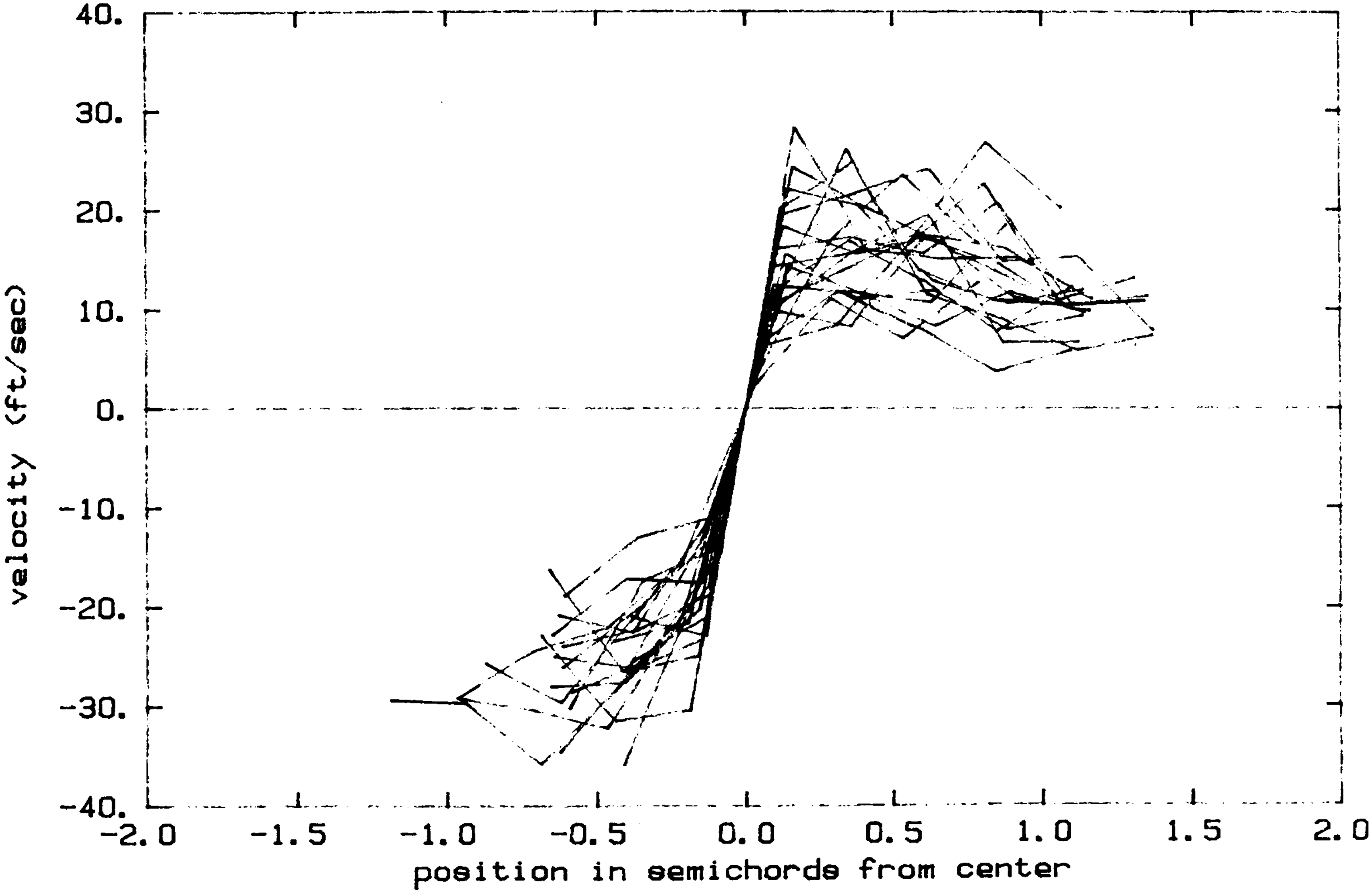

FIGURE 28. SUPERPOSITION OF MANY VORTICES AFTER SHIFTING THE DATA TO CORRECT FOR VORTEX MOTION. ADVANCE RATIO =0.19

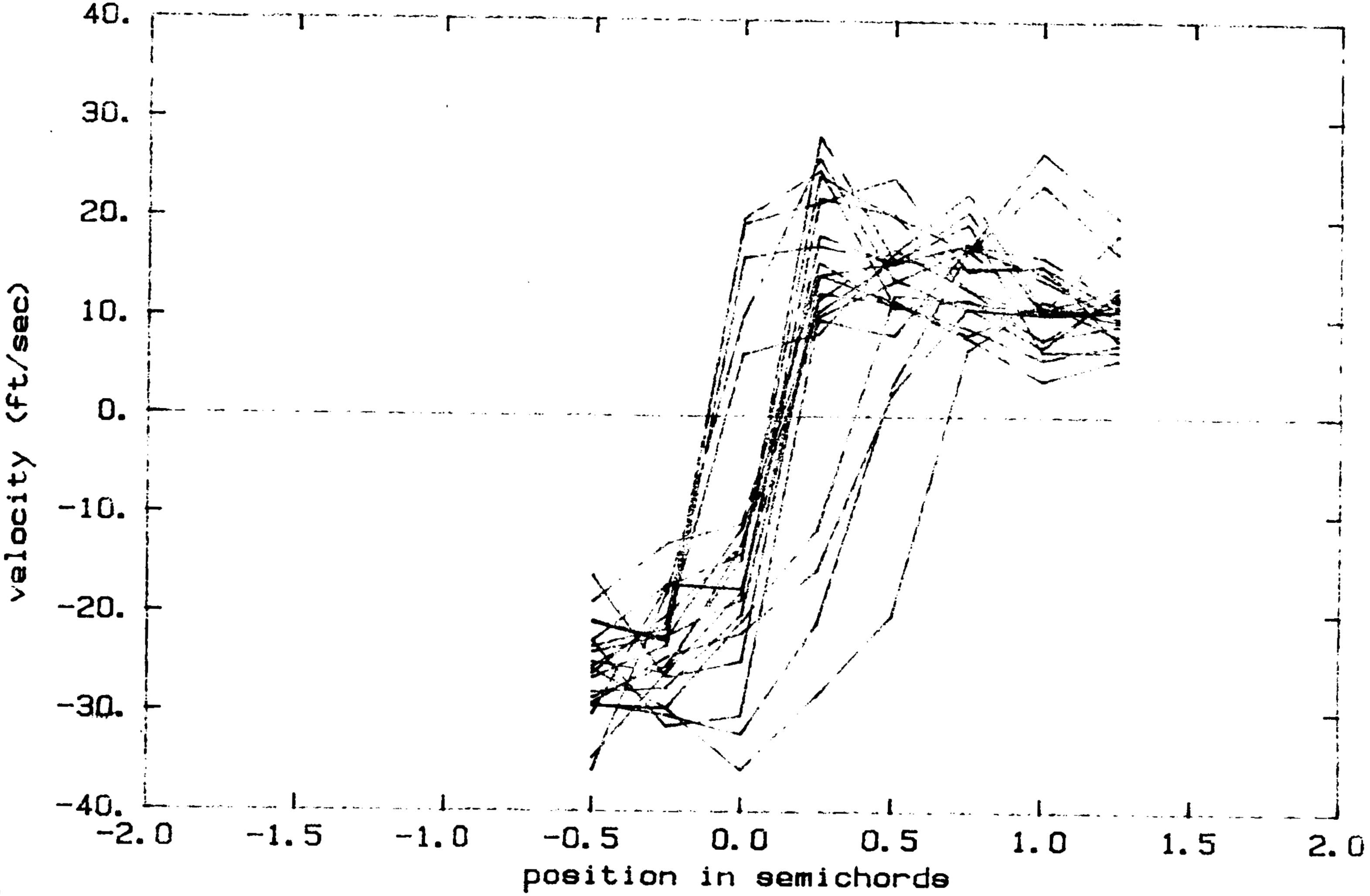

FIGURE 29 a. MANY VORTEX VELOCITY MEASUREMENTS WITH CORRESPONDING DATA POINTS CONNECTED BY LINES. ADVANCE RATIO=0.19

ORIGINAL PAGE IS
OF POOR QUALITY

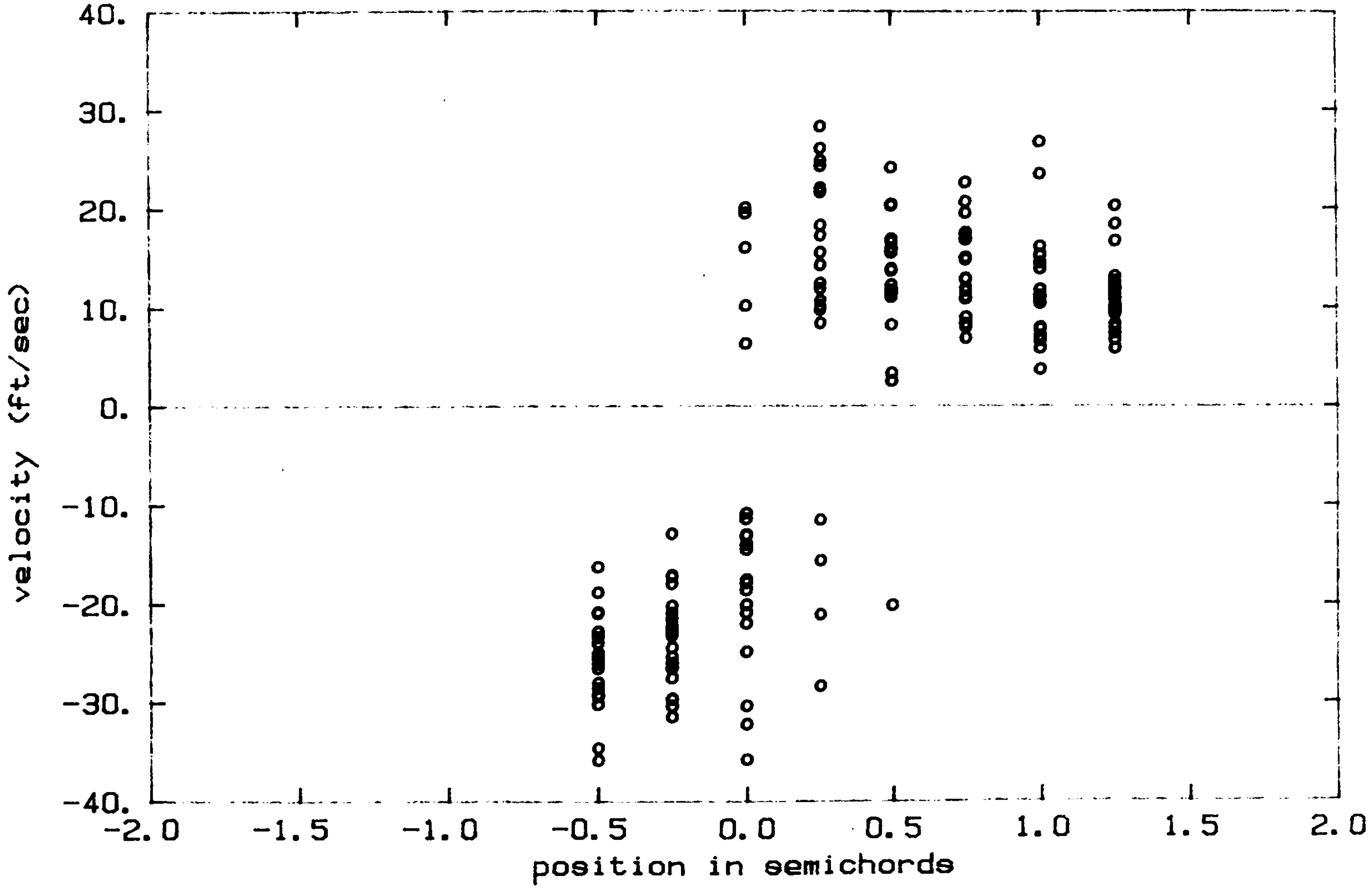

FIGURE 29 b. SAME DATA AS FIGURE 29a WITHOUT CONNECTING CORRESPONDING DATA POINTS. ADVANCE RATIO=.19

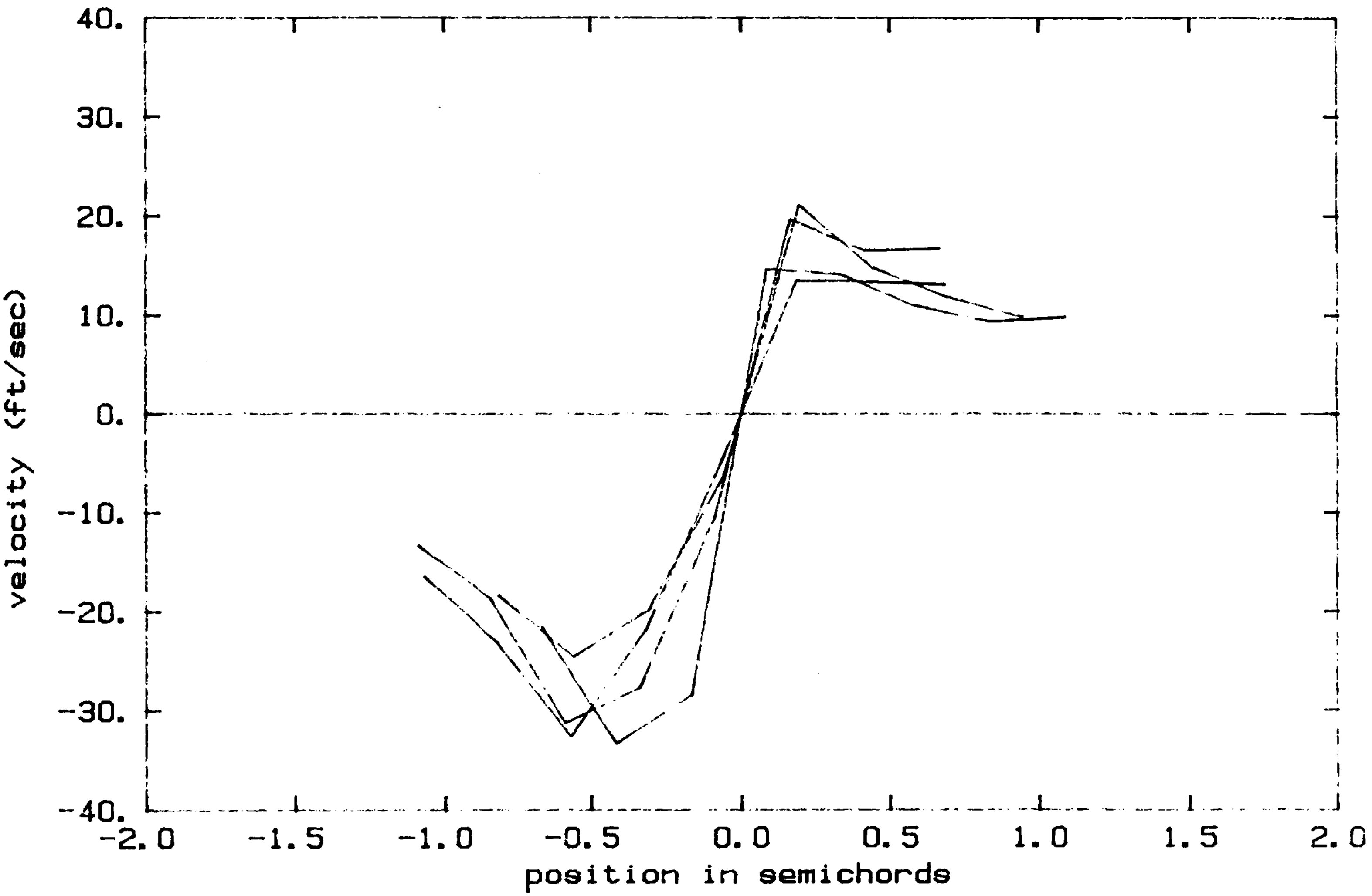

FIGURE 30 a. MEASURED VORTEX VELOCTIIES. DATA SHIFTED TO ACCOUNT FOR VARIATION IN VORTEX POSITION AND CORRESPONDING POINTS CONNECTED. ADVANCE RATIO=.15

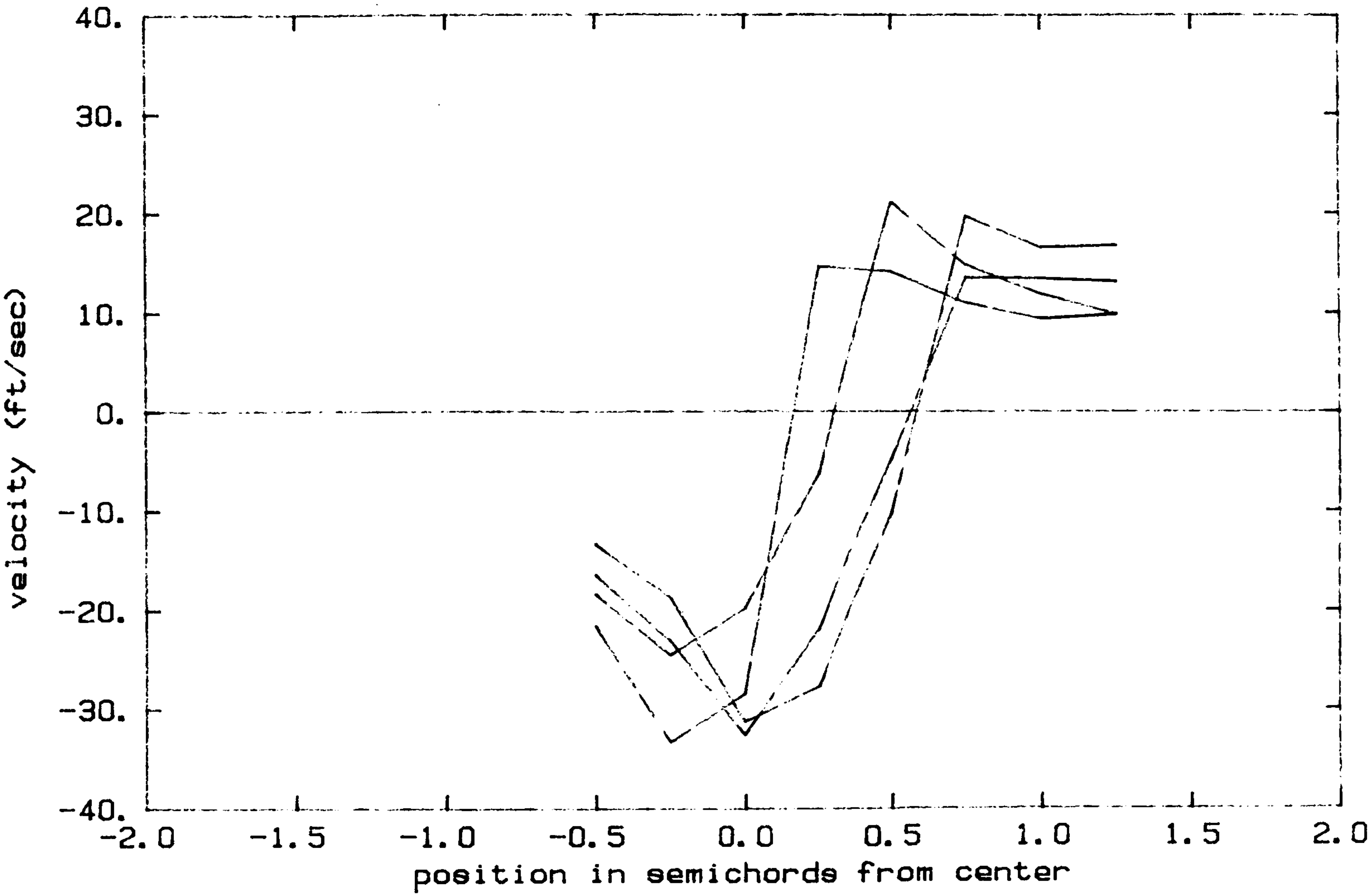

FIGURE 30 b. MEASURED VORTEX VELOCITY DATA WITHOUT SHIFTING TO ACCOUNT FOR VARIATIONS IN VORTEX POSITION. ADVANCE RATIO=.15

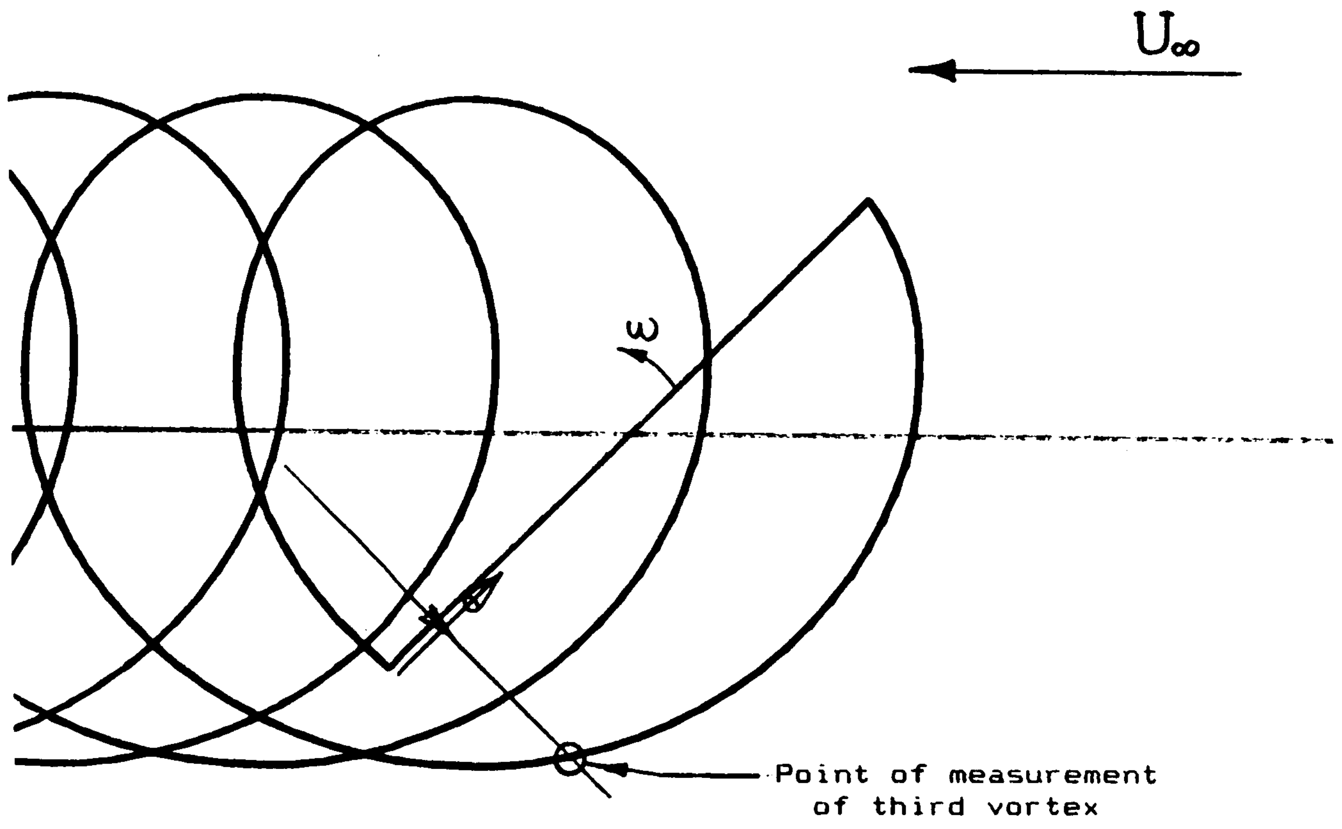

Figure 31. Top view of the experiment at the point of measurement of the third vortex.

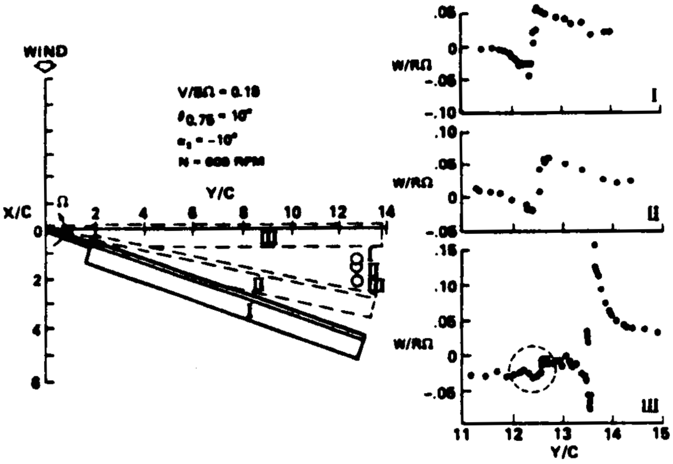

Figure 32. Blade vortex encounter as measured by Biggers and Orloff. [ref 39]. Vortex in I and II is circled in III. The large vortex to the right of the circled vortex was just generated by the blade shown in the figure.

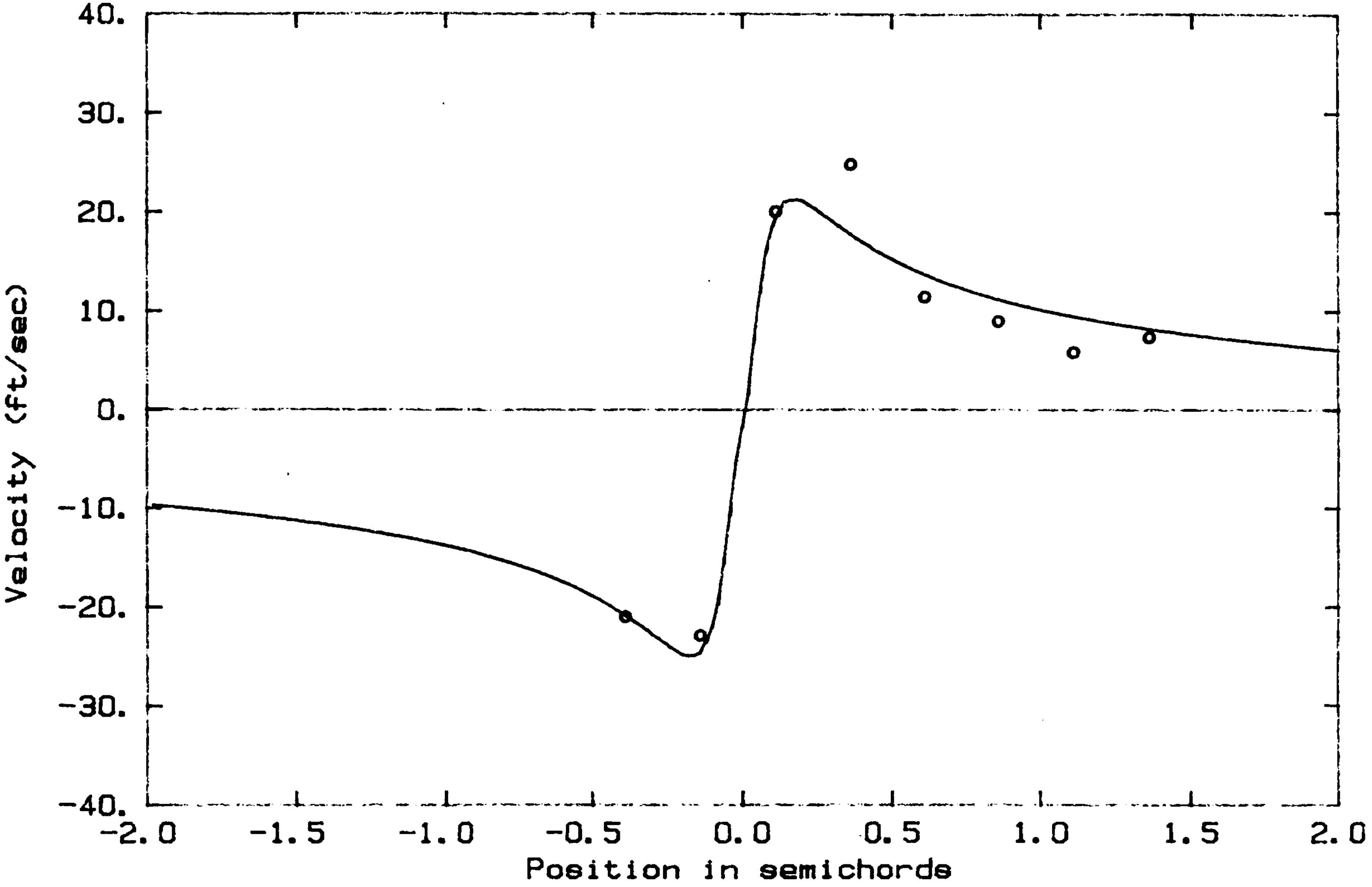

FIGURE 33. MODIFIED BETZ VORTEX FOR SINGLE VORTEX MEASUREMENT.
GAMMA=9.89FT**2/SEC; CO=.1; ADVANCE RATIO=.19

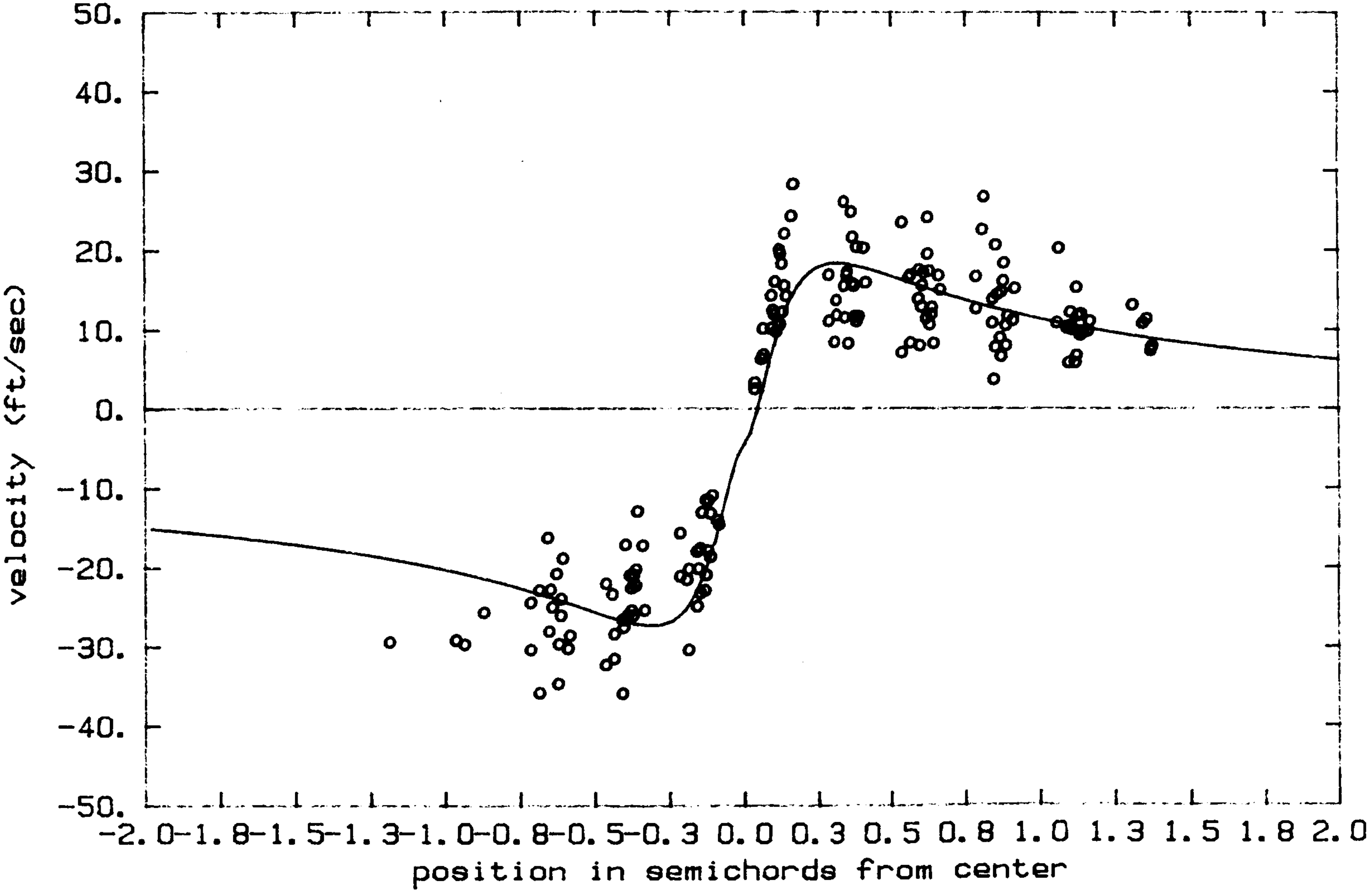

FIGURE 34. MODIFIED BETZ VORTEX DETERMINED AFTER SHIFTING THE DATA TO ACCOUNT FOR VARIATIONS IN THE VORTEX POSITION. GAMMA=13.4; CO=.185 INCHES; ADVANCE RATIO=.19

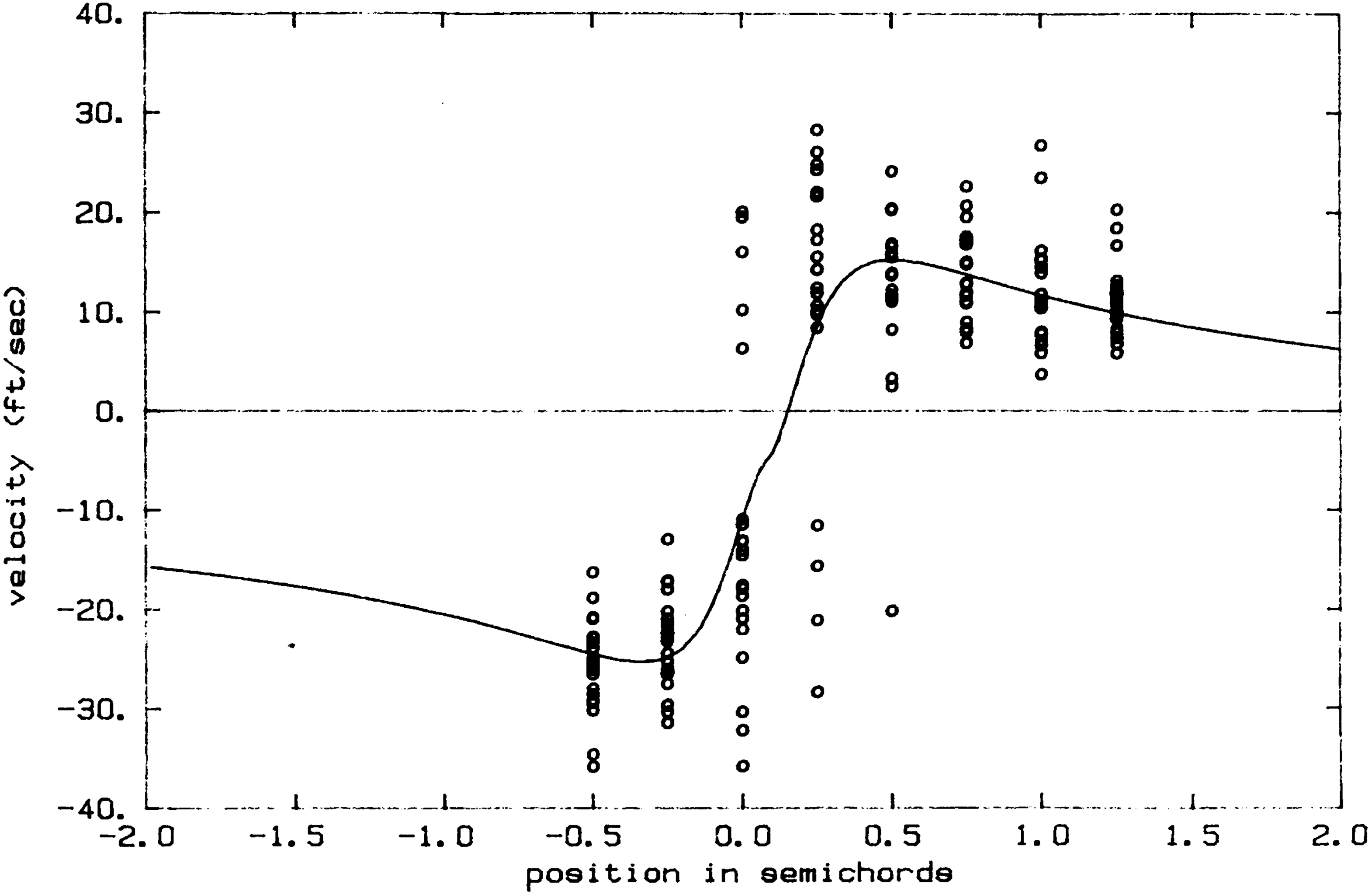

FIGURE 35. MODIFIED BETZ VORTEX MODEL DETERMINED WITHOUT SHIFTING DATA TO ACCOUNT FOR THE VARIATION IN THE VORTEX POSITION. GAMMA=14 FT**2/SEC; CO=.252 INCHES.

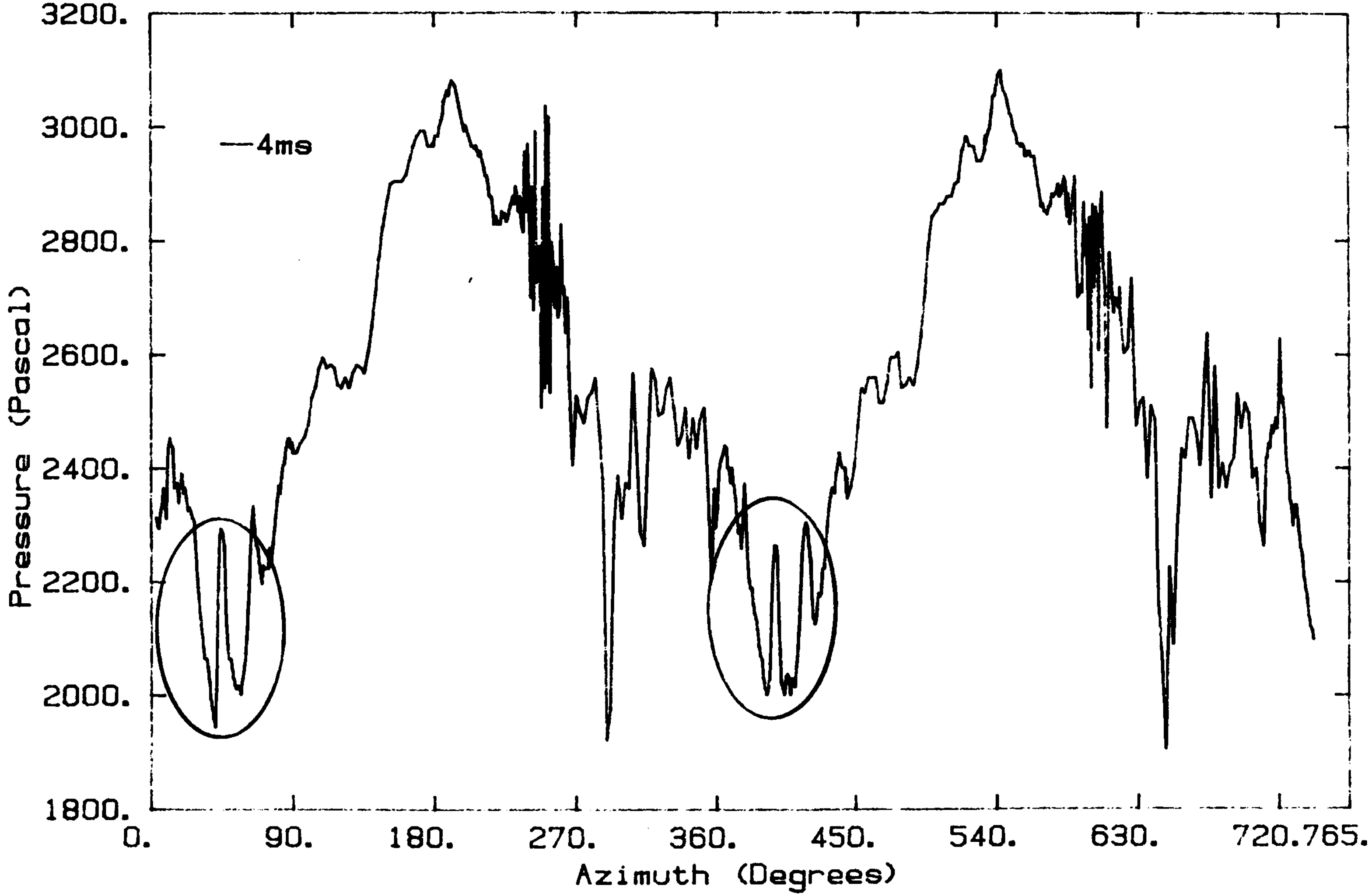

FIGURE 36. MEASURED BLADE PRESSURE AT 99% SPAN, 18.75% CHORD. CIRCLED AREAS ARE THE PRESSURE FLUCTUATIONS RESPONSIBLE FOR BLADE SLAP ACOUSTIC PULSE.

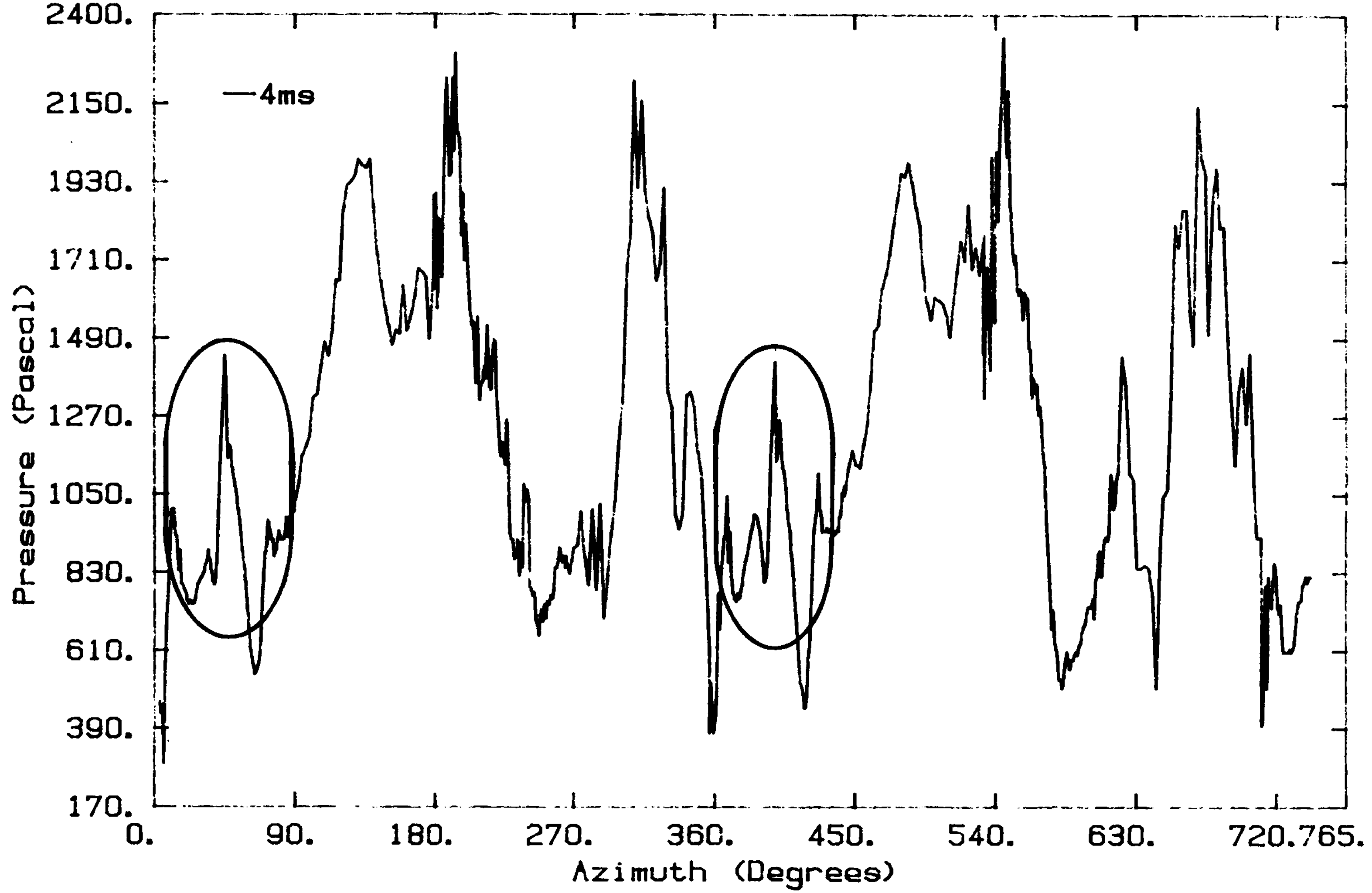

FIGURE 37. MEASURED BLADE PRESSURE DIFFERENTIAL AT 76% SPAN, 18.75% CHORD. CIRCLED AREAS ARE THE PRESSURE FLUCTUATIONS RESPONSIBLE FOR BLADE SLAP ACOUSTIC PULSE.

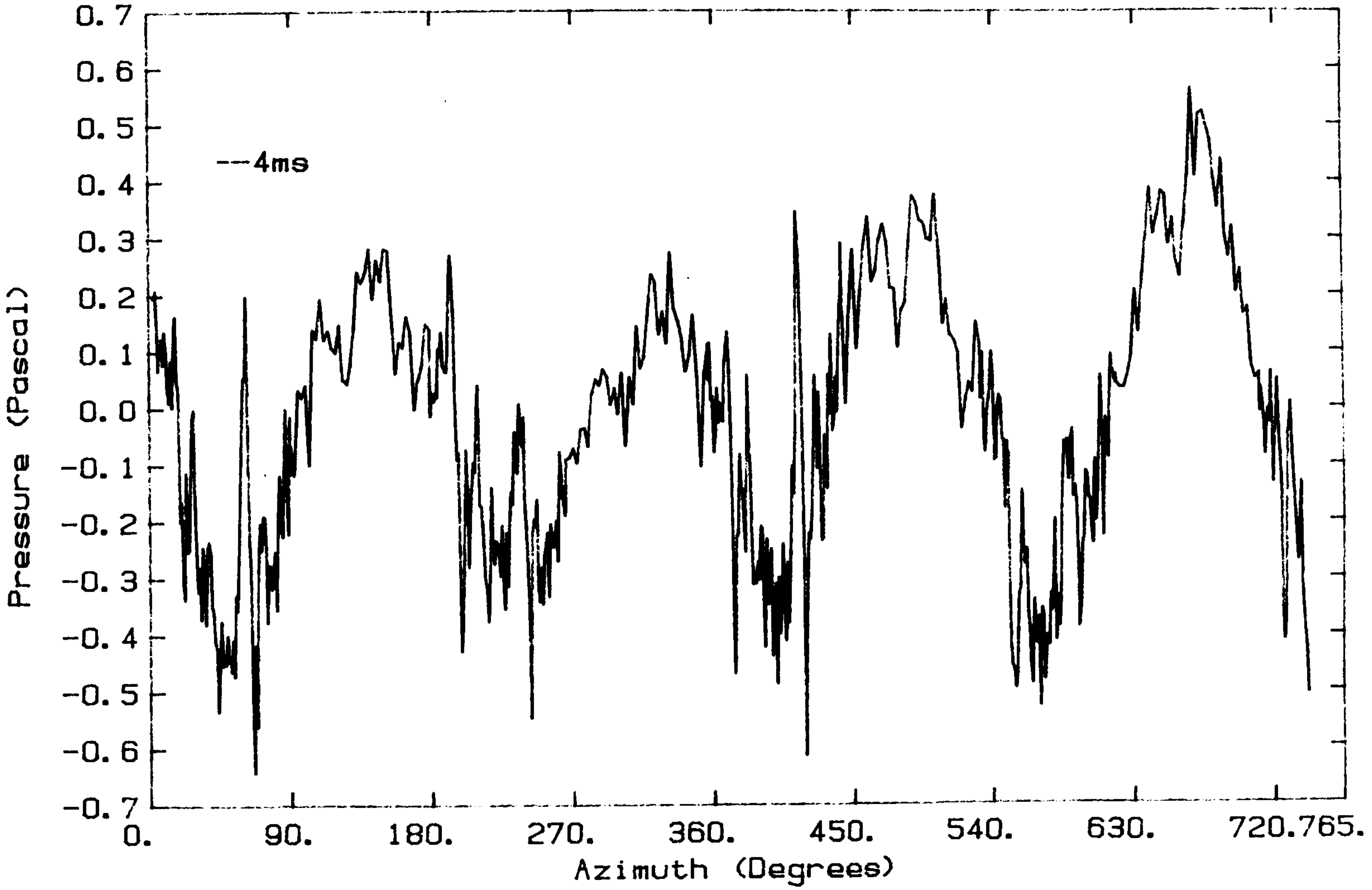

FIGURE 38. MEASURED ACOUSTIC SIGNATURE FOR ADVANCE RATIO OF 0.19

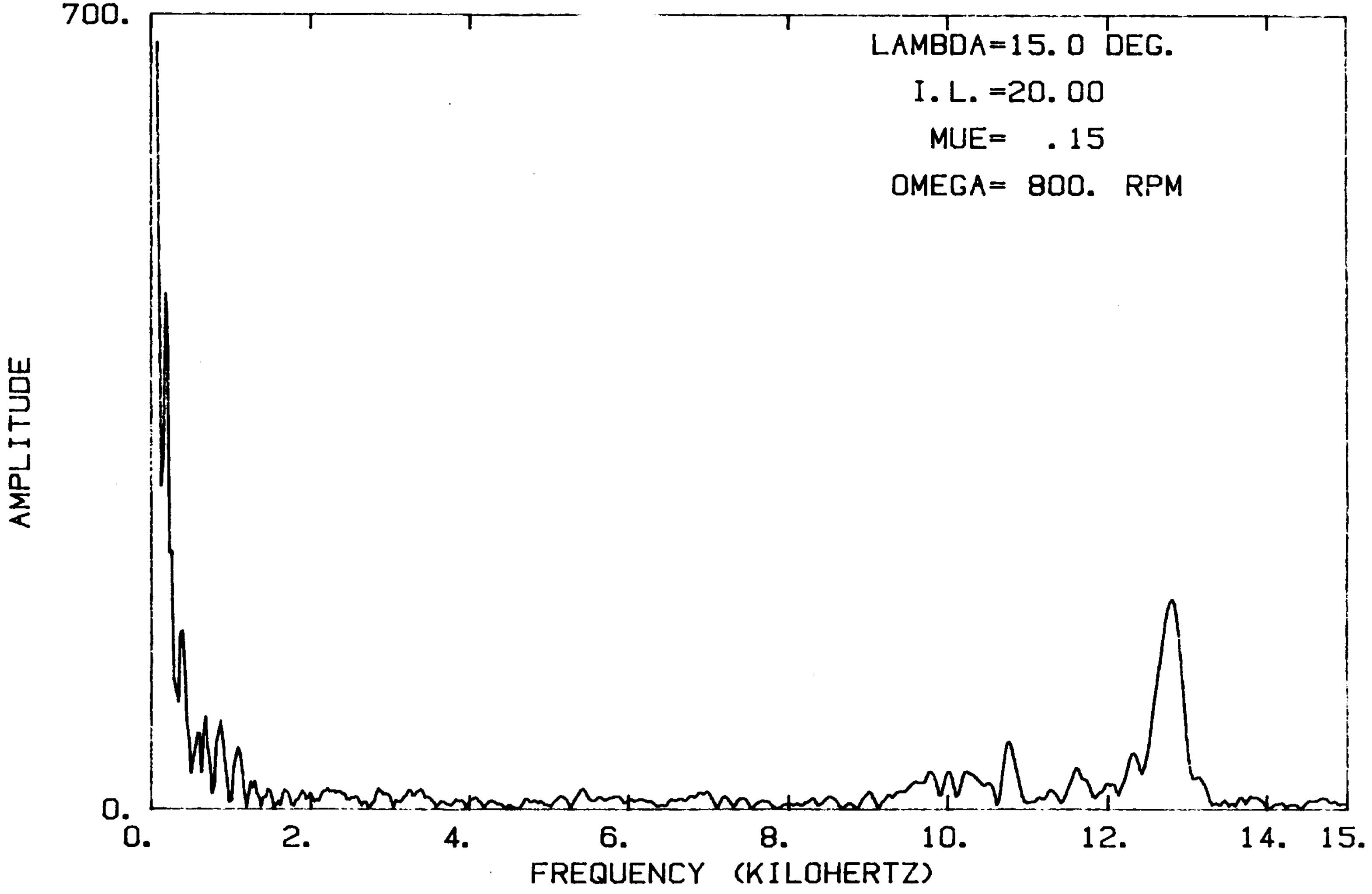

FIGURE 39. SPECTRUM OF REGION OF HIGH FREQUENCY NOISE MEASURED AT 99%SPAN, 18.75% CHORD ON RETREATING SIDE.

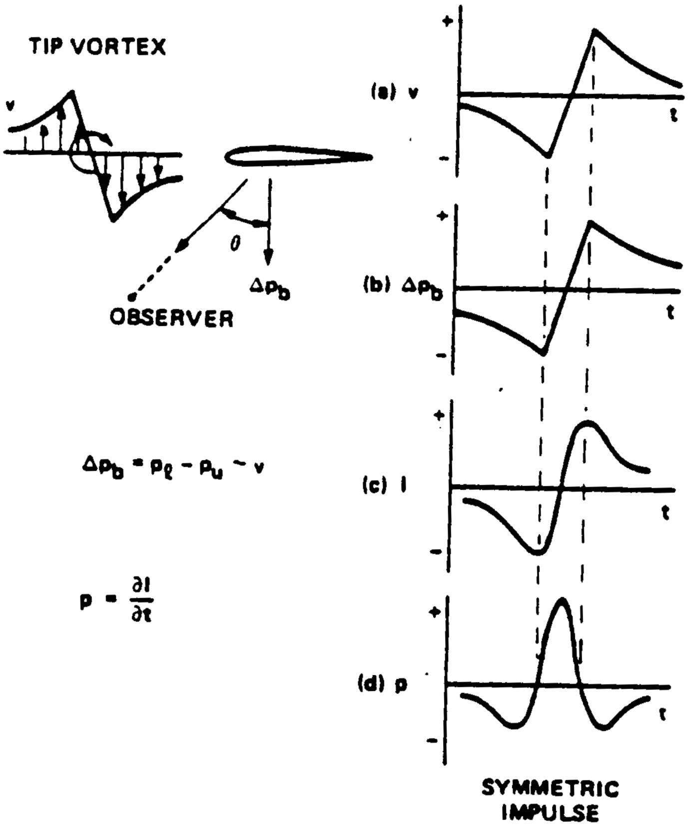

Figure 40. Geometrical relationship of the sinusoidal gust and acoustic pulse. [reference 22]

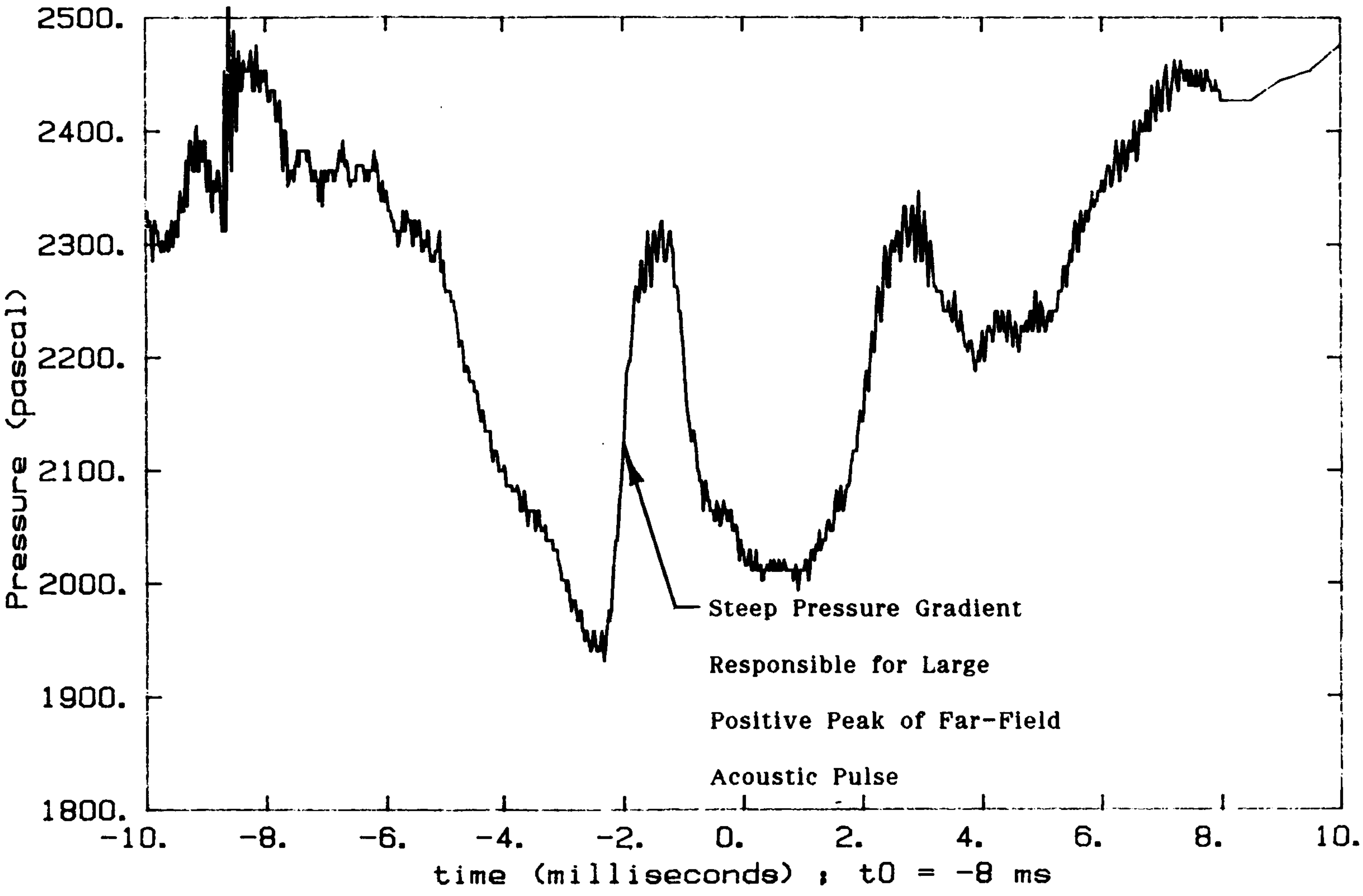

Steep Pressure Gradient Responsible for Large Positive Peak of Far-Field Acoustic Pulse

FIGURE 41. MEASURED PRESSURE AT 99% SPAN, 18.75% CHORD DURING BLADE-VORTEX INTERACTION RESPONSIBLE FOR BLADE SLAP. ADVANCE RATIO=.19

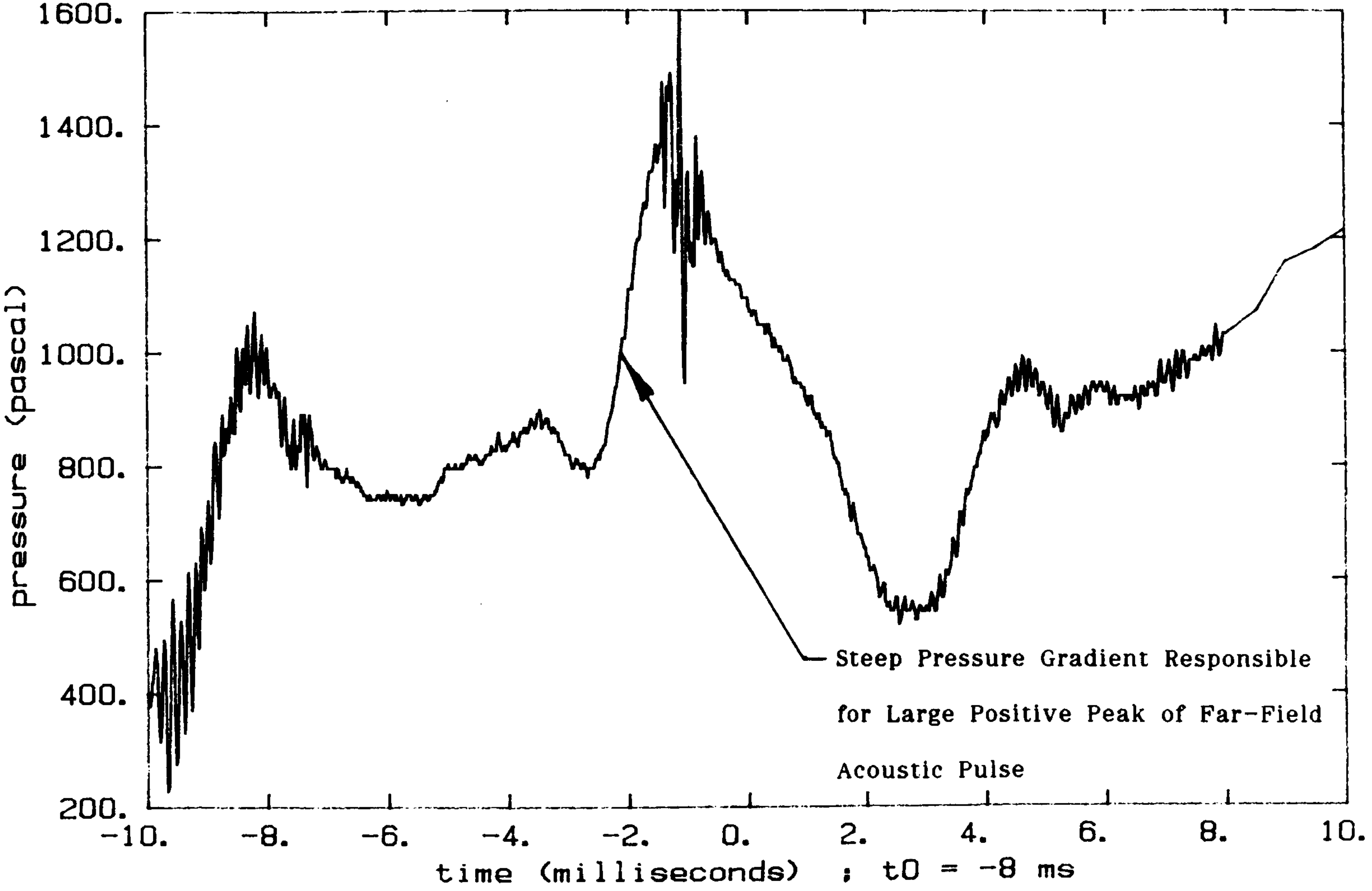

FIGURE 42. MEASURED PRESSURE FROM 76% SPAN, 18.75% CHORD FOR BLADE-VORTEX INTERACTION RESPONSIBLE FOR BLADE SLAP. ADVANCE RATIO=.19

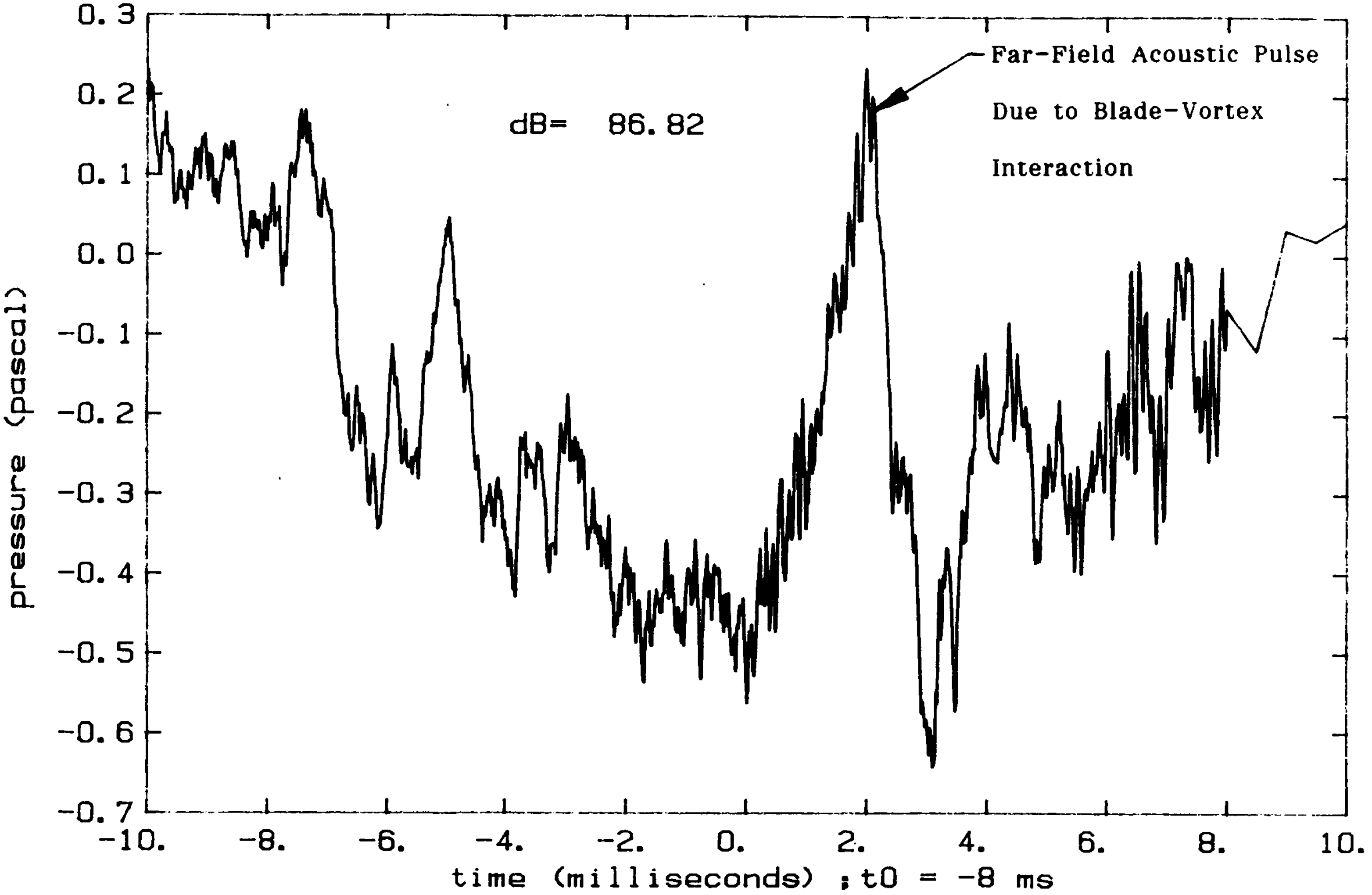

FIGURE 43. MEASURED ACOUSTIC SIGNATURE OF BLADE-VORTEX INTERACTION.
ADVANCE RATIO=. 19

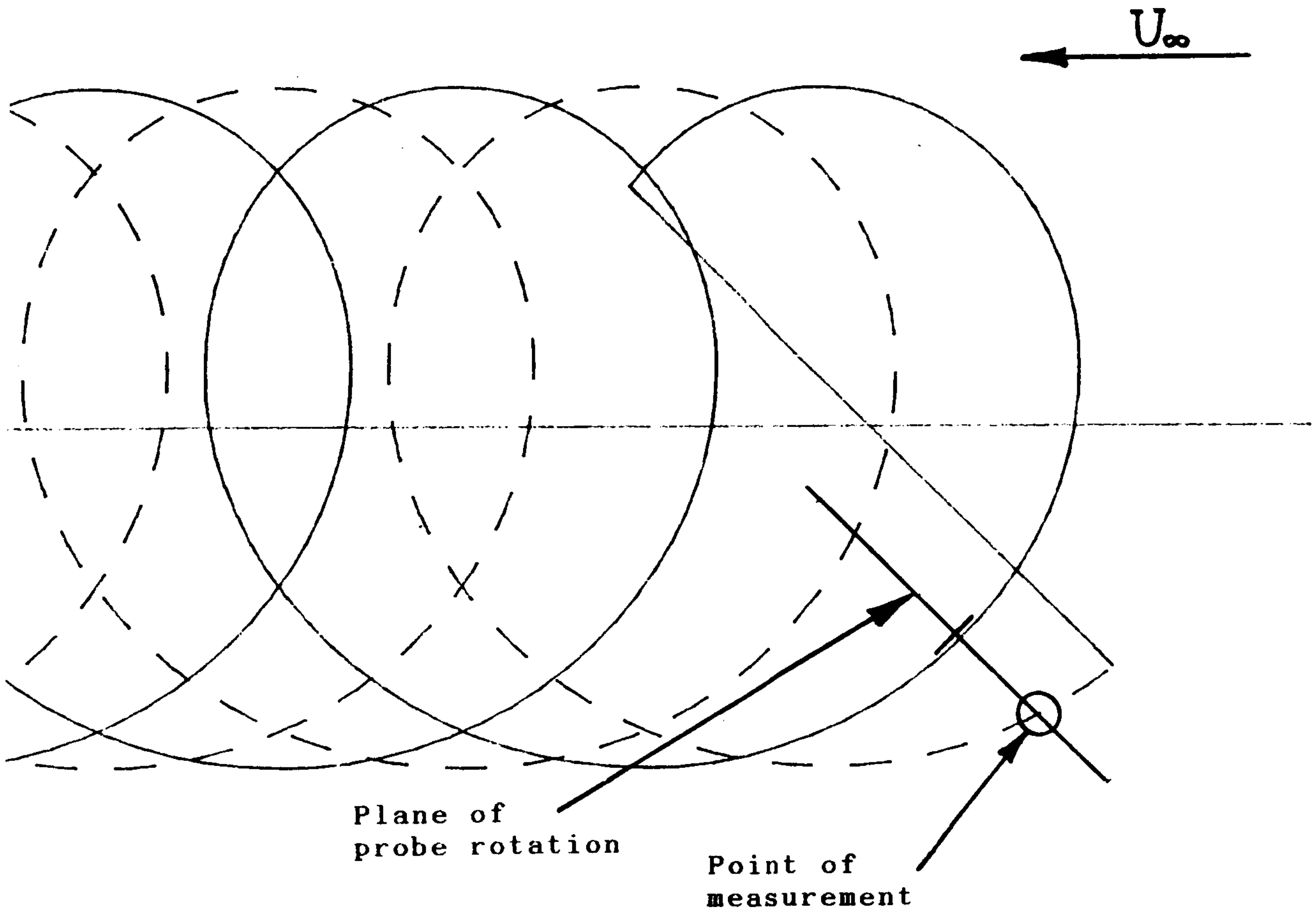

FIGURE 44. LOCATION OF PROBE FOR MEASUREMENT OF TIP VORTEX JUST AFTER VORTEX IS GENERATED. ADVANCE RATIO=.17; AZIMUTH=135 DEGREES.

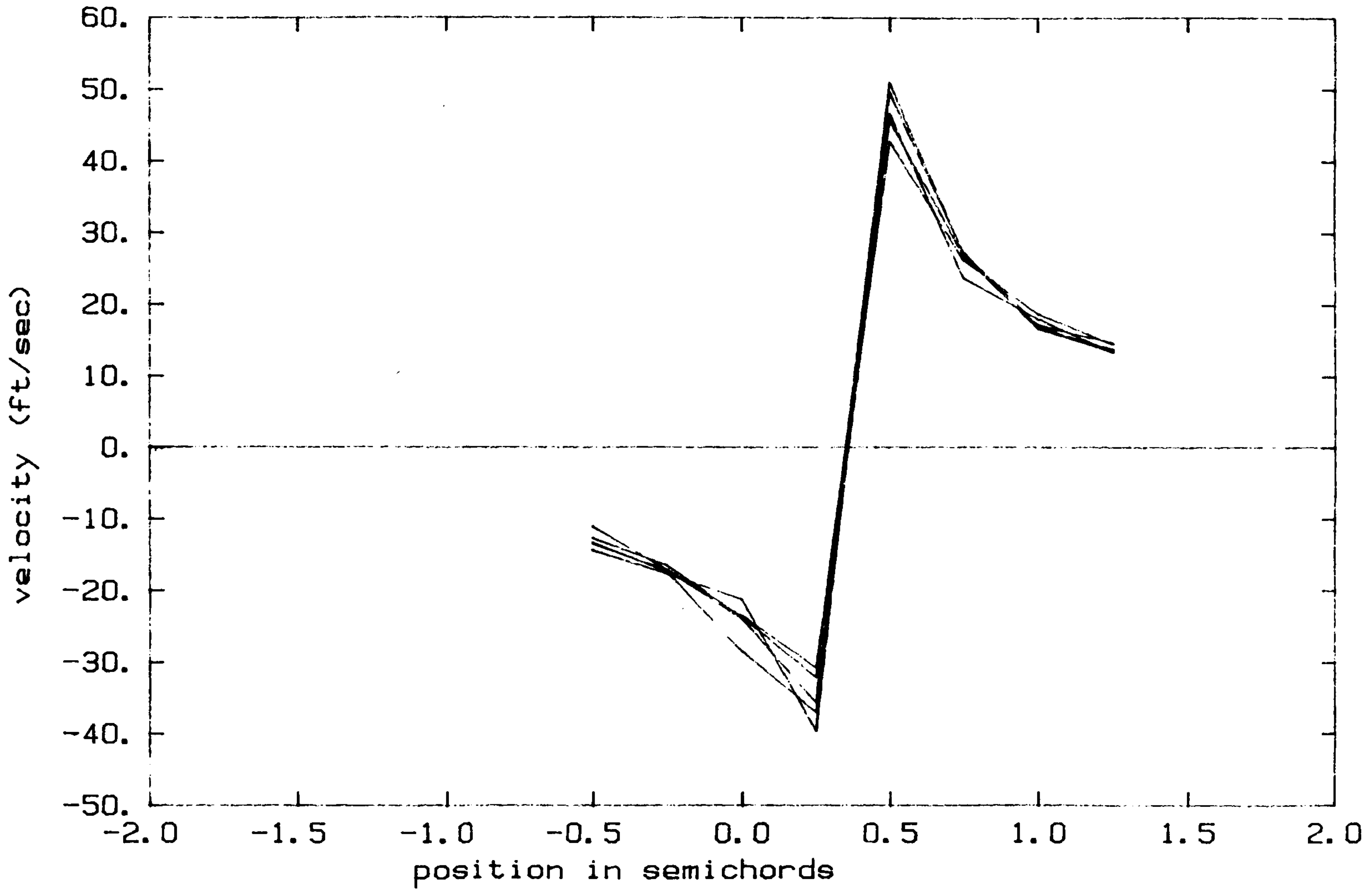

FIGURE 45. TIP VORTEX AS MEASURED JUST AFTER VORTEX IS GENERATED. CORRESPONDING MEASURED VALUES CONNECTED BY LINES. DATA NOT SHIFTED. ADVANCE RATIO=.17

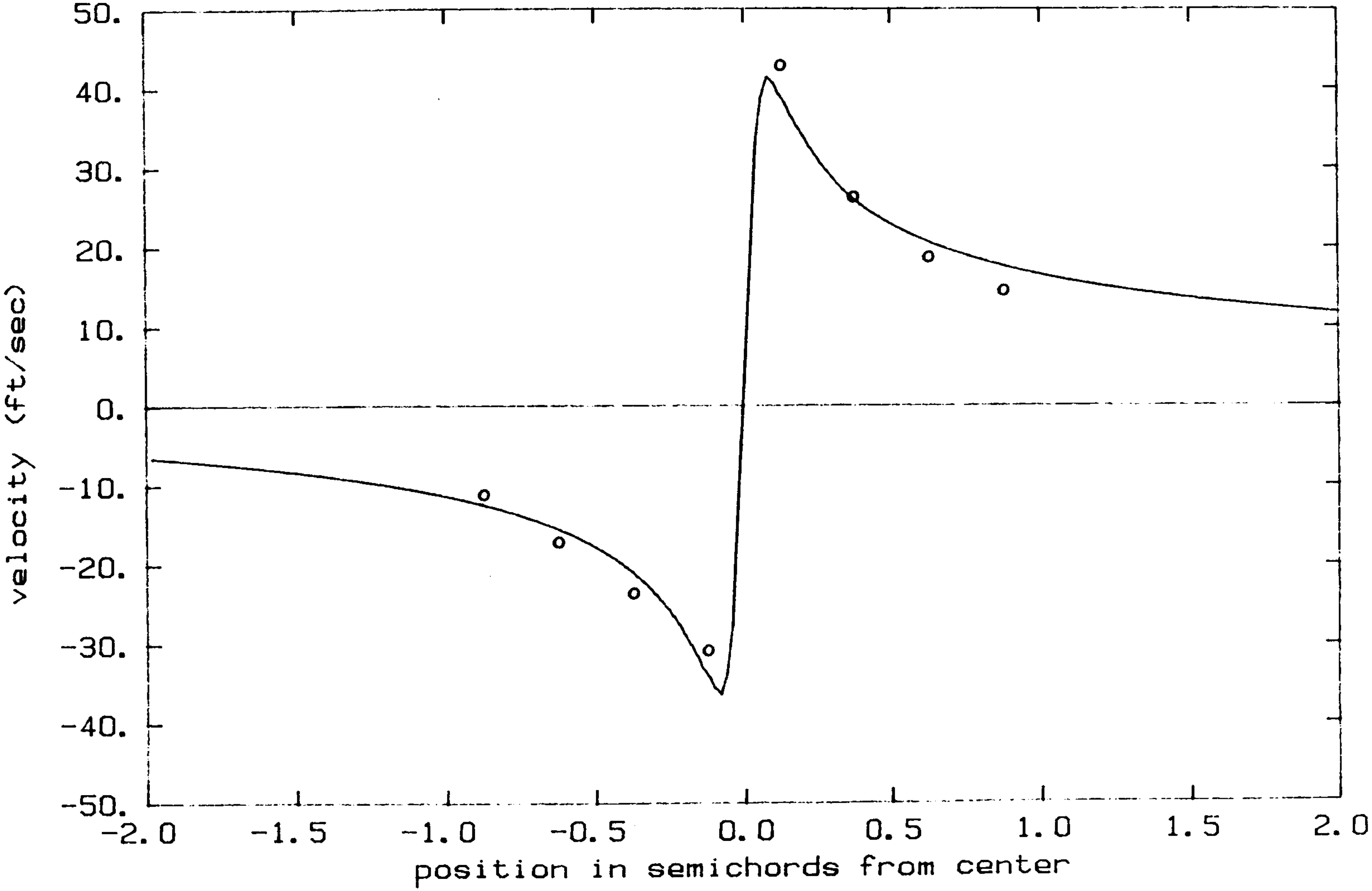

FIGURE 46. MODIFIED BETZ VORTEX MODEL OF VORTEX JUST AFTER GENERATION.
GAMMA=11.4 FT**2/SEC; CO=.048 IN.; ADVANCE RATIO=.17

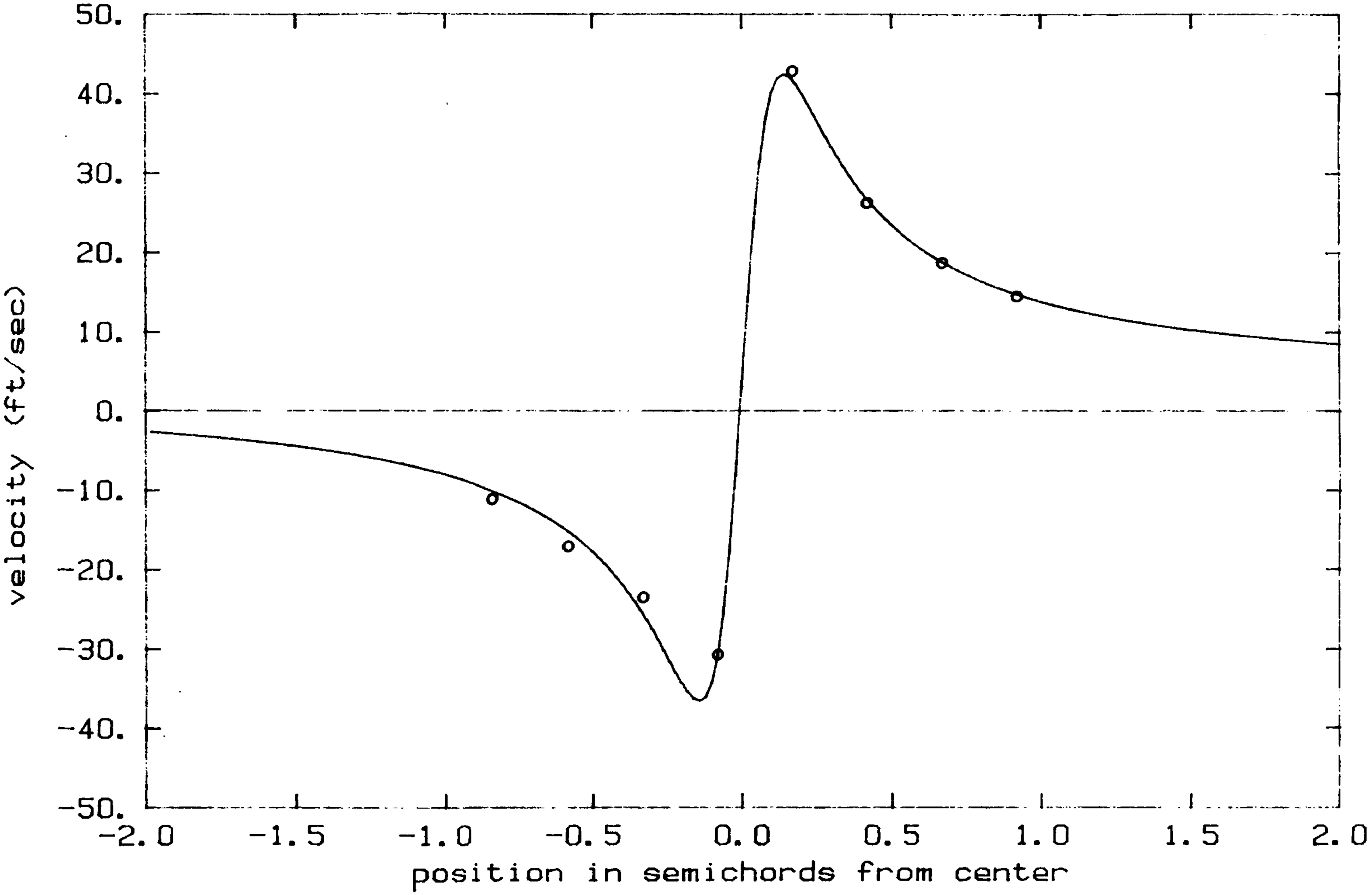

FIGURE 47. FREE VORTEX WITH CORE CURVE FIT OF VORTEX JUST AFTER GENERATION.
GAMMA=5.8 FT**2/SEC; CO=.141; ADVANCE RATIO=.17

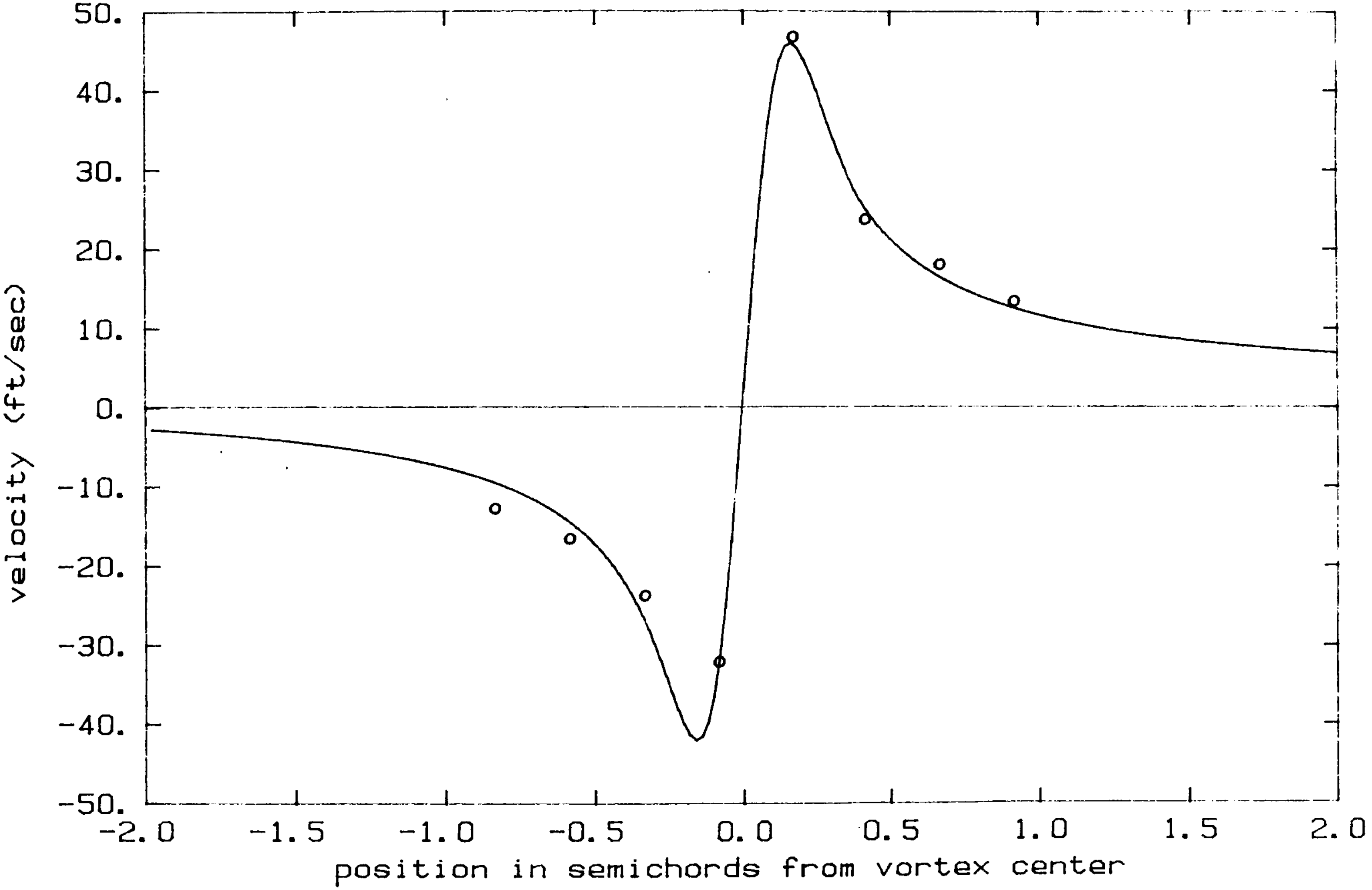

FIGURE 48. EXPONENTIAL VORTEX MODEL OF VORTEX JUST AFTER GENERATION.
GAMMA=5.05 FT**2/SEC; CO=.157 IN.; ADVANCE RATIO=.17

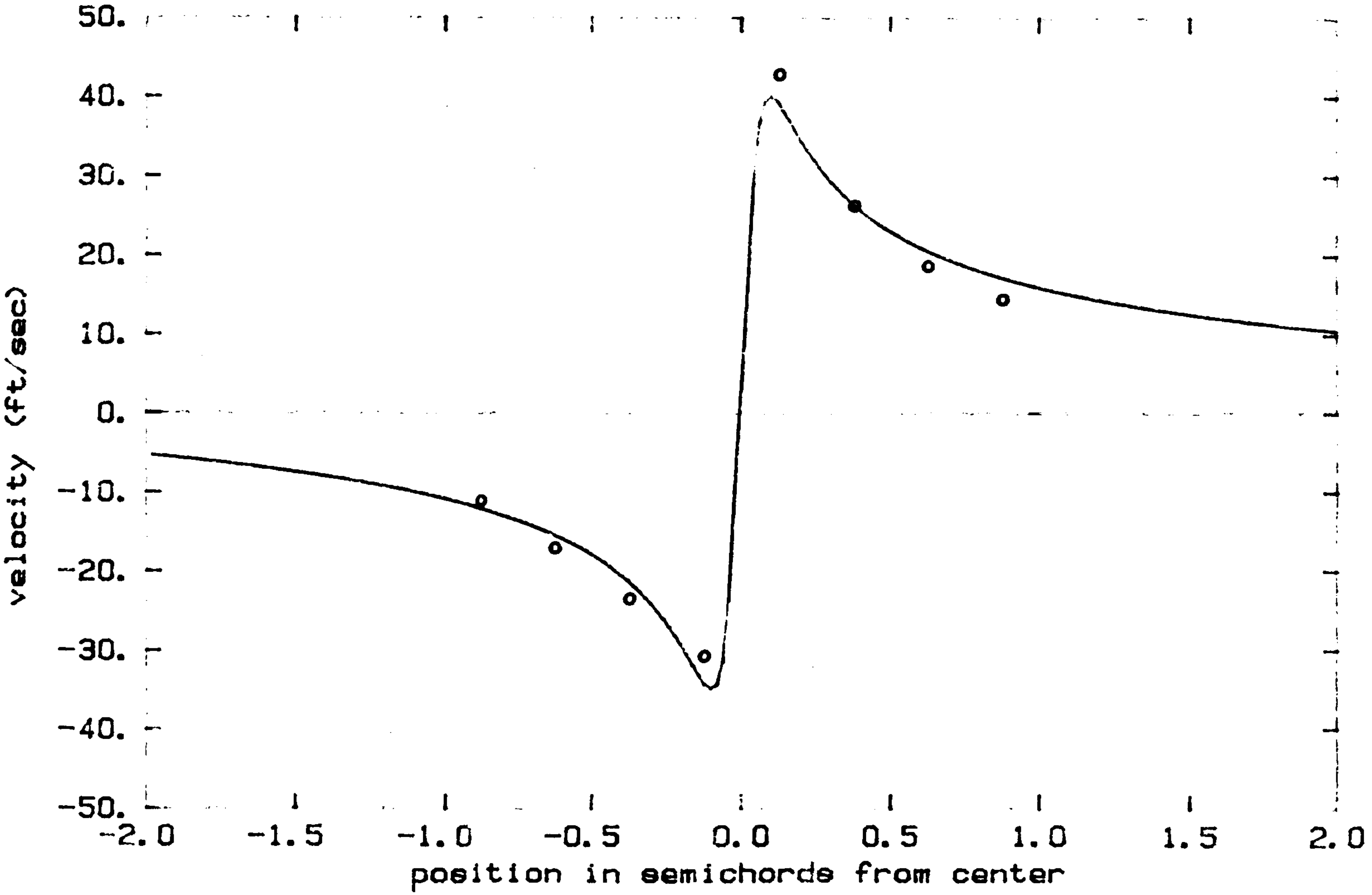

FIGURE 49. MODIFIED BETZ VORTEX MODEL WITH MAXIMUM BLADE CIRCULATION THREE SEMICHORDS FROM TIP. GAMMA=8.3 FT**2/SEC; CO=.056 IN.; ADVANCE RATIO=.17

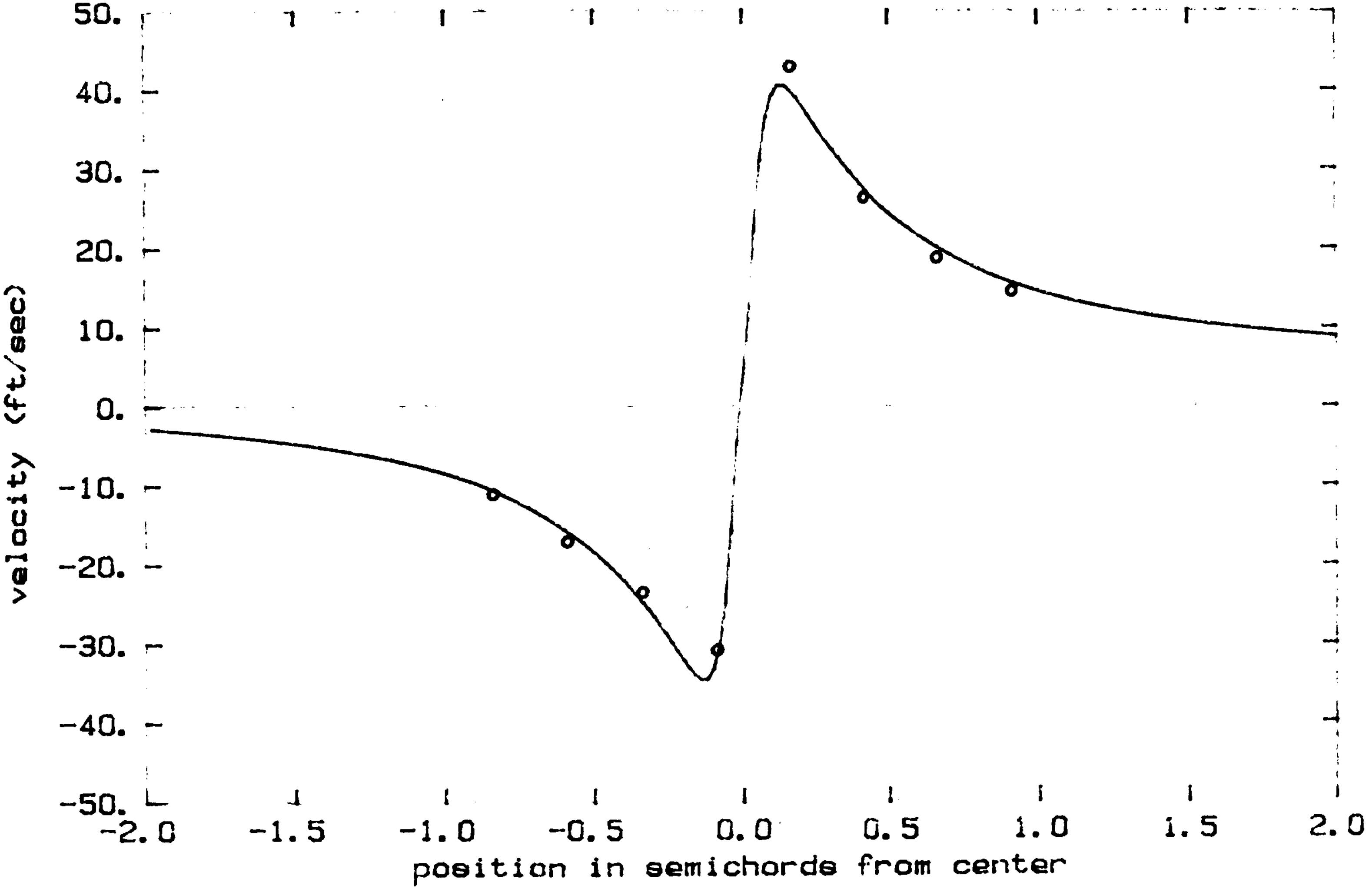

FIGURE 50. MODIFIED BETZ VORTEX MODEL WITH POINT OF MAXIMUM SPANWISE CIRCULATION ONE SEMICHORD FROM THE TIP. GAMMA=6.1FT**/SEC, CO=.082, ADVANCE RATIO=.17

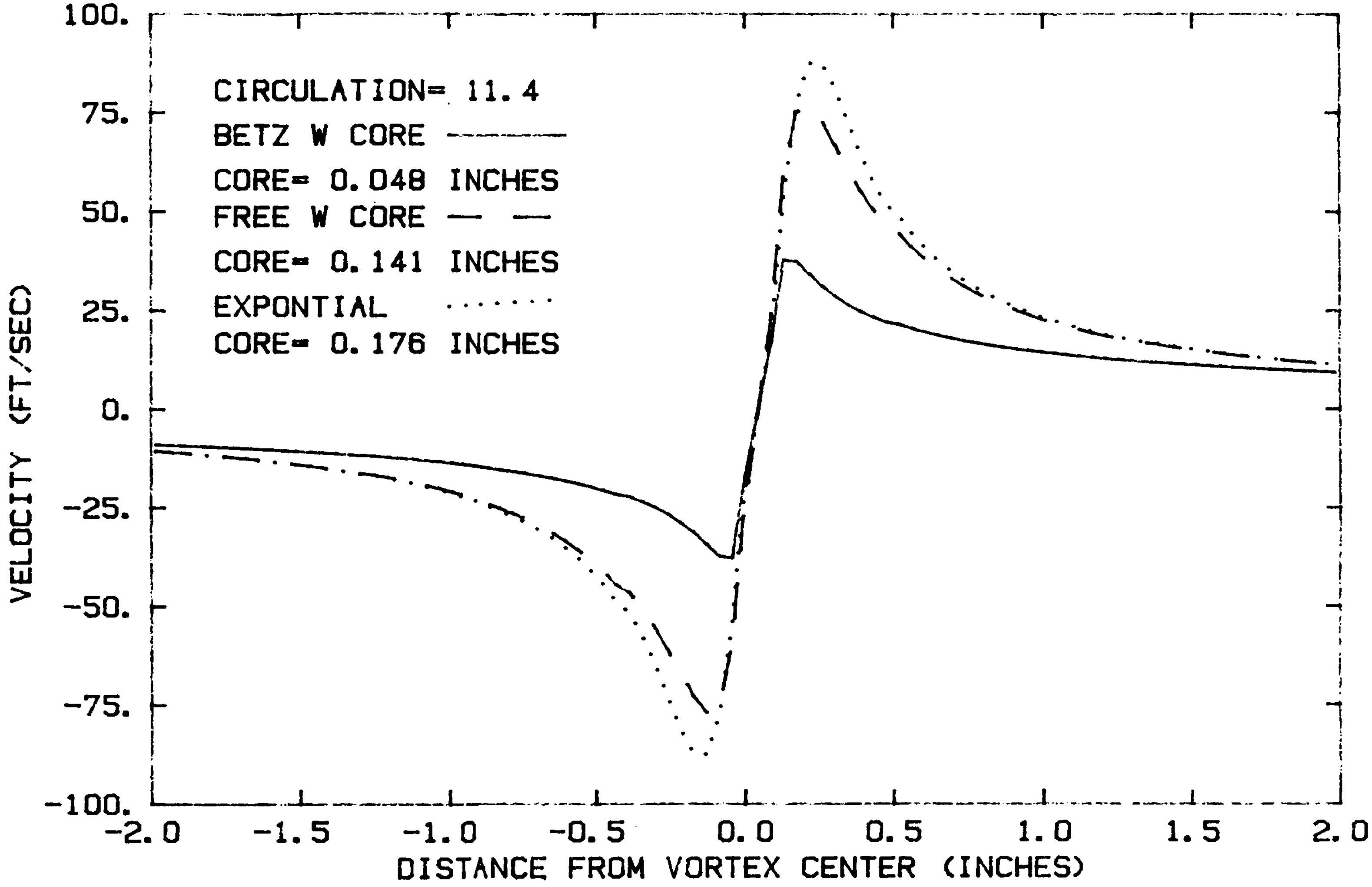

FIGURE 51. ILLUSTRATION OF DIFFERENCE IN VORTEX VELOCITY DISTRUBUTIONS OF THE THREE VORTEX MODELS GIVEN THE SAME CIRCULATION.

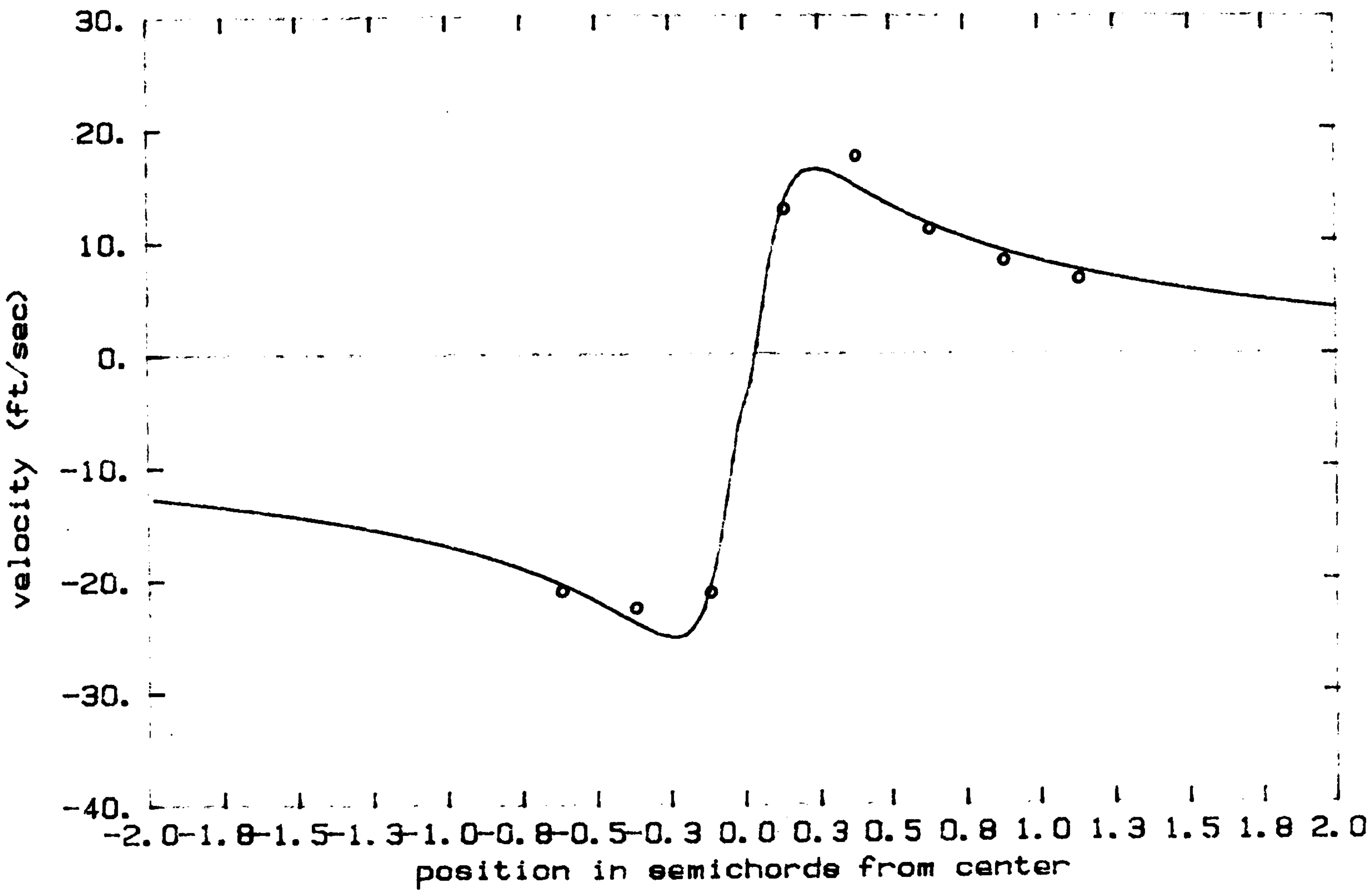

FIGURE 52. MODIFIED BETZ VORTEX MODEL AND DATA FOR THE VORTEX MEASURED JUST BEFORE BLADE-VORTEX INTERACTION. ADVANCE RATIO=.17; GAMMA=10.6FT**2/SEC; CO=.14 IN.

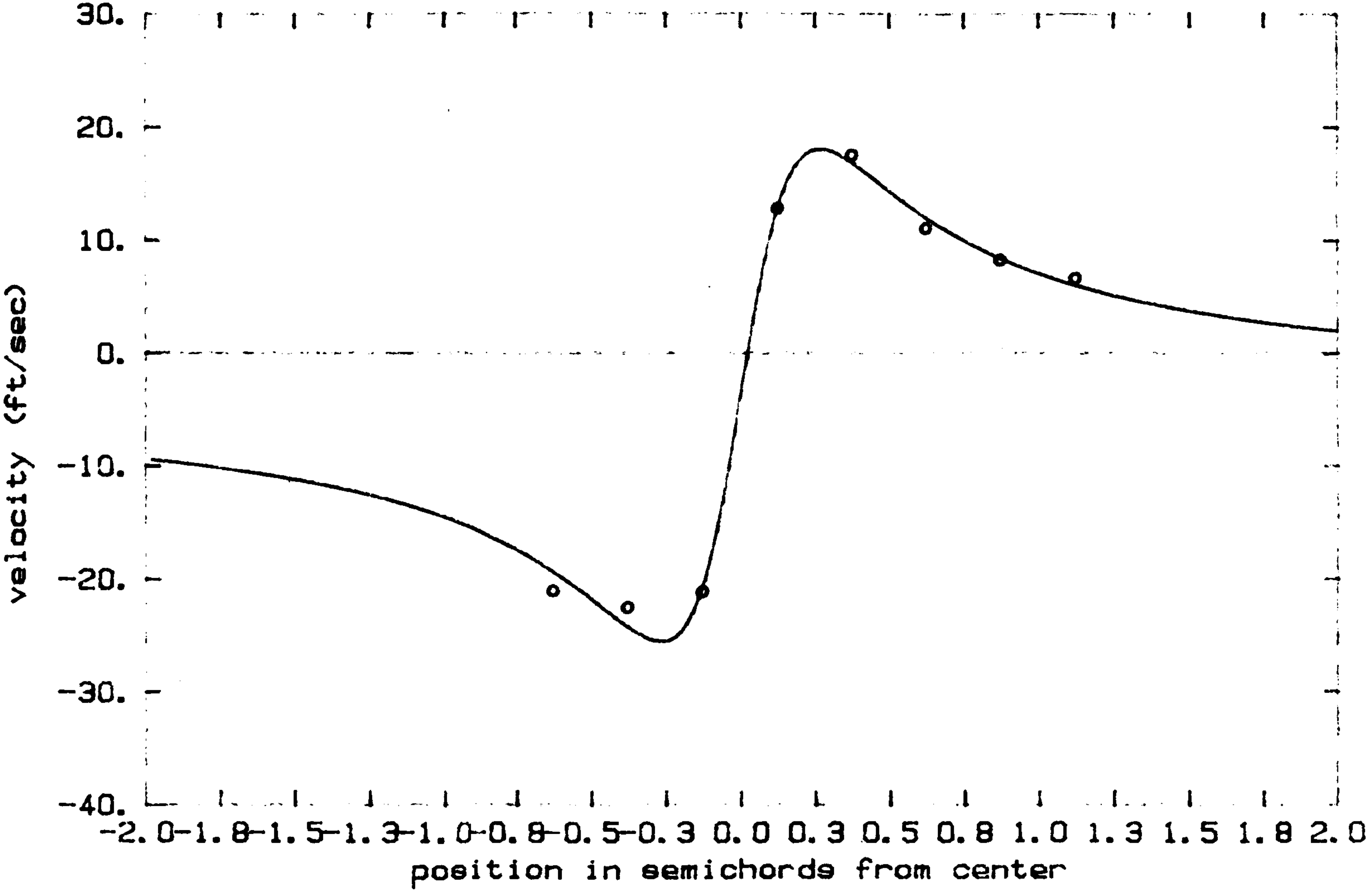

FIGURE 53. FREE VORTEX MODEL WITH CORE. ADVANCE RATIO =.17
GAMMA = 6.1 FT**2/SEC, CO=.265 IN.

ORIGINAL PAGE IS
OF POOR QUALITY

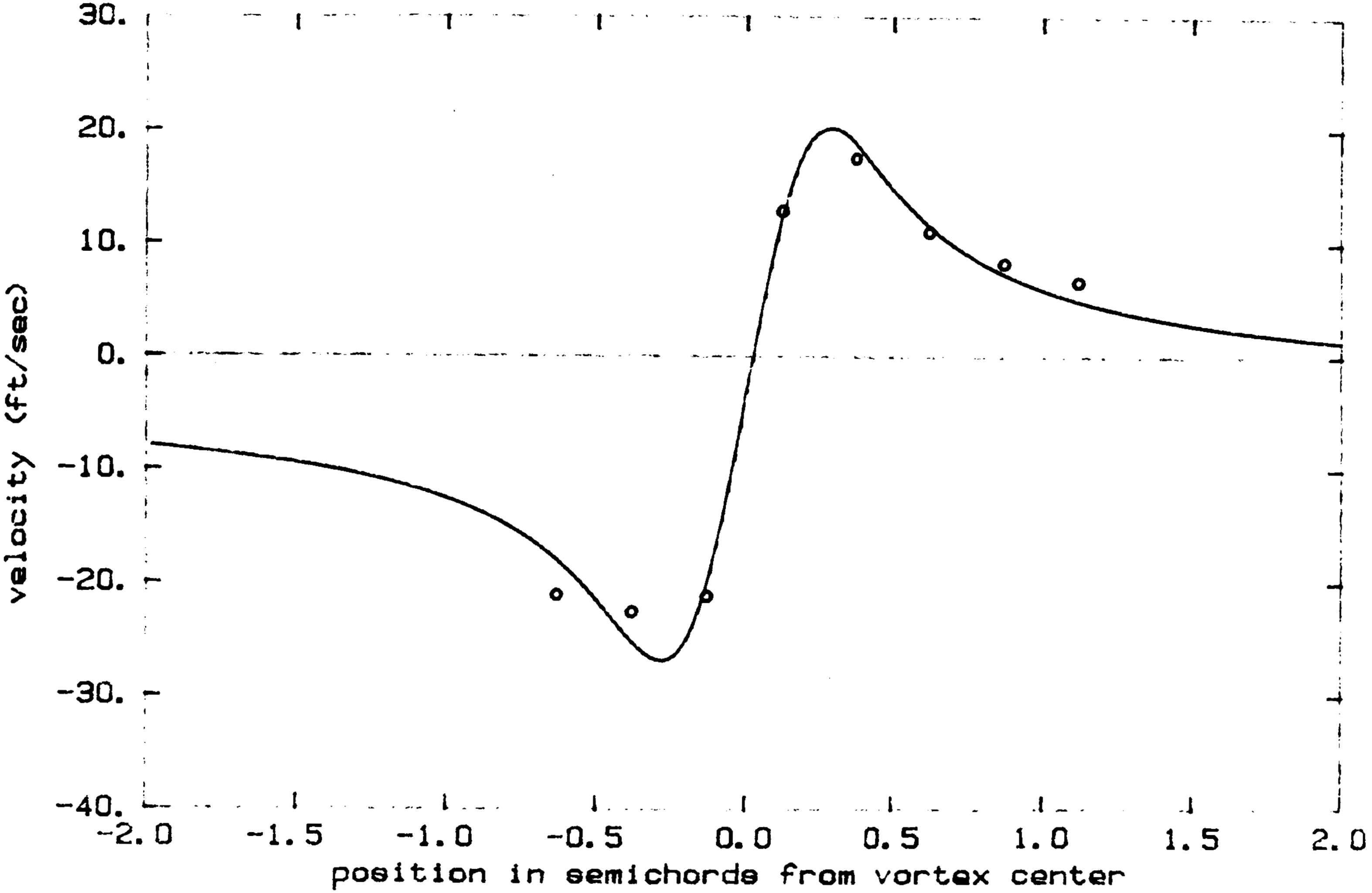

FIGURE 54. EXPONENTIAL VORTEX MODEL. ADVANCE RATIO = 0.17
GAMMA= 4.84 FT**2/SEC; CO=.282 IN.

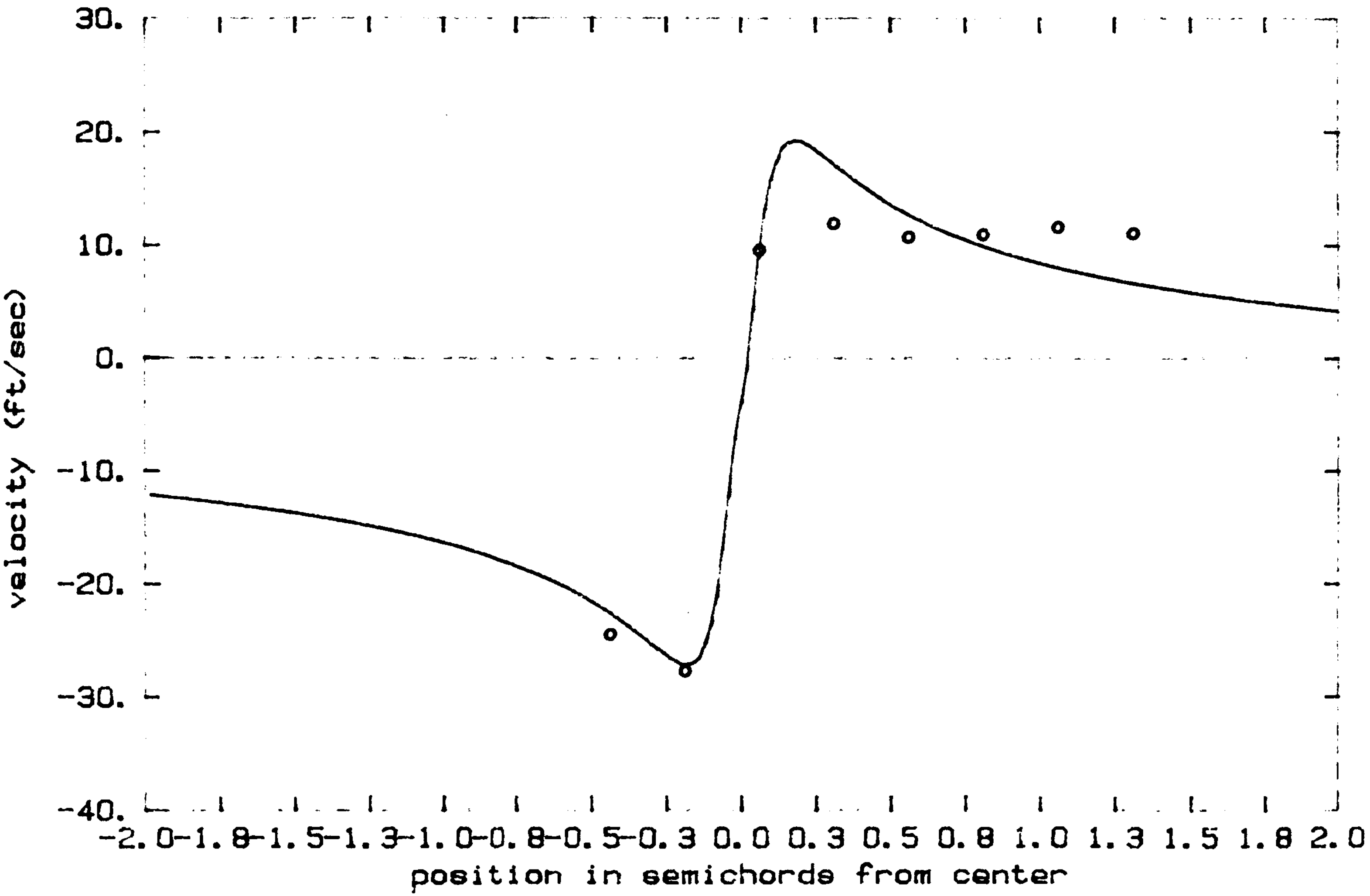

FIGURE 55. MEASURED VORTEX AT ADVANCE RATIO = 0.17 DEMONSTRATING THE VARIATION IN THE VORTEX VELOCITY DISTRIBUTION. GAMMA=10.2 FT**2/SEC, CO=.107 IN.

ORIGINAL PAGE IS OF POOR QUALITY

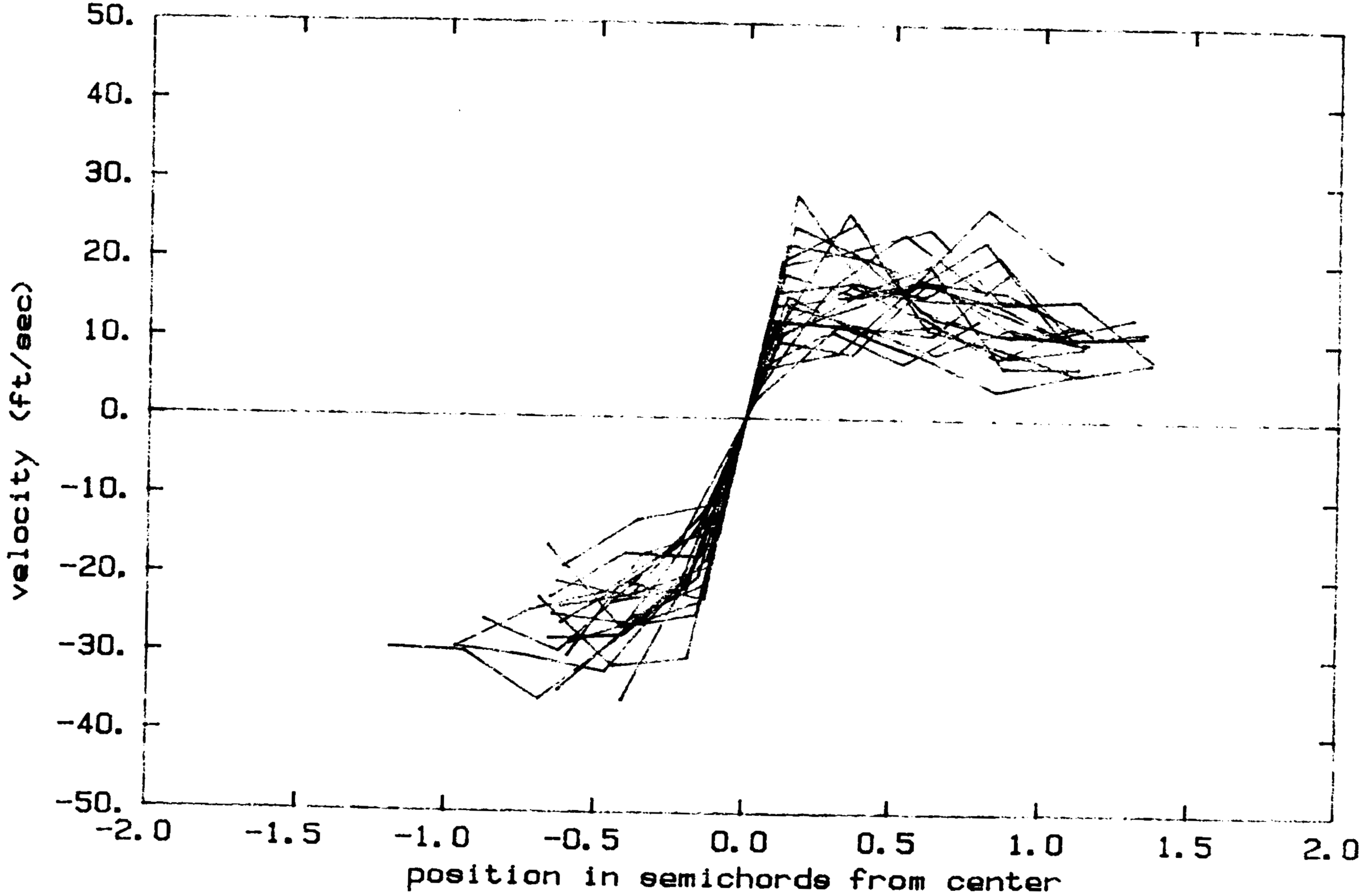

FIGURE 56. MEASURED VORTEX VELOCITIES SHIFTED TO ACCOUNT FOR VARIATIONS IN VORTEX POSITION. CORRESPONDING DATA POINTS CONNECTED BY LINES. ADVANCE RATIO = .19

ORIGINAL PAGE IS
OF POOR QUALITY

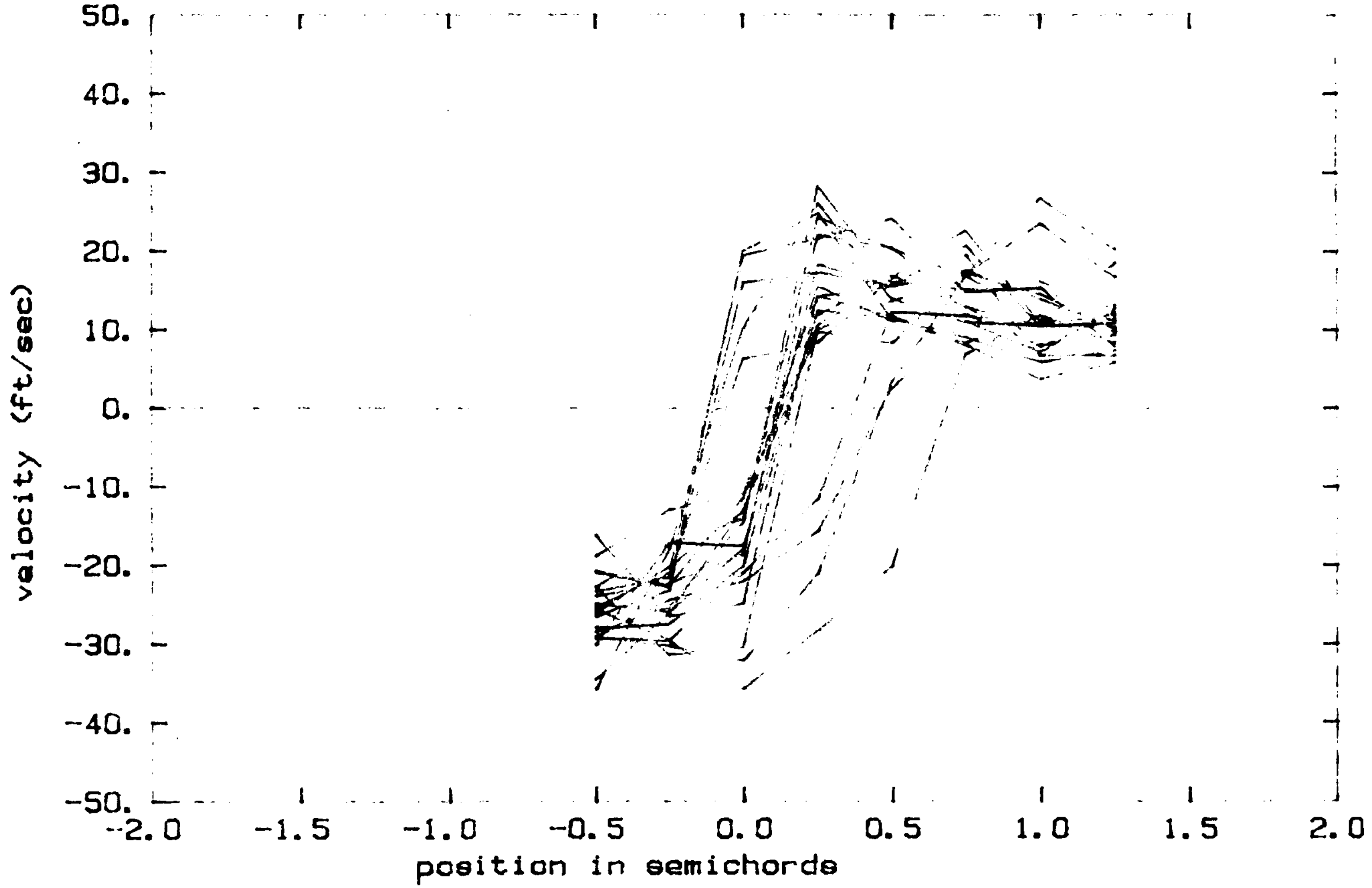

FIGURE 57. MEASURED DATA WITHOUT ADJUSTING FOR VARIATION VORTEX POSITION. ADVANCE RATIO = 0.19 (SAME DATA AS FIGURE 56.)

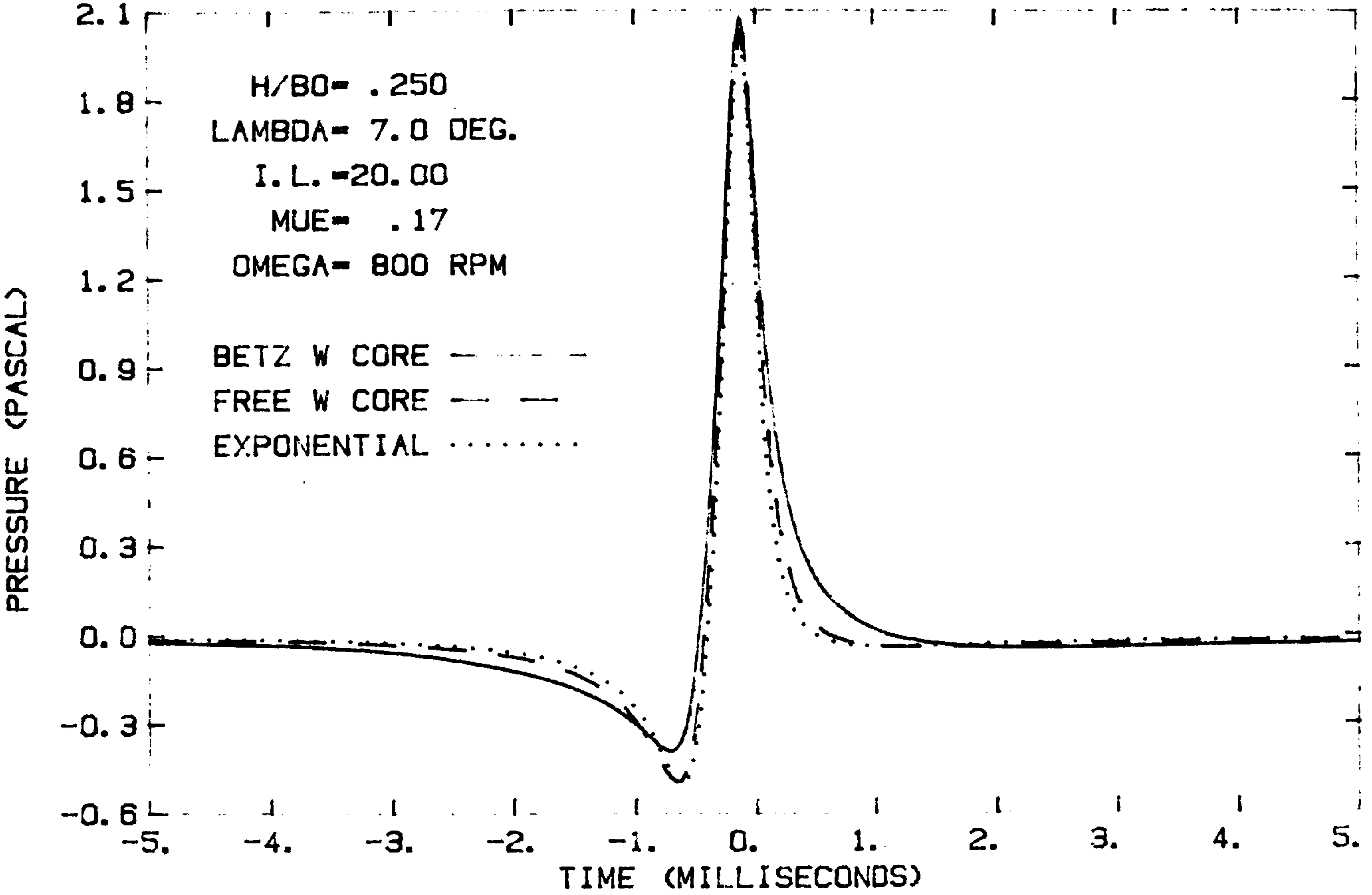

FIGURE 58. COMPARISON OF THE PREDICTED ACOUSTIC PULSES FROM THE THREE VORTEX MODELS FOR SMALL BLADE-VORTEX SEPARATION. (0.25 SEMICHORDS)

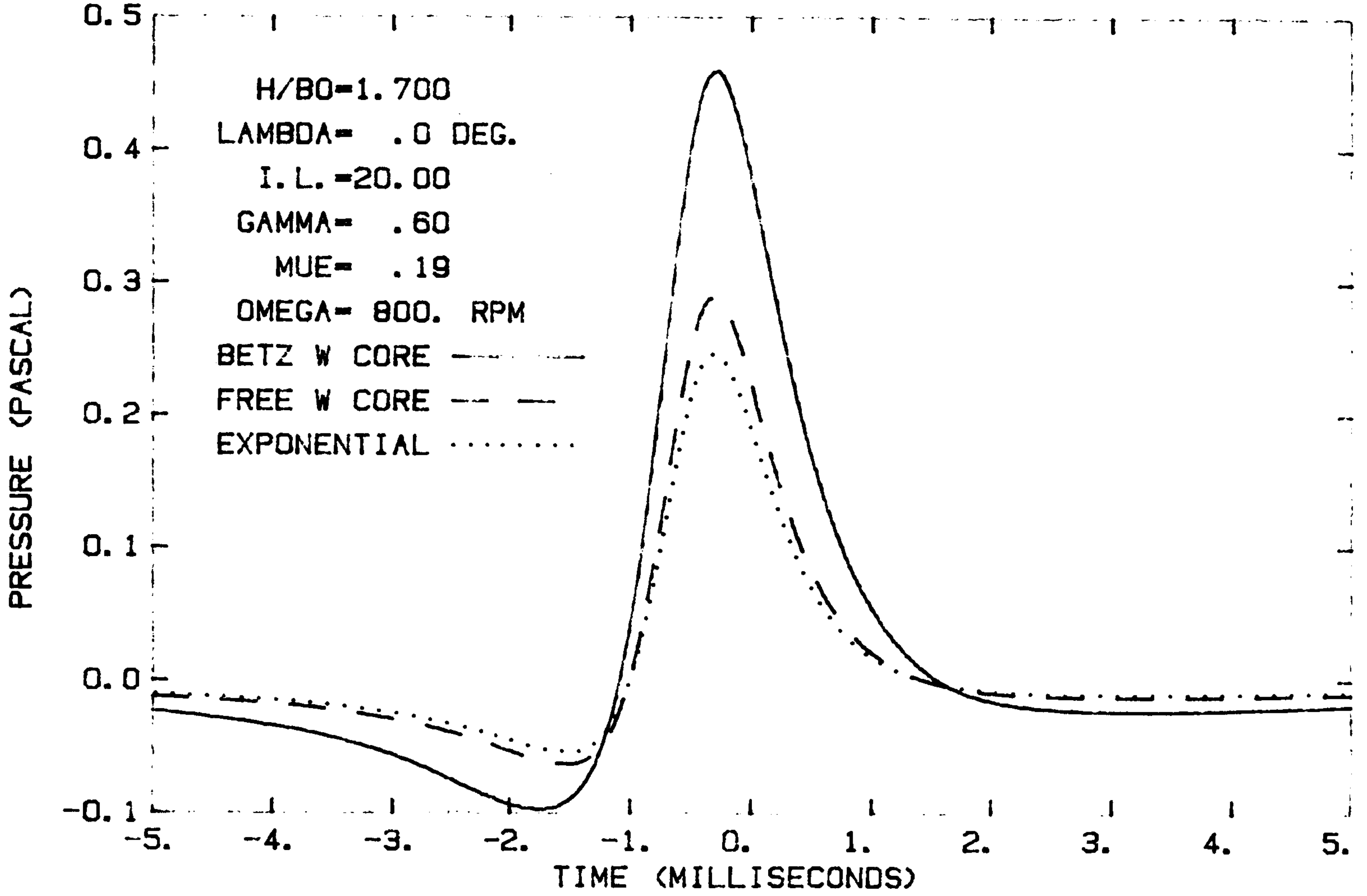

FIGURE 59. COMPARISON OF PREDICTED ACOUSTIC PULSES FOR EACH OF THE VORTEX MODELS WHEN THE BLADE VORTEX SEPARATION IS LARGE. (1.7 SEMICHORDS)

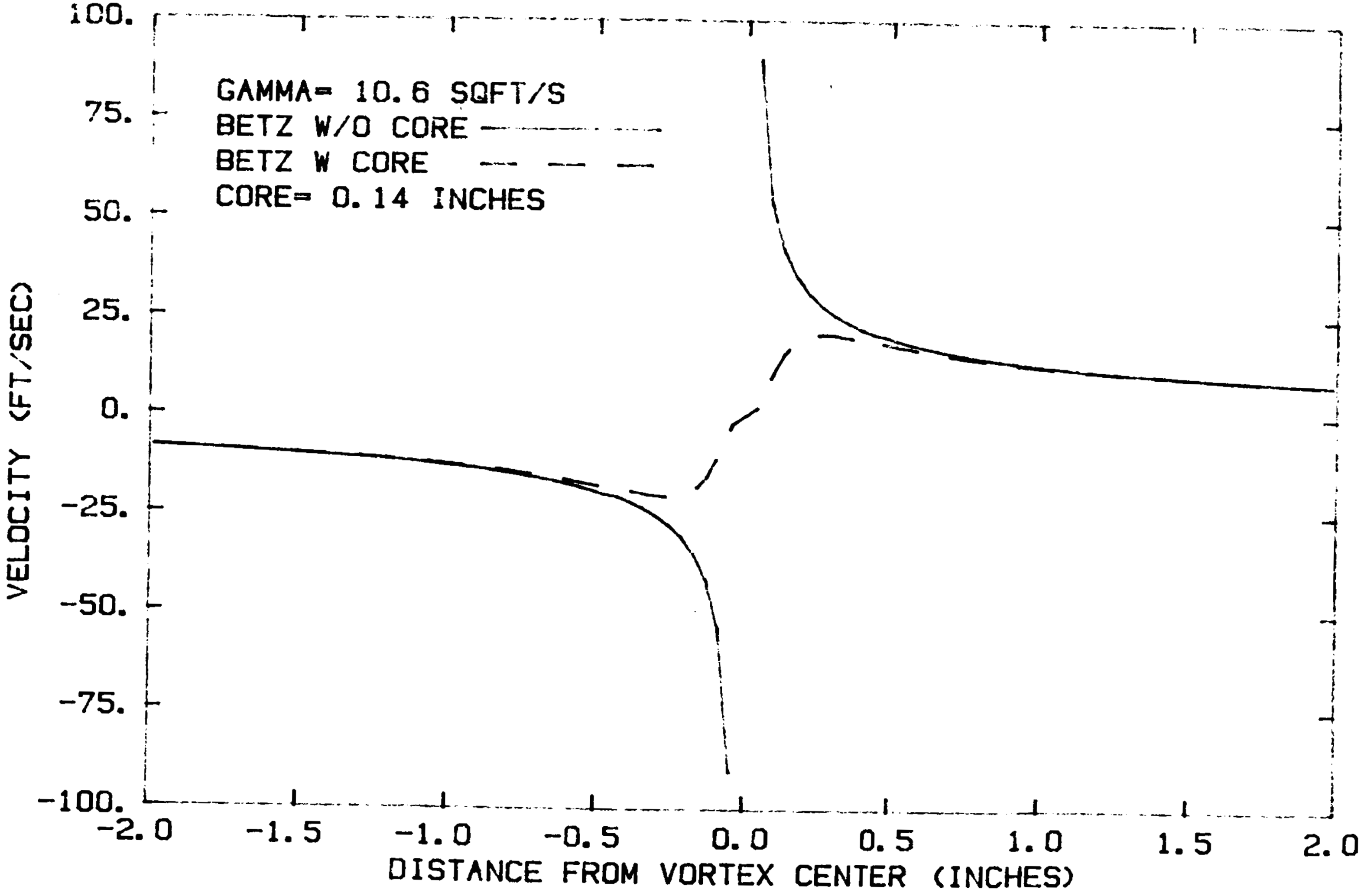

FIGURE 60. COMPARISON OF ORIGINAL BETZ VORTEX MODEL AND MODIFIED BETZ MODEL WITH CORE.

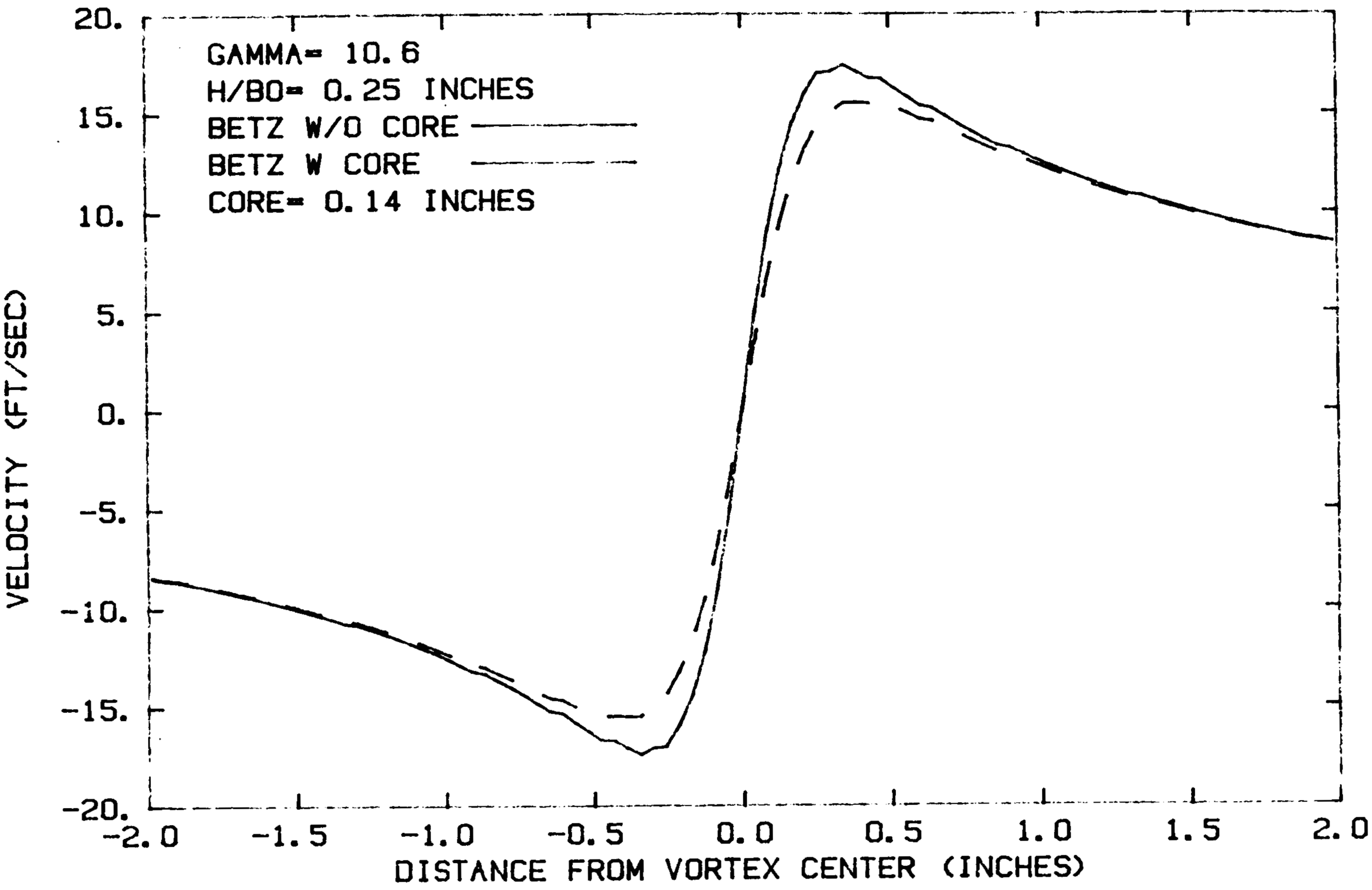

FIGURE 61. COMPARISON OF UPWASH DUE TO BETZ VORTEX AND MODIFIED BETZ VORTEX AT 0.25 SEMICHORD BLADE-VORTEX SEPARATION

ORIGINAL PAGE IS
OF POOR QUALITY

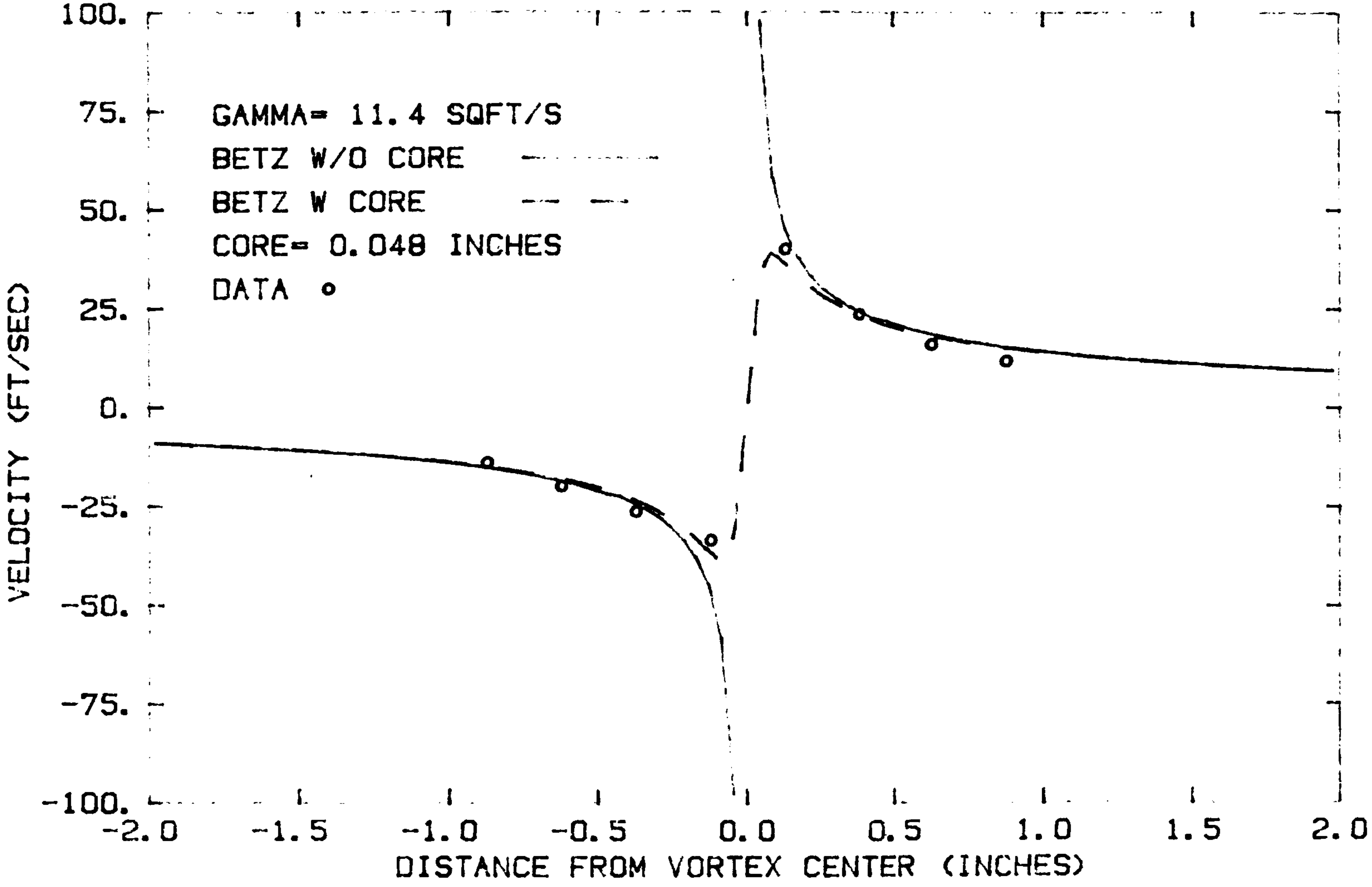

FIGURE 62. COMPARISON OF MEASURED VORTEX DATA, MODIFIED BETZ VORTEX MODEL, AND ORIGINAL BETZ MODEL.

ORIGINAL PAGE IS
OF POOR QUALITY

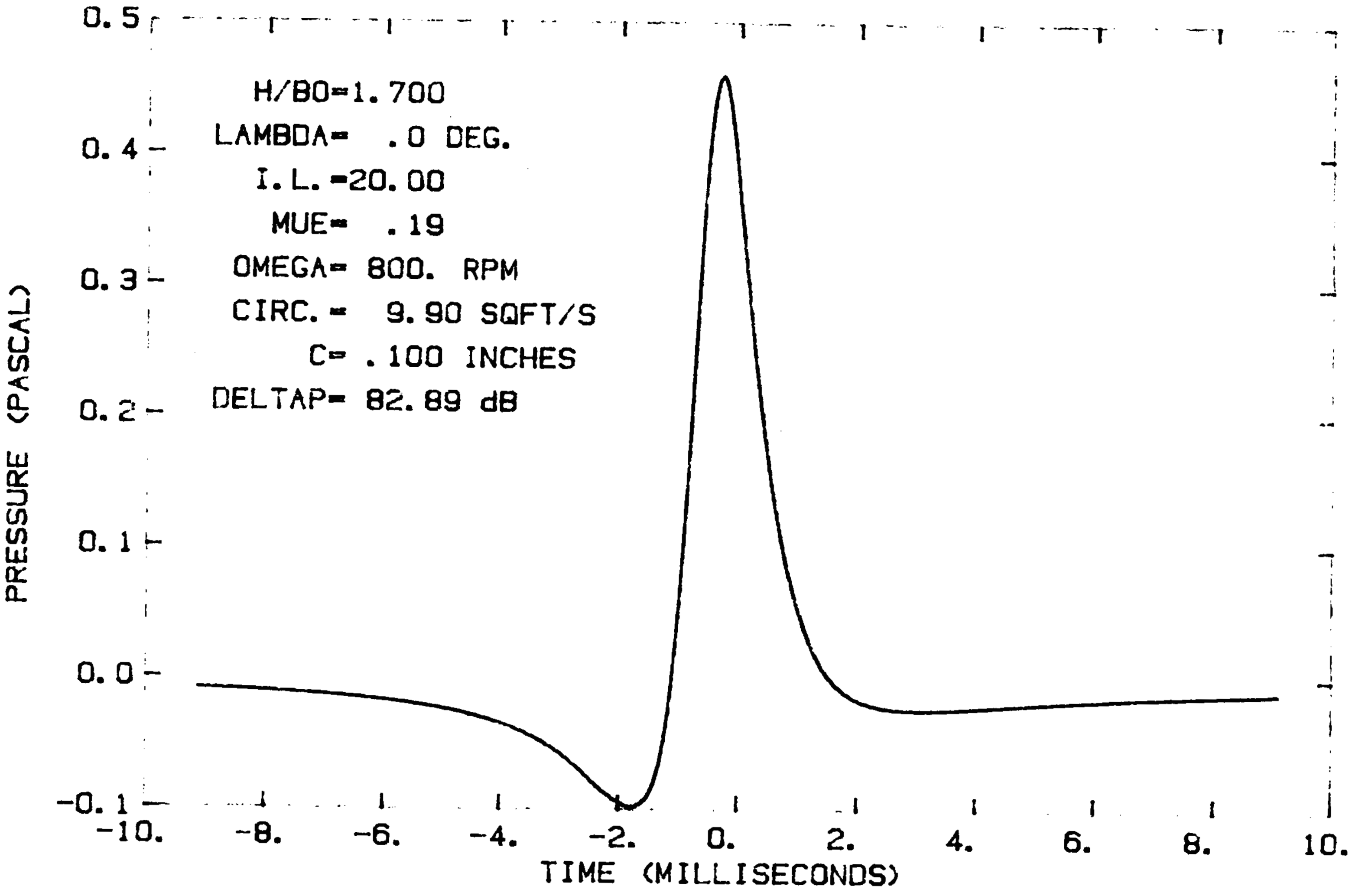

FIGURE 63. PREDICTED ACOUSTIC SIGNATURE

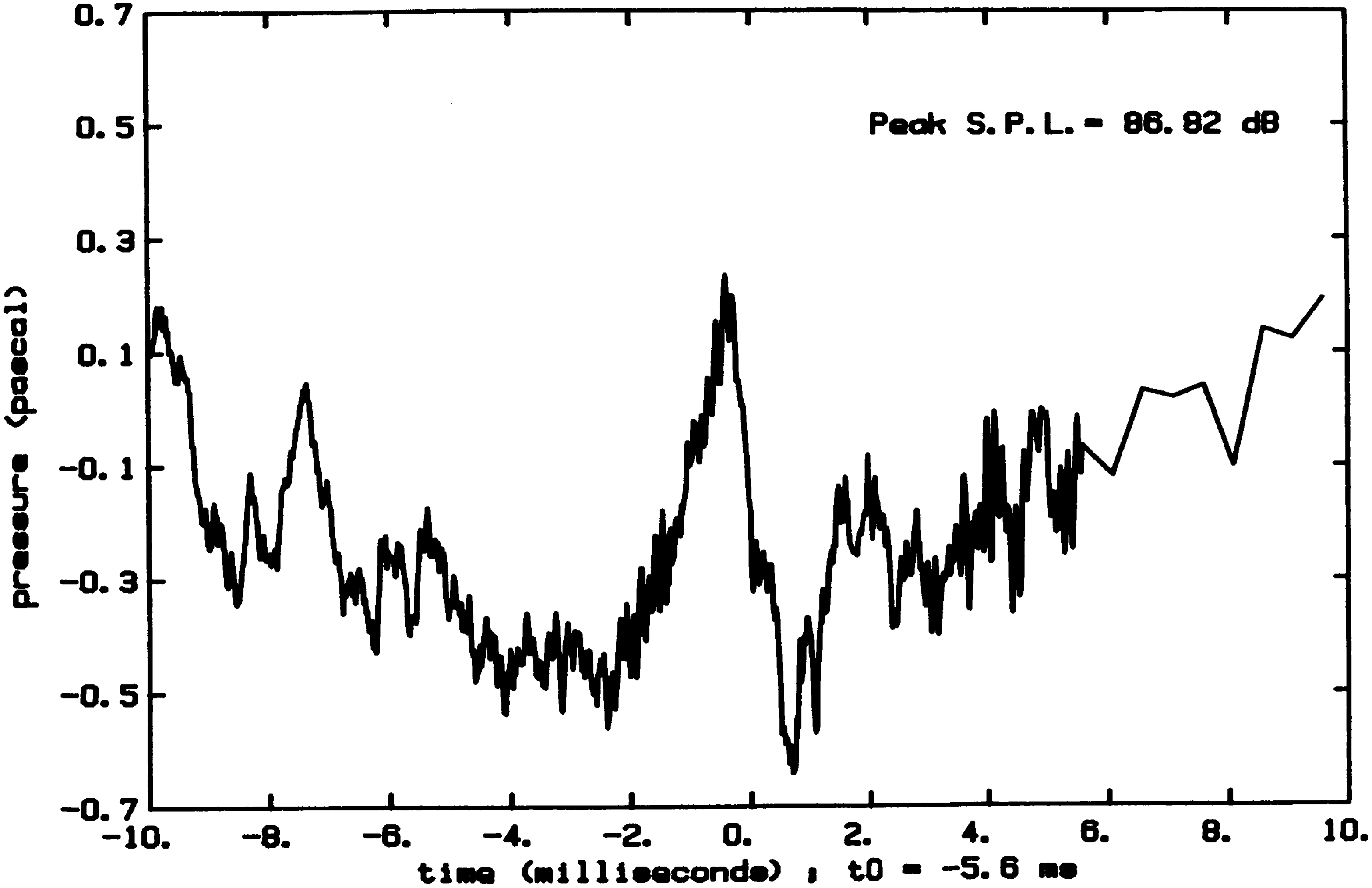

FIGURE 64. MEASURED ACOUSTIC SIGNATURE.
ADVANCE RATIO = 0.19

ORIGINAL PAGE IS
OF POOR QUALITY

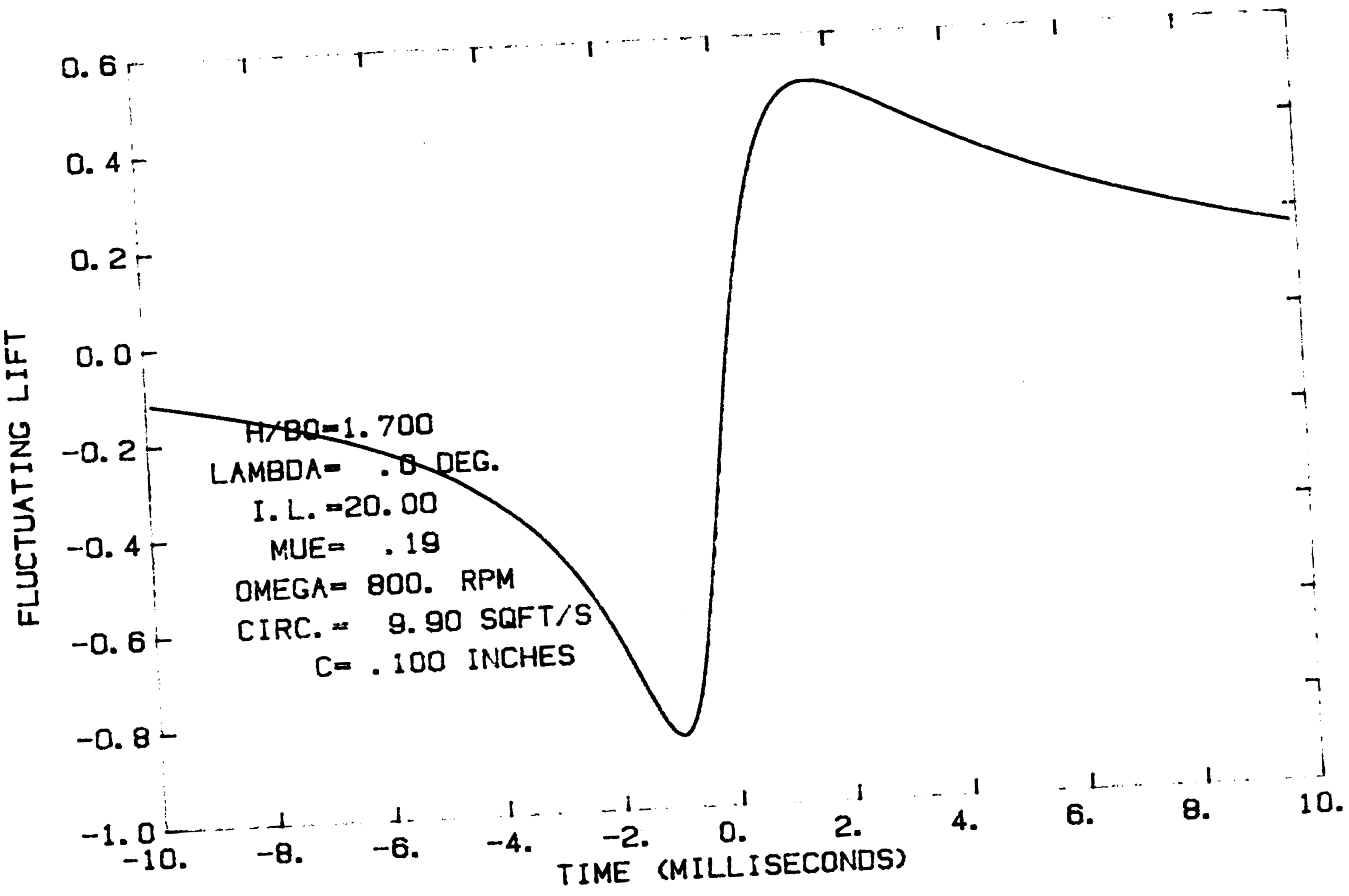

FIGURE 65. PREDICTED FLUCTUATING LIFT USING THE FILOTAS MODEL.

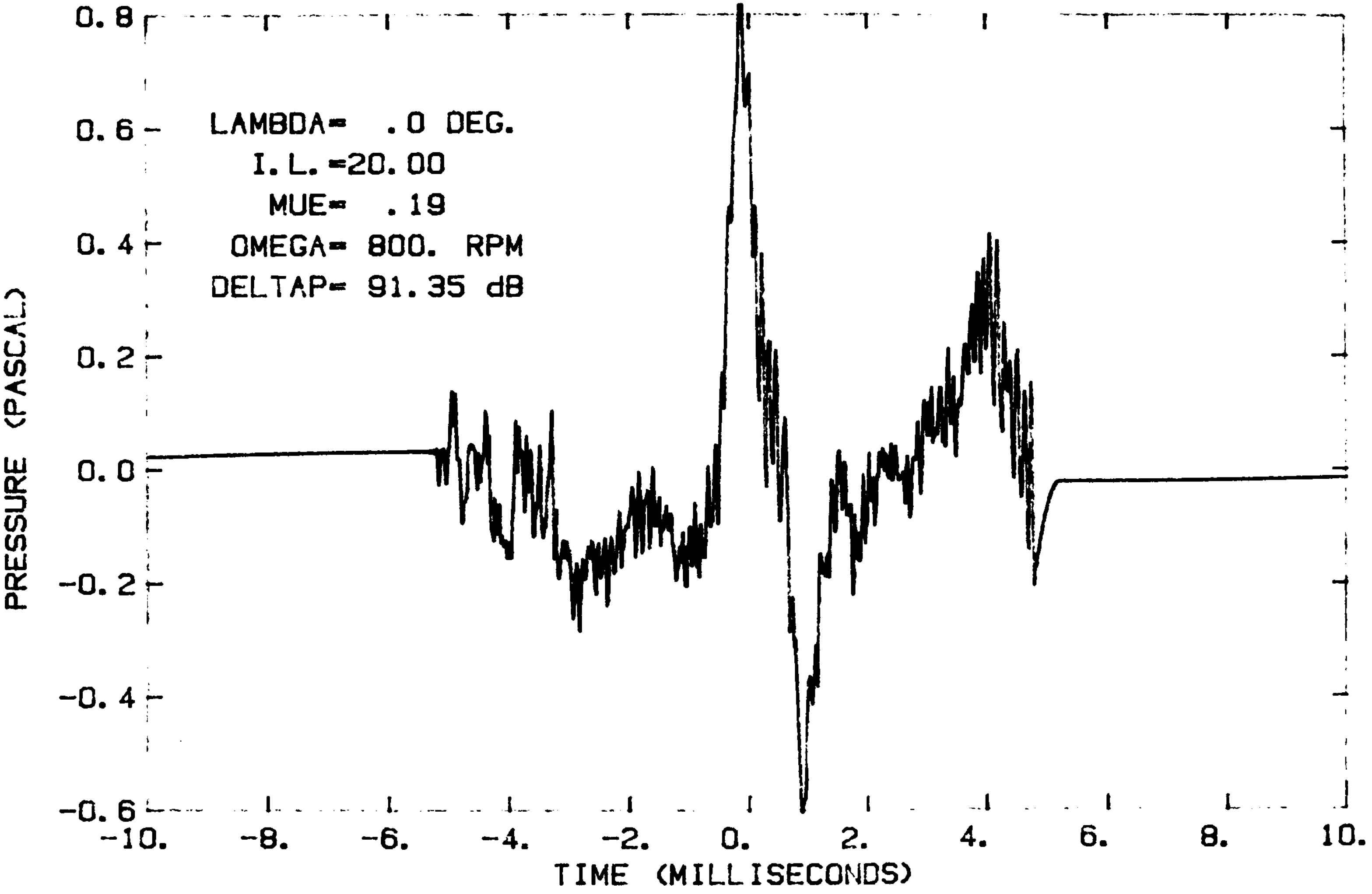

FIGURE 66. ACOUSTIC SIGNATURE PREDICTED FROM 99% SPAN, 18.75% CHORD MEASURED BLADE DIFFERENTIAL PRESSURE.

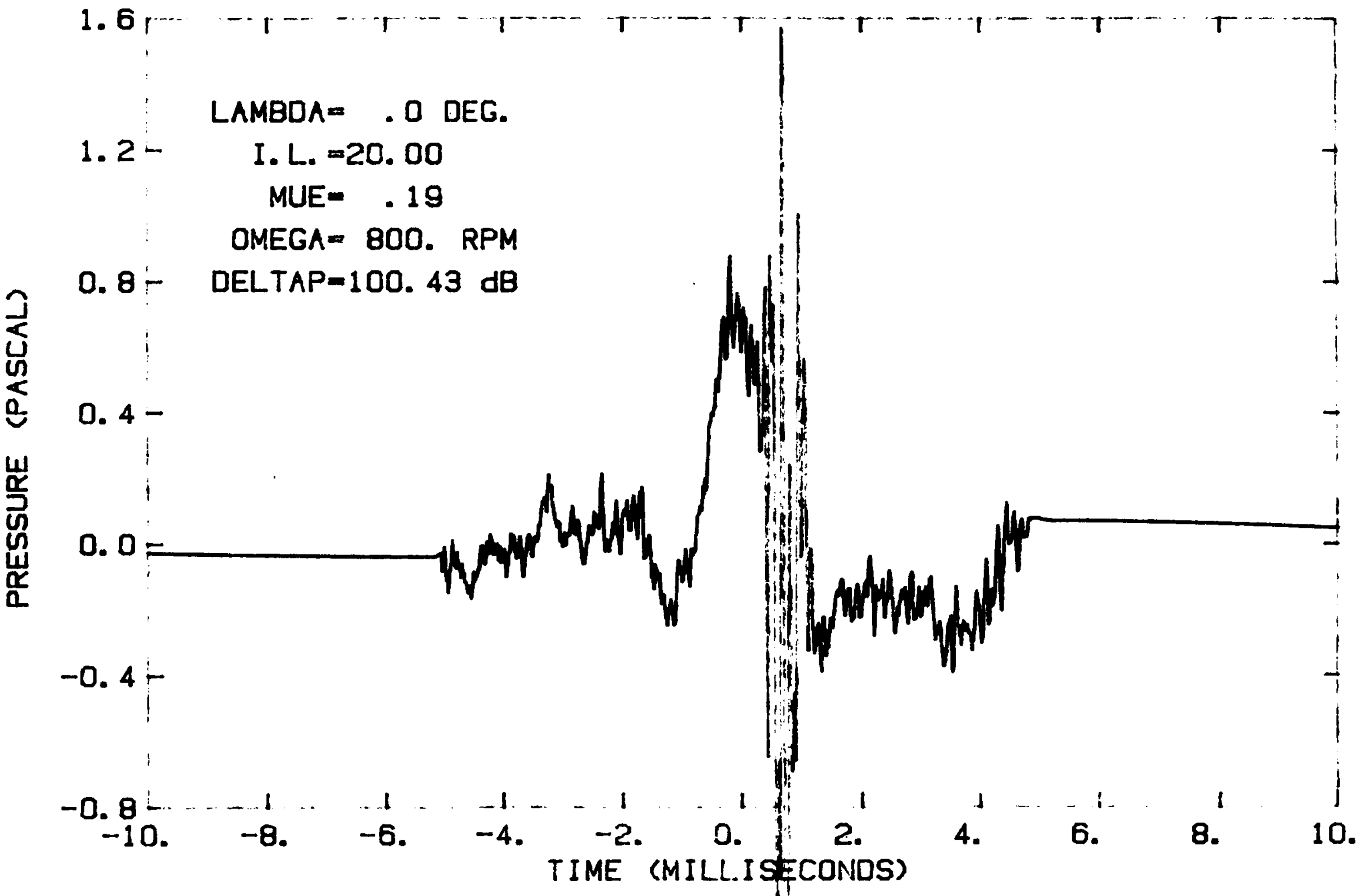

FIGURE 67. ACOUSTIC SIGNATURE PREDICTED FROM MEASURED PRESSURE AT 76% SPAN, 18.75% CHORD.

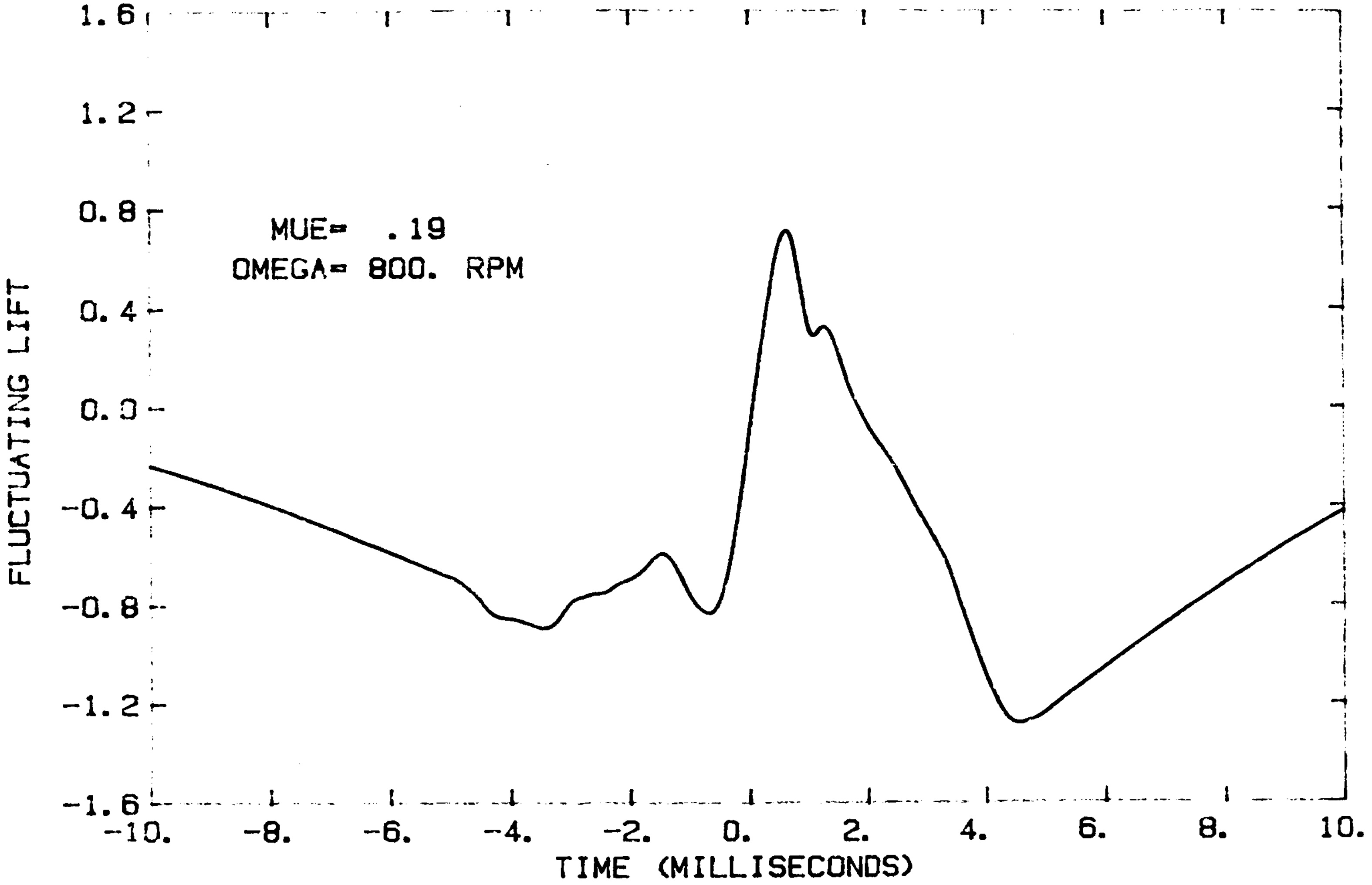

FIGURE 68. LIFT CALCULATED FROM MEASURED PRESSURE AT 76% SPAN AFTER LOW-PASS FILTERING TO REMOVE HIGH FREQUENCIES.

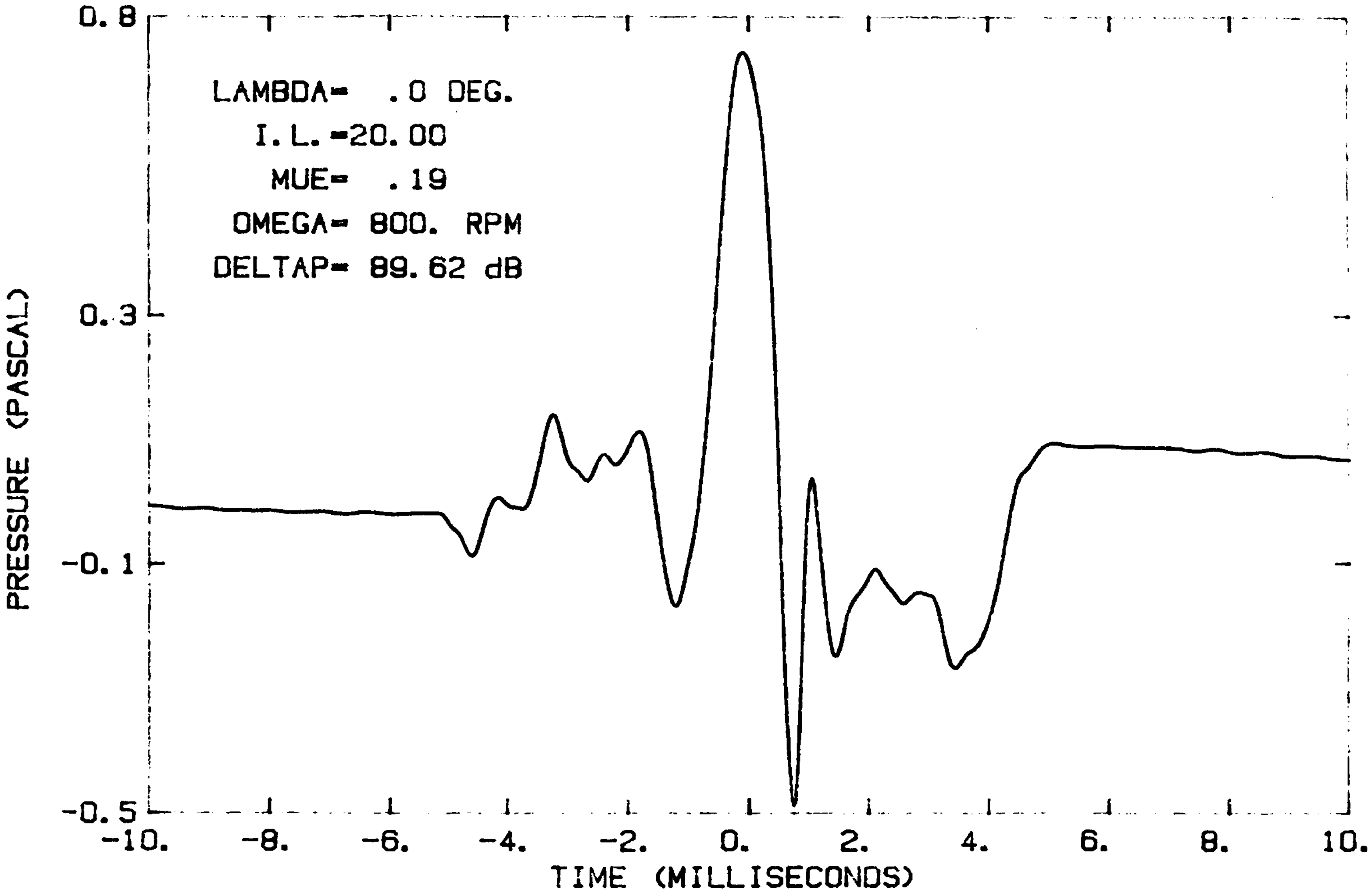

FIGURE 69. ACOUSTIC PULSE PREDICTED FROM LOW-PASS FILTERED MEASURED PRESSURE AT 76% SPAN, 18.75% CHORD.

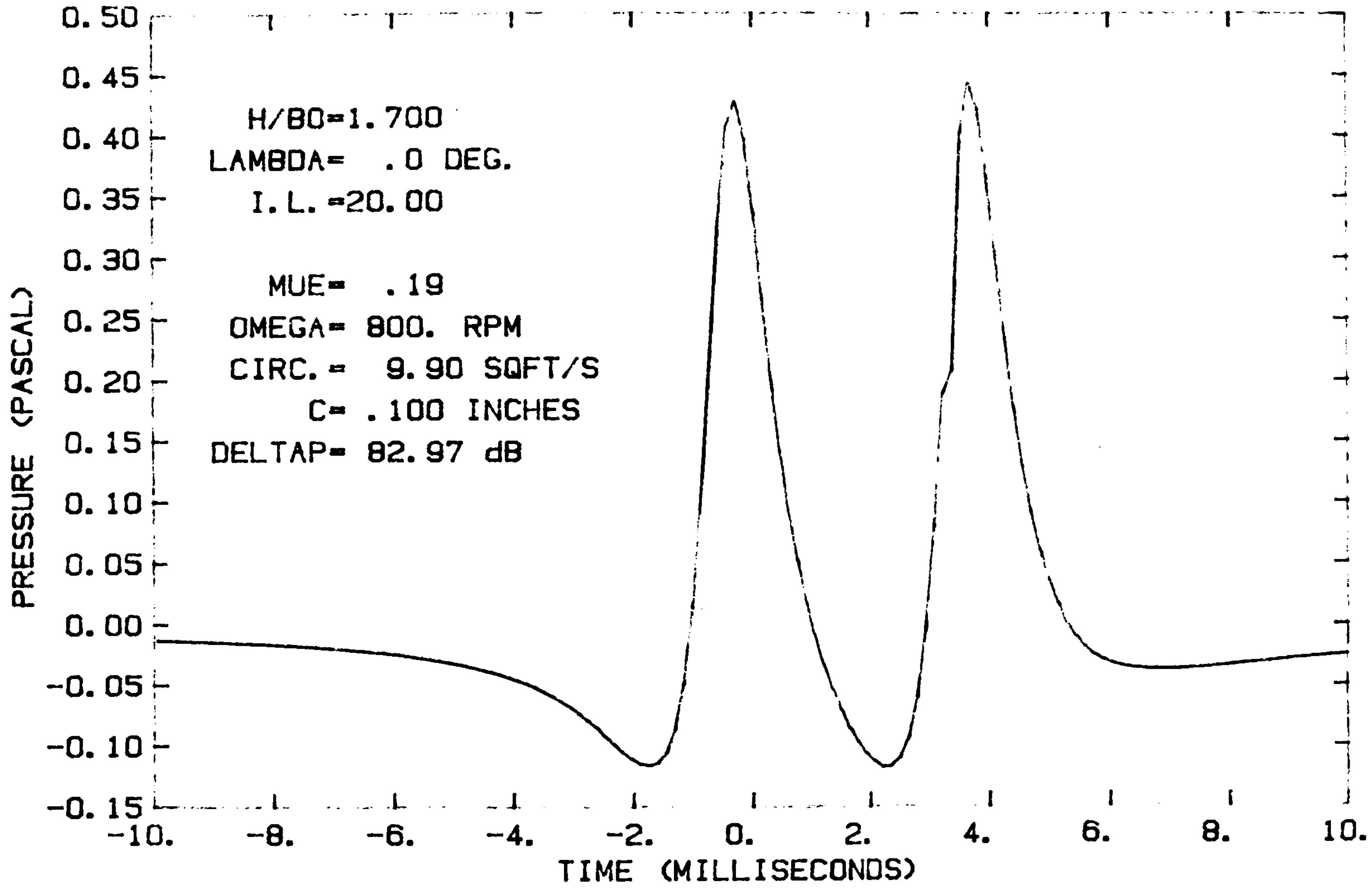

FIGURE 70. PREDICTED ACOUSTIC SIGNATURE USING THE VELOCITY FIELD OF TWO VORTICES AT THE SAME INTERACTION ANGLE.

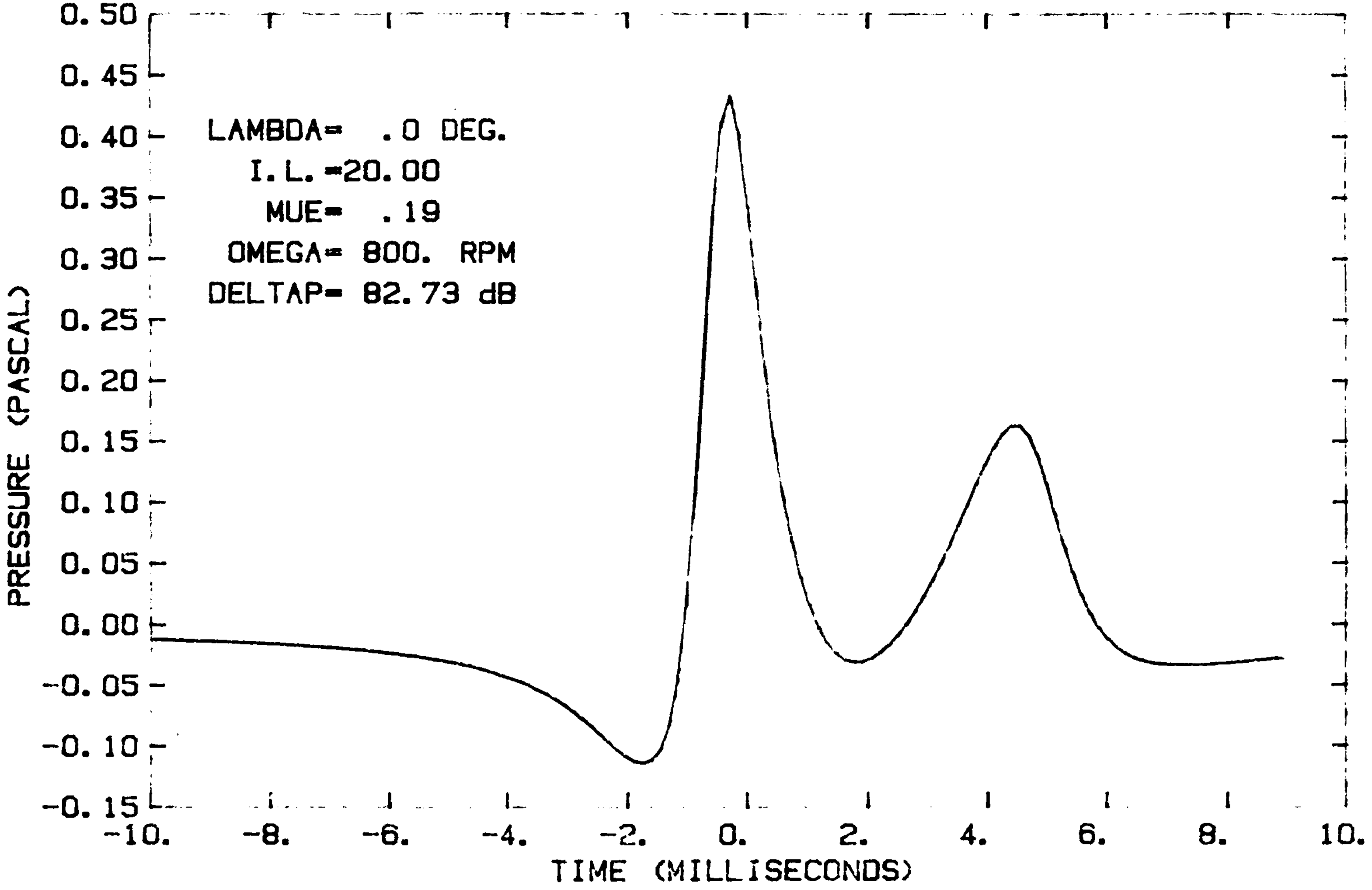

FIGURE 71. PREDICTED ACOUSTIC PULSE USING SUPERPOSITION ACCOUNTING FOR THE LARGE ANGLE OF THE SECOND INTERACTION.

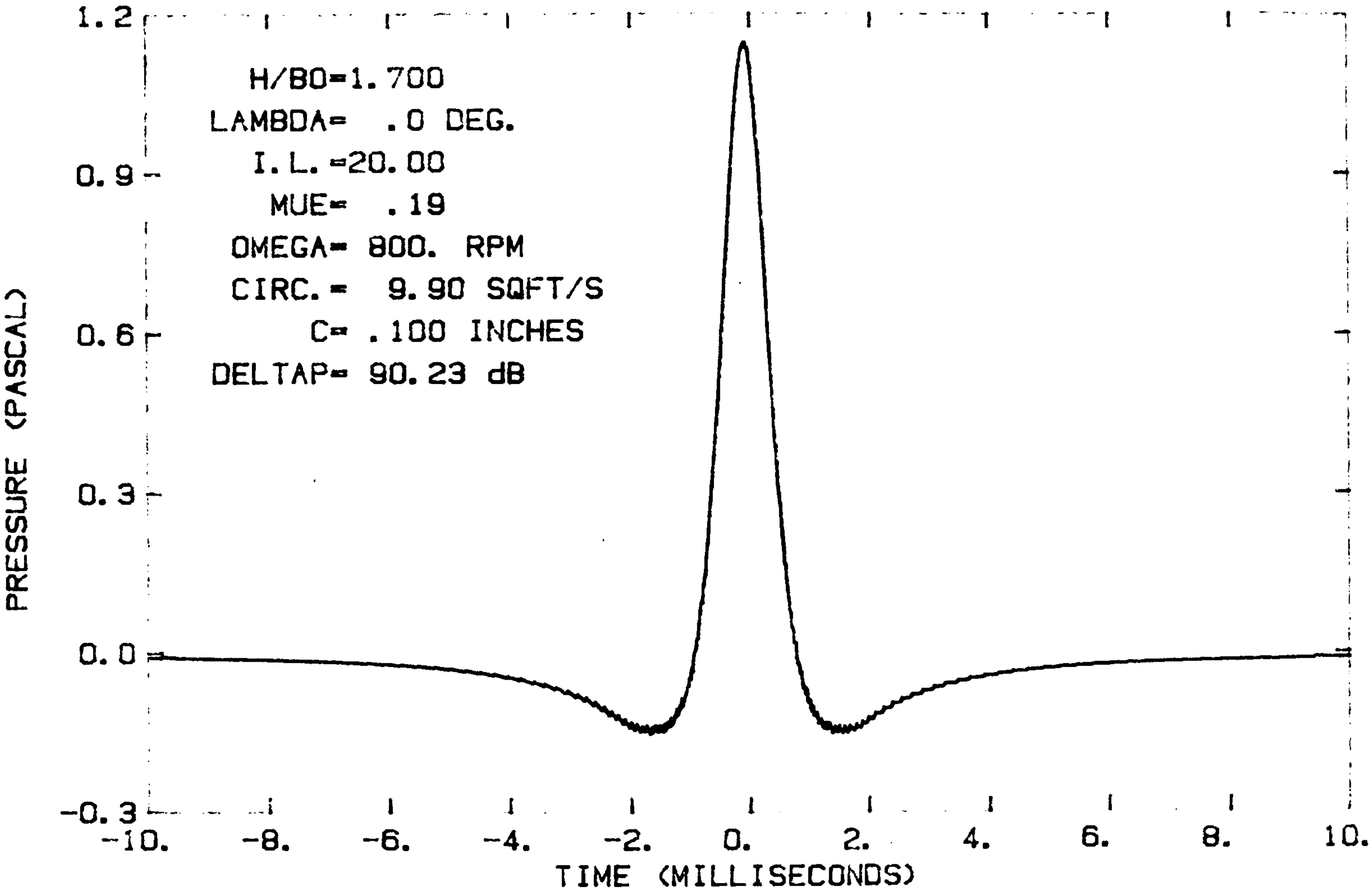

FIGURE 72. ACOUSTIC PULSE PREDICTED USING THE SIMPLE LIFT MODEL.

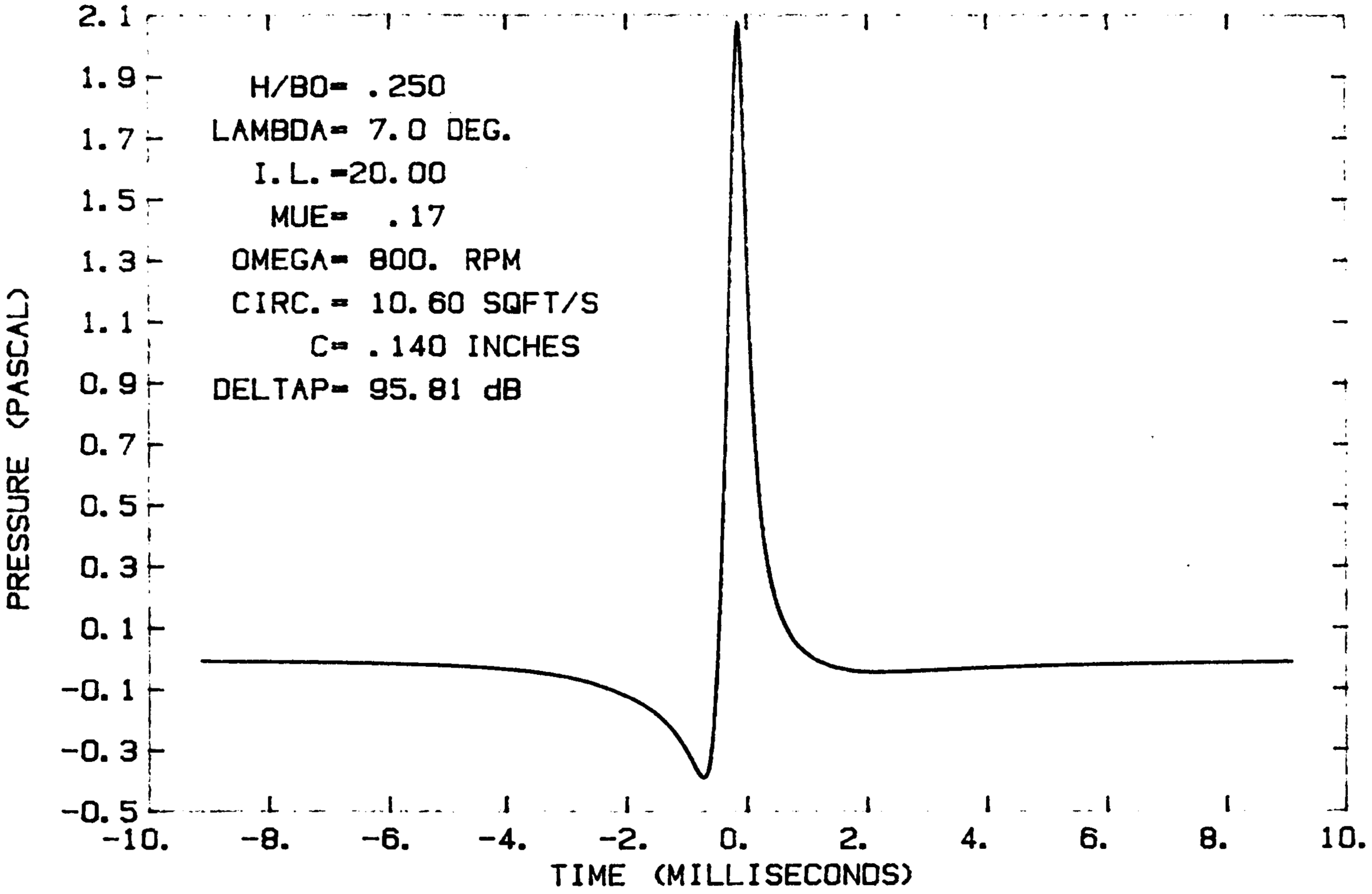

FIGURE 73. PREDICTED ACOUSTIC PULSE.

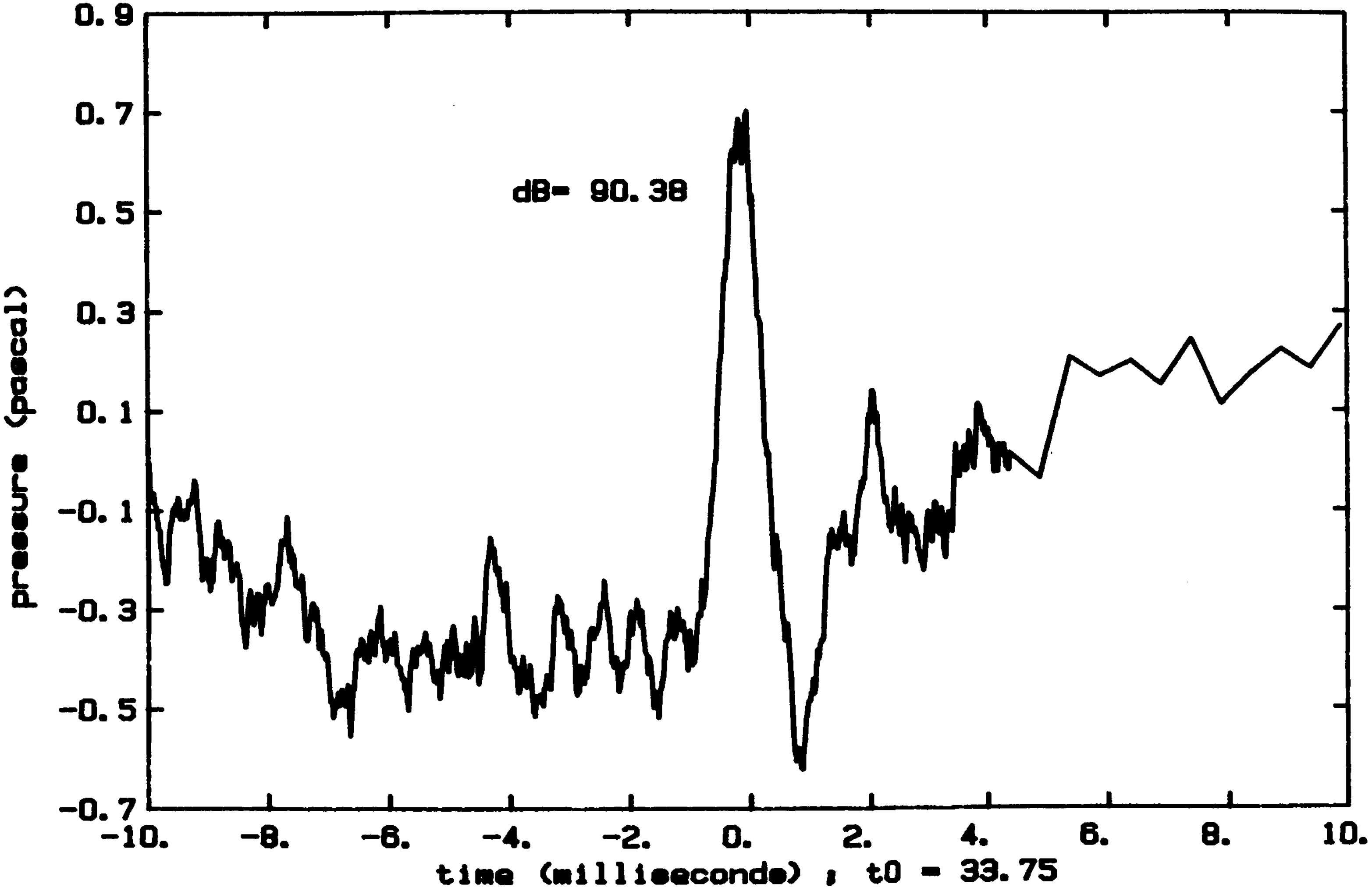

FIGURE 74. MEASURED ACOUSTIC PULSE FOR ADVANCE RATIO OF 0.17

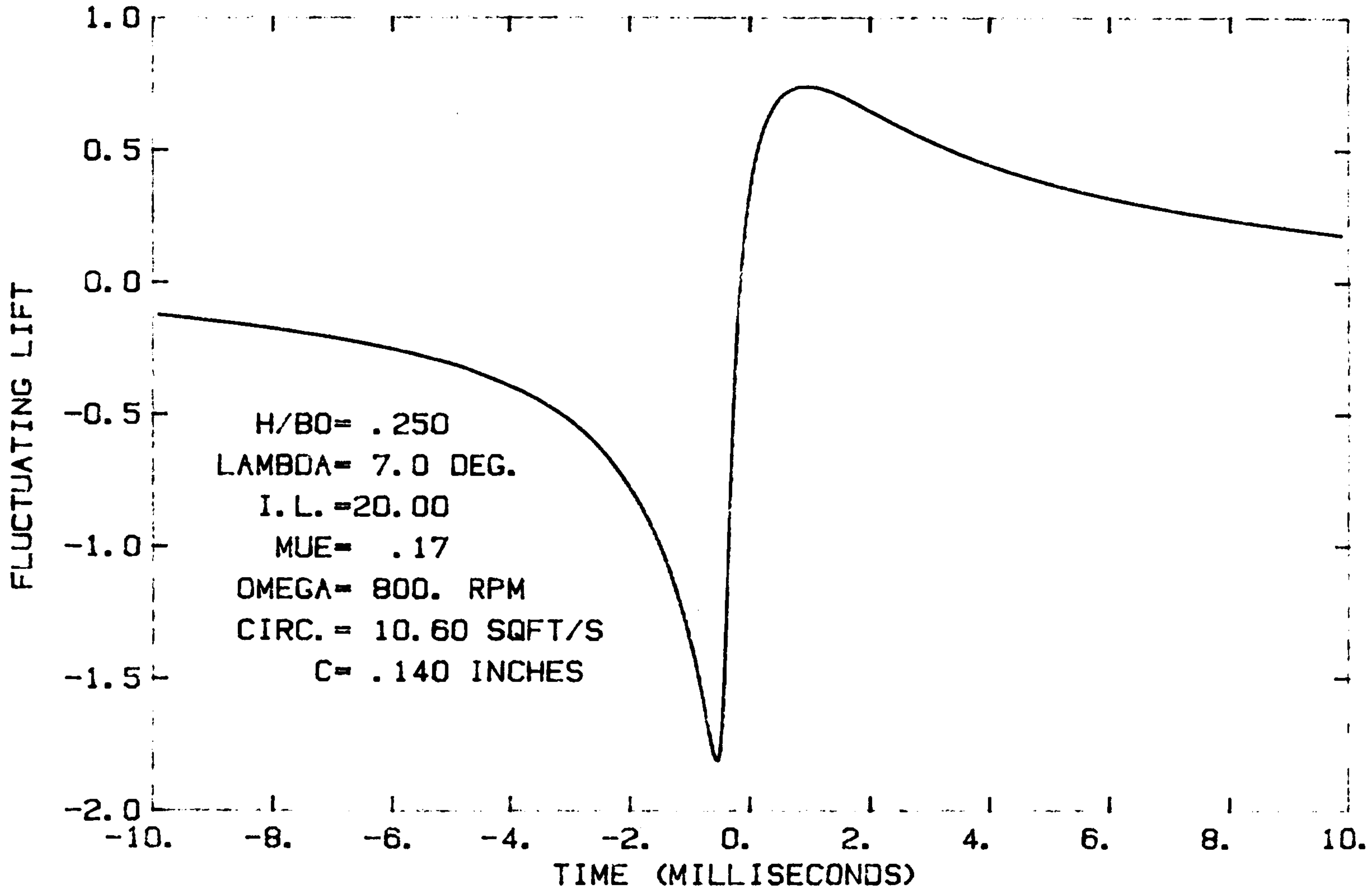

FIGURE 75. PREDICTED FLUCTUATING LIFT USING FILOTAS MODEL.

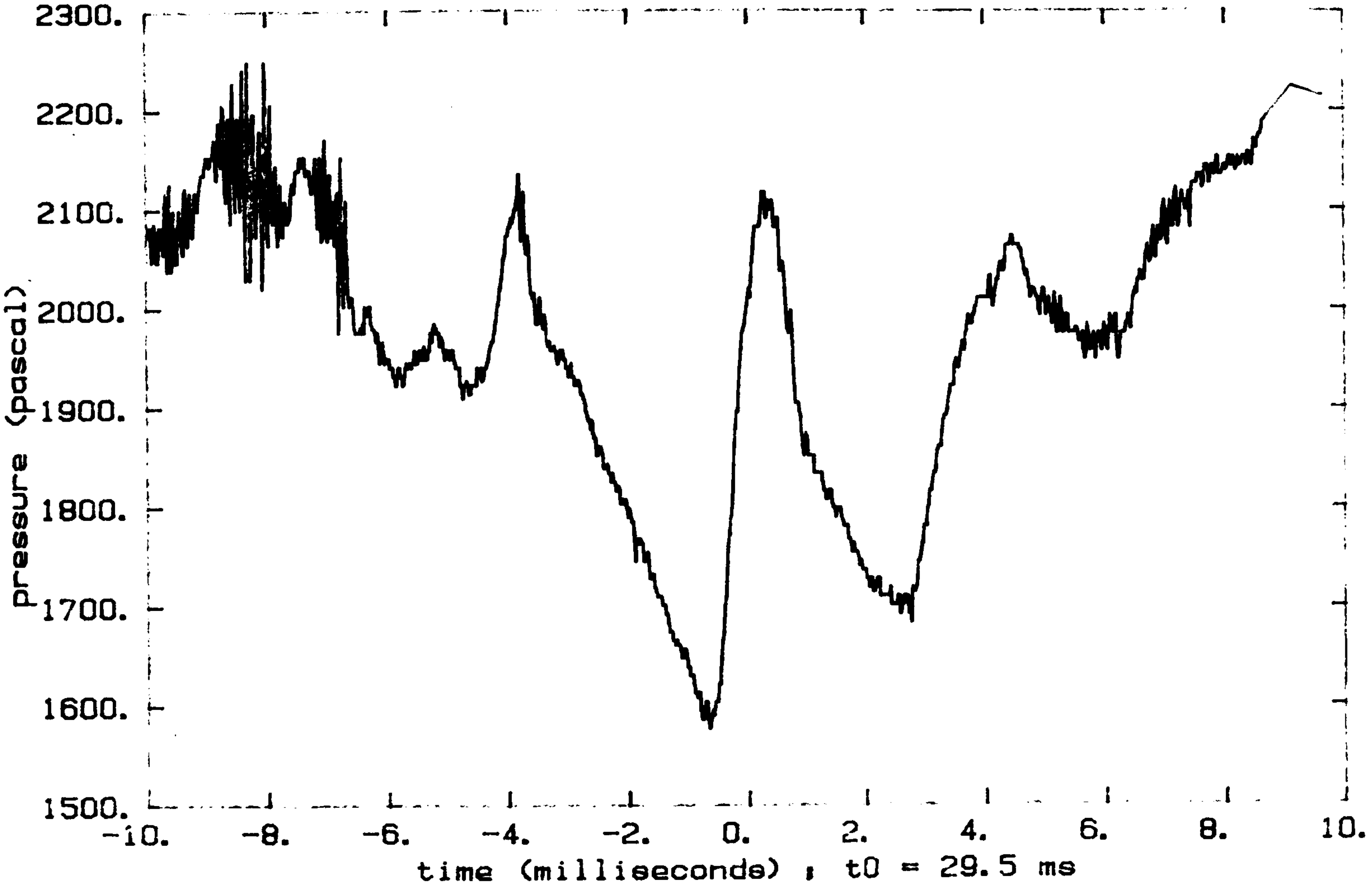

FIGURE 76. MEASURED PRESSURE AT 99% SPAN, 18.75% CHORD.
ADVANCE RATIO = 0.17

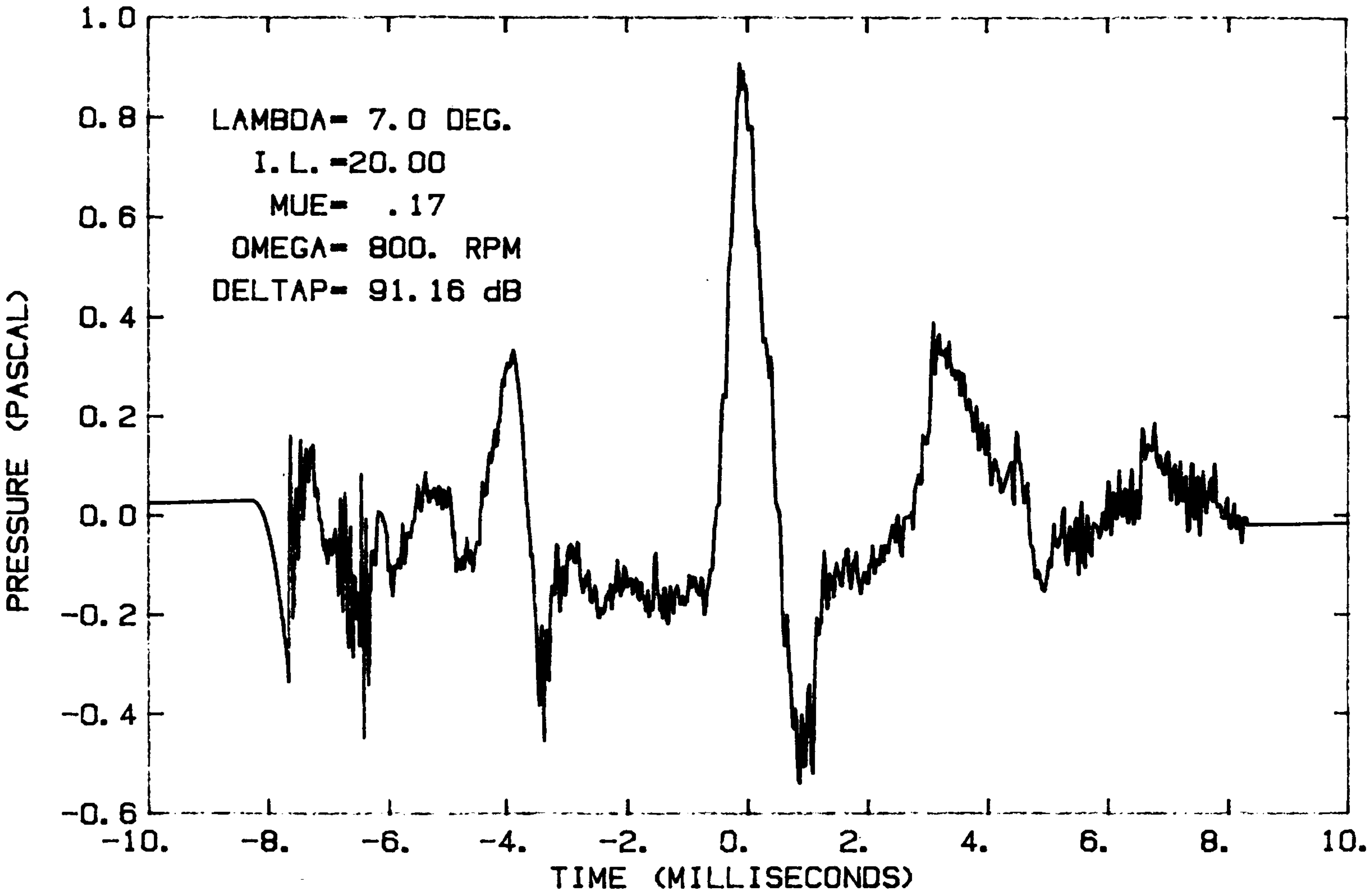

FIGURE 77. ACOUSTIC PULSE PREDICTED FROM PRESSURE MEASUREMENTS AT 99% SPAN, 18.75% CHORD.

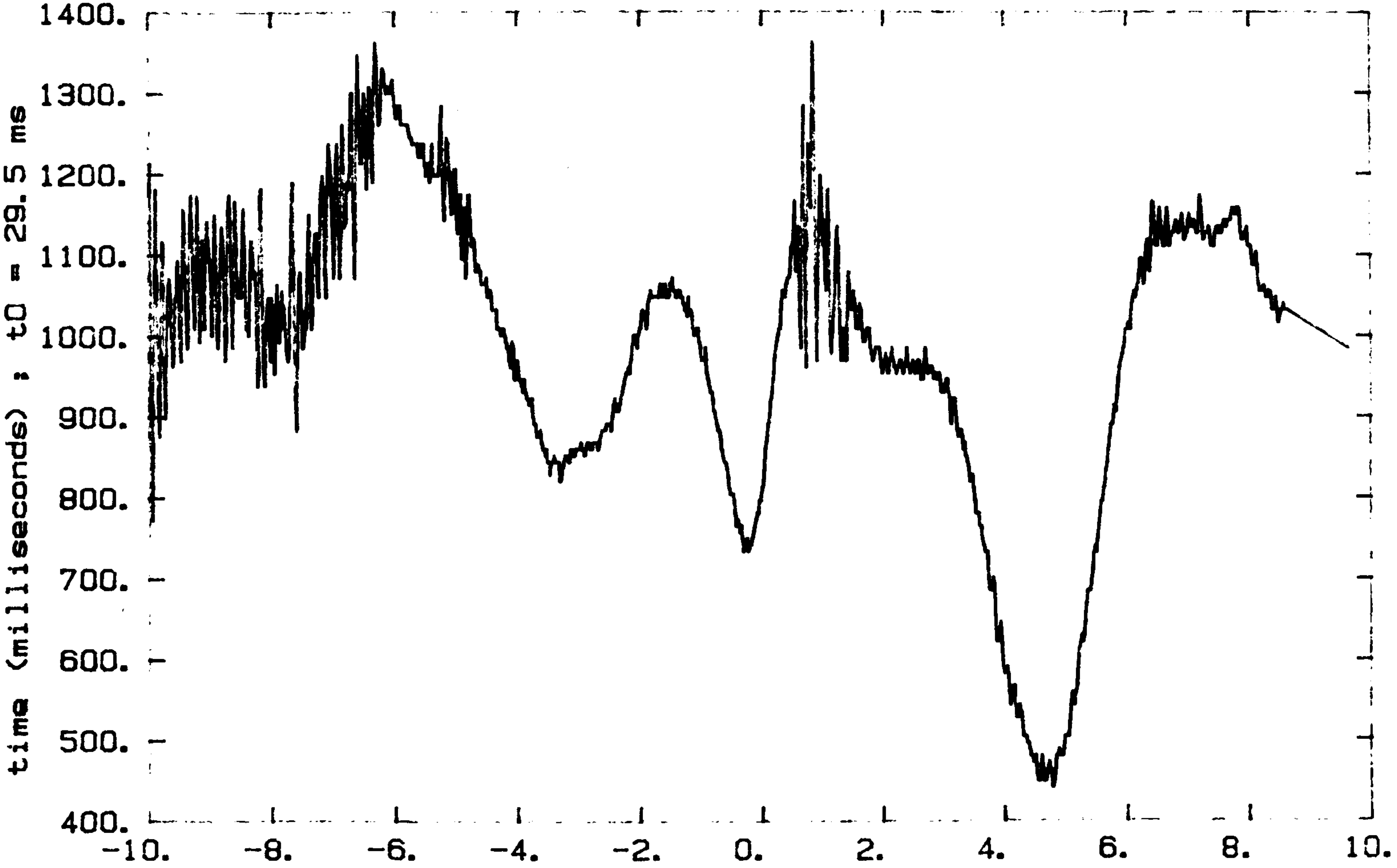

FIGURE 78. MEASURED BLADE DIFFERENTIAL PRESSURE AT 76% SPAN.
18.75% CHORD. ADVANCE RATIO = 0.17

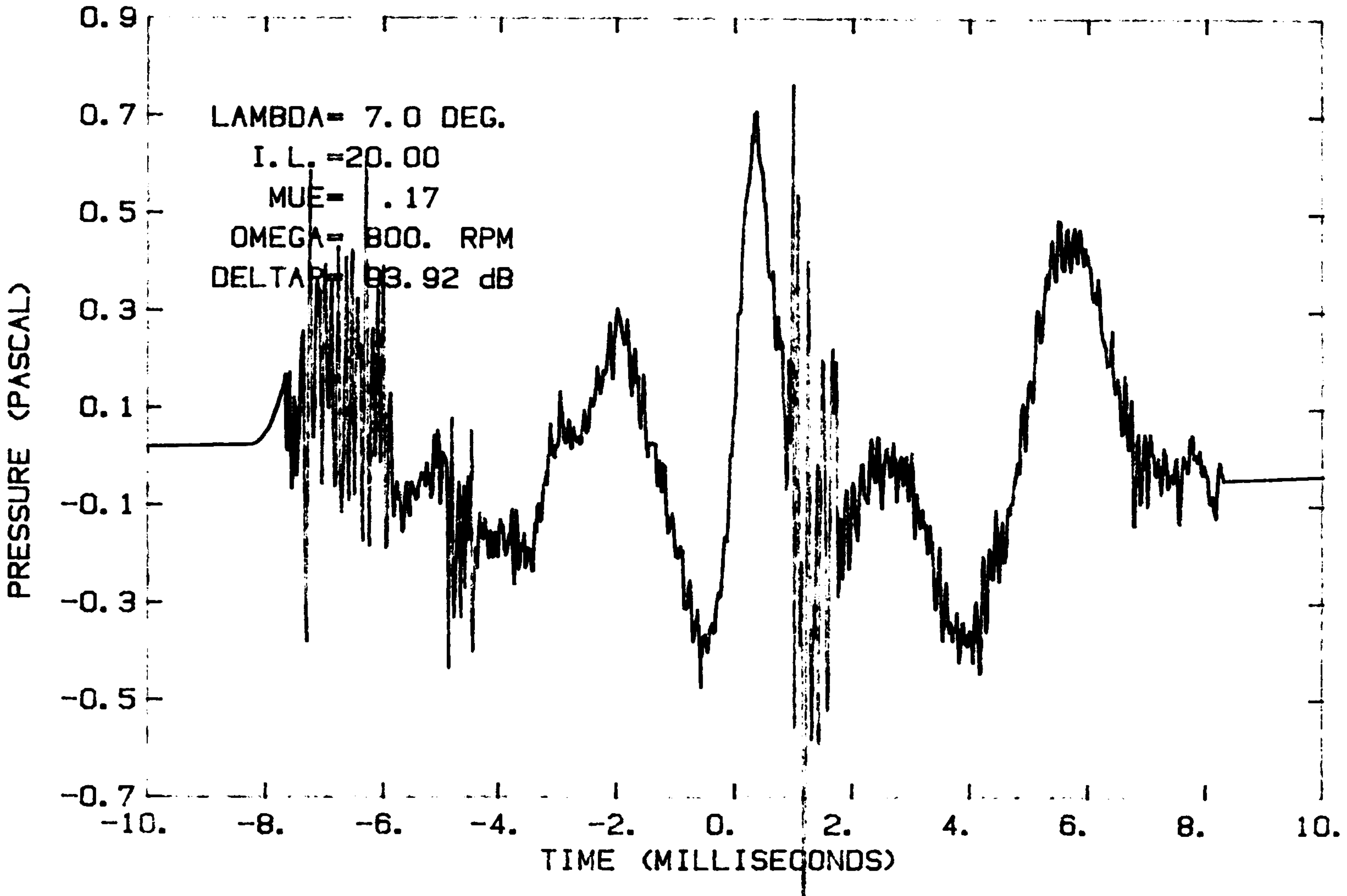

FIGURE 79. PREDICTED ACOUSTIC PULSE USING THE MEASURED PRESSURE AT 76% SPAN, 18.75% CHORD.

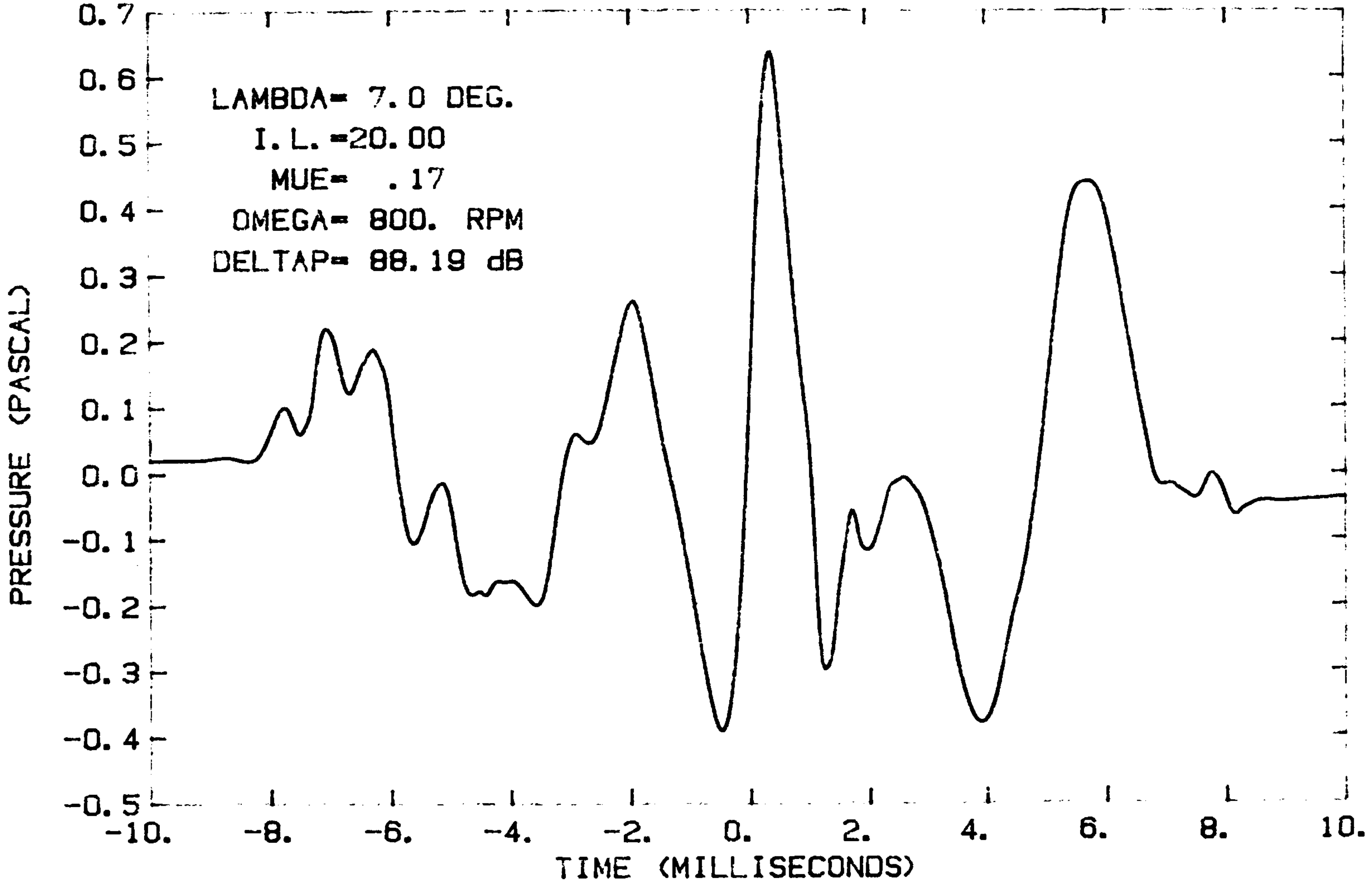

FIGURE 80. ACOUSTIC PULSE PREDICTED FROM THE MEASURED PRESSURE AT 76% SPAN, 18.75% CHORD AFTER LOW-PASS FILTERING.

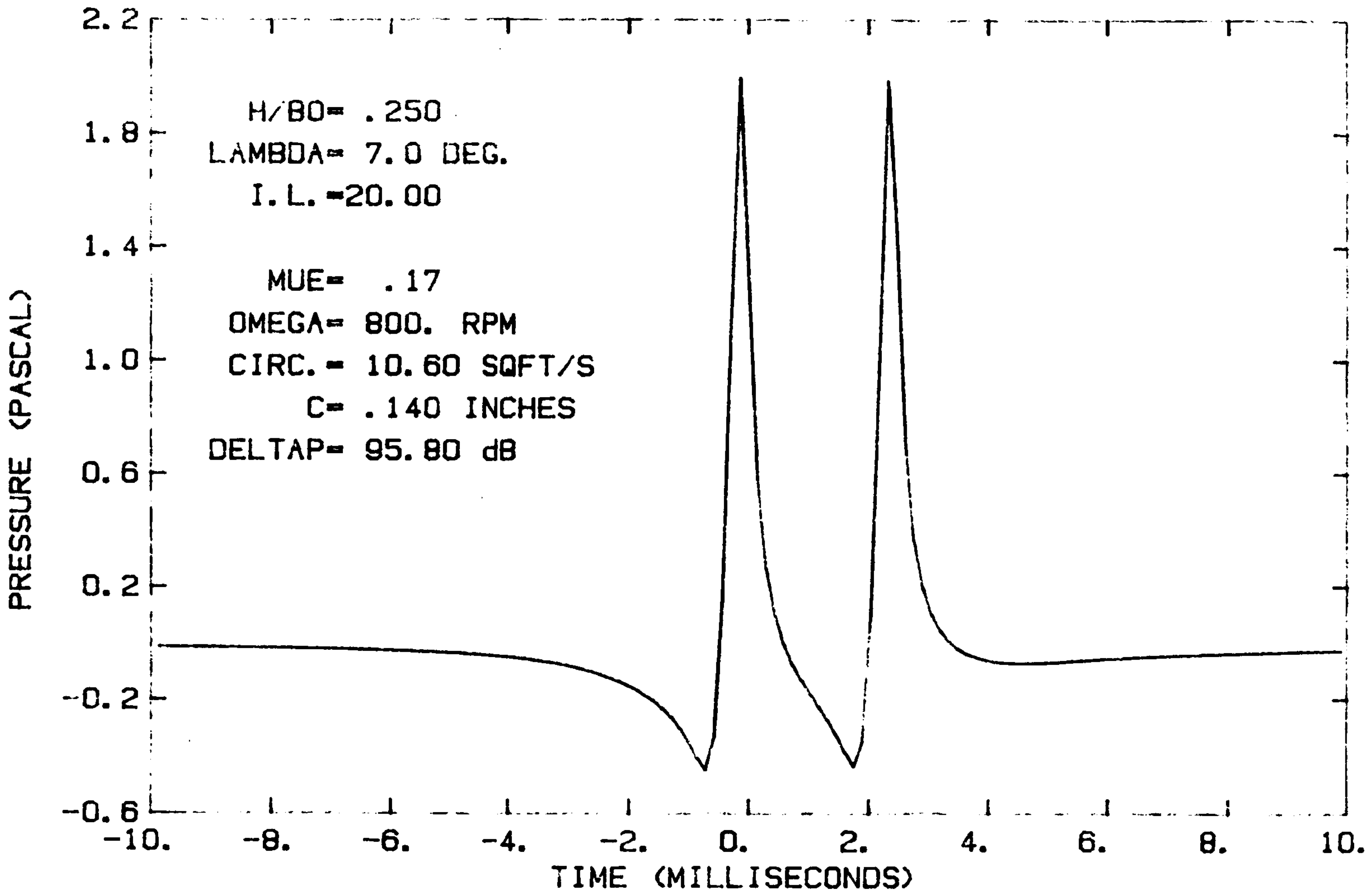

FIGURE 81. PREDICTED ACOUSTIC SIGNATURE USING VELOCITY FIELD OF TWO IDENTICAL VORTICES AT THE SAME INTERACTION ANGLE.

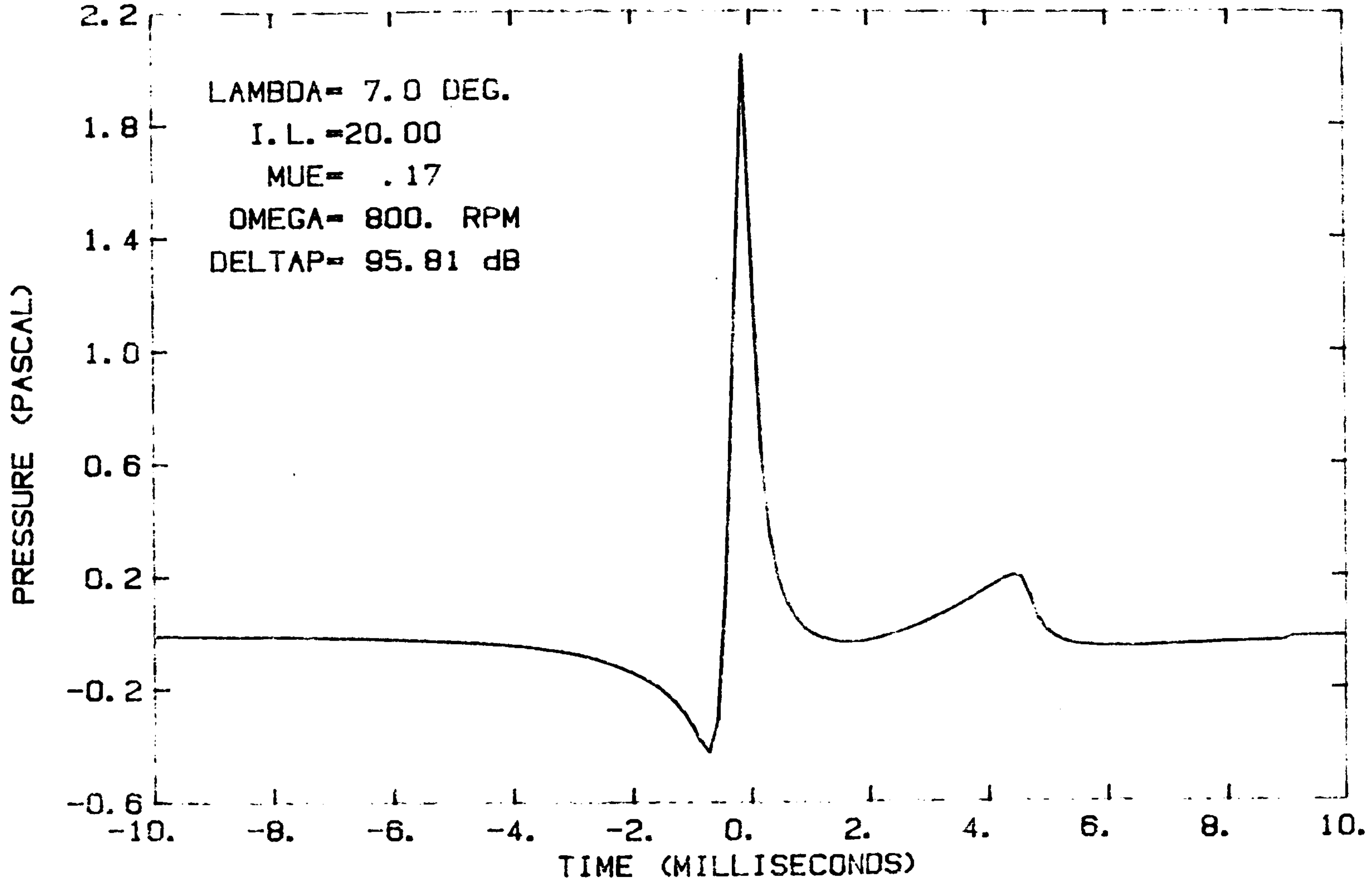

FIGURE 82. PREDICTED ACOUSTIC SIGNATURE USING SUPERPOSITION WITH LARGE ANGLE INTERACTION.

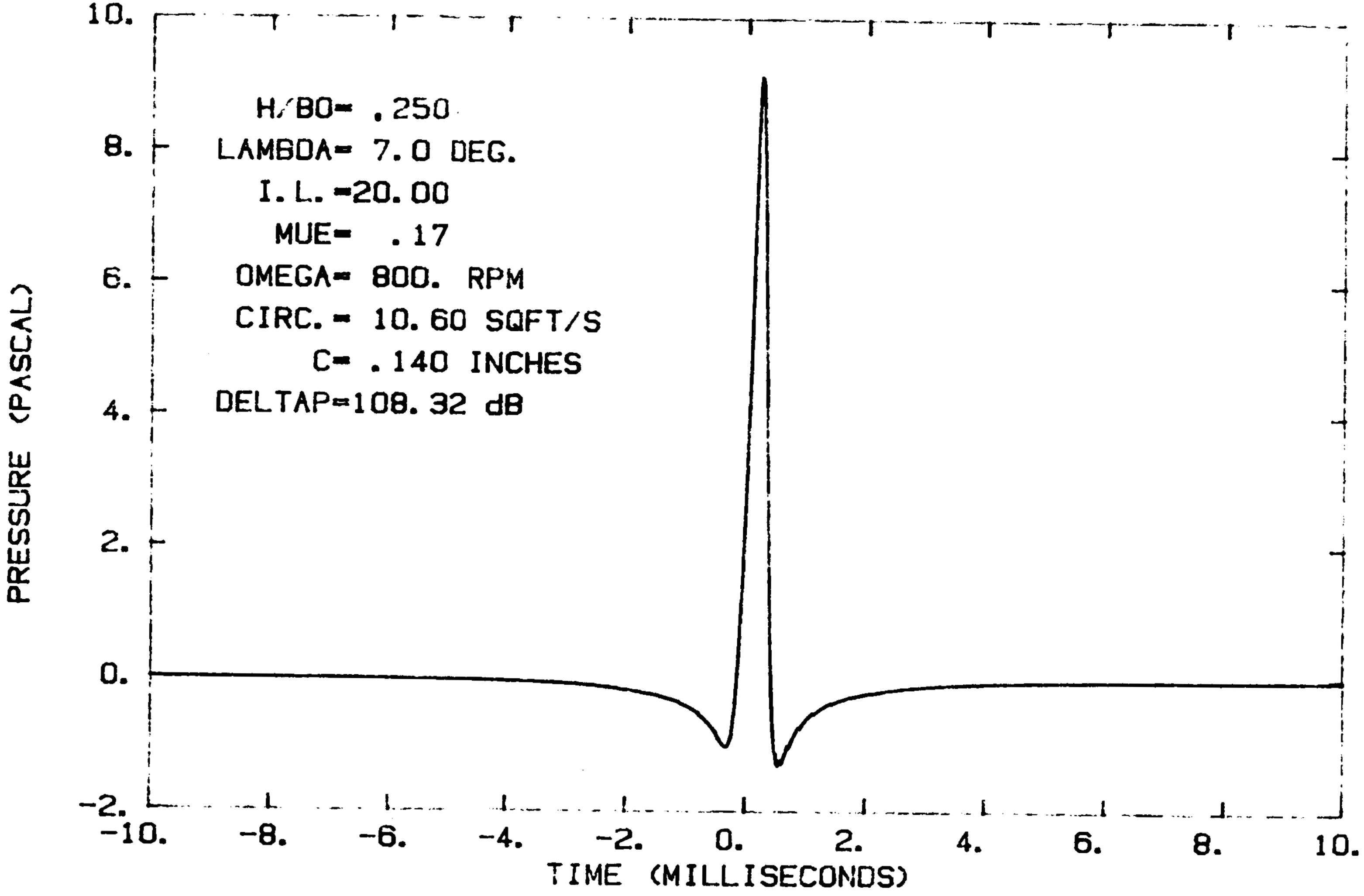

FIGURE 83. PREDICTED ACOUSTIC SIGNATURE USING SIMPLE LIFT MODEL. ADVANCE RATIO = 0.17

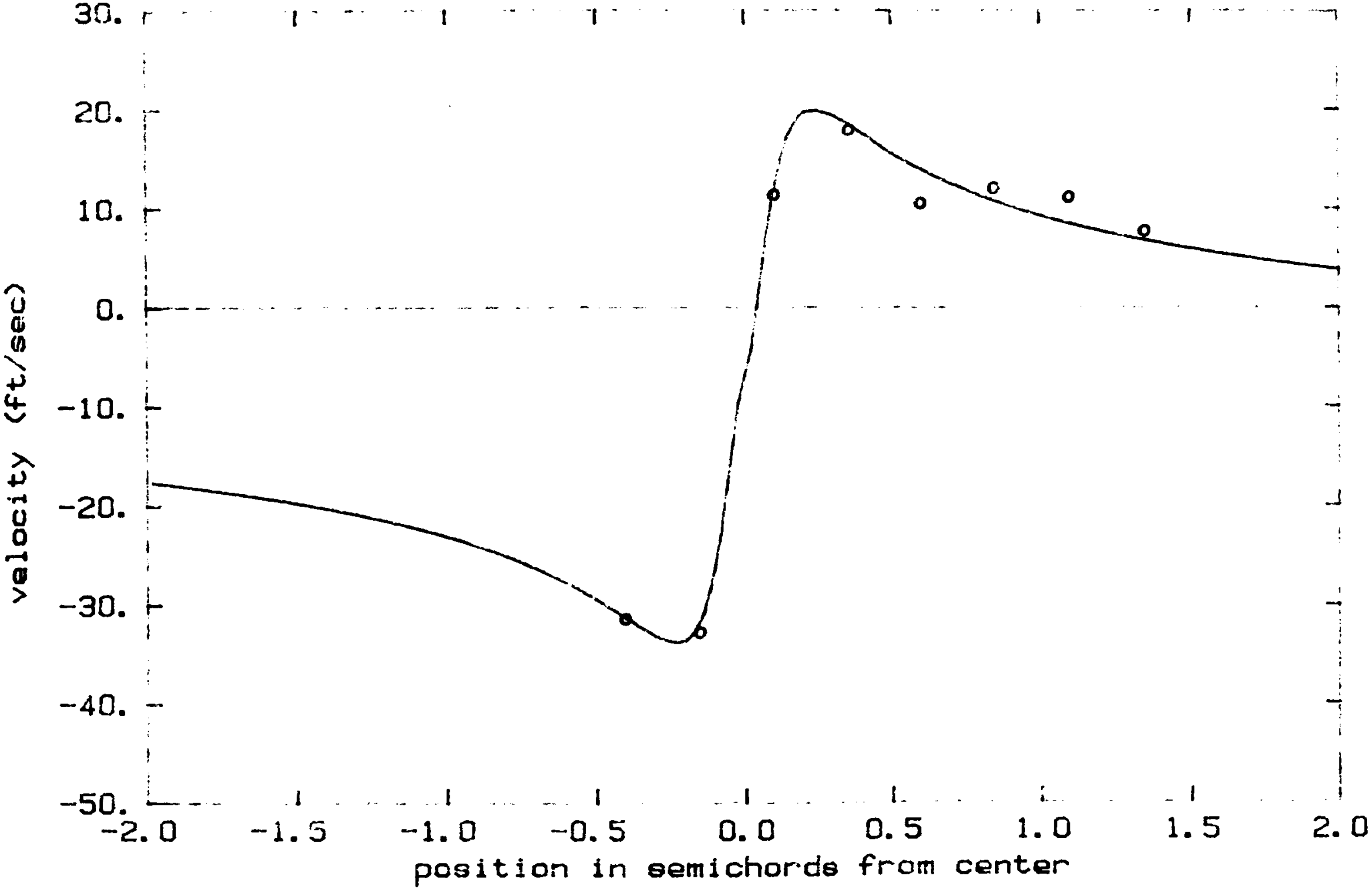

FIGURE 84. VORTEX VELOCITY DISTRIBUTION WITH MODIFIED BETZ VORTEX.
CIRCULATION = 13.5 FT**2/SEC. CORE = 0.137 SEMICHORDS.

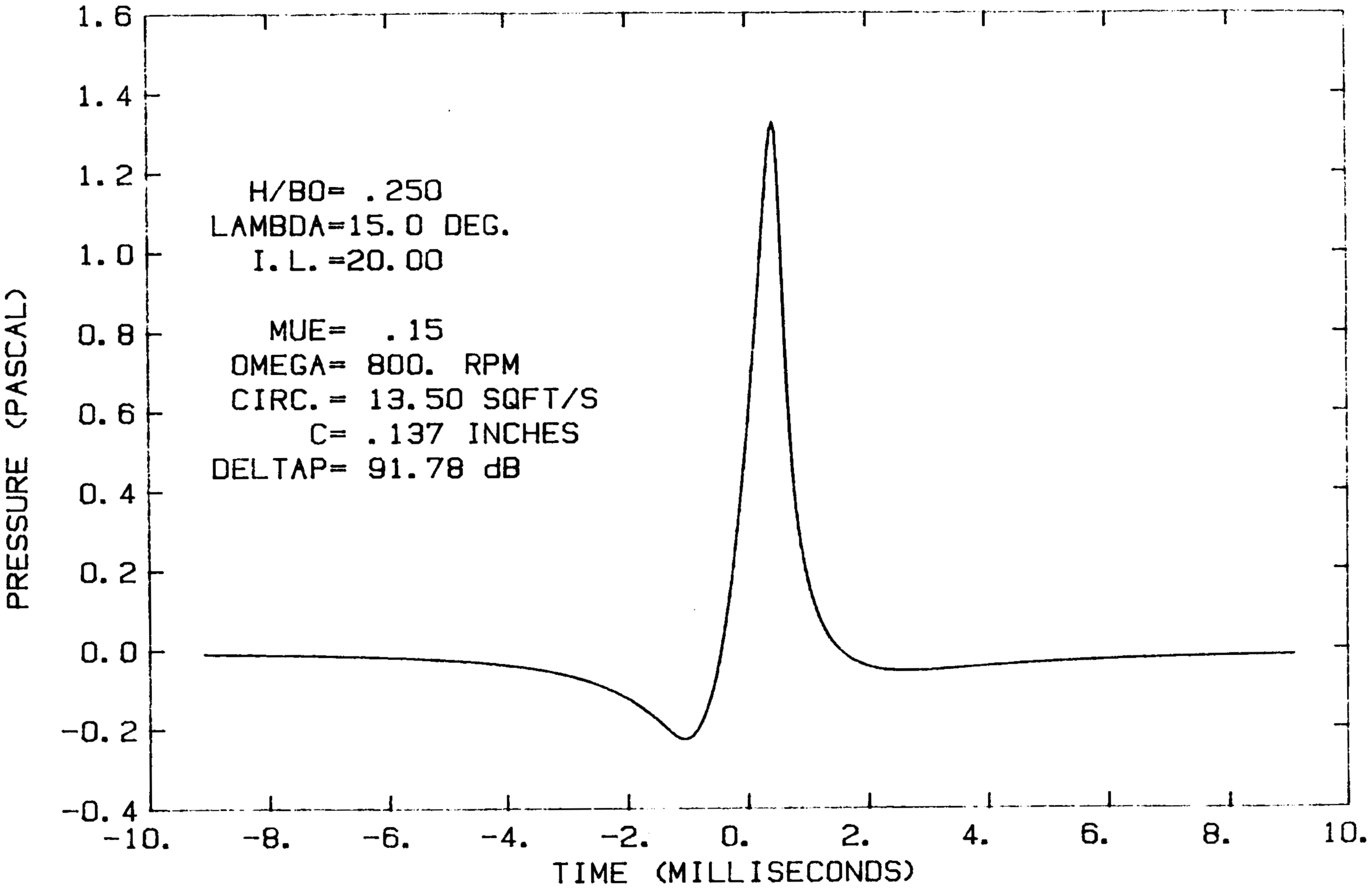

FIGURE 85. PREDICTED ACOUSTIC SIGNATURE FOR ADVANCE RATIO = 0.15

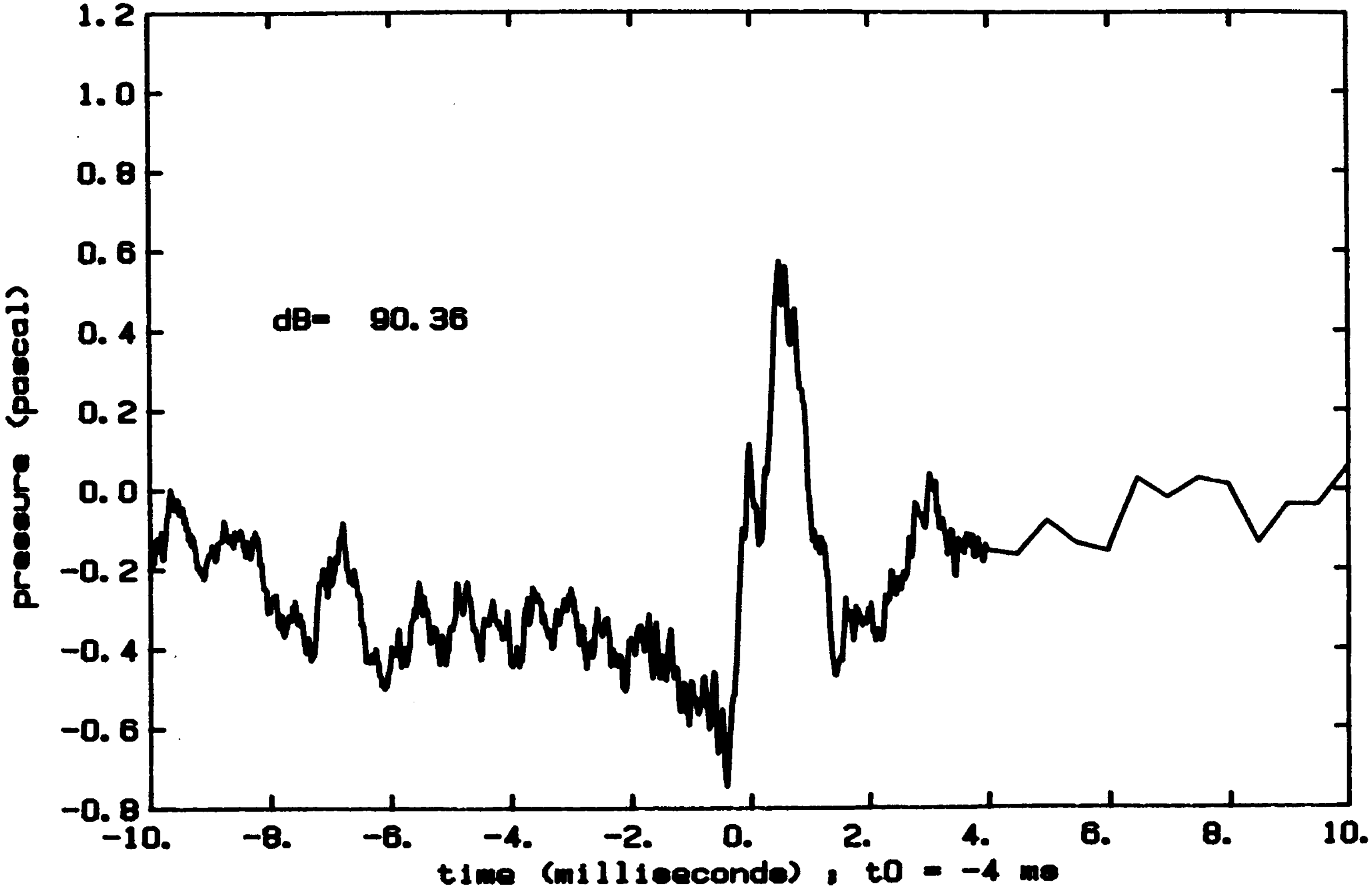

FIGURE 86. MEASURED ACOUSTIC SIGNATURE OF BLADE VORTEX INTERACTION.
ADVANCE RATIO = 0.15

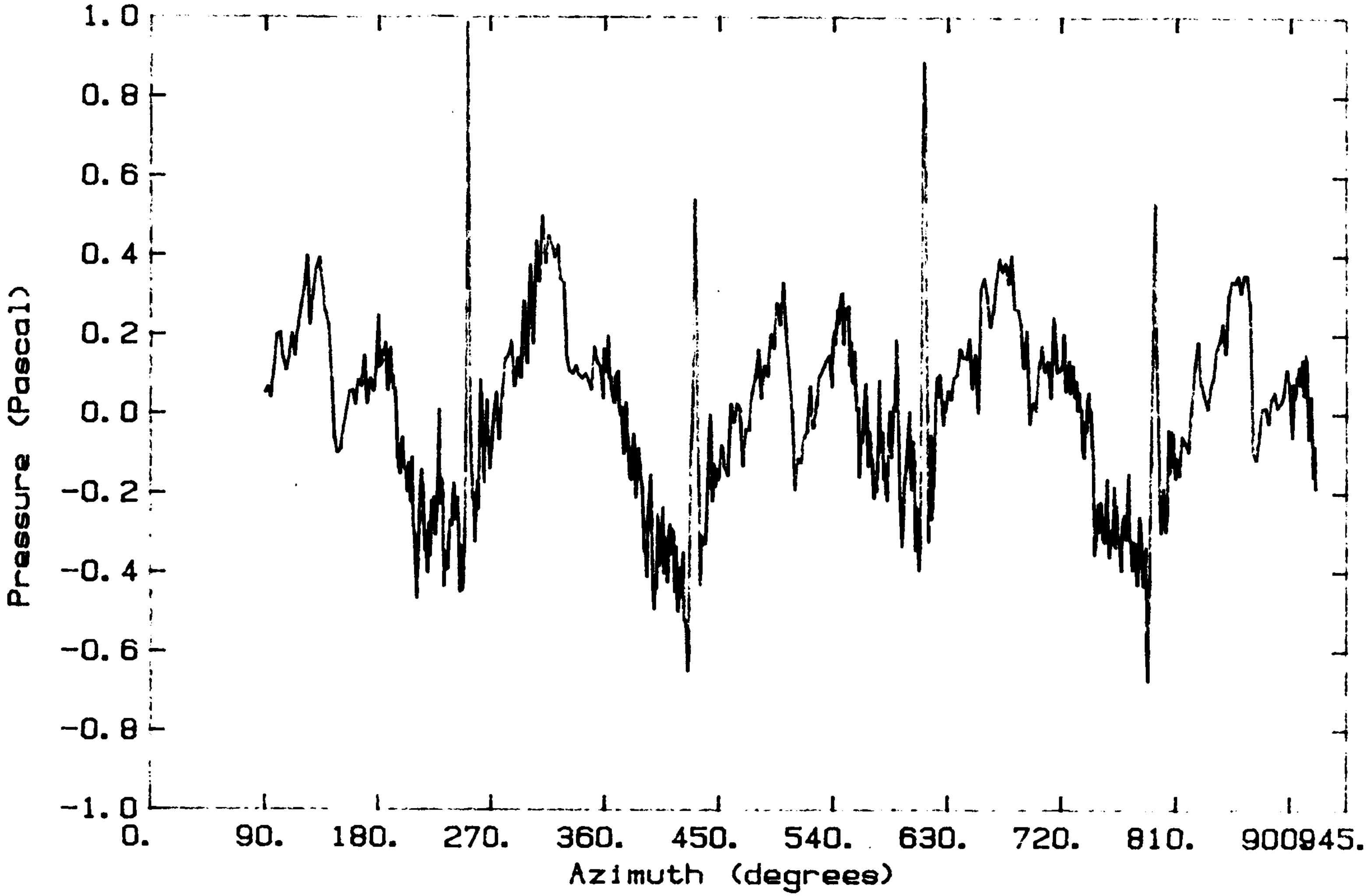

FIGURE 87. ACOUSTIC SIGNATURE AT ADVANCE RATIO OF 0.15.

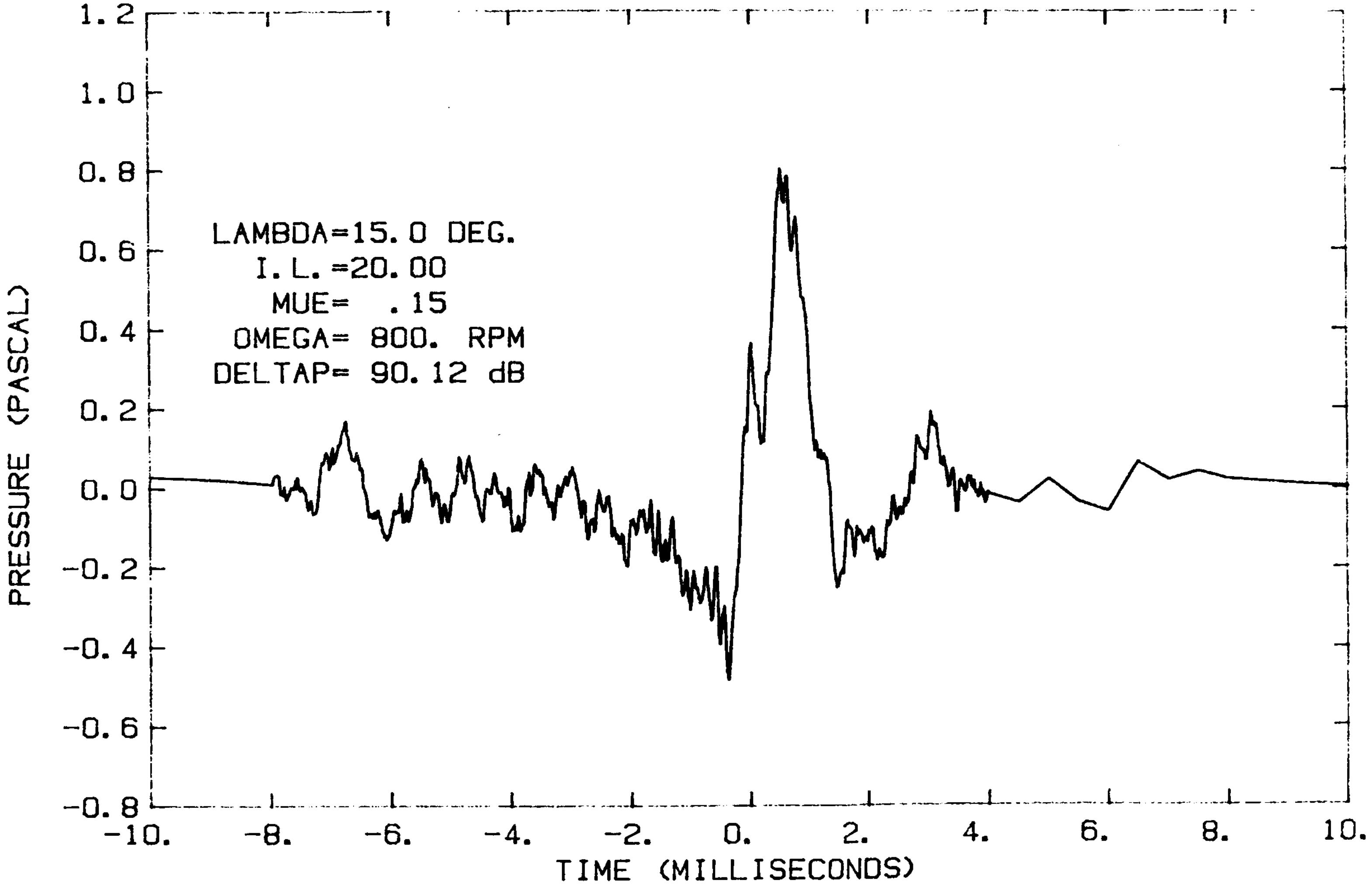

FIGURE 88. HIGH PASS FILTERED MEASURED ACOUSTIC SIGNITURE.
ADVANCE RATIO = 0.15

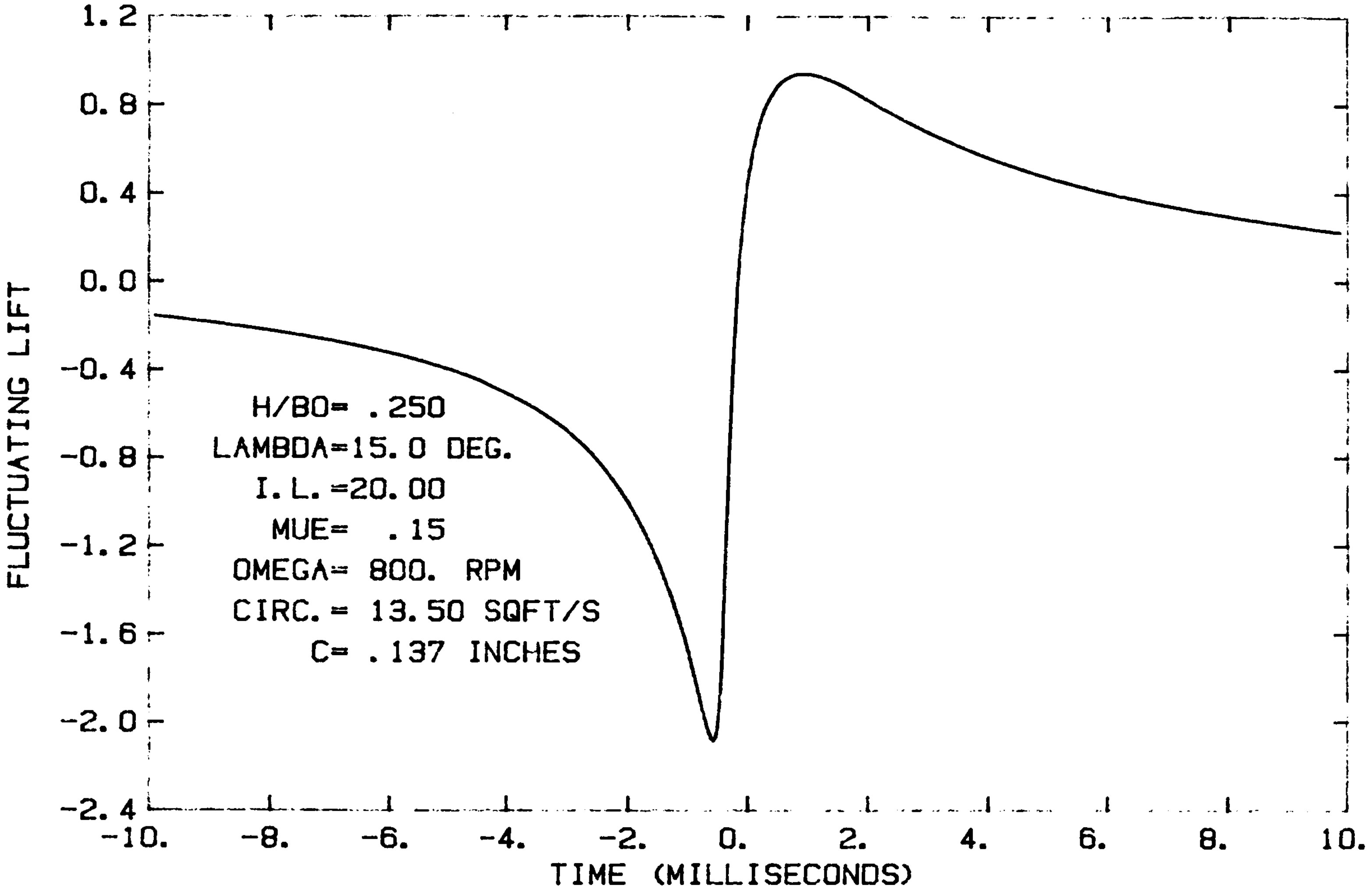

FIGURE 89. PREDICTED FLUCTUATING LIFT.

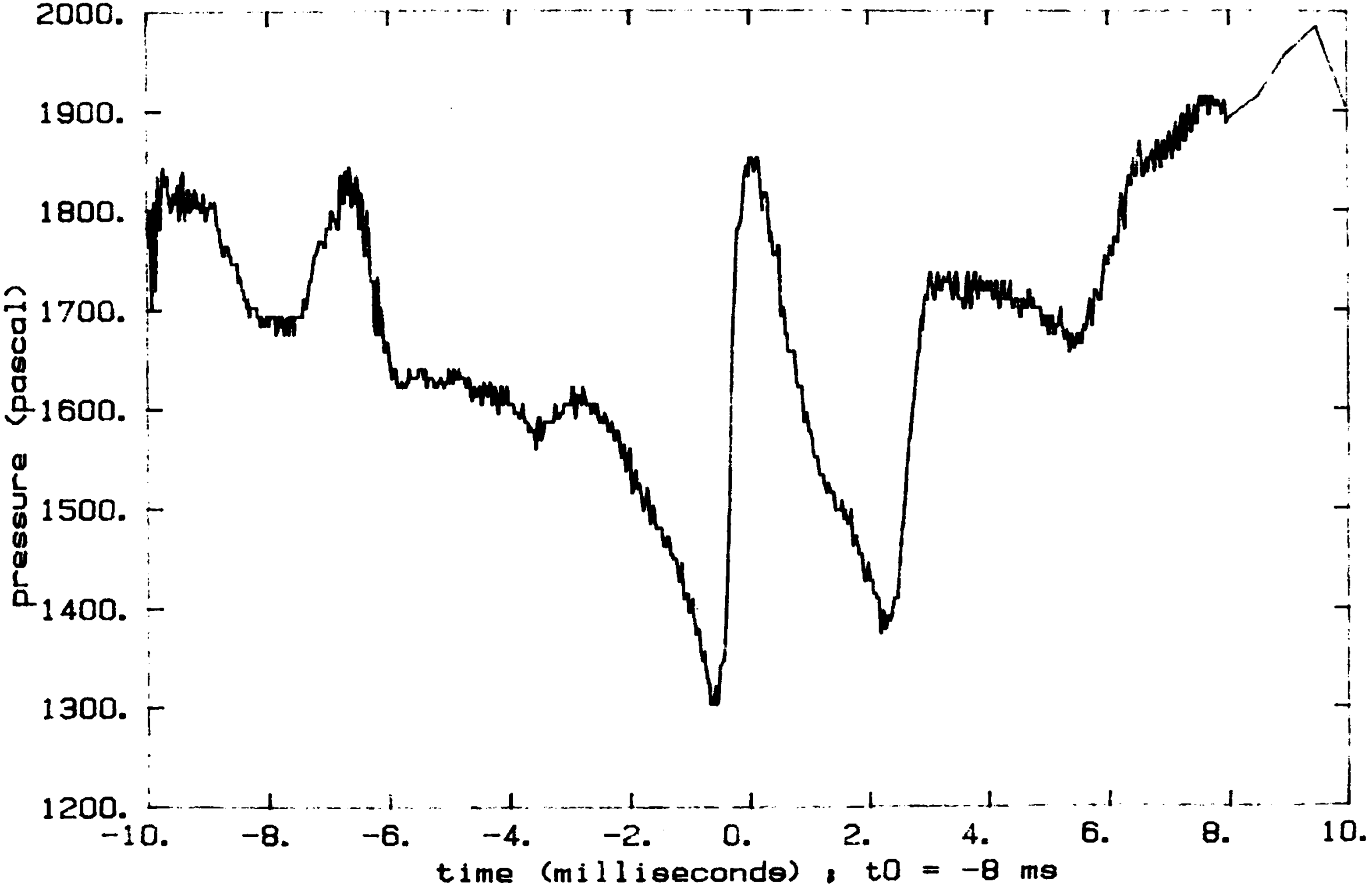

FIGURE 90. MEASURED DIFFERENTIAL PRESSURE AT 99% SPAN, 18.75% CHORD.
ADVANCE RATIO = 0.15

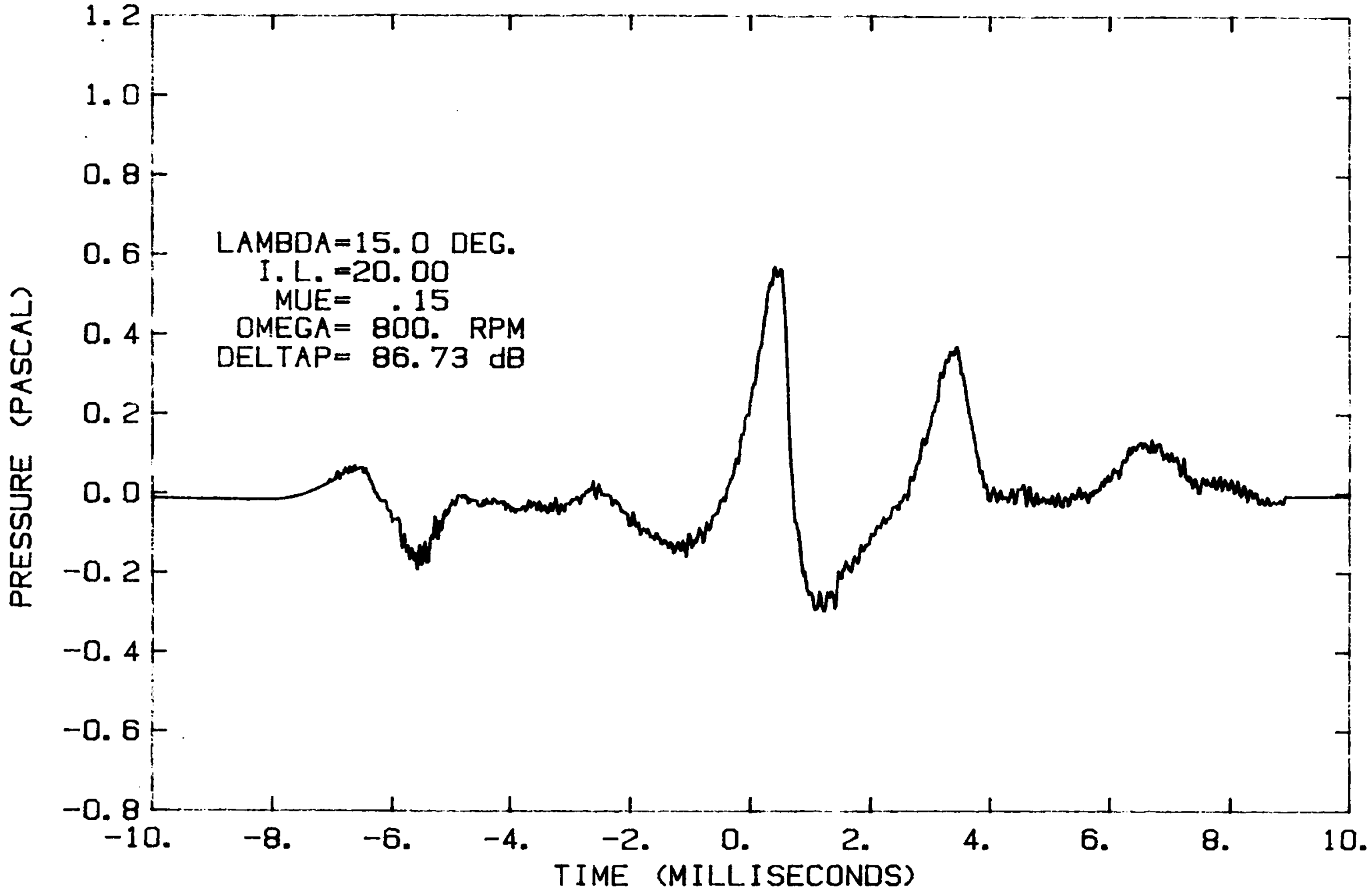

FIGURE 91. PREDICTED ACOUSTIC SIGNATURE USING THE MEASURED PRESSURE FROM 99% SPAN, 18.75% CHORD.

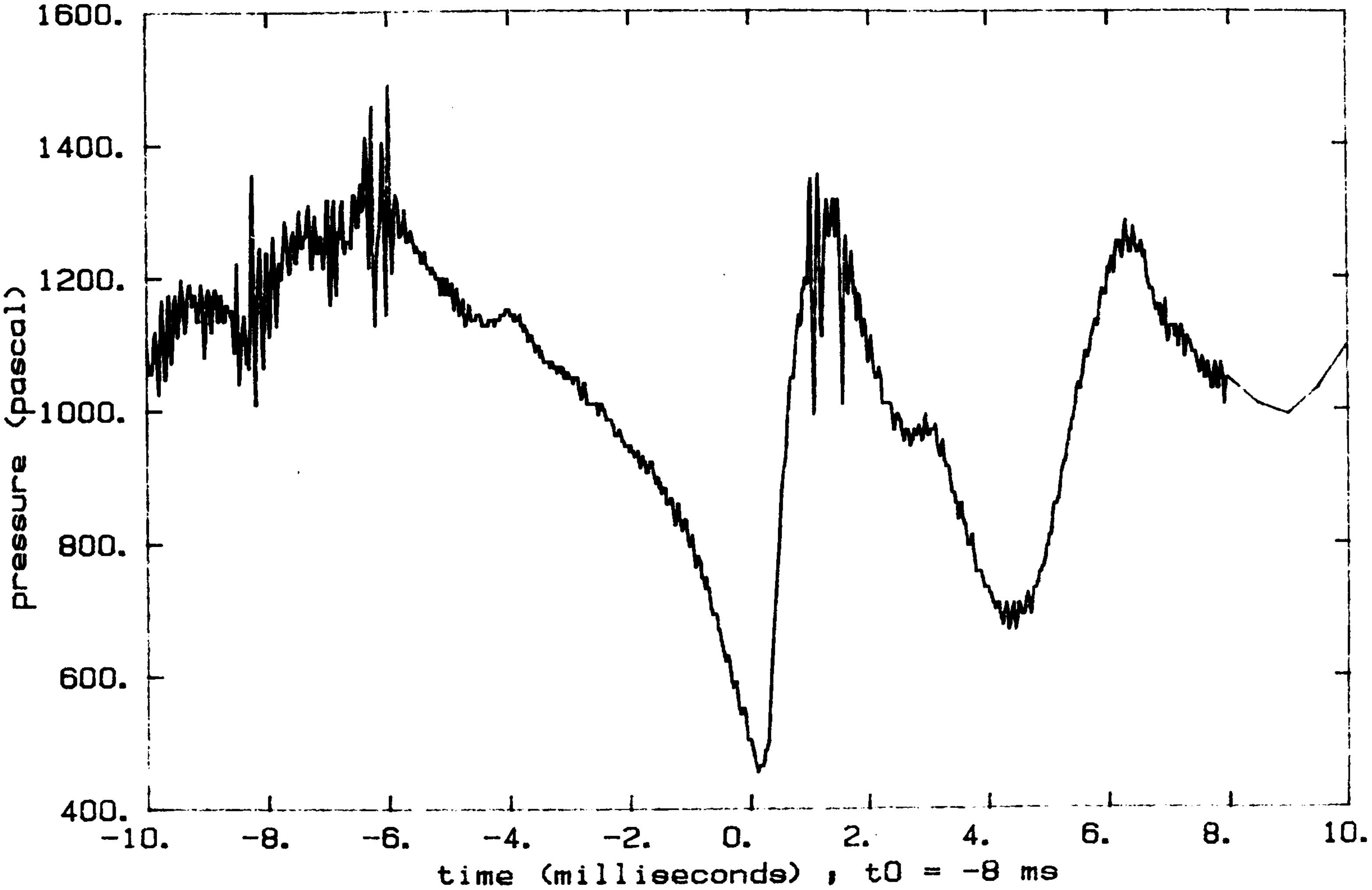

FIGURE 92. MEASURED DIFFERENTIAL PRESSURE AT 76% SPAN, 18.75% CHORD. ADVANCE RATIO OF 0.15.

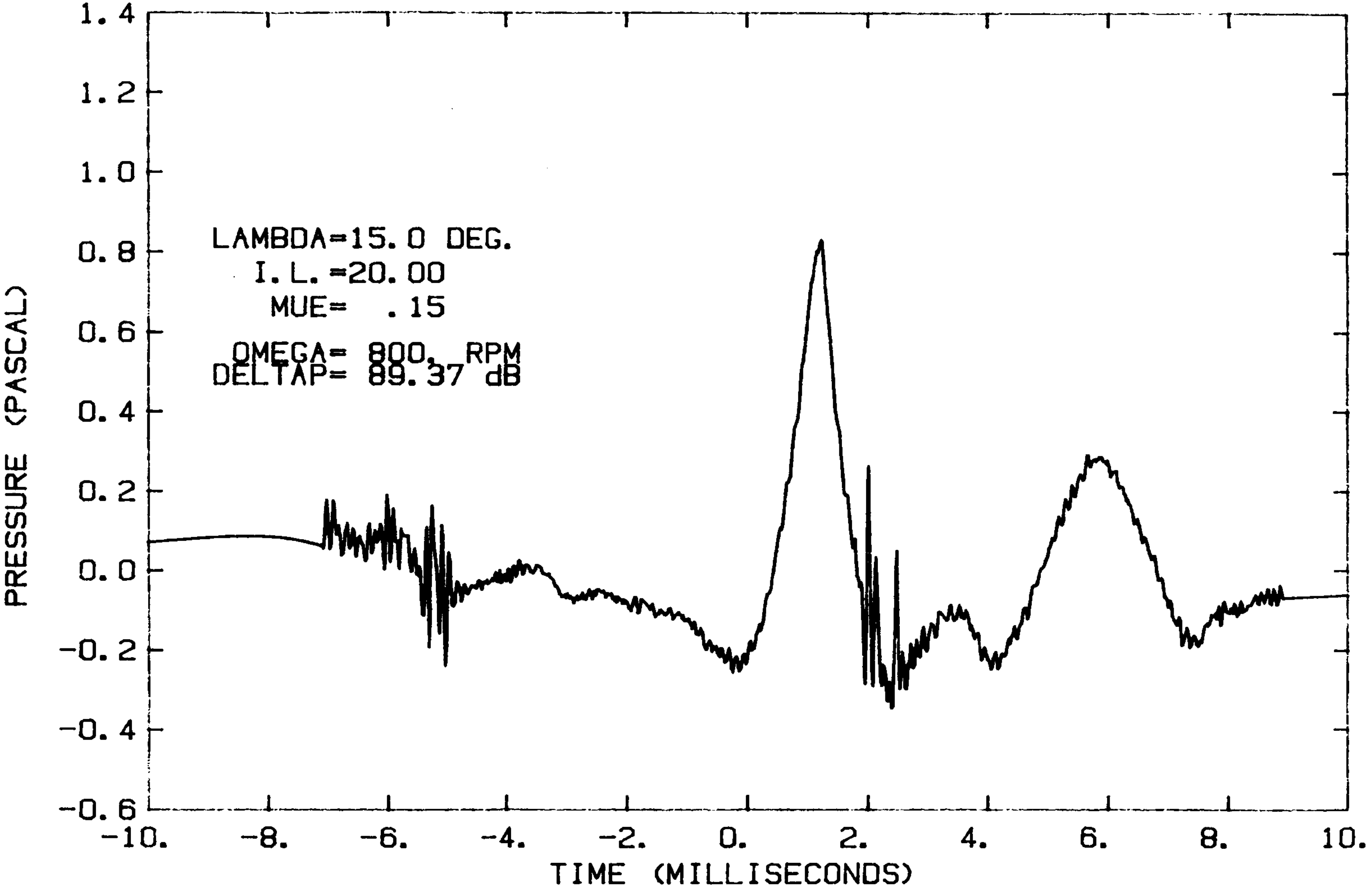

FIGURE 93. PREDICTED ACOUSTIC SIGNATURE USING THE PRESSURE MEASURED AT 76% SPAN, 18.75% CHORD.

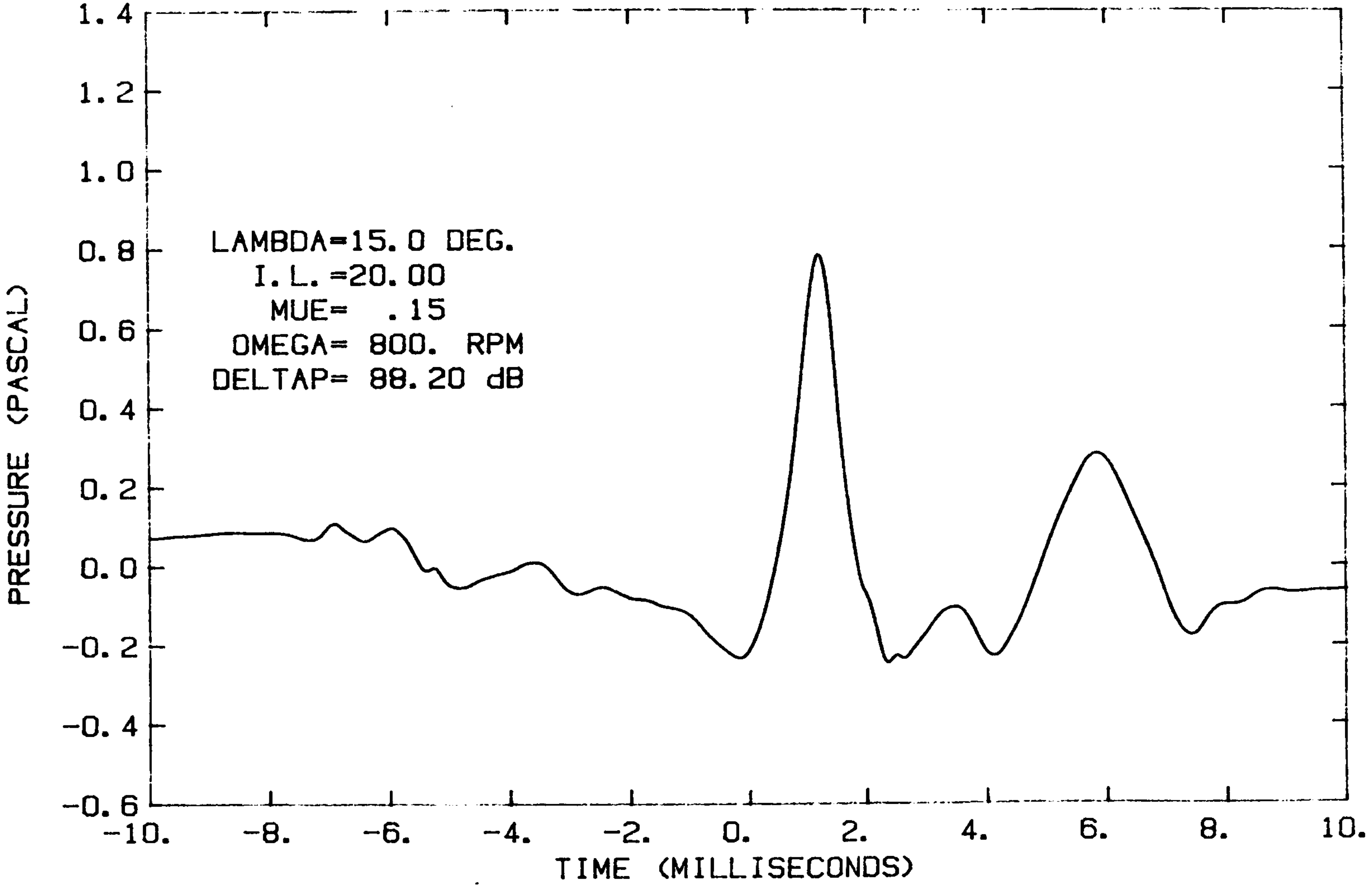

FIGURE 94. PREDICTED ACOUSTIC SIGNATURE USING THE LOW-PASS FILTERED PRESSURE FROM 76% SPAN, 18.75% CHORD.

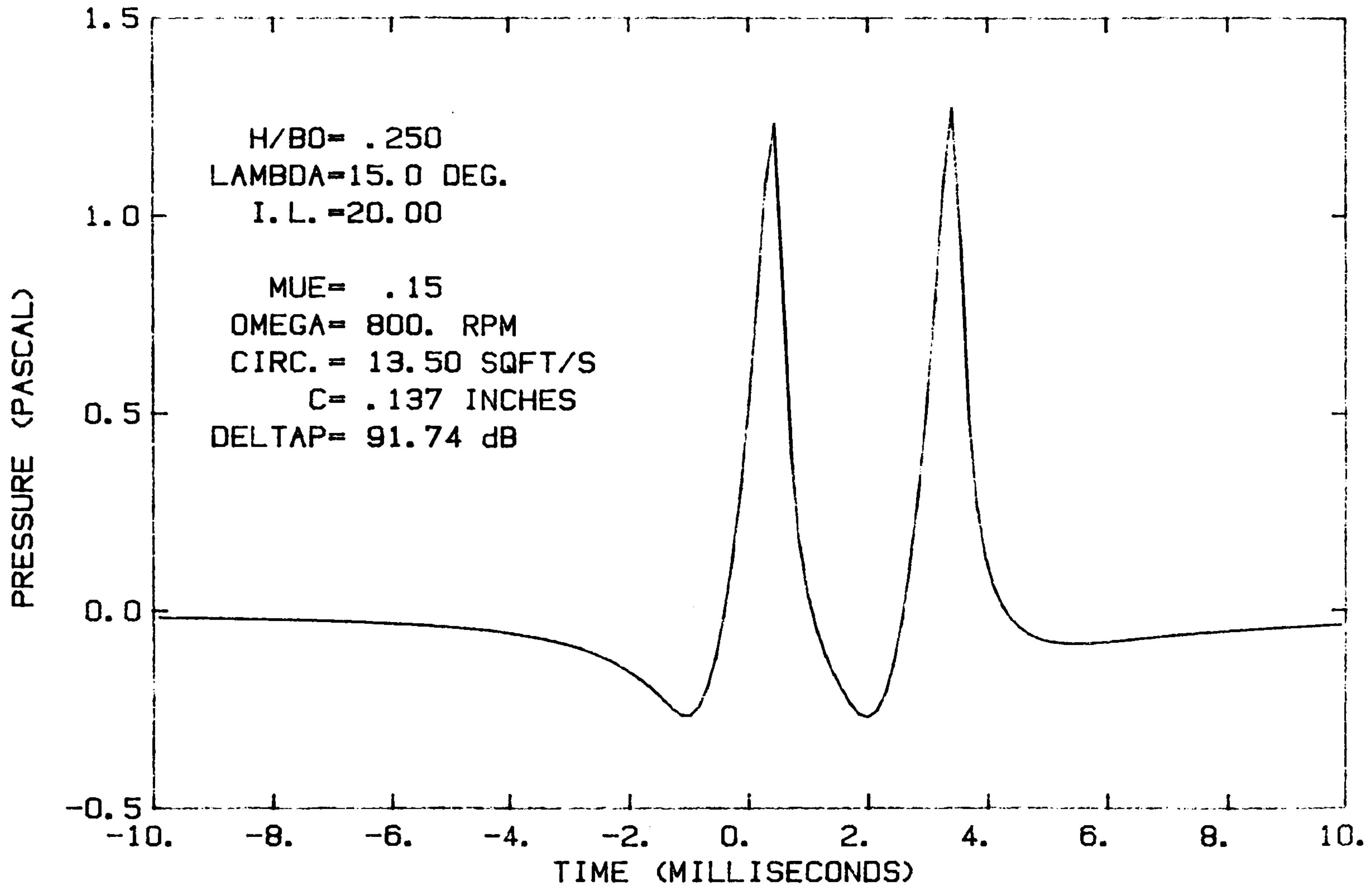

FIGURE 95. PREDICTED ACOUSTIC SIGNATURE USING TWO IDENTICAL VORTICES

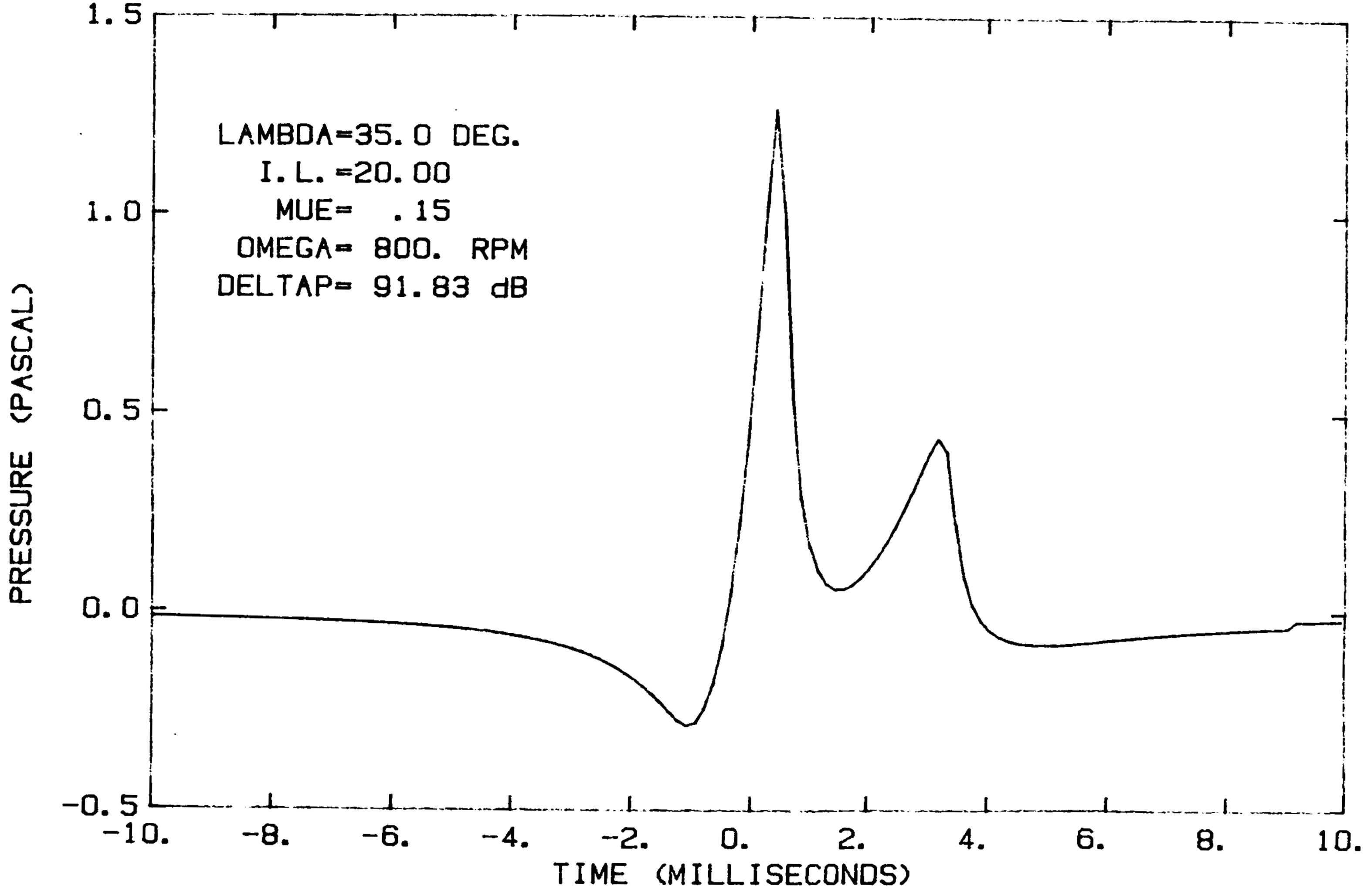

FIGURE 96. PREDICTED ACOUSTIC SIGNATURE USING SUPERPOSITION

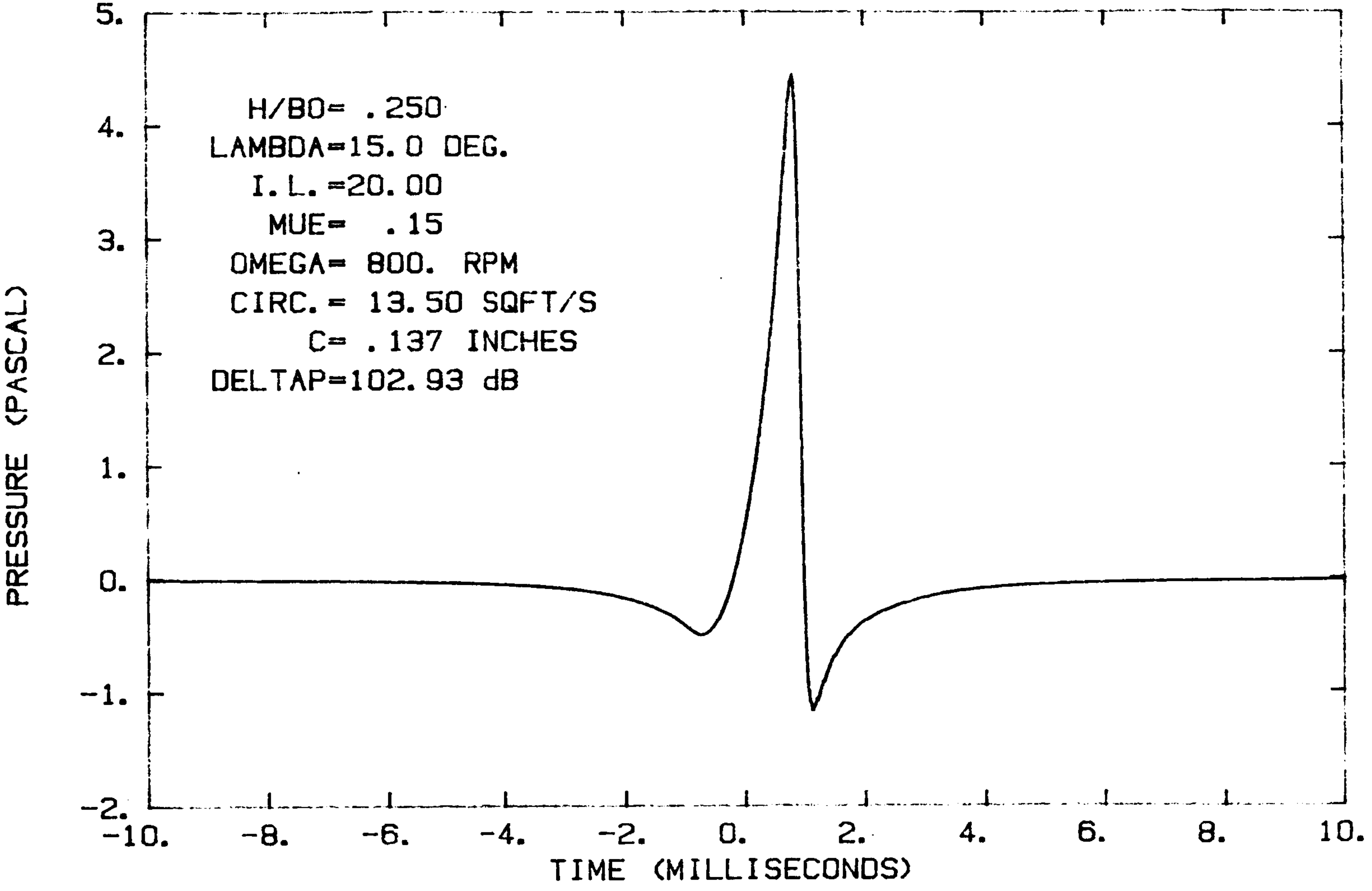

FIGURE 97. PREDICTED ACOUSTIC SIGNATURE USING THE SIMPLE LIFT MODEL

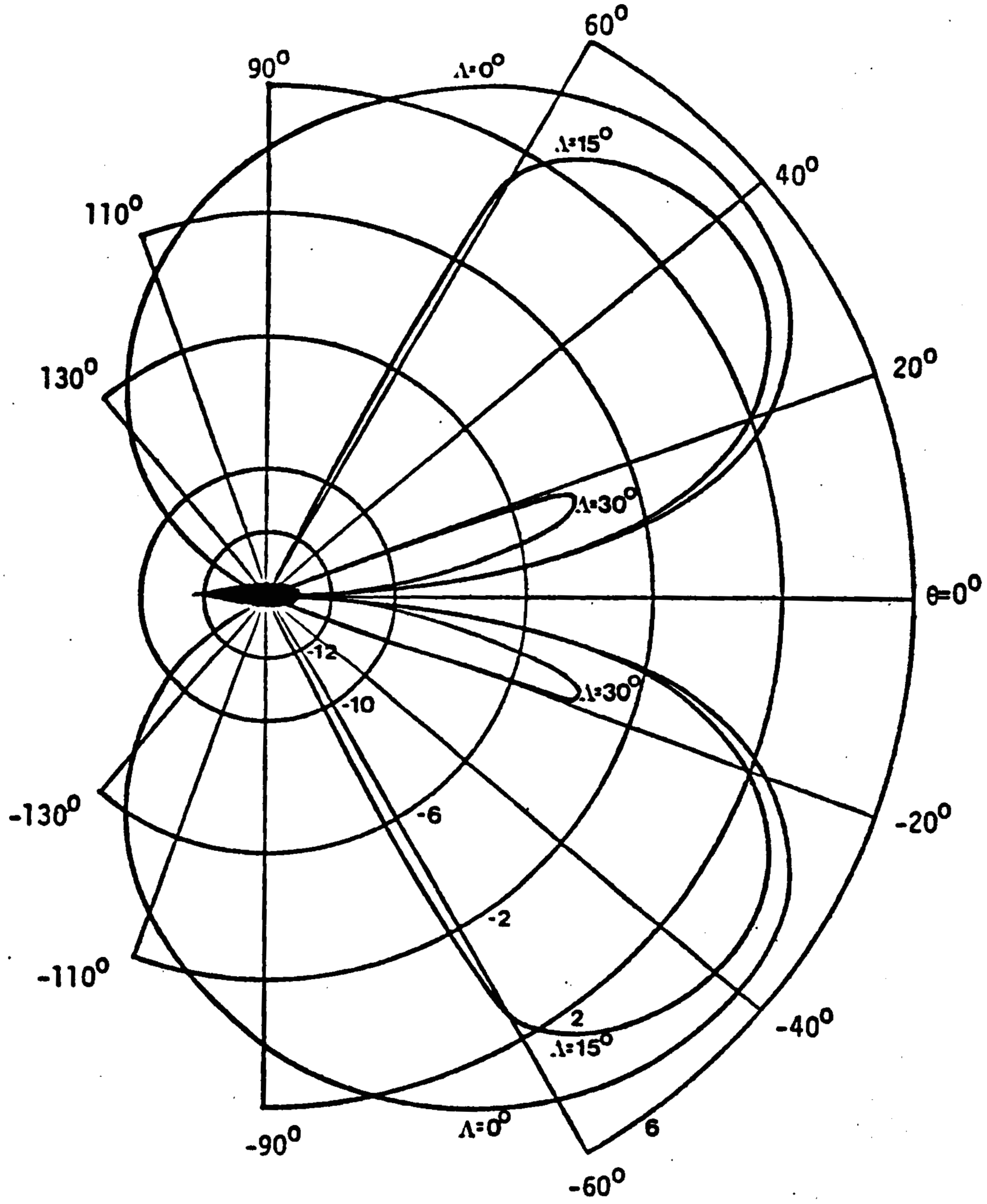

Figure 98. Directivity of blade vortex interaction (from reference [25]

NASA
National Aeronautics and Space Administration

Report Documentation Page

1. Report No.
NASA CR-177454

2. Government Accession No.

3. Recipient's Catalog No.

4. Title and Subtitle
Rotating Hot-Wire Investigation of the Vortex Responsible for Blade-Vortex Interaction Noise

5. Report Date
December 1988

6. Performing Organization Code

7. Author(s)
Richard Remo Fontana

8. Performing Organization Report No.

10. Work Unit No.
505-61-51

9. Performing Organization Name and Address
Massachusetts Institute of Technology
Cambridge, MA

11. Contract or Grant No.
NAG2-182

13. Type of Report and Period Covered
Contractor Report

12. Sponsoring Agency Name and Address
National Aeronautics and Space Administration
Washington, DC 20546-0001

14. Sponsoring Agency Code

15. Supplementary Notes

Point of Contact: Charles A. Smith, Ames Research Center, MS T-032, Moffett Field, CA 94035

16. Abstract

This distribution of the circumferential velocity of the vortex responsible for blade-vortex interaction noise was measured using a rotating hot-wire rake synchronously meshed with a model helicopter rotor at the blade passage frequency. Simultaneous far-field acoustic data and blade differential pressure measurements were obtained. Results show that the shape of the measured far-field acoustic blade-vortex interaction signature depends on the blade-vortex interaction geometry. The experimental results are compared with the Widnall-Wolf model for blade-vortex interaction noise.

17. Key Words (Suggested by Author(s))
Blade-vortex interaction
Rotor noise

18. Distribution Statement
Unclassified-Unlimited

19. Security Classif. (of this report)
Unclassified

20. Security Classif. (of this page)
Unclassified

21. No. of pages
237

22. Price
A11

NASA FORM 1626 OCT 86

For sale by the National Technical Information Service, Springfield, Virginia 22161

PREPARATION OF THE REPORT DOCUMENTATION PAGE

The last page of a report facing the third cover is the Report Documentation Page, RDP. Information presented on this page is used in announcing and cataloging reports as well as preparing the cover and title page. Thus it is important that the information be correct. Instructions for filling in each block of the form are as follows:

Block 1. Report No. NASA report series number, if preassigned.

Block 2. Government Accession No. Leave blank.

Block 3. Recipient's Catalog No. Reserved for use by each report recipient.

Block 4. Title and Subtitle. Typed in caps and lower case with dash or period separating subtitle from title.

Block 5. Report Date. Approximate month and year the report will be published.

Block 6. Performing Organization Code. Leave blank.

Block 7. Author(s). Provide full names exactly as they are to appear on the title page. If applicable, the word editor should follow a name.

Block 8. Performing Organization Report No. NASA installation report control number and, if desired, the non-NASA performing organization report control number.

Block 9. Performing Organization Name and Address. Provide affiliation (NASA program office, NASA installation, or contractor name) of authors.

Block 10. Work Unit No. Provide Research and Technology Objectives and Plans (RTOP) number.

Block 11. Contract or Grant No. Provide when applicable.

Block 12. Sponsoring Agency Name and Address. National Aeronautics and Space Administration, Washington, D.C. 20546-0001. If contractor report, add NASA installation or HQ program office.

Block 13. Type of Report and Period Covered. NASA formal report series; for Contractor Report also list type (interim, final) and period covered when applicable.

Block 14. Sponsoring Agency Code. Leave blank.

Block 15. Supplementary Notes. Information not included elsewhere: affiliation of authors if additional space is required for block 9, notice of work sponsored by another agency, monitor of contract, information about supplements (film, data tapes, etc.), meeting site and date for presented papers, journal to which an article has been submitted, note of a report made from a thesis, appendix by author other than shown in block 7.

Block 16. Abstract. The abstract should be informative rather than descriptive and should state the objectives of the investigation, the methods employed (e.g., simulation, experiment, or remote sensing), the results obtained, and the conclusions reached.

Block 17. Key Words. Identifying words or phrases to be used in cataloging the report.

Block 18. Distribution Statement. Indicate whether report is available to public or not. If not to be controlled, use "Unclassified-Unlimited." If controlled availability is required, list the category approved on the Document Availability Authorization Form (see NHB 2200.2, Form FF427). Also specify subject category (see "Table of Contents" in a current issue of STAR), in which report is to be distributed.

Block 19. Security Classification (of this report). Self-explanatory.

Block 20. Security Classification (of this page). Self-explanatory.

Block 21. No. of Pages. Count front matter pages beginning with iii, text pages including internal blank pages, and the RDP, but not the title page or the back of the title page.

Block 22. Price Code. If block 18 shows "Unclassified-Unlimited," provide the NTIS price code (see "NTIS Price Schedules" in a current issue of STAR) and at the bottom of the form add either "For sale by the National Technical Information Service, Springfield, VA 22161-2171" or "For sale by the Superintendent of Documents, U.S. Government Printing Office, Washington, DC 20402-0001," whichever is appropriate.